Technische Universität München

Max-Planck-Institut für Astrophysik

Modeling Neutrino-Driven Supernova Explosions Across the Stellar Mass and Metallicity Range

Thomas Michael Ertl

Vollständiger Abdruck der von der Fakultät für Physik der Technischen Universität München zur Erlangung des akademischen Grades eines

Doktors der Naturwissenschaften (Dr. rer. nat.)

genehmigten Dissertation.

Vorsitzender:		Univ.-Prof. Dr. Lothar Oberauer
Prüfer der Dissertation:	1.	Priv.-Doz. Dr. Hans-Thomas Janka
	2.	Univ.-Prof. Dr. Björn Gabrecht
	3.	Univ.-Prof. Dr. Norbert Langer

Die Dissertation wurde am 03.08.2016 bei der Technischen Universität München eingereicht und durch die Fakultät für Physik am 18.11.2016 angenommen.

Contents

1. Introduction **1**
- 1.1. Stellar Evolution and Nucleosynthesis 1
- 1.2. Explosion Mechanism of Core-Collapse Supernovae 3
- 1.3. Observations of Core-Collapse Supernovae 5
- 1.4. Outline 7

2. Methodology and Theory of Neutrino-Driven Explosions **9**
- 2.1. Status of “Ab Initio” Supernova Modeling 9
- 2.2. Modeling Recipes in Recent Literature 11
- 2.3. Motivation of the Modeling Assumptions of this Work 12

3. Numerical Realization in Prometheus-Hotb **23**
- 3.1. Hydrodynamics and Self-Gravity 24
- 3.2. Equation of State and Nuclear Reactions 26
  - 3.2.1. Low Densities and Low Temperatures 27
  - 3.2.2. Nuclear Reaction Network 28
  - 3.2.3. Nuclear Statistical Equilibrium 31
  - 3.2.4. Equation of State at High Densities 32
  - 3.2.5. Setup During Core Collapse 33
- 3.3. Neutrino Treatment 34
  - 3.3.1. Deleptonization Scheme 35
  - 3.3.2. Gray Transport Solver 36
- 3.4. Innermost Excised Region and its Boundary Condition 38
  - 3.4.1. Hydrostatic and Contracting Boundary Condition 38
  - 3.4.2. Analytic One-Zone Core-Cooling Model 39
  - 3.4.3. Setup of the Long-Time Evolution 41

4. Calibration and Progenitor Models **43**
- 4.1. Calibration of the Analytic One-Zone Core-Cooling Model 43
  - 4.1.1. SN 1987A and its Progenitor Star Sk -69^o 202 44
  - 4.1.2. The Crab Nebula – Remnant of SN 1054 49
  - 4.1.3. Dynamical Evolution of the Calibration Models 49
  - 4.1.4. Connection of Crab-Like and SN 1987A-Like Progenitor Models . . 55
- 4.2. Sets of Progenitor Models Across the Stellar Mass Range 58

5. A Two-Parameter Criterion for the Explodability of Massive Stars 61
5.1. Introduction 61
5.2. One and Two-Parameter Classifications 68
5.3. Two-Parameter Classification Based on the Theoretical Concept of the Neutrino-Driven Mechanism 72
5.4. Separation Line of Exploding and Non-Exploding Progenitors 75
5.5. Stellar Outliers 80
5.6. Systematics of Progenitor and Explosion Properties in the Two-Parameter Plane 82
5.7. Influence of the Neutron Star Radius 86
5.8. Brief Comparison to Previous Works 87
5.9. Conclusions 89

6. Properties of the Explosive Outflow 93
6.1. Combined Set of Solar-Metallicity Models 93
  6.1.1. Observable Signatures and Their Correlations 94
  6.1.2. Systematics of the Calibration Model 96
  6.1.3. Explosive Nucleosynthesis and Light Curves by Post-Processing with KEPLER 99
6.2. Comparison to Ugliano et al. (2012) 101
  6.2.1. Zero-Age Main-Sequence Mass Outcome Pattern 101
  6.2.2. Low-Mass Progenitor Models 103
  6.2.3. Late-Time Fallback 104
6.3. Further Sets with Solar Metallicity 108
6.4. Sets of Models with Sub-Solar Metallicities 109
6.5. Conclusions 115

7. Compact Remnants 119
7.1. IMF-Weighted Remnant Distributions 120
  7.1.1. Neutron Stars 122
  7.1.2. Black Holes 123
7.2. Metallicity Dependence of BH Formation by Late-Time Fallback 126
  7.2.1. Energy Budget 126
  7.2.2. Fallback by Deceleration of the Shock 131
7.3. Conclusions 134

8. Summary and Conclusions 137

A. Appendix to Chapter 4 – Calibration and Progenitor Models 145
A.1. Combined Set of Solar-Metallicity Progenitors 146
A.2. Solar-Metallicity Set s2002 148
A.3. Solar-Metallicity Set s2007 149
A.4. Solar-Metallicity Set n2006 150

A.5. Ultra Metal-Poor Set u2002 151
A.6. Metal-Free Set z2011 152
A.7. Metal-Free Set z2002 153

B. Appendix to Chapter 6 – Properties of the Explosive Outflow 155
B.1. Combined Set of Solar-Metallicity Progenitors 155
B.2. Solar-Metallicity Set s2002 160
B.3. Solar-Metallicity Set s2007 165
B.4. Solar-Metallicity Set n2006 171
B.5. Ultra Metal-Poor Set u2002 177
B.6. Metal-Free Set z2011 182
B.7. Metal-Free Set z2002 187

C. List of Abbreviations 193

Bibliography 195

Danksagung 203

1. Introduction

The violent deaths of stars in supernova (SN) explosions are extreme events regarding many aspects. They are extremely bright, sometimes brighter than their host galaxy, they eject vast amounts of matter, several times the mass of our Sun, and they expel material at high velocities of about to a significant fraction of the speed of light. But supernovae also deliver essential ingredients for life on our planet as they are the main sources of many heavy elements. Heavy elements formed and ejected in these explosions are needed for the complex chemistry in living organisms (the carbon in the sugar we consume, the oxygen we breath, the iron in our blood, etc.) and they constitute the bulk of our planet's mass (iron, manganese, silicon). In the following we will take a brief look on how and when a star synthesizes these elements, by what mechanism it ejects them into the interstellar medium (ISM) and now it serves as raw material for new stars, planets, and the basis of life. The chapter is based on the historic review by Bethe (1990), the modern reviews on core-collapse supernovae (CCSNe) by Janka et al. (2007; 2012) and Burrows (2013), and the review on massive star evolution by Woosley et al. (2002). At the end of this chapter we will outline the thesis at hand. The current state of SN research and a detailed discussion of our methodology are presented in Chap. 2.

1.1. Stellar Evolution and Nucleosynthesis

Elements heavier than boron are (mostly) synthesized in stars or their compact remnants. Only the lightest elements, hydrogen, helium, and (to some minor extent) lithium, are synthesized primordially in the early universe. Heavy elements only came into existence after the first stars were formed. Stars forge heavy elements by nuclear fusion of lighter elements in their cores and eject them either by winds or by a supernova explosion at the end of their life. During the SN additional heavy elements are produced by explosive burning. These elements are mixed into the ISM, which cools over time and provides the material for a new generation of stars is formed out of it. In this way the heavy-element abundance, the so-called metallicity, of the universe increases with each generation of stars.

All stars begin their life by the fusion of hydrogen to helium and they do this for the longest time of their evolution. Four protons fuse and form an α-particle while releasing two neutrinos and positrons along with the binding-energy difference in the form of thermal energy. The next stage of stellar evolution is helium-core burning, in which the accumulated helium ashes of the previous burning stage become the new fuel. This is generally true for all burning stages: the ashes of the previous burning stage become the fuel for the next. The helium core ignites when the temperature is sufficiently high for the so-called triple-α process, in which three α-particles form carbon. This releases huge amounts of energy, transforming the (hydrogen core-burning) main-sequence star into a (helium-core burning or hydrogen-shell burning) giant star. The phase of helium burning is also the final stage for core nuclear fusion of our Sun and stars with up to eight times the solar mass ($1\,M_\odot = 1.989 \times 10^{33}\,\mathrm{g}$). This final phase is ultimately marked by the ejection of the outer shells in a planetary nebula and the formation of a white dwarf in the center.

The so-formed white dwarf can explode in a thermonuclear supernova, if it is part of a binary system. In this scenario material is added to the degenerate dwarf-star, either by mass transfer or by merging with another white dwarf (e.g., Hillebrandt & Niemeyer, 2000) leading the ignition of the unburned carbon and oxygen from the progenitor star. Which of the two scenarios is (primarily) realized in nature is still unknown.

However, in this work we are not interested in thermonuclear explosions of white dwarfs but another type of SNe. Stars more massive than eight times the mass of our Sun. These stars reach more advanced burning stages beyond helium core-burning. With every new core-burning stage, the star consumes the nuclear fuel on even shorter time scales: carbon core-burning proceeds within only thousands of years and silicon burning within a few days. The hydrogen burning, in contrast, takes millions or even billions of years. The core of a massive star and its late stages "can be envisioned overall as the neutrino-mediated Kelvin-Helmholtz contraction of a carbon-oxygen core, punctuated by occasional delays when the burning of a nuclear fuel provides enough energy to balance neutrino losses" (Woosley et al., 2002). In these advanced evolutionary stages the star produces ever heavier elements by fusion until it reaches an iron core in its center after silicon-shell burning. The iron core itself is an inert object, because the iron-group elements are the most stable in nature. The iron core is stabilized against its gravity by the degeneracy pressure of electrons. At some point it will collapse, releasing its gravitational binding energy in a so-called core-collapse supernova (CCSN). We will see shortly how this proceeds.

Massive stars of different zero-age main-sequence (ZAMS) masses and metallicities evolve differently. All episodes of stellar evolution with core and shell-burning processes determine the final structure of the massive star. The final fate, explosion or not, is tightly connected to the core structure of the massive star. Which massive stars explode is a topic of ongoing scientific research and it is also one of the topics of the thesis at hand.

1.2. Explosion Mechanism of Core-Collapse Supernovae

Energy Reservoir

At the end of its life a massive star consists of concentric shells of the ashes of the previous core-burning stages. In the final episode, the massive star breeds an iron-core in its center by continuous silicon-shell burning. The binding energy of the iron core is the energy reservoir that powers the tremendous explosion, capable of outshining its own host galaxy. The source of energy was identified only a few years after the discovery of the neutron by Baade & Zwicky (1934), who speculated about neutron stars and that these massive, compact objects could be the counterpart of a "supernova", a term they coined as well.

The collapse of the inner core of a massive star forming a neutron star (NS) releases a huge amount of gravitational binding energy that can be extimated by

$$\Delta E_b \approx \frac{G M_{\mathrm{core}}^2}{R} = 3 \times 10^{53} \left(\frac{M_{\mathrm{core}}}{M_\odot}\right)^2 \left(\frac{R}{10\,\mathrm{km}}\right)^{-1} \mathrm{erg}, \tag{1.1}$$

with G denoting the gravitational constant, R being the final radius of the NS, and M_{core} its mass. For a successful explosion only a few percent of this energy needs to be tapped to power the explosive outflow of a SN. The problem to understand a CCSN appears simple, but is still not fully understood, even after more than half a century of research.

Core Collapse and Bounce

The iron core, which is still growing by silicon-shell burning, collapses when it reaches the Chandrasekhar mass limit for the gravitational stability of the stellar core. The mass limit depends quadratically on the lepton number per baryon, which is proportional to the squared electron fraction, Y_e. Note, that the final iron-core mass prior to collapse depends on the progenitor evolution. Some stars can grow more massive iron cores than others leading to different core structures prior to iron-core collapse, which again influences the outcome – explosion or not. The electron fraction is mediated by two weak processes: electron captures on iron-group nuclei and β-decay of neutron-rich nuclei.

The collapse instability proceeds by photodissociation of nuclei removing internal energy from the core and the electrons becoming relativistic. The electron degeneracy pressure can no longer stabilize the iron core against gravity. As consequence, the adiabatic index of the matter is close to or even below 4/3, an indicator for gravitational instability. The core collapse is further aided by the electron captures on nuclei. The loss of neutrinos further decreases the electron fraction and also the lepton number as the generated neutrinos can still escape freely. Again, the Chandrasekhar mass limit provides a qualitative understanding of the effect, because of its quadratic dependence on the lepton number. With the lepton losses of the core, the mass limit is shifted to lower values.

At densities around $\rho_{\text{trap}} \sim 10^{12}\,\text{g}\,\text{cm}^{-3}$ the diffusion time of neutrinos becomes larger than the collapse timescale. The neutrinos are effectively trapped in the core. Consequently, the lepton-losses from the core are effectively stopped and the collapse proceeds homologously until the central density reaches $\rho_{\text{nuc}} \sim 10^{14}\,\text{g}\,\text{cm}^{-3}$. At these nuclear densities the collapse comes to a halt, because the equation of state stiffens by repulsive nuclear forces. A sound wave originating at the center steepens into a shock wave at the edge of the homologous core. This is the so-called core bounce. The shock is launched into the still collapsing iron core, where it looses most of its energy by photodissociation of iron-group nuclei ($\sim 10^{51}$, erg per 0.1 $M_{\odot}$ of iron-core material). Another significant amount of energy is lost by a burst of neutrino emission once the density behind the shock drops below the neutrino-trapping density.

Delayed Neutrino-Driven Mechanism

As a first suggestion, the explosion mechanism was thought to be of a purely fluid-dynamical nature, the so-called *bounce-shock* or *prompt-shock mechanism*. Yet the shock with initially positive post-shock velocities turns into a (radially) stalled accretion shock, which marks the failure of the *bounce-shock mechanism*. Although the *bounce-shock mechanism* fails, it is still of relevance because it sets the stage for the *delayed neutrino-driven mechanism*. The binding energy of the collapsing core of the massive star is channeled into the bounce-shock only by a small fraction, while a larger portion is converted into thermal energy of the newly formed proto-neutron star (PNS). The hot PNS cools almost entirely by the emission of neutrinos. The idea that these neutrinos could be the key for successfully reviving the stalled shock was first advocated by Colgate & White (1966) and later revisited in the form of the delayed mechanism by Wilson (1985).

The neutrinos play their decisive role behind the stalled accretion shock. Two processes contribute to the neutrino luminosity: accretion of material onto the PNS and cooling of the latter. The ram pressure of the infalling material impedes the shock expansion. Matter falling through the shock accretes onto the PNS and drives the latter towards the limit for BH formation, which depends on the unknown equation of state for nuclear matter. [*] Since the stellar fluid is not perfectly transparent to neutrinos as they stream off the neutrinosphere, some neutrinos deposit some of their energy between the PNS and the stalled shock mainly by charged-current reactions on free nucleons, neutrons and protons.

For a successful revival of the stalled accretion-shock, the neutrino energy deposition in the gain region (i.e. the region where net neutrino energy deposition exceeds the cooling due to neutrinos) needs to overcome the ram pressure of the supersonically collapsing outer shells. This condition is captured by the concept of a "critical luminosity" (Burrows &

---

[*] Once a BH forms, the neutrino source is shut off, setting a time limit for the success of the delayed neutrino-driven mechanism of the order of seconds.

Goshy, 1993) for a given mass-accretion rate: if the critical value is surpassed, the shock expands, and the star explodes.

The *delayed neutrino-driven mechanism* is certainly the most promising and most elaborate mechanism for CCSNe. For an overview of alternative explosion mechanisms the reader is pointed to the review by Janka (2012).

Supernova Simulations

The question whether massive stars explode by the delayed neutrino-driven mechanism is subject to ongoing scientific efforts. Numerical simulations are an indispensable method, because the processes of energy conversion in the core of a SN are highly entangled and dynamical. Ideally, self-consistent simulations, which model all relevant physical phenomena and without significant physics constraints are needed to answer the question of shock-revival and explosion. We will elaborate on the current status and the ingredients thought to be needed for shock-revival by neutrinos in Chap. 2, where we will also introduce the approach towards the SN problem chosen in this work: Simplified simulations of CCSNe to explore the effects of the neutrino-driven mechanism on a large set of progenitor models at a reduced computational cost. We can then compare the results of the simulations to the population of observed CCSNe.

1.3. Observations of Core-Collapse Supernovae

Observed CCSNe

SN observations have an old tradition, starting already in the pre-scientific era before telescopes were available. Therefore, observations relied on the unaided eye and only galactic SNe could be observed. One of these historic events was SN 1054 a CCSN observed by Chinese astronomers. The SN was described as a “guest star” that suddenly appeared visible for some time before it vanished again. Today the remnant of SN 1054, the Crab nebula, is one of the most observed objects in the night sky (for a review, see Hester, 2008). What we see today as Crab nebula, is not the light from the explosion itself, but the inner ejecta of the SN illuminated by a pulsar in the center. The pulsar is a fast spinning NS with periods of milliseconds produces, which a magnetically driven wind. Although SN 1054 was not observed spectroscopically when it occurred, modern observations of the remnant indicate the following observational properties: the progenitor star was a massive star at the low-mass end for CCSNe ($8-10\,M_{\odot}$, e.g., Nomoto et al., 1982, Smith, 2013), which exploded with a low final kinetic energy (or explosion energy) of $\sim 0.1\,\mathrm{B} = 10^{50}\,\mathrm{erg}$ (e.g., Tominaga et al., 2013, Smith, 2013, Yang & Chevalier, 2015), and little nickel ejecta masses. The latter powers the light curve by radioactive decay. Also the pulsar, i.e. a rapidly rotating NS, was formed during the explosion illuminating the remnant at the moment. Furthermore, we gain a coarse light curve from the historic records taking the visibility during daytime (23 days) and the time until it was no longer visible at night (653 days) (see Fig. 1 in Smith, 2013). These properties indicate that SN 1054 was a weak explosion concerning kinetic energy and nickel ejecta mass if we compare to the population of observed CCSNe.

A more energetic representative is the SN that was observed in February, 1987 (SN 1987A) in the Large Magellanic Cloud (LMC), a dwarf galaxy orbiting our galaxy, the Milky Way, at a distance of ~ 160 thousand light-years. Although SN 1987A is not a galactic SN it is still close enough to be observed with the naked eye and it has been the closest known SN for ~300 years (Cassiopeia A). The explosion energy (~1.5×10^{51} erg; Arnett et al., 1989, Utrobin et al., 2015) and nickel ejecta mass ($0.07\,M_{\odot}$; Bouchet et al., 1991, Suntzeff et al., 1992) are measured for this SN. In addition, its neutrino signal was observed, and it was possible to identify the progenitor star in archival images, making it an extraordinary event. Its close proximity to earth allowed for the observation of 24 neutrinos (Hirata et al., 1987, Bionta et al., 1987), which constrained the mean energies of the neutrinos and the duration of the signal. The neutrinos originated from the core of the SN and could therefore be a first hint of the neutrino-driven explosion mechanism. The progenitor star was identified to be a blue supergiant (Walborn et al., 1987) This was unexpected at that time. A blue supergiant is more compact than a red supergiant and was therefore thought to be harder to explode.

The observational properties of SN 1054 and SN 1987A are well-constrained and both SNe are extensively modeled by theory. Both SNe will therefore be used as reference for the modeling approach of this work.

Population of CCSNe and Compact Remnants

In this theoretical study, we do not aim at explaining individual SNe, but try to explain observations connected to the population of CCSNe. Many SNe are observed, but due to their distance or shielding by dust only some of their properties can be determined, like the explosion energy or parts of the light curve. If the SN is close enough and not obscured by dust the amount of nickel ejected can be derived from the tail of the light curve.

Determining the progenitor star of a SN is difficult, because a high-resolution image of the region prior to the event is needed as well as a follow-up image to proof that the progenitor candidate is gone. The first unambiguous identification of a progenitor star was the blue supergiant that exploded as SN 1987A. Only in the recent years the list of progenitor stars could be extended (Smartt et al., 2009, Smartt, 2015). The connection of the identified progenitor stars with their approximate (but model-dependent) masses opens a new observational window for CCSNe. These studies suggest that only stars up to about ~ $18\,M_\odot$ explode, while all stars with higher masses die quietly forming BHs. These quietly disappearing stars are searched for (see Reynolds et al., 2015, for candidates).

Another observational source for SN research is the population of compact objects. For the population of NSs, binary systems with one (or two) radio pulsar(s) are observed, and their Keplerian parameters are determined to obtain their gravitational masses (for a recent review see Özel & Freire, 2016). The measured masses range from ~ $1\,M_\odot$ to a current upper limit of ~ $2.0\,M_\odot$ (Demorest et al., 2010). The upper limit imposes an important constraint on the stiffness of the equation of state at high densities. For observing the BH mass distribution, binaries including one BH are needed and even fewer systems are available compared to the binary systems with pulsars (see e.g., Özel et al., 2010, Farr et al., 2011, Kreidberg et al., 2012).

A future source for the mass distribution of compact objects is represented by gravitational wave observations from mergers. It was only recently possible to observe a strong gravitational wave signal from two inspiraling and merging massive BHs (Abbott et al., 2016). Many more GW signals are expected and a mass distribution for compact objects will be deduced over time.

Another signature to be observed of CCSNe and their nucleosynthesis yields are relative elemental abundances. Each site of heavy-element production – stars, CCSNe, Type Ia SNe, NS mergers – contributes to the abundance pattern found in the solar system or observed in the spectra of stars (Lodders, 2003). Each site leaves its own unique imprint, e.g. s-process elements formed in stars in ejected in CCSNe.

The main caveat of both observational signatures, the mass distribution of compact objects and the elemental abundance pattern, is the missing link to their progenitor systems. The link can only be established with the whole population of SNe.

1.4. Outline

All of the aforementioned observations lack final theoretical understanding, i.e. the connection between stellar evolution, the explosion mechanism, the population of observed CCSNe, and the elemental abundances. A proposed SN explosion mechanism, like the neutrino-driven mechanism in its current understanding, needs to be able to explode individual massive stars self-consistently, but at the same time it needs to be able to explain the observed signatures of the population of SNe. We will try to connect these observations to the progenitor models for massive star assuming the neutrino-driven mechanism to be the dominant explosion mechanism.

Previous studies connected progenitor stars and SN explosions by initiating a blast wave with a simple piston (e.g. Woosley & Weaver, 1995, Zhang et al., 2008) or a thermal bomb

(Aufderheide et al., 1991). The obvious caveat of such studies is that no physical mechanism is assumed for the explosion. In consequence, the key quantities of the explosion, i.e. the explosion energy, the nickel ejecta mass, or the remnant mass, need to be imposed. With the study at hand based on the earlier work by Ugliano et al. (2012), we improve on such studies because these quantities result from the simulations rather than being preset.

We perform hydrodynamic supernova simulations in spherical symmetry with approximative neutrino transport of 767 progenitor models across the stellar mass range (9 to 120 $M_\odot$) and different metallicities to explore the progenitor-explosion and progenitor-remnant connections for the neutrino-driven mechanism. We use approximations to reduce computational costs, but are guided by self-consistent simulations and individual observations of well-constraint CCSNe, SN 1054 and SN 1987A. Continuing our simulations beyond shock break-out, we are able to evaluate the nucleosynthesis, light curves, explosion energies, and remnant masses. These are compared to the observed population of SNe.

In the following chapter (Chap. 2) we will discuss the latest results of theoretical CCSN research, report about the efforts to simulate CCSNe *self-consistently*, introduce our *systematic parameter* modeling approach, and compare it to other modeling approaches in the literature. After discussing the methodology, we elaborate on the numerical realization with the neutrino-radiation hydrodynamics code Prometheus-Hotb in Chap. 3. We will list the observational properties, the progenitor models employed, and the simulation results for the two well-observed SNe, SN 1987A and SN 1054 in Chap. 4. We will also introduce all further progenitor models for massive stars that we employ in our study. After that, in Chap. 5, a criterion for the success or failure of a model, a measure for the so-called *explodability* of massive stars, is presented. We can deduce the most important observable signatures – explosion energies, nickel production, neutrino signals, light curves, nucleosynthesis yields, as well as masses and types of the compact remnants – from our simulations if we prolong them beyond shock-breakout through the surface of the star. The observational signatures of CCSNe will be the topic of the Chaps. 6 and 7. In the former we will focus on the properties of the explosive outflow of SNe and in the latter we will be concerned with the compact remnants – BHs and NSs. We will summarize and conclude in Chap. 8.

2. Methodology and Theory of Neutrino-Driven Explosions

In this chapter we will describe the difference between *self-consistent (or "ab initio")* simulations of core-collapse supernovae and *systematic parameter* studies of these phenomena. We will focus on the modeling approach employed in this work, but we will also compare our approach to other modeling strategies in the literature. The very essence of our modeling attempt is to obtain a systematic picture of the landscape of CCSNe rather than to study individual explosions. Our approach is based both on the knowledge gained from observations and from "ab initio" simulations. At the same time, it takes still existing theoretical uncertainties with respect to high-density physics and neutrino interactions into account and makes use of the freedom connected to these uncertainties. We also assume that CCSNe explode by the neutrino-driven mechanism, which is the most promising, most elaborate scenario for shock revival and obtaining the canonical $\sim 10^{51}$ erg for the explosion energy.

Firstly, we will discuss "ab initio" simulations in Sect. 2.1, followed by an overview of complementary modeling attempts in the recent literature in Sect. 2.2. Subsequently, the modeling approach of this work will be introduced in Sect. 2.3 and, especially, how we calibrate our modeling approach to observations. We calibrate to the two well-observed CCSNe, SN 1987A and SN 1054, which are subject of Sect. 2.3. The obtained calibration is then expanded to larger sets of progenitor models with various initial conditions and a wide range of zero-age main-sequence (ZAMS) masses. The progenitor models employed in this study will be introduced in Chap. 4.

The content of this chapter is in parts already published in Ertl et al. (2016a) and Sukhbold et al. (2016), yet only the author's contribution to the latter publication was taken.

2.1. Status of "Ab Initio" Supernova Modeling

"Ab initio", fully self-consistent simulations of stellar core collapse with state-of-the-art treatment of microphysics and neutrino transport do not lead to explosions in spherical symmetry (1D) except for stars with O-Ne-Mg and Fe-cores near the low-mass end of SN progenitors (Kitaura et al., 2006, Janka et al., 2008; 2012, Fischer et al., 2010, Melson et al., 2015b). Axial symmetric simulations (2D) in the recent past have produced successful explosions and underline the fundamental importance of multidimensional effects, but the true meaning of these results with respect to the neutrino-driven mechanism is not finally clear and the current situation is diffuse and contradictive.

On the one hand, some of the 2D explosions set in relatively late and might remain on the weak side (e.g., Marek & Janka, 2009, Suwa, 2012, Suwa et al., 2016, Müller et al., 2012a;b; 2013, Müller & Janka, 2014, Müller, 2015, Hanke, 2014), although such apprehension is speculative because not all simulations could be continued until the explosion energy had saturated (Müller, 2015). On the other hand, the Oak Ridge group obtained explosions much earlier after bounce with shock evolutions being astonishingly similar for 12, 15, 20, and 25 $M_{\odot}$ stars and explosion energies fairly compatible with observations (Bruenn et al., 2013; 2016). In contrast, Dolence et al. (2015) did not find any successes in 2D simulations of the same progenitors but they used a different treatment of gravity, hydrodynamics, equation of state, neutrino transport, and neutrino opacities. The exact reasons for the different findings will have to be clarified by detailed tests and comparisons. One of the first comparative studies for 2D simulations was conducted by O'Connor & Couch (2015). Their comparison showed that 2D simulations with general relativity (GR) or, equally valid, GR corrections to a Newtonian potential (see Marek et al., 2006) are crucial for the success of a model. Purely Newtonian studies fail to yield an explosion and, therefore, any state-of-the-art attempt to simulate CCSNe should include the effects of GR (see Sect. 3.1 for the realization in this study). A systematic study of a series of 2D simulations was conducted by Summa et al. (2016), who assessed the conditions at the onset of the explosion. Taking all relevant contributions into account it was possible to deduce a critical curve above which all simulations lead to successful explosions. This result is an extension to the underlying theory of the "critical luminosity" concept introduced by Burrows & Goshy (1993) and discussed in this work in Chap. 5.

The situation is even more diffuse because current 3D simulations (without symmetry constraint) agree in showing delayed explosions compared to 2D calculations or even no explosions (e.g., Hanke et al., 2012; 2013, Tamborra et al., 2014, Mezzacappa et al., 2015, Couch, 2013, Couch & O'Connor, 2014, Takiwaki et al., 2014) although some studies have proclaimed the opposite behavior (Nordhaus et al., 2010, Burrows, 2013, Dolence et al., 2013). So far only a few recent 3D calculations with highly refined neutrino treatment have obtained successful shock revival by the neutrino-driven mechanism (Melson et al., 2015b;a, Lentz et al., 2015). In addition, progenitor perturbations are a further complication in self-consistent simulations. State-of-the-art, spherical symmetric stellar evolution models do not yield these perturbations and only recently multi-dimensional simulations of the pre-collapse evolution show more realistic perturbations. These perturbations can critically alter the growth of instabilities in the post-bounce phase and even turn a failed explosion into a successful explosion (Arnett & Meakin, 2011, Couch & Ott, 2013, Müller & Janka, 2015, Couch et al., 2015, Müller et al., 2016b). Interestingly, the 3D simulation of a low-mass (9.6 $M_{\odot}$) progenitor with detailed neutrino physics, whose explosion energy approached its saturation level, was found to explode more energetically in 3D than in 2D (Melson et al., 2015b). This result is in line with a 2D-3D comparison in the 11–12 $M_\odot$ range conducted by Müller (2015). In both studies accretion downflows and the re-ejection of neutrino-heated matter were observed to be different in 2D and 3D because of geometry dependent differences of the Kelvin-Helmholtz instability and flow fragmentation. The 3D models therefore suggest that explosions in 2D are massively affected by the assumption of rotational symmetry around the polar grid axis and by an inverse turbulent energy cascade, which tends to amplify energy on the largest possible scales (Hanke et al., 2012) and also produces numerical artifacts in the post-explosion accretion phase of the neutron star (Müller, 2015). It must therefore be suspected that the early onset of explosions and the extremely unipolar or bipolar deformations along the symmetry axis obtained in many 2D models could be artifacts of the imposed symmetry constraints.

2.2. Modeling Recipes in Recent Literature

Before 3D modeling will have become a routine task and results will have converged, neutrino-driven explosions of large sets of progenitor stars can be explored for their observational implications only by referring to simplified modeling approaches. Several different recipes have been introduced for this recently. Ugliano et al. (2012) used an analytic PNS core-cooling model in connection with a neutrino transport approximation in 1D hydrodynamic explosion simulations (described in detail in Chap. 3), thus improving the simpler, time-dependent boundary neutrino luminosity prescribed by previous users of the simulation code (Kifonidis et al., 2006, Scheck et al., 2004; 2006; 2008, Arcones et al., 2007, Arcones & Janka, 2011) and the even simpler neutrino light-bulb treatment (without any transport approximation) applied by Janka & Müller (1996) and Kifonidis et al. (2003). O'Connor & Ott (2011) resorted to a scaling parameter f_heat to artificially enhance the neutrino heating by charged-current processes behind the stalled shock in 1D hydrodynamic models with approximate neutrino treatment. Nakamura et al. (2015) performed an extensive set of 2D simulations with simplified neutrino transport despite the grains of salt mentioned in Sect. 2.1 (see also Horiuchi et al., 2014, for cautioning against the 2D results). Pejcha & Thompson (2015) applied a semi-analytic model to determine the onset times of the explosions, using neutrino luminosities from 1D calculations of accreting PNSs, and estimated explosion properties by analytic arguments. Suwa et al. (2016) also performed 2D simulations and suggested analytic approximations for describing diffusion and accretion components of the neutrino luminosities from PNSs and a free-fall treatment for the collapse of the overlying stellar layers. Perego et al. (2015) invented a method named "PUSH", which they applied to trigger explosions artificially in their general relativistic, 1D hydrodynamic core-collapse and PNS formation modeling with sophisticated neutrino transport. PUSH gradually switches on and off additional neutrino heating of chosen strength during a chosen period of time. This procedure is assumed to mimic the effects of multi-D hydrodynamics in the postshock region. The extra heating is coupled to the *heavy-lepton neutrino* emission from the PNS. Recently, (Müller et al., 2016a) solved a large set of simple differential equations and scaling laws for the shock propagation, the behavior of the neutron star and its neutrino emission, influencing the heating conditions and the explosion energetics. Their approach is guided by a set of self-consistent simulations and numerical experiments for the different phases of the explosion. By this they can process a very large grid of thousands of supernova progenitors efficiently, but still with a large number of free parameters.

All of these recipes contain larger sets of parameters and degrees of freedom, which are either varied in exploring different cases (e.g., Pejcha & Thompson, 2015) or are adjusted by comparison to more complete models (e.g., Suwa et al., 2016) or by reproducing observational benchmarks like those set by SN 1987A (Ugliano et al., 2012, Perego et al., 2015). The models of Ugliano et al. (2012), Ertl et al. (2016a), Sukhbold et al. (2016) and those in the present work assume that the explosion trigger is tightly coupled to the physics that reflects the main differences between different progenitor stars, namely to the post-bounce accretion history of the collapsing stellar core and the corresponding accretion luminosities of ν_e and $\bar{\nu}_e$. It remains to be seen if this modeling concept will be supported by future developments towards a more complete understanding of the physics of the central engine that powers the explosion in the context of the neutrino-driven mechanism.

2.3. Motivation of the Modeling Assumptions of this Work

The analytic NS-core model introduced by Ugliano et al. (2012) in combination with their approximate transport solver for treating the accretion component of the neutrino luminosity as well as neutrino cooling and heating between PNS and shock, is an attempt to realize the tight coupling of accretion behavior and explodability in close similarity to what is found in current 2D simulations (e.g. those of Marek & Janka, 2009, Müller et al., 2012a;b; 2013, Müller & Janka, 2014). Since 1D models with elaborate neutrino physics and a fully self-consistent calculation of PNS cooling miss the critical condition for explosions by far, it is *not the goal* of Ugliano et al. (2012) to closely reproduce the neutrino emission properties of such more sophisticated calculations. Rather than that it is the goal to approximate the *combined effects of neutrino heating and multi-dimensional postshock hydrodynamics* by a simple and computationally efficient neutrino source model, which allows for the fast processing of large progenitor sets including the long-time evolution of the SN explosion to determine also the shock breakout and fallback evolution.

Free parameters in the NS core model and the prescribed contraction behavior of the inner grid boundary are calibrated by matching basic observational features (explosion energy, ^{56}Ni yield, total release of neutrino energy) of SN 1987A and SN 1054. This is intended to ensure that the overall properties of the neutrino-source model are anchored on empirical ground. Of course, the setting of the parameter values cannot be unambiguous when only a few elements of a single observed SN are used for deriving constraints. However, the approximate nature of the neutrino source treatment as a whole does not require the perfectly accurate description of each individual model component in order to still contain the essence of the physics of the system like important feedback effects between accretion and outflows and neutrinos, which govern the progenitor-dependent variations of the explodability (Chap. 5) and the SN properties (Chaps. 6 and 7). A reasonable interplay of the different components is more relevant than a most sophisticated representation of any single aspect of the neutrino source model.

In detail, the basic features of our 1D realization of the neutrino-driven mechanism along the lines of Ugliano et al. (2012) are the following:

- The possibility of an explosion is coupled closely to the progenitor-dependent strength and evolution of the post-bounce accretion. This is achieved not only by taking into account the accretion luminosity through the approximate neutrino transport scheme (see Sect. 3.3.2), but also through the response of the PNS-core to the presence of a hot accretion mantle (see Sect. 3.4). The evolution of the latter is explicitly followed in our hydrodynamic simulations, which track the accumulation of the collapsing stellar matter around the inner PNS core. The existence of the mantle layer enters the analytic core model in terms of the parameter m_{acc} for the mass of this layer and the corresponding accretion rate $\dot{m}_{\mathrm{acc}}$.

- The inner $1.1\,M_{\odot}$ core of the PNS is cut out and replaced by a contracting inner grid boundary and a corresponding boundary condition in our model. This inner core is considered to be the supranuclear high-density region of the nascent NS, whose detailed physics is still subject to considerable uncertainties. This region is replaced by an analytic description, whose parameters Γ, ζ, $R_{\mathrm{c}}(t)$, and n (see Ugliano et al., 2012) are set to the same values for all stars except for the lowest masses where $R_{\mathrm{c}}(t)$ is varied additionally This makes sense because the supranuclear phase is highly incompressible, for which reason it can be expected that the volume of the core is not largely different during the explosion phase for different PNS masses. Moreover, the neutrino diffusion timescale out of this core is seconds, which implies that its neutrino emission is of secondary importance during the shorter post-bounce phase when the explosion develops. Despite its simplicity, our core treatment still includes progenitor and accretion dependent variations through the mass m_{acc} of the hot accretion mantle of the PNS and the mass-accretion rate $\dot{m}_{\mathrm{acc}}$, whose influence on the inner core is accounted for in Eqs. (1)–(4) of Ugliano et al. (2012) and (see Sect. 3.4) for describing the energy evolution of the core model.

- The onset of the explosion is considerably delayed (typically between several 100 ms and about a second) with a slow (instead of abrupt) rise of the explosion energy during the subsequent shock acceleration phase, when an intense neutrino-driven wind ejects matter and delivers power to the explosion. Neutrino heating cannot deposit the explosion energy impulsively, because the ejected matter needs to absorb enough energy from neutrinos to be accelerated outwards. The rate of energy input to the explosion is therefore limited by the rate at which matter can be channeled trough the heating region. A long-lasting period (hundreds of milliseconds to more than a second) of increasing energy is characteristic of neutrino-driven explosions (Fig. 2.1) and is observed as gradual growth of the explosion energy also in 2D explosion models, e.g., by Scheck et al. (2006) and Bruenn et al. (2016). To achieve this behavior in our 1D models the core-neutrino source needs to keep up high neutrino luminosities for a more extended period of time than found in fully self-consistent SN simulations, where the rapid decline of the mass-accretion rate at the surface of the iron core and at the interface of silicon and silicon-enriched oxygen layers leads to a strong decrease of the accretion luminosity. The longer period of high neutrino emission is compensated by a somewhat underestimated early post-bounce neutrino luminosity (Fig. 2.1) in order to satisfy the energy constraints set by the total gravitational binding energy of the forming NS.

- The timescale and duration of the growth of the explosion energy in multi-D models of neutrino-driven SNe are connected to an extended period of continued accretion and simultaneous shock expansion that follows *after* the revival of the stalled shock (see Marek & Janka, 2009). Persistent accretion thereby ensures the maintenance of a significant accretion luminosity, while partial re-ejection of accreted and neutrino-heated matter boosts the explosion energy. In our 1D simulations the physics of such a two-component flow cannot be accurately accounted for. In order to approximate the consequences of this truly multi-dimensional phase, our 1D models are constructed with two important properties: On the one hand they refer to a high level of the PNS-core luminosity for about one second. On the other hand they are set up to possess a more extended accretion phase that precedes the onset of the delayed explosion before the intense neutrino-driven wind pumps energy into the explosion. The power and mass loss in this wind are overestimated compared to sophisticated neutrino-cooling simulations of PNSs. However, this overestimation of the wind strength has its justification: The early wind is supposed to mimic the mass ejection that is fed in the multi-dimensional case by the inflow and partial re-ejection of matter falling towards the gain radius during the episode of simultaneous accretion and shock expansion. The enhanced wind mass counterbalances the extra mass accretion by the PNS during the long phase before the shock acceleration is launched, and this enhanced wind mass is of crucial importance to carry the energy of the neutrino-powered blast.

Figure 2.1 shows the post-bounce evolution of the stalled SN shock, the onset of the explosion, energy evolution, and the time evolution of the neutrino emission properties for three representative progenitor models simulated with our approach. We show a low-mass case with a ZAMS mass of $14.0\,M_{\odot}$, a case with an intermediate ZAMS mass of $21.0\,M_{\odot}$ and a high-mass case with a ZAMS mass of $27.0\,M_{\odot}$. The models are taken from

Sukhbold & Woosley (2014) and explode with a certain parameter choice for the PNS core model, called w18.0, which is a model for the progenitor of SN 1987A. The details of the parameter choice are not relevant here, but will be discussed later in this section and in Sect. 4.1 for the progenitor models employed. The figure illustrates the typical behavior of an exploding model regardless of the applied parameter choice: the shock stagnation at a radius of approximately 200 km lasts between ∼700 ms and 900 ms and can exhibit the well-known oscillatory expansion and contraction phases, which signal proximity to the explosion (see e.g., Buras et al., 2006a, Murphy & Burrows, 2008, Fernández, 2012). The explosion sets in shortly after the Si/Si+O composition shell interface (manifest itself as a sudden increase in entropy above $s = 4\,\mathrm{k_B}$ and, therefore, denoted by M_4) has fallen through the shock and well before additional $0.3\,M_\odot$ (denoted by $M_4 + 0.3$) have collapsed. High neutrino luminosities are maintained by high mass-accretion rates and, after the onset of the explosion, by a contribution from the core emission (dashed lines in the luminosity panel of Fig. 2.1) that grows until roughly one second. The current models underestimate the surface luminosity of heavy-lepton neutrinos compared to more sophisticated simulations because of the chosen modest contraction of the inner boundary of the computational grid (which leads to underestimated temperatures in the accretion layer of the PNS) and because neutrino-pair production by nucleon-nucleon bremsstrahlung is not taken into account. We did not upgrade our treatment in this respect because ν_μ and ν_τ are not of immediate relevance for our study since the explosion hinges exclusively on the heating by ν_e and $\bar{\nu}_e$.

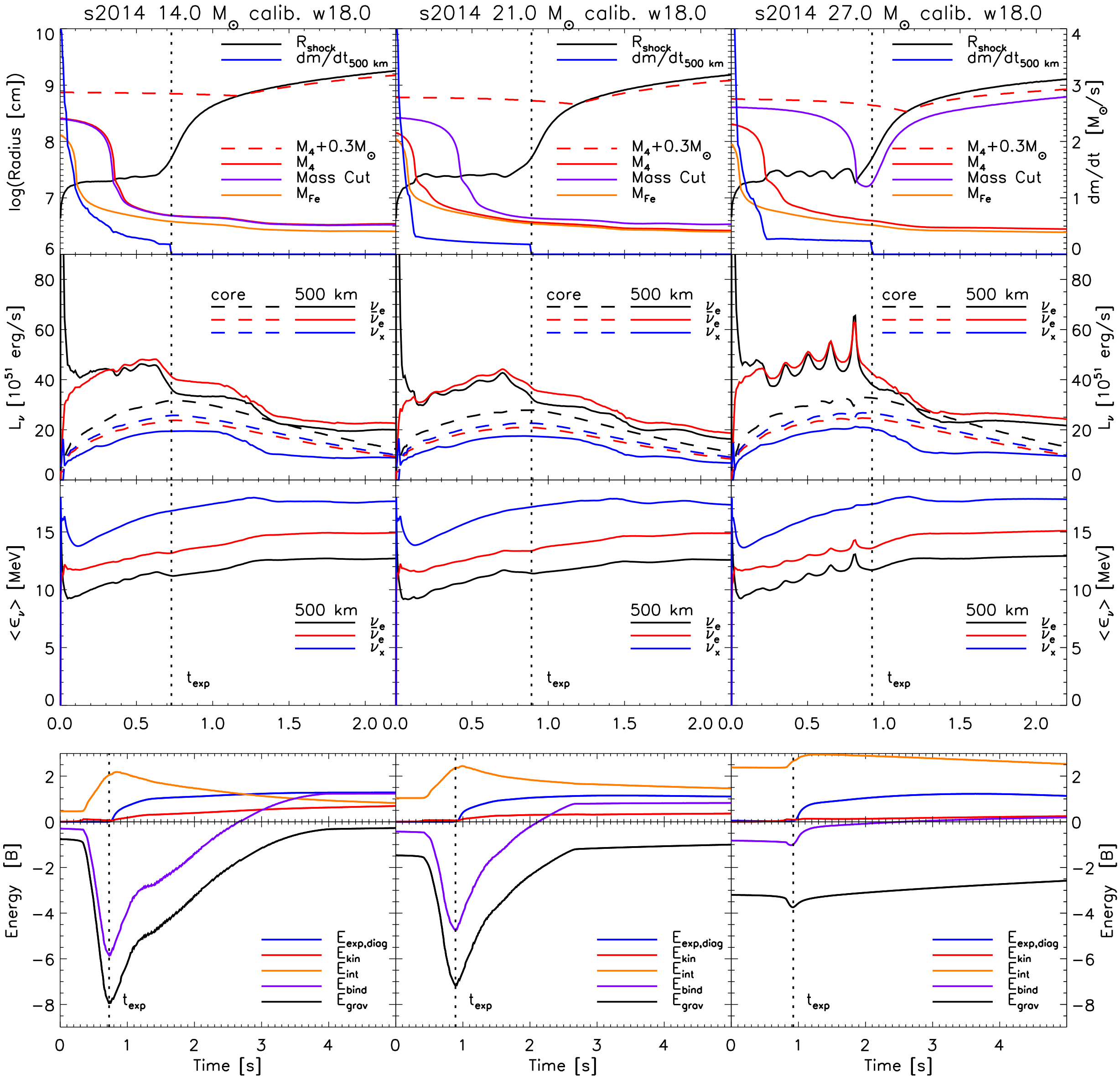
s2014 14.0 M$_\odot$ calib. w18.0
s2014 21.0 M$_\odot$ calib. w18.0
s2014 27.0 M$_\odot$ calib. w18.0
log(Radius [cm])
dm/dt [M$_\odot$/s]
R$_{shock}$
dm/dt$_{500\ km}$
M$_4$+0.3M$_\odot$
M$_4$
Mass Cut
M$_{Fe}$
L$_\nu$ [10^{51} erg/s]
core
500 km
ν_e
$\bar{\nu}_e$
ν_x
<ϵ_ν> [MeV]
t$_{exp}$
Energy [B]
E$_{exp,diag}$
E$_{kin}$
E$_{int}$
E$_{bind}$
E$_{grav}$
Time [s]
0.0
0.5
1.0
1.5
2.0
0
1
2
3
4
6
7
8
9
10
20
40
60
80
5
15
-2
-4
-6
-8

Figure 2.1.: Models s14.0 (*left*), s21.0 (*middle*), and s27.0 (*right*) of the s2014 progenitor series by Sukhbold & Woosley (2014) as exemplary cases of successful explosions with the w18.0 calibration as example. The *top panels* display as functions of post-bounce time the radius of the outgoing shock (black line), the mass-accretion rate measured at 500 km (blue line; scale on the right side), the radii of the iron core (orange), the mass coordinates $M_4 = m(s = 4)$ (red) and $M_4 + 0.3$ (red dashed), and the trajectory of the final mass cut (after completion of fallback; purple). The *second panels from top* show the time evolution of the luminosities of ν_e, $\bar{\nu}_e$, and a single species of heavy-lepton neutrinos ν_x as labeled in the plot, measured at 500 km (solid lines) and at the inner grid boundary (dashed lines). The *third panels from top* show the mean energies of all neutrino kinds as radiated at 500 km. The vertical dotted lines indicate the onset time of the explosion as the moment when the outgoing shock passes the radius of 500 km. The *bottom panels* provide the time evolution of the diagnostic energy of the explosion (integrated energy of all postshock zones with positive total energy; blue line). Also shown are the kinetic energy (red), gravitational energy (black), and internal energy (orange) as integrals over the whole, final SN ejecta between the final mass cut (after fallback) on the one side and the stellar surface on the other. The total (binding) energy (purple) as the sum of these energies ultimately converges to the diagnostic energy and both of these energies asymptote to the final explosion energy. While this convergence is essentially reached after ∼4 s in the case of s14.0, the expansion of shocked matter in the s21.0 model and thus the energy evolution is slowed down at ∼ 2.7 s by the high densities in the stellar core. The s27.0 model becomes gravitationally unbound (i.e., the total binding energy becomes positive) even more slowly because of the very massive stellar core. The convergence of total energy and diagnostic energy takes tens of seconds in this case.

Details of the Calibration Procedure

Replacing the inner core of the PNS by a contracting inner boundary of the computational mesh introduces a number of free parameters, whose settings allow one to achieve the desired accretion and neutrino-emission behavior as detailed above. On the one hand, our model contains parameters for the prescription of the contraction of the grid boundary, on the other hand there are parameters for the simple high-density core model (cf. Ugliano et al., 2012, and references therein). While the core-model parameters (Γ, ζ, $R_{\rm c}(t)$, n) regulate the neutrino-emission evolution of the excised, high-density core of the PNS, the prescribed grid-boundary radius, $R_{\rm ib}(t)$, governs the settling of the hot accretion mantle of the PNS. Because of partially compensating influences and dependences, not all of these parameters have a sensitive impact on the outcome of our study. Again, more relevant than a highly accurate description of individual components of the modeling is a reasonable reproduction of the overall properties of the accretion and neutrino emission history of the stalled SN shock and mass accumulating PNS. For example, the moderate increase of the mean neutrino energies with time and their regular hierarchy ($\langle\epsilon_{\nu_e}\rangle < \langle\epsilon_{\bar{\nu}_e}\rangle < \langle\epsilon_{\nu_x}\rangle$; Fig. 2.1) are not compatible with the most sophisticated current models (Marek & Janka, 2009, Müller & Janka, 2014,see, e.g.,). They reflect our choice of a less extreme contraction of the $1.1\,M_\odot$ shell than found in simulations with soft nuclear equations of state for the core matter, where the PNS contracts more strongly and its accretion mantle heats up to higher temperatures at later post-bounce times (compare Scheck et al. 2006 and see the discussion by Pejcha & Thompson 2015). Our choice is motivated solely by numerical reasons (because of less stringent time-step constraints), but it has no immediate drawbacks for our systematic exploration of explosion conditions in large progenitor sets. Since neutrino-energy deposition depends on $L_\nu\langle\epsilon_\nu^2\rangle$, the underestimated mean neutrino energies at late times can be compensated by higher neutrino luminosities L_ν of the PNS core.

The neutrino emission from the PNS-core region is parametrized in accordance with basic physics constraints. This means that the total loss of electron-lepton number is compatible with the typical neutronization of the inner $1.1\,M_\odot$ core, whose release of gravitational binding energy satisfies energy conservation and virial theorem (see Ugliano et al., 2012). Correspondingly chosen boundary luminosities therefore ensure a basically realistic deleptonization and cooling evolution of the PNS as a whole and of the accretion mantle in particular, where much of the inner-boundary fluxes are absorbed and reprocessed. Again, a proper representation of progenitor-dependent variations requires a reasonable description of the overall system behavior but does not need a very high sophistication of all individual components of the system.

Agreement with the constraints from SN 1987A employed in our work (i.e., the observed explosion energy, ^{56}Ni mass, total neutrino energy loss, and the duration of the neutrino signal) can be achieved with different sets of values of the PNS core-model parameters. Using only one observed SN case the parameter set is underconstrained and the choice of suitable values is ambiguous. It is therefore not guaranteed that the calibration works equally well in the whole mass range of investigated stellar models.

Calibration for the Low ZAMS-Mass Limit

In particular stars in the low ZAMS-mass regime ($M_{\mathrm{ZAMS}} \lesssim 12$–$13\,M_{\odot}$) possess properties that are distinctly different from those of the adopted SN 1987A progenitors and in their mass neighborhood. Stars with $M_{\mathrm{ZAMS}} \lesssim 12$–$13\,M_{\odot}$ are characterized by a very shallow density gradient outside of the iron core. Because of their structural similarities and distinctive differences compared to more massive stars, Sukhbold et al. (2016) call progenitors below roughly 12–13 $M_{\odot}$ “Crab-like”, which we will adopt. In contrast to stars above this mass limit, which we termed “SN 1987-like”.

Stars below $\sim 10\,M_{\odot}$ were found to explode easily in self-consistent, sophisticated 1D, 2D, and 3D simulations (Kitaura et al., 2006, Janka et al., 2008, Fischer et al., 2010, Wanajo et al., 2011, Janka et al., 2012, Melson et al., 2015b) with low energies (less than or around $10^{50}\,\mathrm{erg} = 0.1\,\mathrm{B}$) and little nickel production ($< 0.01\,M_{\odot}$), in agreement with observational properties concluded from detailed analysis of the Crab remnant (e.g., Yang & Chevalier, 2015). We therefore consider the results of these state-of-the-art SN models together with the empirical constraints for the Crab supernova as important benchmarks that should be reproduced by our approximate 1D modeling of neutrino-powered explosions.

The results of Ugliano et al. (2012) revealed a problem in this respect, because they showed far more energetic explosions of stars in the low-mass domain than expected on grounds of the sophisticated simulations and from observations of the Crab. Obviously, the neutrino-source calibration used by Ugliano et al. (2012) is not appropriate to reproduce “realistic” explosion conditions in stars with very dilute shells around the iron core. Instead, it leads to an overestimated power of the neutrino-driven wind and therefore overestimated explosion energies. In particular, the strong and energetic wind is in conflict with the short period of simultaneous postshock accretion and mass ejection after the onset of the explosion in $\lesssim 10\,M_{\odot}$ stars. Since the mass-accretion rate is low and the duration of the accretion phase is limited by the fast shock expansion, the energetic importance of this phase is diminished by the small mass that is channeled through the neutrino-heating layer downwards in convective flows (Kitaura et al., 2006, Janka et al., 2008, Wanajo et al., 2011, Janka et al., 2012, Melson et al., 2015b). In order to account for these features found in the most elaborate simulations of low-mass stellar explosions, the neutrino-driven wind power of our parametric models has to be reduced.

In Ertl et al. (2016a) we applied a “quick fix” to cure this problem of over-energetic low ZAMS-mass explosions by using a linear scaling of the compression parameter ζ of the PNS core model (see Sect. 3.4.2 for the PNS core model), coupled to a measure for the core structure for progenitors with ZAMS masses lower than $13.5\,M_{\odot}$. Here, as well as in Sukhbold et al. (2016), we elaborate on the background of this measure and introduce an alternative, similarly effective but physics-wise more transparent approach than the adhoc ζ-modification. We will present the details of the calibration along with the progenitor models and the PNS core-model parameters in Sect. 4.1. Here we will restrain ourselves to the physical explanation on how we alter our core-model parameters for the low ZAMS-mass limit: Figure 2.2 shows the time evolution of the $1.1\,M_\odot$ cores (corresponding to the mass excised and treated by the analytic core-cooling model in our approach) for two self-consistent PNS cooling simulations with all relevant microphysics (Mirizzi et al., 2016), carried out with the nuclear EOS of Lattimer & Swesty (1991). We can conclude that the contraction behavior and final radius of the innermost $1.1\,M_\odot$ of the PNS depend on the mass of the newly formed NS in a microphysical model. The slower and less extreme contraction in the case of the low-mass PNS compared to the high-mass PNS suggest that less neutrino energy is more gradually released in the low-mass case. This difference needs to be taken into account when modeling the explosions of the low ZAMS-mass (Crab-like) progenitor stars in order to avoid the overestimation of the explosion energy in this subset of the progenitors.

Because the simple one-zone core model does not allow to just adopt the core-radius evolution from a self-consistent simulation, we calibrate the "Crab-like" explosions by reproducing the observationally inferred explosion energy of SN 1054 ($\sim$0.05–0.15 B; Tominaga et al. 2013, Smith 2013, Yang & Chevalier 2015) and ^{56}Ni mass ($\lesssim 10^{-2}\,M_\odot$; Tominaga et al. 2013, Smith 2013) with a suitable progenitor model (see Sect. 4.1.2). We then connect the obtained contraction of the analytic core-cooling model (not the physical inner boundary) to the contraction of the core-cooling model of the SN 1987A-like progenitors. Consequently, the core-cooling model of progenitor models with low PNS mass, being closer to the progenitor model for SN 1054, contracts more moderately than models with higher PNS masses, closer to SN 1987A-like models.

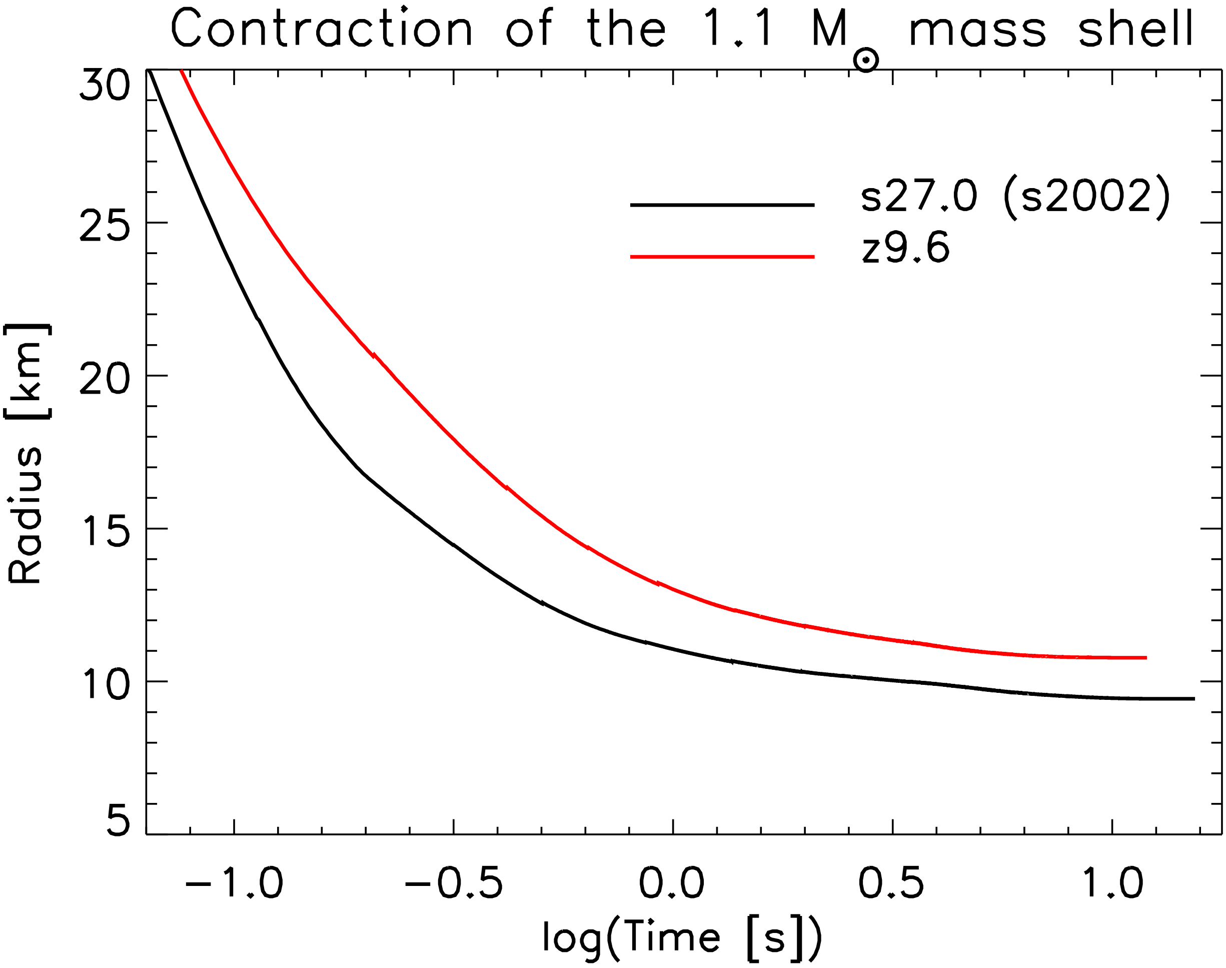

Figure 2.2.: Radius of the 1.1 $M_\odot$ core as a function of post-bounce time for a low-mass neutron star (baryonic mass 1.36 $M_\odot$; gravitational mass 1.25 $M_\odot$) characteristic of the 9.6 $M_\odot$ progenitor (red line), and for a high-mass neutron star (baryonic mass 1.78 $M_\odot$; gravitational mass 1.59 $M_\odot$) characteristic of a 27 $M_\odot$ progenitor (black line). Both cores were evolved in a self-consistent PNS cooling simulation with detailed neutrino transport and the L&S 220 high-density EOS of Lattimer & Swesty (1991). The same simulations were recently reported by Mirizzi et al. (2016). The different contraction behavior of the high-density cores of low-mass and high-mass PNSs is obvious.

3. Numerical Realization in Prometheus-Hotb

After assessing the methodological approach by which we model core-collapse supernovae (CCSNe) in this work, we need to discuss the equations that need to be solved and how they are treated numerically. For the desired systematic picture of CCSNe it is crucial that the numerical method is capable of simulating hundreds of progenitor models efficiently. The code that solves all relevant equations is called PROMETHEUS-HOTB and described in a series of publications: Fryxell et al. (1989), Kifonidis et al. (2006), Scheck et al. (2004; 2006; 2008), Arcones et al. (2007), Arcones & Janka (2011), Ugliano et al. (2012), Ugliano (2012), Ertl (2012), Ertl et al. (2016a) and Ertl et al. (2016a).

PROMETHEUS is the hydrodynamics module including self-gravity of the stellar plasma (described in Sect. 3.1) and the option for an arbitrary, realistic model of the equation of state (EOS). The hydrodynamic solver is the base module of the code and all additional physical models are introduced as source terms in an operator-split way to the solver. One of these source terms is the effect of nuclear reactions, which will be discussed in Sect. 3.2 together with the different models for the EOS.

The second part of the name is HOTB, which is descriptive for the purpose of the code. It was mainly used to simulate the hot-bubble region that develops after core-bounce. It is the neutrino-heated region behind the shock (Janka, 2001). To simulate the evolution of the hot-bubble region efficiently, the inner core of the proto-neutron star (PNS) is excised and replaced by a point mass. It is separated from the computational domain by a hydrostatic, contracting boundary (Sect. 3.4). On top of this, Ugliano et al. (2012) introduced an analytic one-zone core-cooling model for the evolution of the neutrino luminosity injected into the computational domain at the inner boundary. The neutrino propagation and interaction is then followed through the star by an efficient gray neutrino-transport solver. It accounts for the heating and cooling of the stellar fluid due to weak interactions of the neutrinos and is therefore decisive for the outcome of a CCSN. The gray neutrino-transport approximation, the inner grid boundary condition, and the analytic one-zone core-cooling model that is employed after bounce will be discussed in Sect. 3.3. Ertl (2012) implemented the deleptonization scheme by Liebendörfer (2005) (described in Sect. 3.3). It is employed to simulate the effects of neutrino losses during core collapse until shortly after core bounce without excision of the inner core.

With all of these ingredients, PROMETHEUS-HOTB is able to simulate the evolution of a progenitor model of a massive star from the onset of core collapse (as provided by stellar evolution calculations) beyond the shock breakout when the shock reaches the surface of the star. Having advanced our simulations to this stage, we are able to determine all important observables including the final fallback mass.

3.1. Hydrodynamics and Self-Gravity

The hydrodynamics solver PROMETHEUS by Fryxell et al. (1989) is the main module whereupon all other solvers are built. The plasma of a collapsing star can be treated as a shear-free fluid, and therefore followed by solving a set of non-linear partial differential equations, namely the Euler equations. The Euler equations are the following, but supplemented with an additional source term for gravity f_{g}, for nuclear reactions Q_{nuc} addressed in Sect. 3.2, and for neutrino interactions $Q_{\nu,e}$ described in Sect. 3.3:

- the continuity equation,

$$\frac{\partial \rho}{\partial t} + \nabla \cdot (\rho \mathbf{v}) = 0, \tag{3.1}$$

- the momentum equation,

$$\frac{\partial \rho \mathbf{v}}{\partial t} + \nabla \cdot (\rho \mathbf{v}\mathbf{v}) = -\nabla P + \rho \mathbf{f}_{\mathrm{g}}, \tag{3.2}$$

- and the energy equation,

$$\begin{aligned} \frac{\partial \rho e_{\mathrm{tot}}}{\partial t} + \nabla \cdot (\rho e_{\mathrm{tot}} \mathbf{v}) &= -\nabla \cdot (P\mathbf{v}) + \rho \mathbf{v} \cdot \mathbf{f}_{\mathrm{g}} + \rho Q_{\nu,e} + \rho Q_{\mathrm{nuc}} \\ \text{with} \quad e_{\mathrm{tot}} &= \epsilon + \frac{1}{2}|\mathbf{v}|^2, \end{aligned} \tag{3.3}$$

where ρ is the baryon density, $\mathbf{v}$ is the velocity vector of the fluid, e_{tot} is the specific energy, including the specific internal energy ϵ and the specific kinetic energy $\frac{1}{2}|\mathbf{v}|^2$, P is the pressure and t is the time. These equations are solved by the means of an exact Riemann solver as described by Colella & Glaz (1985). For such a high-order, exact Riemann solver a numerical problem arises at shocks, the so-called odd-even decoupling. In order to prevent this PROMETHEUS switches to an approximate HLLE Riemann solver (Einfeldt, 1988) in shocks instead of the high-order scheme. The reconstruction of the states is done with the piecewise parabolic method (PPM) by Colella & Woodward (1984). PPM is third-order accurate in the spatial dimensions and second-order accurate in time.

So far, the described method solves the left-hand side of Eqs. (3.1) – (3.3) without the above-mentioned source terms. The source terms are then calculated in an operator splitting step independent of each other and separated from the hydrodynamic solution. This allows for a modular structure of the code and adds flexibility when adding additional physical models. The closure of the Euler equations as well as the accounting for the source terms is provided by an appropriate model for the EOS relating all thermodynamic quantities to each other (see Sect. 3.2).

The time step in our explicit method is determined by the Courant-Friedrichs-Lewy (CFL) condition,

$$\Delta t = C_{\mathrm{CFL}} \frac{\Delta x}{(|\mathbf{v}| + c_s)}, \tag{3.4}$$

relating the time step Δt by a dimensionless factor C_{CFL} with the extent of a zone Δx, the absolute value of the local velocity $|\mathbf{v}|$, and the local sound speed c_s. The dimensionless CFL factor C_{CFL} is set to a value less than unity, which limits information propagating more than one zone per time step.

Due to the CFL condition the solution of the Riemann problem is a local problem. In contrast the hydrodynamic problem, which is restricted by the local sound speed, changes in the gravitational potential propagate unhindered with the speed of light through the star. In the Newtonian approximation, gravity can be assumed to act instantaneously on the whole computational domain and needs to be separated from the hydrodynamic problem. Because of this the gravitational force f_{G} is accounted for in an operator split step. PROMETHEUS already includes a solver for Newtonian self-gravity of the stellar fluid in its original version. f_{g} is defined by the negative gradient of the gravitational potential $-\nabla\Phi$. The gravitational potential Φ is obtained by solving Poisson's equation, $\Delta\Phi = 4\pi G\rho$ with G being the gravitational constant, that relies solely on the density profile in the Newtonian case.

But the simple Newtonian case was found to be unfit to tackle the supernova problem (see Sect. 2.1). Due to the extreme conditions in the core of a massive star and the resulting compact remnant (either a neutron star or a black hole) general relativity (GR) cannot be neglected. Rampp & Janka (2002) described corrections to the simple Newtonian case which account for some of the effects of GR. This was further improved based on a detailed comparison to a simulation with full GR by Marek et al. (2006). The improved version of the GR-corrected Newtonian potential was adapted to HOTB by Arcones et al. (2007). Latter work adapted the GR corrections for late neutrino wind phases and the inner boundary condition.

The starting point for the GR corrections in Hotb is the equation for the relativistic Tolman-Oppenheimer-Volkoff (TOV) potential,

$$\Phi_{\rm TOV}(r) = -4\pi G \int\limits_0^r \frac{{\rm d}r'}{r'^2} \left[\frac{m_{\rm TOV}}{4\pi} + \frac{r'^3(P+p_\nu)}{c^2} \right] \frac{1}{\Gamma^2} \left(\frac{\rho c^2 + \rho\epsilon + P}{\rho c^2} \right), \tag{3.5}$$

which is a function of the specific energy ϵ, the local gas pressure P, the neutrino pressure p_ν and a term for the TOV mass,

$$m_{\rm TOV}(r) = 4\pi \int\limits_0^r {\rm d}r'\, r'^2 \left(\rho + \frac{\rho\epsilon + E}{c^2} + \frac{vF}{\Gamma c^2} \right) \Gamma, \tag{3.6}$$

which depends on internal energy density $\rho\epsilon$ and a contribution by neutrino properties, neutrino energy density E and neutrino flux F. Based on the improvements by Marek et al. (2006) the TOV mass is further multiplied by the metric function,

$$\Gamma = \sqrt{1 + \frac{v^2}{c^2} - \frac{2Gm_{\rm TOV}}{rc^2}}. \tag{3.7}$$

A further complication is introduced to the GR-corrected gravitational potential by the boundary condition of the excised core. In the Newtonian case, a constant point mass or a mass-flux corrected point mass are enough to describe the contribution of the excised region for a hydrostatic boundary condition or an open boundary condition, respectively. However, in the GR-corrected case we need to account for neutrino losses $L_\nu^{\rm ib}$ of the excised region injected at the boundary and for the compression work due to the contraction of the inner boundary $R_{\rm ib}$. The core contribution to the TOV mass accounts for both and evolves them in time as follows:

$$m_{\rm TOV}(R_{\rm ib}, t) = m_{\rm TOV}(R_{\rm ib}, 0) - \int\limits_0^t {\rm d}t'\, L_\nu^{\rm ib} - \int\limits_0^t {\rm d}t'\, 4\pi R_{\rm ib}^2(t') P_{\rm ib}(t') \frac{{\rm d}R_{\rm ib}}{{\rm d}t'}. \tag{3.8}$$

Note that $m_{\rm TOV}(R_{\rm ib}, 0)$ is the initial TOV-mass at the radius where the inner boundary $R_{\rm ib}$ is introduced in each phase and it is introduced after core bounce for the first time. The TOV mass of the core $m_{\rm TOV}(R_{\rm ib}, t)$ is then evolved in time and successively moved further out after each phase.

3.2. Equation of State and Nuclear Reactions

Prometheus allows for an arbitrary, realistic model of the EOS that provides the closure to the Euler equations and also accounts for the changes in the thermodynamic state by the source terms. We will discuss nuclear reactions (the source term Q_{nuc}) together with the EOS here, because both are tightly coupled for high temperatures and densities. In general, a model for the EOS in the Supernova environment needs to cover the conditions present in the hydrogen envelope with its low densities and temperatures, as well as the high densities (and high temperatures) present in the nascent neutron star.

Figure 3.1 shows a schematic of our setup for the EOS and the treatment of nuclear reactions in the density-temperature plane. The physical model has been improved since the work by Ertl (2012) in some aspects and we will highlight them in the following. Especially, a problem that occurred at late times ($\gtrsim$ 6 s) was fixed: pulses originating at the surface of the PNS increased the explosion energy artificially. This problem was connected to the high-density region in the PNS interior. It was solved by increasing the spatial resolution at the surface of the PNS. There, the density gradient is steepest and therefore a high spatial resolution is necessary. It is significantly higher than the resolution used by Ugliano et al. (2012). The latter work applied a simple EOS without nucleon-nucleon interactions resulting in a flatter density gradient at the PNS surface. We improved on this and utilized the L&S 220 by Lattimer & Swesty (1991) for the high-density EOS in our simulations, which takes strong forces into account. The result is a more realistic, yet steeper decline of the density at the surface of the PNS and a different radial behavior in time. The standard grid of Ugliano et al. (2012) was found to be too coarse and had to be refined. In the course of this, the boundaries of the different models for the EOS were changed and a low-density nuclear statistical equilibrium (NSE) solver was implemented. We will describe the setup and the improvements below starting with the low-density and low-temperature regime.

3.2.1. Low Densities and Low Temperatures

For densities lower than $\rho_0 = 10^3\,\mathrm{g\,cm^{-3}}$ or temperatures lower than $T_0 = 10^8\,\mathrm{K}$, we employ the so-called Helmholtz EOS by Timmes & Swesty (2000). The EOS in this regime is well-known and can be calculated analytically for all components: radiation, nuclei, electrons and positrons. The Helmholtz EOS is an analytic implementation of all components except for the electron-positron part being tabulated. Within the electron-positron table a biquintic Hermite polynomial is used as interpolation function. This interpolation method guarantees thermodynamic consistency and, at the same time, high computational efficiency. The Helmholtz EOS is called after the states are constructed by the Riemann solver. The new density ρ, specific internal energy ϵ and number fractions of all isotopes Y_i of the new states are input to the EOS routine. The EOS routine completes the thermodynamic state by calculating the remaining thermodynamic quantities, like pressure P (used by the Riemann solver for the next time step), temperature T, and entropy s.

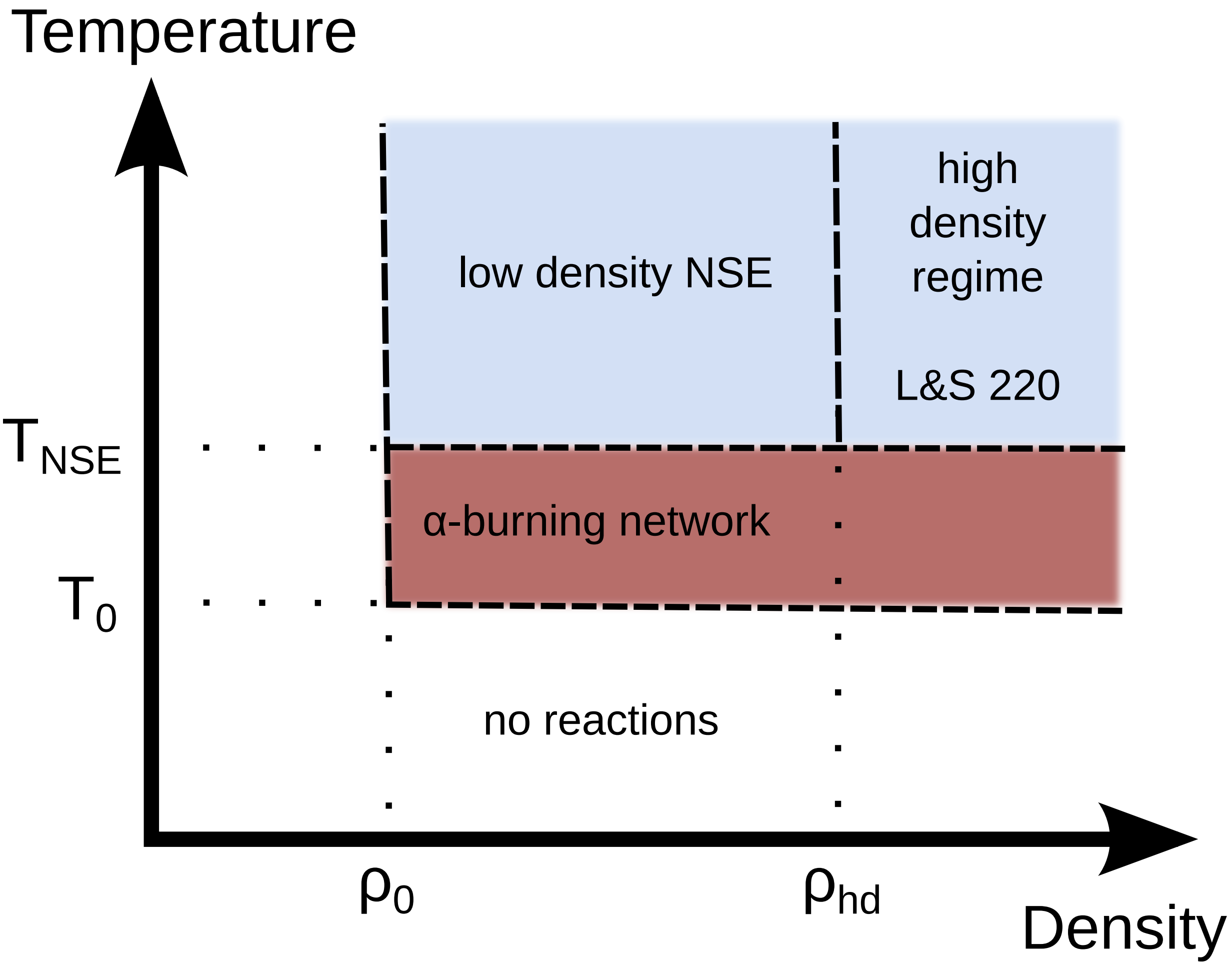

Figure 3.1.: Schematic of the density-temperature plane for the different models of the equations of state (EOS) and different regimes for nuclear reactions are displayed as implemented in Hotb. Blue regions indicate nuclear statistical equilibrium (NSE), while red regions indicate rate-dependent nuclear reactions. White regions are regions without nuclear reactions where nuclei are solely advected with the fluid flow, but remain unchanged otherwise. ρ_{hd} separates the Helmholtz EOS by Timmes & Swesty (2000) from the high-density EOS (at high temperatures $T > T_{\mathrm{NSE}}$). We use the L&S 220 by Lattimer & Swesty (1991) as high-density EOS in our simulations.

3.2.2. Nuclear Reaction Network

The release or consumption of energy by nuclear reactions is dynamically negligible and not considered in the low-temperature regime, but becomes evermore important with increasing temperatures. In an intermediate regime with temperatures higher than T_0 we employ an α-chain reaction network by Mueller (1986). The network solver considers the following 14 nuclei in the α-chain (listed by increasing mass number):

^{4}He (α), ^{12}C, ^{16}O, ^{20}Ne, ^{24}Mg, ^{28}Si, ^{32}S, ^{36}Ar, ^{40}Ca, ^{44}Ti, ^{48}Cr, ^{52}Fe and ^{56}Ni (plus $^{56}\mathrm{Ni}_{\mathrm{Tracer}}$).

In addition to these nuclei, free nucleons, neutrons ^{1}n and protons ^{1}p are present. All nuclei and nucleons are advected with the flow of the plasma by solving an advection equation for each species i,

$$\frac{\partial \rho Y_i}{\partial t} + \nabla \cdot (\mathbf{v} \rho Y_i) = 0, \tag{3.9}$$

with Y_i being the number fraction of the isotopes. To ensure that the mass of each isotope is conserved and only altered by nuclear reactions, we use the consistent multi-fluid advection (CMA) scheme by Plewa & Müller (1999). The scheme ensures that the sum of the mass fractions for all advected, massive species $X_i = Y_i A_i$ (A_i being the atomic mass number) is unity after every time step. In addition, an advection equation is solved for the electron fraction, which is not treated by the CMA scheme.

The network-solver calculates rate-dependent nuclear reactions along the chain of α-nuclei. These nuclear reactions are fully coupled to the hydrodynamics by a source term,

$$\delta t Q_{\mathrm{nuc}} = n_{\mathrm{B}} \Delta \bar{m} c^2 = n_{\mathrm{B}} \sum_i (Y_{i,t_n} - Y_{i,t_{n+1}}) B_i(Z, A), \tag{3.10}$$

accounting for the consumption or release of internal energy. This is done by calculating the change in the mean baryon mass $\Delta \bar{m}$. The binding energy per nucleus i is defined as,

$$B_i(Z, A) = [(A - Z) m_n + Z m_p - m_i] c^2, \tag{3.11}$$

where m_n and m_p are the masses of free neutrons and protons, respectively, and m_i is the mass of the i^{th} nucleus. The i^{th} nucleus is composed of $(A - Z)$ neutrons and Z protons.

In addition to the energy source term, nuclear reactions destroy or produce nuclei and consequently, change the number fractions of nuclei Y_i. The Helmholtz EOS accounts for both, the energy source term changing the internal energy density and the change of the composition, updating the thermodynamic state.

Note that the hydrodynamic timescale can be much larger than the timescale of nuclear reactions. So-called subcycling is necessary, which means that for every hydrodynamic time step several reaction network time steps are performed. After every subcycle of the network solver the thermodynamic state is updated by the Helmholtz EOS accounting for both source terms. The release of energy after every subcycle and the coupling to the stellar fluid in general was implemented after the work by Ugliano et al. (2012). The change of the internal energy per subcycle needs to be further restricted to $< 5\,\%$ per time step of the network as suggested by Mueller (1986). Whenever the limit is reached the time step is halved and recalculated.

The goal of employing the α-network is to capture bulk nucleosynthesis. This means getting a handle on the synthesized nickel during the explosion. The radioactive decay of the ejected nickel powers the light curve of the supernova which is one of the main observable signatures. Another purpose of the network is a good approximation of the energy release and consumption by nuclear reactions. This energy conversion influences the dynamical evolution of the model.

The α-network does not provide detailed nucleosynthesis of hundreds of isotopes. Here are a few reasons why detailed nucleosynthesis is not desired: A simple reason is computational efficiency. More species require the inversion of a larger matrix (two-dimensional, where every entry corresponds to a possible reaction path with reaction rate between two nuclei) by the solver and therefore a higher computational cost. Another reason is the freedom connected to our parameter approach. The nucleosynthesis for individual isotopes depends sensitively on details of the dynamical evolution of a model. The exact onset of the explosion, for example, or the expansion timescale of the shock after the onset of the explosion are ambiguous in our approach. Finally, the nucleosynthesis depends sensitively on the electron fraction,

$$Y_{\mathrm{e}} = \frac{n_{\mathrm{e}^-} - n_{\mathrm{e}^+}}{n_{\mathrm{B}}}, \tag{3.12}$$

defined as the ratio of the number densities of unbalanced electrons (number density of positrons n_{e^+} subtracted from the number density of electrons n_{e^-}) and baryons n_{B}. The electron fraction is only altered by weak forces. Weak interactions are followed with an approximate gray neutrino-transport solver in our approach. However, the gray neutrino-transport scheme is unable to reproduce the electron fractions Y_e reliably if compared to more sophisticated transport solvers (see subsequent section). Thielemann et al. (1996) showed that the production of ^{56}Ni is sensitive to the conditions present during the onset of the explosion when heavy elements are formed.

Nevertheless, we try to account for this deficiency of the α-network by introducing a tracer nucleus accounting for the approximate nature of the transport solver. Whenever, ^{56}Ni is produced by a nuclear reaction, but the electron fraction is below $Y_e < 0.49$ a tracer nucleus ($^{56}\mathrm{Ni}_{\mathrm{Tracer}}$) is produced instead. The abundance of the tracer nucleus can be envisioned as the error bar of the total nickel production, because at least some of the tracer will form neutron-rich nuclei in a detailed nucleosynthesis calculation.

On the other end of the mass scale, the nucleons are a further deficiency of the network. The nucleons are advected with the fluid flow but not part of the reaction network. Nucleons would freeze-out when entering the regime of the α-network and their energy contribution would not be accounted for if they recombine. Instead of only advecting the nucleons we set them to recombine to α-particles when they enter the regime of the network solver. The release of binding energy by the recombination is then accounted for by the Helmholtz EOS. This is, of course, an approximation resulting in an inconsistency of the composition Y_i and the separately evolved electron fraction Y_e. We use this approximation, because a set of neutrons, protons and α-nuclei cannot represent the thermodynamic state correctly: Mean charge number $\bar{Z}$, mean mass number $\bar{A}$ and mean binding energy per nucleon $\bar{B} = \bar{m}/m_{\mathrm{u}}$ (m_{u} being the atomic mass unit) in our small network disagree with the results of a larger reaction network. Especially, if the electron fraction is not equal to 0.5, charge conservation dictates the presence of free nucleons (neutrons or protons) for our set of nuclei. But free nucleons increase the Boltzmann pressure,

$$P_{\mathrm{B}} = N_{\mathrm{A}} k_{\mathrm{B}} T \sum_i Y_i, \tag{3.13}$$

with N_{A} being the Avogadro constant and k_{B} being the Stefan–Boltzmann constant, by increasing the number of particles and the consumption of internal energy, compared to a composition composed of heavy nuclei. We improve on this by sacrificing charge conservation in this intermediate nuclear-burning regime. The recombination of the nucleons to α-particles results in a more realistic mean binding energy per nucleon and total number of particles. Consequently, the energy release and the Boltzmann pressure are better realized. The electron fraction Y_e and the mean charge number $\bar{Z}$ are inconsistent, but the Helmholtz EOS needs a mean charge number $\bar{Z}$ as input. As another improvement towards a more realistic representation of the thermodynamic state we use the electron fraction Y_e which is separately advected multiplied by the mean atomic mass number per nucleon $\bar{A}$ instead of the mean charge number per nucleon $\bar{Z}$ obtained from the composition. The mean atomic mass number per nucleon $\bar{A} = (\sum_i X_i/A_i)^{-1}$ is obtained using the charge-inconsistent mass fractions X_i and the corresponding mass numbers A_i of each nucleus. The Helmholtz EOS then uses both, the mean atomic number $\bar{A}$ and the new mean charge number $\bar{Z}_{\mathrm{new}} = \bar{A} Y_e$ as input.

3.2.3. Nuclear Statistical Equilibrium

Increasing the temperature even further we enter the regime of nuclear statistical equilibrium (NSE). In our simulations, the temperature above which NSE is assumed is $T_{\mathrm{NSE}} = 7 \times 10^9\,\mathrm{K}$. This temperature is sufficiently high enough that the reaction rates of all nuclear reactions are quasi time-independent (compared to the hydrodynamical timescale) and can be considered instantaneous. The thermodynamic state therefore no longer depends on the composition Y_i, but is solely a function of the density ρ, temperature T, and electron fraction Y_e. All of the nuclear chart is now accessible instantaneously and the composition of the previous time step does not affect the new composition. The internal energy in NSE is no longer a conserved quantity as it was the case in the regime without nuclear reactions. Now, the sum of the internal energy density $\rho\epsilon$ and the rest-mass energy density e_{rm} is conserved because mass can transform instantaneously into internal energy and vice versa. But numerically, PROMETHEUS still evolves and conserves the total energy density $e_{\mathrm{tot}} = \epsilon + \frac{1}{2}|\mathbf{v}|^2$ (ϵ denotes the specific internal energy and $\frac{1}{2}|\mathbf{v}|^2$ is the kinetic energy density). To be able to follow the so-called relativistic energy density $e_{\mathrm{rel}} = e_{\mathrm{tot}} + e_{\mathrm{rm}}$, which is the conserved in NSE, we need to be able to follow the rest-mass energy density e_{rm} as well. We use the fact that PROMETHEUS already evolves the rest-mass energy density by the advection equations for the individual species. Knowing the binding energy B_i

(see Eq. 3.11) of each nucleus and all number fractions Y_i one can calculate the desired rest-mass energy density,

$$e_{\mathrm{rm}} = n_{\mathrm{B}} \sum_i Y_i B_i, \tag{3.14}$$

with n_{B} being the baryon number density and therefore the relativistic energy density e_{rel}. The new thermodynamic state is a function of density ρ, relativistic energy density e_{rel}, and electron fraction Y_e. Technically, the thermodynamic state is calculated by the Helmholtz EOS using the number fractions Y_i from the tabulated composition in NSE. The low-density NSE region in the (ρ,T)-plane (see Fig. 3.1) was not included in the setup by Ertl (2012). For the NSE as realized in HOTB in the low-density regime ($\rho < \rho_{\mathrm{hd}}$) we use the same nuclei that are also present in the α-burning network plus the nucleons (the tracer is not considered here). The NSE-table in the (ρ,T,Y_{e})-plane is constructed by the routines provided by Kifonidis (2004) (private communication). Another practical reason to switch to a NSE-solver is again computational efficiency, because a rate-dependent burning network and its time step are correlated with the speed of nuclear reactions, which increase with temperature.

3.2.4. Equation of State at High Densities

Finally, if we increase the density further above ρ_{hd} while staying above the temperature for NSE T_{NSE}, we enter the high-density regime (the regime of the nuclear EOS). Note, temperatures below T_{NSE} and densities above ρ_{hd} are never realized in our simulations. In the high-density (and high-temperature) regime the matter is densely packed and interactions between nucleons start to play a role. At the same time, we enter a theoretically unknown regime for the thermodynamic state of matter, which is also out of reach for any terrestrial experiment. Knowledge about the state of matter in this regime relies solely on astrophysical observations.

The uncertainties connected to the nuclear EOS is part of the reason, why we excise the innermost region of the PNS after core bounce and employ a parameterized model for the region. Nevertheless, we utilize the nuclear EOS by Lattimer & Swesty (1991) based on a liquid drop model in the version with an incompressibility modulus of bulk nuclear matter of $K = 220\,\mathrm{MeV}$. The L&S 220 (as we will abbreviate it from now on) is widely used in self-consistent simulations of core-collapse supernovae (recent examples are Hanke et al., 2013, Tamborra et al., 2014, Melson et al., 2015a;b, Lentz et al., 2015, O'Connor & Couch, 2015, Summa et al., 2016) and is in agreement with current observational constraints for the most massive neutron stars as measured by Demorest et al. 2010 and Antoniadis et al. 2013. Based on these measurements a proposed model for the nuclear EOS needs to be able to stabilize a NS against gravity of at least $2\,M_{\odot}$ (gravitational mass).

Another reason for implementing a high-density EOS are the nucleon-nucleon interactions which start to be become important at around $10^{12}\,\mathrm{g\,cm^{-3}}$. Such densities are part of the computational domain even if we excise the innermost core. We are now able to simulate the PNS surface and its steep density gradient more realistically than done by Ugliano et al. (2012). We certainly improved the physical modeling in this respect when we use the L&S 220 above a density of $\rho_{\rm hd} = 10^{11}\,{\rm g\,cm^{-3}}$. The L&S 220 has its downside as it is not in good agreement with the analytically, well-known thermodynamic state of the matter in the low-density limit. This is the reason why we substituted it for the low-density NSE regime.

The matter in this regime is also in NSE and we need to be able to follow the internal energy density $e_{\rm int}$ as well as the rest-mass energy density $e_{\rm rm}$ (as described in the previous section). Only the sum of the two contributions, the relativistic energy density $e_{\rm rel}$ is conserved in NSE. The L&S 220 and its liquid drop model for the baryon composition in NSE considers free nucleons, α-particles, and a representative heavy nucleus and returns this as a thermodynamic state. The nucleons and α-particles are trivially brought into agreement with HOTB, because they are already part of the set of advected species. The representative heavy nucleus on the other hand poses a problem, because it is given with a non-integer atomic mass number $A_{\rm heavy}$ and charge number $Z_{\rm heavy}$. Our set of advected α-nuclei cannot represent most combinations of $A_{\rm heavy}$ and $Z_{\rm heavy}$. We overcome this by discarding the atomic charge number $Z_{\rm heavy}$ and only considering the atomic mass number $A_{\rm heavy}$ of the representative heavy nucleus. We assign the heavy nucleus to the nucleus with an atomic mass number closest to $A_{\rm heavy}$. We then calculate the rest-mass contribution by the new, assigned composition and subtract it from the relativistic energy density $e_{\rm rel}$ which is provided by the L&S 220. The resulting approximate internal energy density and the mass fractions are then advected as done in the low-density NSE regime to conserve energy. Note that the assigned heavy nucleus only survives, if it gets advected from the high-density regime directly to the regime of the α-burning network.

3.2.5. Setup During Core Collapse

During collapse the setup we described in the previous sections is not applicable and we have to use the L&S 220 for a larger part of the density-temperature plane. We do not excise the innermost core in this phase. To be able to follow collapse and the formation of the shock we need to simulate until supernuclear densities are reached in the center (around the uniform nuclear saturation density of $\sim 2.5 \times 10^{14}\,{\rm g\,cm^{-3}}$). The EOS stiffens at these densities and a pressure wave originates that turns into the supernova shock at the edge of the homologous core. HOTB was not capable of simulating the collapse phase and the formation of the shock and relied on models being simulated with PROMETHEUS-VERTEX (Rampp & Janka, 2002, Buras et al., 2006a). Only since a nuclear EOS was implemented (Ertl, 2012) we can follow core collapse with a simple scheme for the neutrino losses (introduced in Sect. 3.3.1).

For the setup during collapse, the boundaries of the NSE regime is moved. NSE is assumed down to very low densities of $\rho_{\mathrm{hd}} = 3 \times 10^7\,\mathrm{g\,cm^{-3}}$ and temperatures of $T_{\mathrm{NSE}} = 5 \times 10^9\,\mathrm{K}$. The low-density NSE solver is not applied and we rely only on the L&S 220 to provide the composition in NSE. The reason for this is a similar one as for the recombination of free nucleons to α-particles at the edge of the α-burning regime. The progressing deleptonization of the matter results in a decreasing electron fraction far below 0.5. For our standard composition with free nucleons and α-nuclei, this would lead to the production of free nucleons instead of heavy neutron-rich nuclei. The collapse of the iron core would be slowed down or even stopped by the increased Boltzmann pressure resulting in a delayed collapse of the core. The transient feature would perturb the layers above the iron core which are already collapsing and the internal structure of the star would be distorted compared to the result of the stellar evolution calculation. For a smooth, transient-free collapse, we use the high-density EOS, which covers heavy neutron-rich nuclei. Nevertheless, the low-density limit of the L&S 220 is inconsistent with the analytic solution of the Helmholtz EOS. But the matter that is treated with the L&S 220 during collapse is completely incorporated within the shock. It separates low-density and high-density EOS after bounce when we switch to the aforementioned setup.

3.3. Neutrino Treatment

In order to simulate core-collapse supernovae, it is crucial to consider neutrinos and their interactions. They are the key ingredient for the successful revival of the stalled accretion shock. For the dynamical process of shock revival, we need to solve the Boltzmann transport equation for neutrino radiation. We employ several approximations with varying degrees of sophistication, to be able to simulate a progenitor model from the onset of core collapse until the neutrino-driven wind becomes dynamically unimportant in an exploding case or the decision can be made that the star does not explode. The core collapse up to 2 ms after core bounce (when the post-shock entropy reaches a value of $3\,k_{\mathrm{B}}$ per baryon for the first time) is followed by a simple and efficient numerical scheme for the deleptonization by Liebendörfer (2005), which is described in Sect. 3.3.1. The so-called deleptonization scheme avoids a solution of the Boltzmann equation by reducing the problem to local source terms based on a template extracted from a self-consistent simulation. A detailed comparison to a self-consistent simulation can be found in Ertl (2012). The latter work also shows how we continue after the time when the deleptonization scheme is not applicable anymore. In section 3.3.2 we present how the Boltzmann equation is solved. We make use of a gray neutrino-transport solver for the post-bounce evolution of a model as described by Scheck et al. (2006) outside of an excised innermost core. At the boundary of the excised core, a boundary condition is imposed, which will be presented in section 3.4. Initially after bounce, the innermost $0.5\,M_{\odot}$ are excised, but the excised region later extended to $1.1\,M_{\odot}$. At the inner boundary of $0.5\,M_{\odot}$, a constant neutrino luminosity is injected until the shock encloses $1.25\,M_{\odot}$. After the shock has passed this mass coordinate, the boundary is moved to $1.1\,M_{\odot}$ and the neutrino luminosity is calculated by an analytic

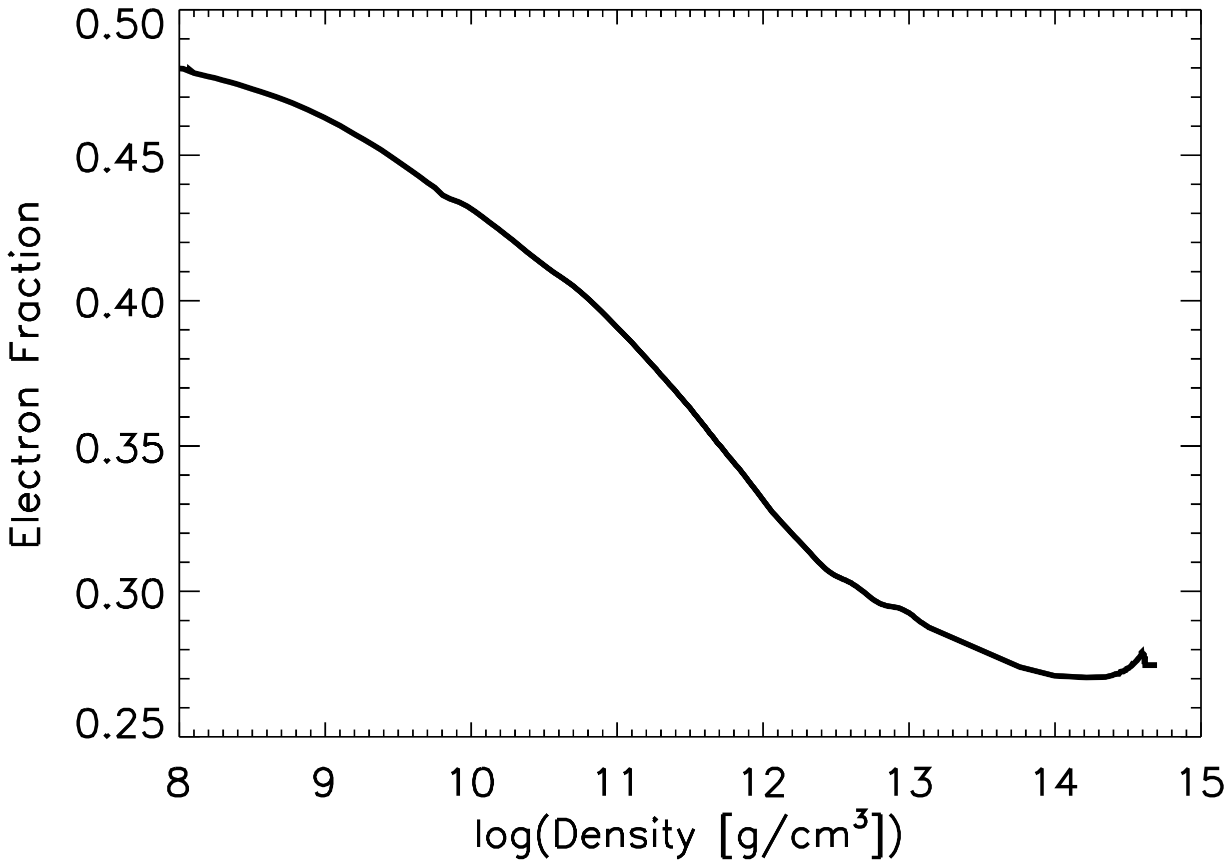

Figure 3.2.: Electron fraction as a function of density, $Y_e(\rho)$, for modeling the deleptonization of the collapsing stellar iron core during the infall phase until core bounce according to the approximate treatment of Liebendörfer (2005). *(This figure is already published in Ertl et al. (2016a).)*

one-zone core-cooling model with a set of tuneable parameters.

3.3.1. Deleptonization Scheme

We make use of an efficient, simple approximation to neutrino transport from the onset of core collapse until shortly ($\sim 2\,\mathrm{ms}$) after core bounce. Liebendörfer (2005) described a scheme by which one can exchange the numerically expensive solution of a transport problem with a local problem. The scheme approximates the deleptonization of the iron core leading to its collapse and the formation of a shock at core bounce (when nuclear densities are reached in the center).

The deleptonization scheme distinguishes three regimes for neutrino matter interactions. Starting with high densities, neutrinos are assumed to be trapped above $\rho_{\mathrm{trap}} \approx 2 \times$

$10^{12}\,\mathrm{g/cm^3}$ and the electron fraction only follows the prescribed $Y_e(\rho)$ (first parameter) profile extracted from a first-principle simulation. It is save to neglect neutrino stress in this regime as shown by the satisfying results of Ertl (2012). For lower densities, neutrinos thermalize and transfer a part of their energy to the plasma until they reach their mean escape energy E_ν^{esc} (second parameter). This holds when $\mu_e - \mu_n + \mu_p - E_\nu^{\mathrm{esc}} > 0$ is met, where μ_e, μ_n, and μ_p are the chemical potentials of electrons, neutrons and protons respectively. To account for the thermalization of neutrinos an entropy source term,

$$\frac{\delta s}{\delta t} = -\frac{\delta Y_e}{\delta t}\frac{\mu_e - \mu_n + \mu_p - E_\nu^{\mathrm{esc}}}{T}, \tag{3.15}$$

is calculated in this regime and accounted the EOS with density, entropy, and electron fraction as input. If the condition for thermalization is not met, we are in the third regime, where neutrinos stream away unhindered (at least without relevant dynamical effect).

Ertl (2012) described the deleptonization scheme in greater detail and compared simulations utilizing this scheme to simulations with a more elaborate neutrino treatment by PROMETHEUS-VERTEX, a first-principle code with electron-capture rates by Langanke et al. (2003). The good agreement found by the latter work was further improved by employing a bounce profile extracted from PROMETHEUS-VERTEX. The $Y_e(\rho)$ profile (extracted at bounce) was provided by Müller (2013) (private communication) and is displayed in Fig. 3.2 .

3.3.2. Gray Transport Solver

For the evolution of a model after core bounce, the nature of neutrino contributions changes. During collapse, a local description for neutrino losses is sufficient to follow the evolution, but after core bounce, when a stalled accretion-shock has formed, it is important to be able to follow neutrino production at one site and neutrino interaction with energy deposition or consumption at another. We therefore utilize a solver by Scheck et al. (2006) providing an approximate solution to the Boltzmann transport problem.

In the following, we will summarize the scheme while pointing out its main assumptions. We start with the full problem, which is determined by the Boltzmann transport equation,

$$\frac{1}{c}\frac{\partial}{\partial t}I + \mu\frac{\partial}{\partial r}I + \frac{1-\mu^2}{r}\frac{\partial}{\partial \mu}I = S, \tag{3.16}$$

with $I = I(t, r, \epsilon, \mu)$ denoting the specific intensity of the radiation and $S = S(t, r, \epsilon, \mu)$ is a general source function accounting for all interactions. We start with a solid-angle integration of the Boltzmann transport equation in our approximate gray-transport scheme. The word “gray” means that the energy spectrum of the neutrinos is not evolved in time, but only the mean neutrino energy. The energy spectrum is assumed to be Fermi-Dirac shape. These two simplifications reduce the Boltzmann transport equation to the zeroth angular momentum representation of the equation,

$$\frac{\partial}{\partial t}E + \frac{1}{r^2}\frac{\partial}{\partial r}(r^2 F) = Q^+ - Q^-. \tag{3.17}$$

while Q^+ is the emission term and $Q^- = \kappa_a cE$ the absorption term where κ_a is the absorptivity. The former source function S is split into Q^+ and Q^- and both are treated separately. Another approximation is connected to the flux factor $f(r,t) := F(r,t)/cE(r,t)$ (ratio of neutrino flux F and neutrino energy density E multiplied by the speed of light c) which is assumed to be constant in time $\partial f/\partial t = 0$. This approximation is based on sophisticated transport simulations (e.g., Buras et al., 2003; 2006a;b) showing little variability of the flux factor f. Applying this approximation to Eq. (3.17) together with $L := 4\pi r^2 F = 4\pi r^2 fcE$ results in an equation for the evolution of the neutrino luminosity:

$$\frac{\partial}{\partial t}L + c_{\mathrm{eff}}\frac{\partial}{\partial r}L = 4\pi r^2(Q^+ - Q^-). \tag{3.18}$$

with $c_{\mathrm{eff}} := cf(r,t)$ denoting an effective speed for the propagation of neutrinos. In case of vanishing source terms, $Q^+ = Q^- = 0$, the equation for the evolution of the neutrino luminosity (Eq. 3.18) is reduced to the solution of a simple advection equation along characteristics $r(t) = r_0 - c_{\mathrm{eff}}t$. If the effective speed c_{eff} is known the solution of Eq. (3.18) is much simpler than the initial Boltzmann transport problem of Eq. (3.16). But a problem arises, because the effective speed c_{eff} is coupled to the flux factor $f(r,t)$, which depends on the solution of the Boltzmann transport problem itself. Scheck et al. (2006) argue that $f(r,t)$ can be well-fitted by an r-dependent function that in turn depends on the steepness of the density profile. This approximation together with the assumption that the (medium-dependent) coefficients Q^+ and $\tilde{\kappa} := \kappa_a/f = 4\pi r^2 Q^-/L$ are constant between two points along the characteristics leads to an analytically integrable function:

$$\begin{gathered} L(r,t) = L(r^\star, t^\star)e^{-\tilde{\kappa}_{\mathrm{eff}}(t-t^\star)} + \frac{4\pi Q^+}{\tilde{\kappa}^3}\times \\ \{[1 - e^{-\tilde{\kappa}_{\mathrm{eff}}(t-t^\star)}][1 + (\tilde{\kappa}r^\star - 1)^2] + \tilde{c}_{\mathrm{eff}}(t-t^\star)[2\tilde{\kappa}r^\star + \tilde{\kappa}c_{\mathrm{eff}}(t-t^\star) - 2]\}. \end{gathered} \tag{3.19}$$

This function is solved by Hotb analytically following the neutrino luminosity from the boundary of the innermost excised region (see subsequent section) in time and radius along the computational grid. $(r^\star, t^\star)$ is the interpolated state along a characteristic in time or space. The choice of the characteristic for the integration of Eq. (3.19) can be found in Scheck et al. (2006).

We will now briefly discuss the neutrino-matter interactions that are taken into account by the transport scheme. All interactions are calculated with the assumption that the energy spectrum has a Fermi-Dirac shape. Weak interactions allow for the inelastic charged-current processes,

$$\nu_{\mathrm{e}} + \mathrm{n} \rightleftharpoons \mathrm{p} + \mathrm{e}^- \tag{3.20}$$

and

$$\bar{\nu}_{\mathrm{e}} + \mathrm{p} \rightleftharpoons \mathrm{n} + \mathrm{e}^{+}. \tag{3.21}$$

Charged W bosons are exchanged between electron neutrinos ν_{e} or electron anti-neutrinos $\bar{\nu}_{\mathrm{e}}$ and nucleons, neutrons n and protons p^{+} respectively. Furthermore, thermal pair-production processes are considered in the gray transport scheme:

$$\mathrm{e}^{+} + \mathrm{e}^{-} \rightleftharpoons \bar{\nu}_i + \nu_i \quad \text{with } i = \mathrm{e}, \mu, \tau. \tag{3.22}$$

Lastly, elastic neutrino scattering off nuclei (A), neutrons, protons, electrons, and positrons,

$$\nu_i + x \rightleftharpoons \nu_i + x \quad \text{with } x = \mathrm{A},\ \mathrm{n},\ \mathrm{p}^{+},\ \mathrm{e}^{-},\ \mathrm{e}^{+}, \tag{3.23}$$

is also considered.

3.4. Innermost Excised Region and its Boundary Condition*

In this section we will discuss the physical model for the central region and how it is connected to the computational domain. The inner boundary condition together with the analytic one-zone core-cooling model are the heart of our modeling approach. A set of free tuneable parameters is connected to the core model and applied to the post-bounce evolution of the progenitor models. By adjusting these parameters, we gain the freedom to calibrate progenitor models to observations of their explosions. We will begin with discussing the boundary condition and afterwards the analytic one-zone core-cooling model.

3.4.1. Hydrostatic and Contracting Boundary Condition

After core bounce we exclude the inner high-density core of the PNS at densities significantly above the neutrinospheric region from the hydrodynamical modeling, and replace them by an inner, contracting grid boundary. Excluding the high-density core of the PNS from direct modeling can be justified by the still incomplete knowledge of the equation of state in the supernuclear regime and significant uncertainties in the neutrino opacities in dense, correlated nuclear matter, which overshadow all fully self-consistent modeling.

We excise the innermost $0.5\,M_{\odot}$ after bounce and replace it by a boundary model. For the hydrodynamics, we apply the conditions that are needed to maintain hydrostatic equilibrium at this Lagrangian grid boundary (Janka & Müller, 1996). Concerning neutrino losses

---

*This section is part of the author's contribution to Sukhbold et al. (2016), yet adjusted to fit to the narrative of this work.

from the excised, region we impose a constant neutrino-luminosity $10^{52}\,\mathrm{erg\,s^{-1}}$ and follow it with our gray neutrino transport solver on the computational domain until the shock encloses $1.25\,M_\odot$. The shock reaches this position a few tens of milliseconds after core bounce and it has tuned into a stalled accretion shock by this time in all progenitor models. This early phase is described and compared to self-consistent simulations including the neutrino signal by Ertl (2012). Latter work found good agreement to the post-bounce properties by PROMETHEUS-HOTB and the self-consistent simulations with PROMETHEUS-VERTEX especially for the region outside of innermost $1.1\,M_\odot$ of the PNS.

The region inside the central $1.1\,M_\odot$ of the PNS is again excised from the computational volume and is replaced by the contracting, hydrostatic inner grid boundary after the early phase. The shrinking of the cooling and deleptonizing PNS is mimicked by the contraction of the inner grid boundary, R_{ib}, which is described by an exponential function (Eq. 1 in Arcones et al., 2007) for the core boundary radius,

$$R_{\mathrm{ib}}(t) = R_{\mathrm{ib,final}} + (R_{\mathrm{ib,initial}} - R_{\mathrm{ib,final}})e^{-t/t_0}, \tag{3.24}$$

with the initial radius of the inner boundary $R_{\mathrm{ib,initial}} = R(1.1\,M_\odot$ at $\sim 10\,\mathrm{ms}) \sim 60\,\mathrm{km}$ and the parameters $t_0 = 0.4\,\mathrm{s}$ and $R_{\mathrm{ib,final}} = 20\,\mathrm{km}$ (also given in Sect. 2 of Ugliano et al., 2012). In order to avoid too severe time-step restrictions that could hamper the tracking of the combined evolution of PNS and ejecta over more than 15 s we choose the case of "standard" instead of "rapid" contraction shown in Fig. 1 of Scheck et al. (2006). This may lead to an underestimation of the accretion luminosity and of the gradual hardening of the radiated neutrino spectra compared to self-consistent supernova simulations, but in our approach this can well be compensated by a corresponding adjustment of the calibration of the inner core as neutrino source. Since the accretion luminosity computed by the transport adds to the core luminosity imposed at the inner grid boundary, the calibration sets constraints to the combined value of these two contributions.

3.4.2. Analytic One-Zone Core-Cooling Model

As detailed in Ugliano et al. (2012), we describe the high-density PNS core of mass $M_{\mathrm{c}} = 1.1\,M_\odot$ by a simple one-zone model under the constraints of energy conservation and the Virial theorem including the effects associated with the growing pressure of the accretion layer, whose accumulation around the PNS core is followed by our hydrodynamic simulations. The one-zone core model provides a time-dependent total core-neutrino luminosity, $L_{\nu,\mathrm{c}}(t)$, which determines the boundary luminosity imposed at the inner grid boundary (at R_{ib}) of the computational grid, suitably split between ν_e, $\bar{\nu}_e$, and heavy-lepton neutrinos (see Ugliano et al. 2012 and Scheck et al. 2006). Besides the luminosities of the different neutrino species, also the mean energies (or spectral temperatures) of the inflowing neutrinos are prescribed at R_{ib} (cf. Ugliano et al. 2012).

The total core-neutrino luminosity $L_{\nu,\mathrm{c}}(t)$ is determined by the core mass, M_{c}, the core radius, $R_{\mathrm{c}}(t)$, the rate of contraction of this radius, $\dot{R}_{\mathrm{c}}(t)$, the mass of the PNS accretion mantle around the core, m_{acc} (taken to be the mass between the inner grid boundary and a lower density of $10^{10}\,\mathrm{g\,cm^{-3}}$), and the mass-accretion rate of the PNS, $\dot{m}_{\mathrm{acc}}$, as computed in our hydrodynamical runs. Equation (4) of Ugliano et al. (2012) for the core luminosity can be rewritten as

$$L_{\nu,\mathrm{c}}(t) = \frac{1}{3(\Gamma-1)}\left[(3\Gamma-4)(E_{\mathrm{g}}+S)\,\frac{\dot{R}_{\mathrm{c}}}{R_{\mathrm{c}}} + S\,\frac{\dot{m}_{\mathrm{acc}}}{m_{\mathrm{acc}}}\right] , \tag{3.25}$$

with the factors

$$E_{\mathrm{g}}+S \;=\; -\frac{2}{5}\,\frac{GM_{\mathrm{c}}}{R_{\mathrm{c}}}\left(M_{\mathrm{c}}+\frac{5}{2}\,\zeta\,m_{\mathrm{acc}}\right) , \tag{3.26}$$

$$S \;=\; -\zeta\,\frac{GM_{\mathrm{c}}m_{\mathrm{acc}}}{R_{\mathrm{c}}} , \tag{3.27}$$

and with the adiabatic index Γ and coefficient ζ $(=\mathcal{O}(1))$ being free parameters of the model. We note that through the S-dependent terms the PNS-core luminosity depends on the structure of the progenitor star, which determines the mass-accretion rate $\dot{m}_{\mathrm{acc}}$ and thus the mass m_{acc} of the accretion mantle of the PNS. The core radius as a function of time is prescribed by

$$R_{\mathrm{c}}(t) \;=\; R_{\mathrm{c,f}} + \frac{R_{\mathrm{c,i}}-R_{\mathrm{c,f}}}{(1+t)^{n}} , \tag{3.28}$$

where the time t is measured in seconds. The initial PNS core radius, $R_{\mathrm{c,i}}$, is set equal to the initial radius of the inner boundary of the hydrodynamic grid, $R_{\mathrm{ib}}^{\mathrm{i}}$, and the final PNS core radius, $R_{\mathrm{c,f}}$, as well as the exponent n are also free parameters of our model. Note that R_{c} should be considered as a representative radius of the high-density core. Since we grossly simplify the radial structure of the PNS core by a one-zone description, the numerical value of R_{c} has no exact physical meaning except that it represents a rough measure of the size of the PNS core. However, neither its time evolution nor its final value need to be equal to the inner boundary radius of the hydrodynamic grid or to the radius of the $1.1\,M_{\odot}$ core of a self-consistently computed PNS model using a nuclear EOS. Nevertheless, with a suitably chosen (calibrated) time dependence of R_{c}, our model is able to reproduce basic features of the neutrino emission of cooling PNSs, and the choice of n and $R_{\mathrm{c,f}}$ can be guided by the temporal behavior of $R_{\mathrm{c}}(t)$ in sophisticated PNS cooling calculations (see below).

Since both of the expressions of Eqs. (3.26) and (3.27) are negative and $\dot{R}_{\mathrm{c}} < 0$ and $\dot{m}_{\mathrm{acc}} > 0$ for the contracting and accreting PNS, the first term in the brackets on the r.h.s. of Eq. (3.25) is positive while the second term is negative. The former term represents the gravitational binding energy release as a consequence of the PNS-core settling in the gravitational potential including the compressional work delivered by the surrounding accretion layer. In contrast, the latter (negative) term accounts for the additional internal energy (and pressure) of the core that is needed for gravitational stability when the overlying mantle grows in mass. This second term thus reduces the energy that can be radiated in neutrinos.

3.4.3. Setup of the Long-Time Evolution

We employ the gray neutrino-transport solver for $\sim 15\,\mathrm{s}$ after core bounce. After this time, the effects of neutrino-heating and with it the neutrino-driven wind become dynamically insignificant. We switch off the gray neutrino-transport solver and the analytic core-cooling model. Afterwards, we follow the flow of the stellar plasma by the hydrodynamic solver PROMETHEUS. With the neutrino-source being shut off, temperatures are low enough that nuclear reactions can be neglected as well. We move the boundary to higher radii, initially to $10^9\,\mathrm{cm}$ and then to $10^{10}\,\mathrm{cm}$, which increases the time step by avoiding small zones in the center and increases computational efficiency. The boundary is now an open boundary condition. The supernova shock is followed until the fallback mass has converged and can be determined. This happens, potentially, after the supernova shock has reached the surface of the star. The progenitor model is therefore extended with a quadratically declining density profile up to $10^{15}\,\mathrm{cm}$ under the constraint that not more than $0.5\,M_\odot$ is added. This is the standard setup also used by Ugliano et al. (2012).

4. Calibration and Progenitor Models

With the approach discussed in the previous two chapters we are able to evolve many hundred progenitor models at low computational costs from the onset of iron-core collapse beyond shock-breakout at the surface of the star, a successful supernova (SN) explosion. The progenitor models are provided at the onset of core collapse and evolved up to this point by 1D stellar evolution calculations with varying initial conditions (zero-age main-sequence (ZAMS) mass, metallicity, etc.). In this chapter we will list and discuss all employed progenitor models in our study. We will start with the progenitor models applied to calibrate the analytic core-cooling model. Afterwards, we will discuss the sets of progenitor models we apply the obtained parameter choice to. These large sets of progenitor models only became available in the last decade (e.g., Woosley et al., 2002, for one of the first large sets) and offer a new way of probing the systematics of core-collapse supernovae (CCSNe).

The content of this chapter is in parts already published in Ertl et al. (2016a) and Sukhbold et al. (2016), yet only the author's contribution to the latter publication was taken.

4.1. Calibration of the Analytic One-Zone Core-Cooling Model

We discussed the idea behind the calibration procedure already in Chap. 2: We assume the neutrino-driven mechanism to explode massive stars and especially assume it to be the mechanism by which SN 1054 and SN 1987A exploded, our standard cases. For the calibration we take into account the uncertainties connected to high-density physics and the neutrino opacities. We excise the high-density interior of the proto-neutron star (PNS) and replace it by an analytic one-zone core-cooling model (see Sect. 3.4.2) with a set of free tuneable parameters (Γ, ζ, $R_\mathrm{c}(t)$, n). The core-model is calibrated by by tuning the free parameters such that the explosion energy and the nickel ejecta mass reproduced. In the following we will give an overview of the observed properties of both SNe, state the obtained core-model parameters, describe the model dynamics, and explain how the chosen parameters are then applied to simulate large sets of progenitor models.

4.1.1. SN 1987A and its Progenitor Star Sk -69^o 202

Observation of the Progenitor Star and the SN Explosion

SN 1987A has been studied for nearly three decades and is one of the SNe with the tightest constraints on its observed properties, because it was the closest to earth in modern times. It is therefore the best choice of a standard case in our calibration procedure. It was possible to measure the explosion energy (final kinetic energy) of about 1.5×10^{51} erg (Arnett et al., 1989, Utrobin et al., 2015), the light curve, and with the tail of the light curve the nickel ejecta mass amounting to $0.07\,M_\odot$ (Bouchet et al., 1991, Suntzeff et al., 1992). The explosion energy and the nickel ejecta mass are the observables we use to calibrate the core-cooling model for an appropriate progenitor model. But both are also observed for many other supernovae. Still, SN 1987A is unique, especially in two key aspects: For one, it was possible to identify the progenitor star for the first time in archival images (Sk -69^o 202 in the Large Magellanic Cloud (LMC) by Walborn et al., 1987) and, for another, a neutrino signal from the SN was observed. SN 1987A is the only SN where it was possible to detect a neutrino signal. Due to the proximity to earth, SN 1987A has been the only SN up to now where the detection of neutrinos was possible.

For the progenitor star and its immediate evolution before explosion the following constraints could be deduced from observations: The identified pre-SN star was a blue supergiant (Type B3-I) with an effective temperature of $14,000 - 17,000\,\mathrm{K}$ (Humphreys & McElroy, 1984, Crowther et al., 2006, Smith, 2007) and a luminosity of $3 - 6 \times 10^{38}\,\mathrm{erg\,s^{-1}}$ (Humphreys & McElroy, 1984, Arnett et al., 1989). Fig. 4.1 shows the position of the observed progenitor star in the Hertzsprung-Russell (HR) diagram (including some model trajectories from stellar evolution calculations for the progenitor star). Using the temperature and the luminosity, a radius of $2 - 4 \times 10^{12}\,\mathrm{cm}$ can be deduced for the star. In addition, the luminosity contains information about the helium core mass, because the helium (shell-) burning powers the luminosity of the supergiant. For the measured luminosity a helium core mass of $6 \pm 1\,M_\odot$ (e.g. Woosley, 1988) can be theoretically inferred.

Apart from the direct observation of the progenitor star, the SN light curve poses further constraints on the structure of the progenitor star. The SN shock had to travel through at least $10\,M_\odot$ of envelope material and this material was mainly composed by hydrogen, but enriched in helium and nitrogen (Woosley, 1988, Shigeyama et al., 1988). The explosion also revealed an approximate mass of ejected oxygen of $1.4 \pm 0.7\ M_\odot$ (Fransson & Kozma, 2002). Another constraint on the progenitor and its pre-SN evolution is imposed by the colliding wind structure observed shortly after the explosion. The progenitor star must have been a red supergiant before it died as a blue supergiant (Woosley et al., 1988).

SN 1987A was also exceptional because of the detected neutrino events (to be precise, electron anti-neutrino ($\bar{\nu}_e$) events). Detectors on earth measured neutrinos for the first time (and only time) coming from a SN (Hirata et al., 1987, Bionta et al., 1987). By this

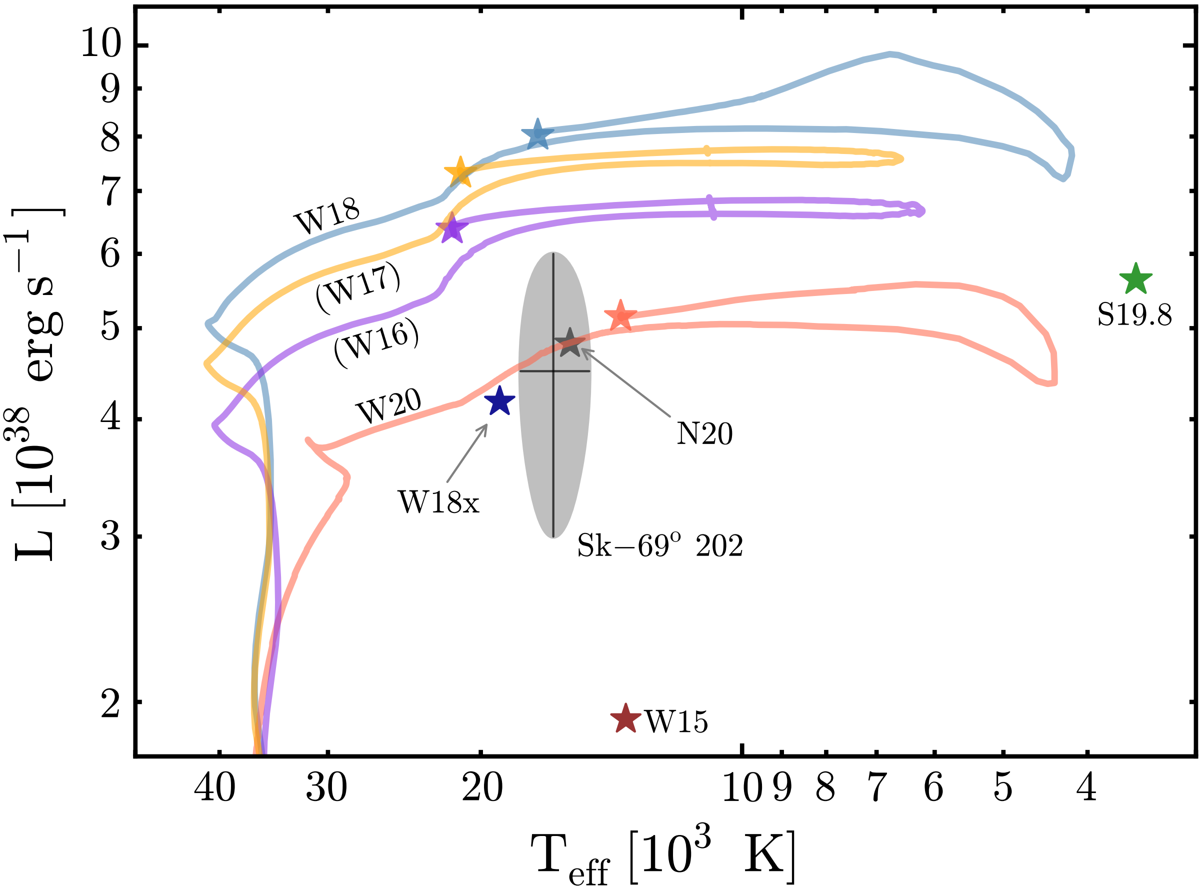

Figure 4.1.: Hertzsprung-Russell diagram for the SN 1987A progenitors used in this study. The shaded region shows the observed properties of Sk -69^o 202 including the error bars. The symbols mark the endpoint of the evolution for each model. Model S19.8 (s19.8 in this work) produced a red supergiant; all the rest are blue supergiants at the time of core collapse, but were preceded by a phase as a red supergiant. Models W16, W17, W18 (w18.0 here), and W18x included rotation; the rest were non-rotating. Model W15 (w15.0 here) was an early model evolved with KEPLER, that relied on now outdated physical modeling to produce a blue supergiant. Model N20 (n20.0 here) was a construct obtained by joining a 6 $M_\odot$ helium star to an envelope. All models beginning with a "W" were calculated using the KEPLER code assuming reduced metallicity and restricted semiconvection. Model W18x had 3/4 the angular momentum of Model W18, but was otherwise identical. *(This figure is taken from Sukhbold et al. (2016), but was not part of the author's contribution to the latter work.)*

observation the neutrino signal could be constrained in its mean neutrino energies (about ~ 15 MeV) and its duration, which is of the order of seconds (~ 10 s). In fact Kamiokande II (Hirata et al., 1987) observed 8 neutrino events in the first two seconds and additional 3 events after another 7 seconds.

Models for the Progenitor Star and Calibration Results

The properties of the explosion of SN 1987A are constrained by observations: nickel ejecta mass and explosion energy are fixed, as well as the approximate cooling behavior (duration and mean energy of the neutrinos) of the PNS is known. Furthermore the observations also put constraints on the progenitor star and therefore restrict the pre-SN model we can employ for calibration. It should be a blue supergiant with a total mass of $15 - 20\,M_\odot$, a $\sim 6\,M_\odot$ helium core and a hydrogen envelope of roughly $10\,M_\odot$. All of these constraints are considered to some extent in our calibration procedure. For the calibration of the core-model parameter we choose five different progenitors: We start with model s19.8, a red supergiant of a series of progenitor models with solar metallicity published by Woosley et al. (2002), which was already employed for the calibration procedure to SN 1987A in Ugliano et al. (2012) and is also used here for comparison. Furthermore, we use four blue supergiant pre-supernova models for the progenitor star of SN 1987A: w15.0 (ZAMS mass of $15\,M_\odot$; Woosley et al. 1988), w18.0 ($18\,M_\odot$, evolved with rotation; Woosley et al. 2007), w20.0 ($20\,M_\odot$; Woosley et al. 1997), and n20.0 ($20\,M_\odot$; Shigeyama & Nomoto 1990, Nomoto & Hashimoto 1988, Saio et al. 1988). The compactness values defined by O'Connor & Ott (2011) as

$$\xi_M \equiv \frac{M/M_\odot}{R(M)/1000\,\mathrm{km}}\,, \tag{4.1}$$

which are a measure for the core structure, as well as the explosion and remnant parameters of these models are listed in Table 4.1.

Models w15.0 and n20.0 are "historical" models produced right after the observation of SN 1987A. Model n20.0 is the combination of a separately evolved $6\,M_\odot$ helium core and a hydrogen envelope. The w15.0 progenitor model is an early model evolved with Kepler, that relies on now outdated opacities, reduced metallicity, and restricted semiconvection in order to produce a blue supergiant. Fig. 4.1 also shows some model tracks of more recent models in the HR diagram, where W18x, W16 and W17 are the most recent ones, but are not employed in this study and left for future work. We employ models w18.0 and w20.0 (W18 and W20 in Fig. 4.1, respectively) for which stellar evolution tracks are available and displayed in the figure. Model w20.0 uses more modern opacities in comparison to model w15.0, and comes close to the observed luminosity and surface temperature of Sk -69^o 202. Model w18.0 fulfills the constraints mentioned before by a reduced metallicity, restricted semiconvection, and substantial rotation, but produces the largest helium core of all models and is consequently too luminous (see Fig. 4.1). More information on the progenitor models can found in the publication by Sukhbold et al. (2016).

Table 4.1.: Calibration models with explosion and remnant properties

		s19.8[a,b]	**w15.0**[c]	**w18.0**[b]	**w20.0**[b]	**n20.0**[b]	**z9.6**[b]
Progenitor Properties							
$\boldsymbol{\xi_{1.5}}$[d]		1.03	0.34	0.76	0.98	0.87	0.00023
$\boldsymbol{\xi_{1.75}}$[d]		0.35	0.09	0.26	0.35	0.36	0.00011
$\boldsymbol{\xi_{2.0}}$[d]		0.22	0.03	0.16	0.18	0.19	0.00009
$\boldsymbol{\xi_{2.5}}$[d]		0.14	0.01	0.10	0.06	0.12	0.00008
$\boldsymbol{M_{\mathrm{Fe}}}$[e]	$[M_\odot]$	1.45	1.27	1.42	1.45	1.68	1.30
$\boldsymbol{M_4}$[f]		1.53	1.32	1.47	1.62	1.68	1.37
$\boldsymbol{\mu_4}$[g]		0.066	0.036	0.053	0.047	0.044	0.0015
$\boldsymbol{M_{3000}}$[h]	$[M_\odot]$	1.62	1.42	1.56	1.65	1.67	1.37
CO-core mass[i]	$[M_\odot]$	4.74	1.68	3.20	2.50	3.79	1.37
He-core mass[j]	$[M_\odot]$	6.01	4.12	7.57	5.87	6.03	1.68
H-envelope mass[k]	$[M_\odot]$	13.79	10.88	10.43	14.13	14.00	7.92
Properties of the Explosion							
$\boldsymbol{E_{\mathrm{exp}}}$[l]	[B]	1.30	1.41	1.25	1.24	1.49	0.16
$\boldsymbol{M_{^{56}\mathrm{Ni}}}$[m]	$[\boldsymbol{M_\odot}]$	0.072	0.045	0.056	0.063	0.036	0.006
$\boldsymbol{M_{\mathrm{tracer}}}$[n]	$[\boldsymbol{M_\odot}]$	0.034	0.046	0.036	0.027	0.052	0.006
$\boldsymbol{t_{\mathrm{exp}}}$[o]	[ms]	750	580	730	620	560	155
$\boldsymbol{M_{\mathrm{ej}}}$[p]	$[\boldsymbol{M_\odot}]$	12.98	13.70	15.42	17.81	14.84	8.26
$\boldsymbol{E_{\mathrm{exp}}/M_{\mathrm{ej}}}$	$[\mathrm{B}/\boldsymbol{M_\odot}]$	0.100	0.103	0.081	0.070	0.100	0.020
$\boldsymbol{M_{\mathrm{ns}}}$[q]	$[\boldsymbol{M_\odot}]$	1.55	1.32	1.48	1.56	1.55	1.34
$\boldsymbol{M_{\mathrm{wind}}}$[r]	$[\boldsymbol{M_\odot}]$	0.096	0.088	0.081	0.089	0.117	0.019
$\boldsymbol{M_{\mathrm{fb}}}$[s]	$[10^{-2}\boldsymbol{M_\odot}]$	0.298	0.018	0.310	0.168	0.243	0.016
$\boldsymbol{t_{\nu,90}}$[t]	[s]	4.27	5.18	4.16	4.73	3.97	9.40
$\boldsymbol{E_{\nu,\mathrm{tot}}}$[u]	[100 B]	3.68	2.81	3.32	3.61	3.48	1.97

[a] Model from the s2002 model series by Woosley et al. (2002) [b] Progenitor properties are valuated for a central density of $5 \times 10^{10}\,\mathrm{g\,cm^{-3}}$. [c] Progenitor properties at core bounce are given because earlier data are not available. [d] Compactness ξ_M (Eq. 4.1).

[e] Iron-core mass defined as the core where $\sum_{\{i|A_i>46\}} X_i > 0.5$ for nuclei with mass numbers A_i and mass fractions X_i. [f] Normalized mass M_4 (Eq. 5.2).

[g] Normalized mass derivative, μ_4 (Eq. 5.5). [h] Mass enclosed by 3000 km, M_{3000}.

[i] Mass coordinate where X(He)≤0.2. [j] Mass coordinate where X(H)≤0.2. [k] Pre-SN mass subtracted by the He-core mass. [l] Final explosion energy, including binding energy of preshock progenitor (1 B = 1 bethe = 10^{51} erg). [m] Ejected ^{56}Ni mass produced by explosive burning with late-time fallback taken into account. [n] Mass of neutron-rich tracer nucleus ejected in neutrino-driven wind material with neutron excess (fallback is taken into account). [o] Post-bounce time of onset of explosion, when shock expands beyond 500 km. [p] Mass ejected in the explosion. [q] Final baryonic neutron-star mass including late-time fallback (initially ejected mass, after the onset of the explosion, but falling back after some time on the compact remnant). [r] Neutrino-driven wind mass measured by mass between gain radius at t_{exp} and preliminary mass cut (mass coordinate separating compact remnant and ejecta) *before* fallback. [s] Fallback mass. [t] Emission time for 90% of the radiated neutrino energy. [u] Total radiated neutrino energy.

We simulate all of these models with Hotb varying the parameters of the core-cooling model for each progenitor model and aiming at reproducing the explosion energy and ejected ^{56}Ni mass of SN 1987A. The observed values are $E_{\mathrm{exp}} = (1.50 \pm 0.12) \times 10^{51}\,\mathrm{erg}$ (Utrobin, 2005), $E_{\mathrm{exp}} \sim 1.3 \times 10^{51}\,\mathrm{erg}$ (Utrobin & Chugai, 2011), and $M_{\mathrm{Ni}} = 0.0723$–$0.0772\,M_{\odot}$ (Utrobin et al., 2015), but numbers reported by other authors cover a considerable range (cf. Handy et al. 2014 for a compilation). The explosion energy that we accept for a SN1987A model in the calibration process is guided by the ejected ^{56}Ni mass (which fully accounts for short-time and long-time fallback) and the ratio of E_{exp} to the ejecta mass in the ballpark of estimates based on light curve analyses (cf. Table 4.2 for our values).

Table 4.2.: PNS core-model parameters

Calibration Model	$R_{\mathrm{c,f}}$ [km]	Γ	ζ	n	E_{exp}[a] [B]	M(^{56}Ni+ 1/2 Tr)[b] [$M_{\odot}$]
s19.8	6.5	3.0	0.90	2.96	1.30	0.089
w15.0	6.0	3.0	0.60	3.10	1.41	0.068
w18.0	6.0	3.0	0.65	3.06	1.25	0.074
w20.0	6.0	3.0	0.70	2.84	1.24	0.076
n20.0	6.0	3.0	0.60	3.23	1.49	0.062
z9.6	7.0	3.0	0.65	1.55	0.16	0.0087

[a] Final explosion energy, including binding energy of preshock progenitor ($1\,\mathrm{B} = 1\,\mathrm{bethe} = 10^{51}\,\mathrm{erg}$). [b] Ejected ^{56}Ni mass plus half of the Tr mass produced by explosive burning with late-time fallback taken into account.

Because of the "gentle" acceleration of the SN shock by the neutrino-driven mechanism (also in 3D simulations, see Utrobin et al., 2015), it is difficult to produce this amount of ejected ^{56}Ni just by shock-induced explosive burning. $M_{^{56}\mathrm{Ni}}$ in Table 4.2 mainly measures this component but also contains ^{56}Ni from proton-rich neutrino-processed ejecta. However, also neutrino-processed ejecta and the neutrino-driven wind with a slight neutron excess could contribute significantly to the ^{56}Ni production. The electron fraction Y_e of these ejecta is set by ν_e and $\bar{\nu}_e$ interactions and depends extremely sensitively on the properties (luminosities and spectra) of the emitted neutrinos, which our transport approximation cannot reliably predict and which also depend on subtle effects connected to multi-dimensional physics and neutrino opacities. For these reasons we consider the ^{56}Ni as uncertain within the limits set by the true ^{56}Ni yield from our network on the low side and, in the maximal case, all tracer material added to that. We therefore provide as possible ^{56}Ni production of our models the range $M_{^{56}\mathrm{Ni}} \leq M_{^{56}\mathrm{Ni}}^{\mathrm{total}} \leq M_{^{56}\mathrm{Ni}} + M_{\mathrm{tracer}}$.

Note that we do not calculate light curves for the progenitor models. The light curve additionally constrains the envelope structure of the progenitor models, because it is a tracer for the layers the SN shock has to run through. The red supergiant model s19.8 would be completely off and also none of the blue supergiant models reproduces the observed light curve perfectly (see Utrobin et al., 2015, Fig. 11). Still, this is an issue of stellar evolution and of the outer layers and is not connected to the core structure. Calibrating the explosion energy and the nickel ejecta mass is basically unaffected by the outer shells.

4.1.2. The Crab Nebula – Remnant of SN 1054

Although the SN explosion that produced the Crab nebula was a historic SN taking place in the pre-scientific age, many observable properties are known for the event. Even some information about the light curve can be extracted from the observations (only by eye) by Chinese astronomers (see Smith, 2013, Fig. 1). The Crab supernova SN 1054 is considered to be connected to the explosion of a $\sim 10\,M_{\odot}$ star (e.g., Nomoto et al., 1982, Smith, 2013), and its explosion energy is estimated to be up to only $0.05 - 0.15 \times 10^{50}$ erg (e.g., Tominaga et al., 2013, Smith, 2013, Yang & Chevalier, 2015). Its ^{56}Ni production is also small if compared to the yields of SN 1987A and amounts to $\lesssim 10^{-2}\,M_{\odot}$(Tominaga et al., 2013, Smith, 2013). This fact lends support to the results of recent, self-consistent 1D and multi-dimensional supernova models of $\lesssim 10\,M_{\odot}$ stars (e.g., Kitaura et al. 2006, Fischer et al. 2010, Melson et al. 2015b), whose low explosion energies and low nickel production agree with the Crab observations.

We discussed the deficiency and ambiguity of a calibration by one event already in Sect. 2.3. A second calibration model is needed to get the low-mass limit consistent with the mentioned observations for the Crab as well as the findings of self-consistent simulations. Guided by the simulations conducted by Melson et al. (2015b) we choose the z9.6 model, a model with primordial metallicity and a very steep density gradient (cf. Fig. 4.2 and 4.3). Although, the metallicity is not in agreement with the metallicity of the Crab progenitor star, other models in this mass range with solar metallicity have a very similar core structure and reproduce the inferred explosion energy and ^{56}Ni ejecta mass of SN 1054 for the same parameter choice as found for z9.6. That is why model z9.6 can be used equally well for the calibration procedure.

4.1.3. Dynamical Evolution of the Calibration Models

Figures 4.2 and 4.3 show the density profiles of the full star (upper panel) and of the core region (lower panel) versus radius and versus enclosed mass, respectively. Model z9.6 is easily distinguishable by its steep density decline, as well as its larger final radius compared to the blue supergiants. s19.8 is also a red supergiant and extends to the largest radius, but has a similar core structure as models w18.0, w20.0, and n20.0. w15.0 is significantly different and is somewhat in between the Crab model and the SN 1987 progenitor models.

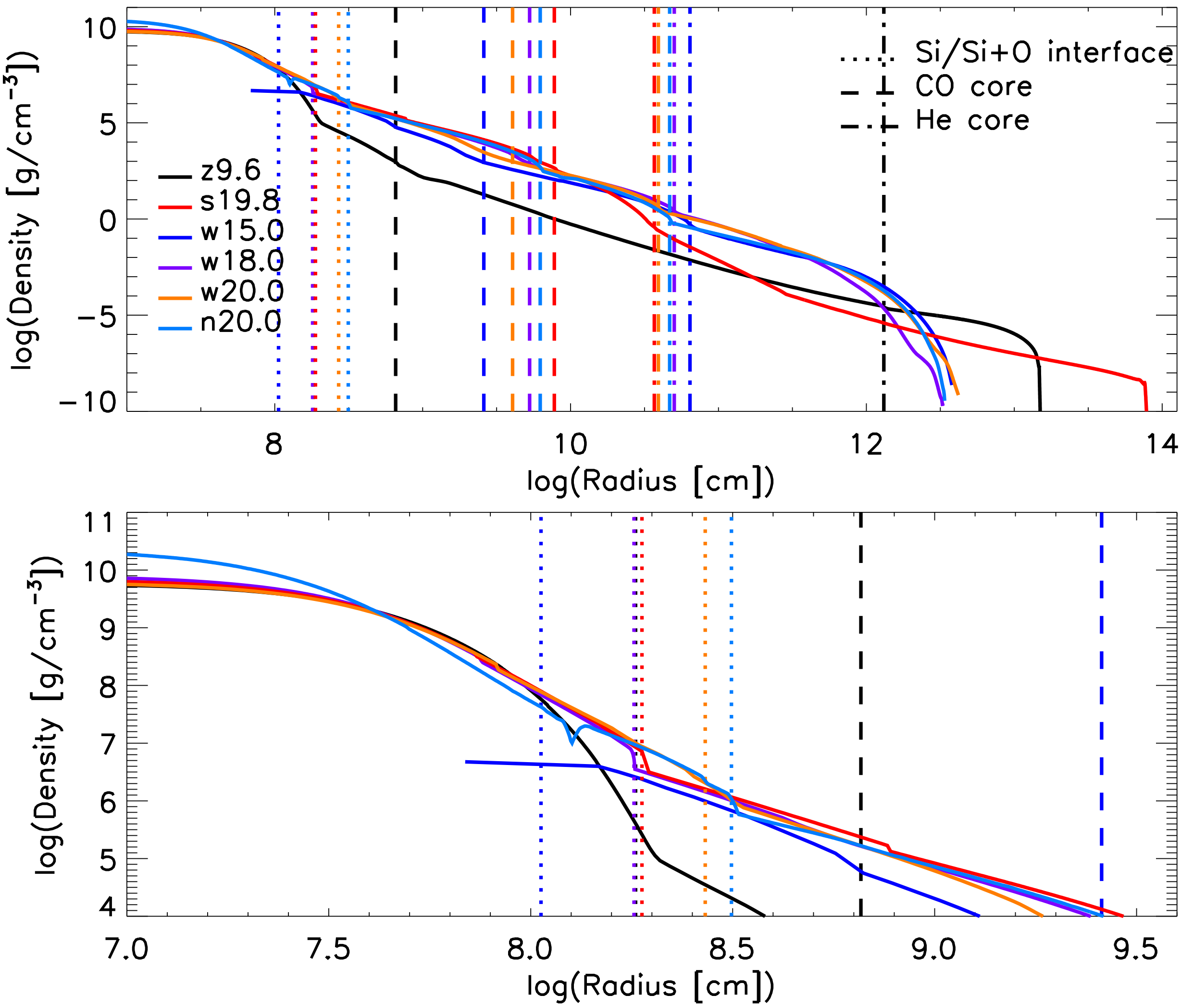

Figure 4.2.: Density as a function of radius for all progenitor models employed for the calibration procedure. The upper panel depicts the whole star while the lower panel is a zoom on the core-region. Displayed are the SN 1987A-like progenitor models (blue supergiants w15.0, w18.0, w20.0, and n20.0 and the red supergiant s19.8). For the Crab-like calibration we employ the red supergiant z9.6. Furthermore, the shell interface between Si and Si+O (dotted lines) is defined as the coordinate with an entropy value of $s = 4$, the boundary of the CO core (dashed lines) is defined by the point where X(He)$\leq$0.2, and the boundary of the He core is defined by the point where X(H)$\leq$0.2. Note, that the pre-collapse core of model w15.0 is not available.

Still, as we will discuss later, the parameter choice of the core-model yields a core behavior compatible with the other calibration models. All in all, a variety of core and envelope structures is realised in our set of models, which is ideal to represent the uncertainties connected to the progenitor star of SN 1987A and its internal structure. The outer structure

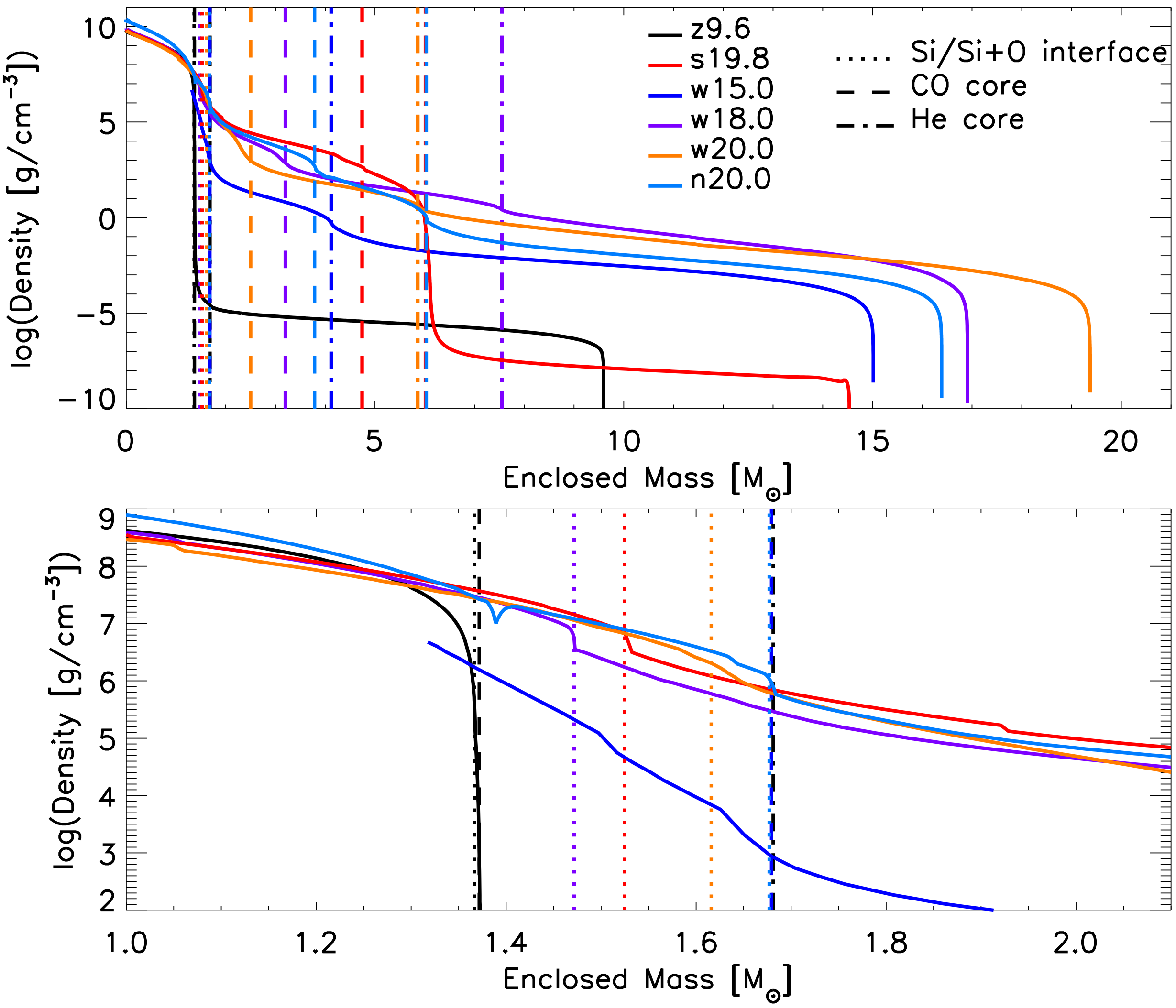

Figure 4.3.: Same as Fig. 4.3, but for density as function of enclosed mass instead of radius.

is not important for the nickel production, because only little mass falls back, consuming the nickel produced by the explosion. Still, a red supergiant will lead to a completely different light curve with an extended plateau (Type IIP) other than is observed in SN 1987A.

The basic explosion properties of all SN 1987A calibration models considered here can be found in Table 4.1. Figure 4.4 shows the evolution towards explosion for our calibration models z9.6, w18.0, and n20.0. Figure 4.5 depicts the evolution of models w15.0, s19.8, and w20.0. The shock radius and characteristic mass trajectories as well as neutrino luminosities and mean neutrino energies are given in the upper panels, and the different contributions to the ejecta energy in the lower panels.

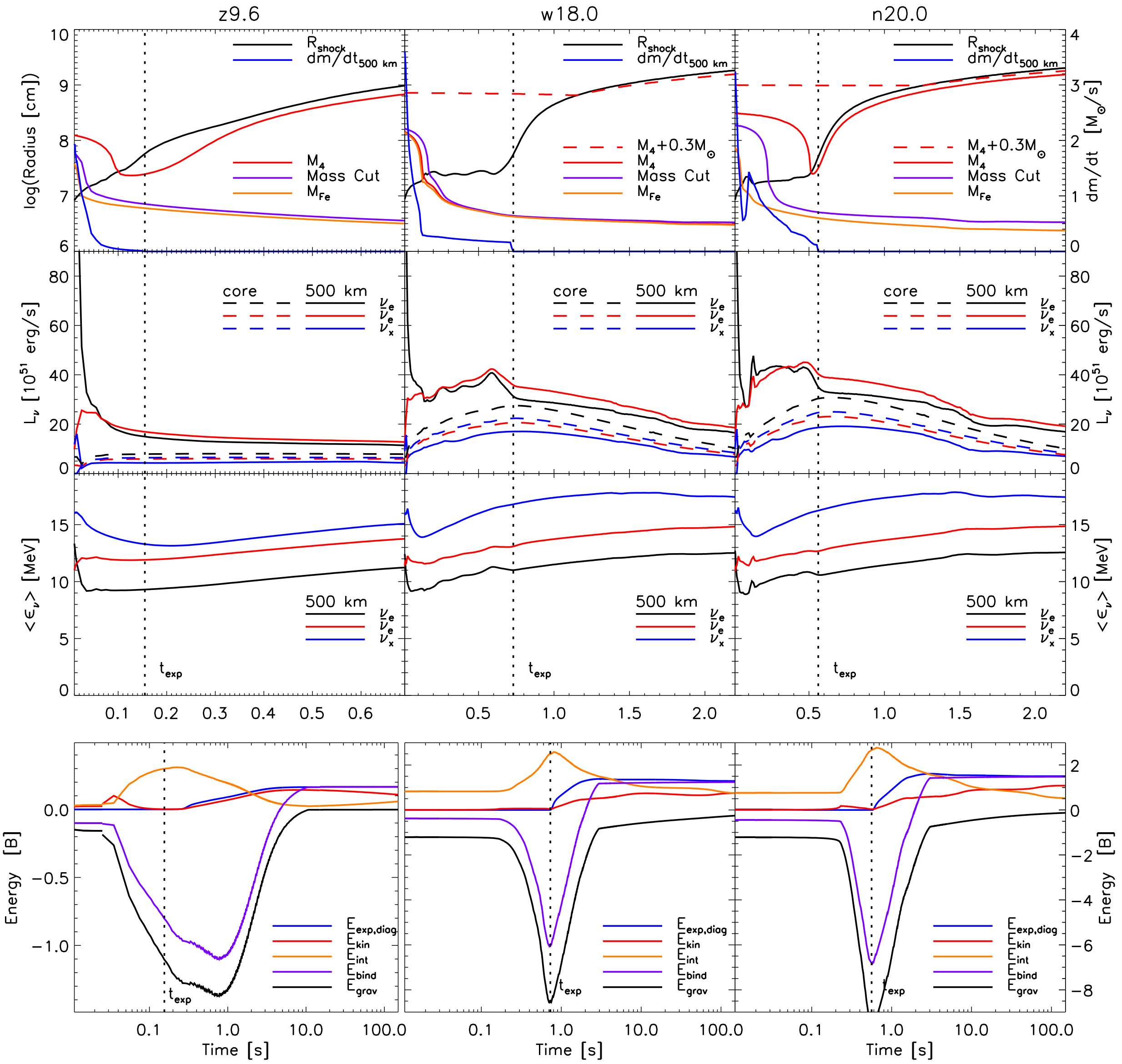
z9.6
w18.0
n20.0
log(Radius [cm])
dm/dt [$M_\odot$/s]
R_{shock}
$dm/dt_{500\ km}$
M_4+0.3$M_\odot$
M_4
Mass Cut
M_{Fe}
L_ν [10^{51} erg/s]
core
500 km
ν_e
$\bar{\nu}_e$
ν_x
$<\epsilon_\nu>$ [MeV]
t_{exp}
0.1
0.2
0.3
0.4
0.5
0.6
1.0
1.5
2.0
Energy [B]
$E_{exp,diag}$
E_{kin}
E_{int}
E_{bind}
E_{grav}
10.0
100.0
Time [s]

Figure 4.4.: Time evolution of the Crab-like calibration model z9.6 (*left*), and of the SN 1987A-like calibration models w18.0 (*middle*) and n20.0 (*right*). The *top panels* display as functions of post-bounce time the radius of the outgoing shock (black line), the mass-accretion rate measured at 500 km (blue line; scale on the right side), the radii of iron core (orange), $M_4 = m(s = 4)$ (red; s is the entropy per nucleon), $M_4 + 0.3\,M_\odot$ (red dashed), and trajectory of the final mass cut (after completion of fallback; purple). The *second panels from top* show the luminosities of ν_e, $\bar{\nu}_e$, and a single species of heavy-lepton neutrinos ν_x as labeled in the plot, measured at 500 km (solid lines) and at the inner grid boundary (dashed lines). The *third panels from top* show the mean energies of all neutrino species as radiated at 500 km. The vertical dotted lines indicate the onset time of the explosion defined by the moment when the outgoing shock passes the radius of 500 km. The *bottom panels* display the diagnostic energy of the explosion (integrated energy of all post-shock zones with positive total energy; blue line). Also shown are the kinetic energy (red), gravitational energy (black), and internal energy (orange) as integrals over the whole, final SN ejecta between the final mass cut (after fallback) on the one side and the stellar surface on the other. The total (binding) energy (purple) as the sum of these energies ultimately converges to the diagnostic energy and both of these energies asymptote to the final explosion energy. While this convergence is essentially reached after $\sim$10 s in the case of z9.6, the convergence of total energy and diagnostic energy takes tens of seconds in the other two cases.

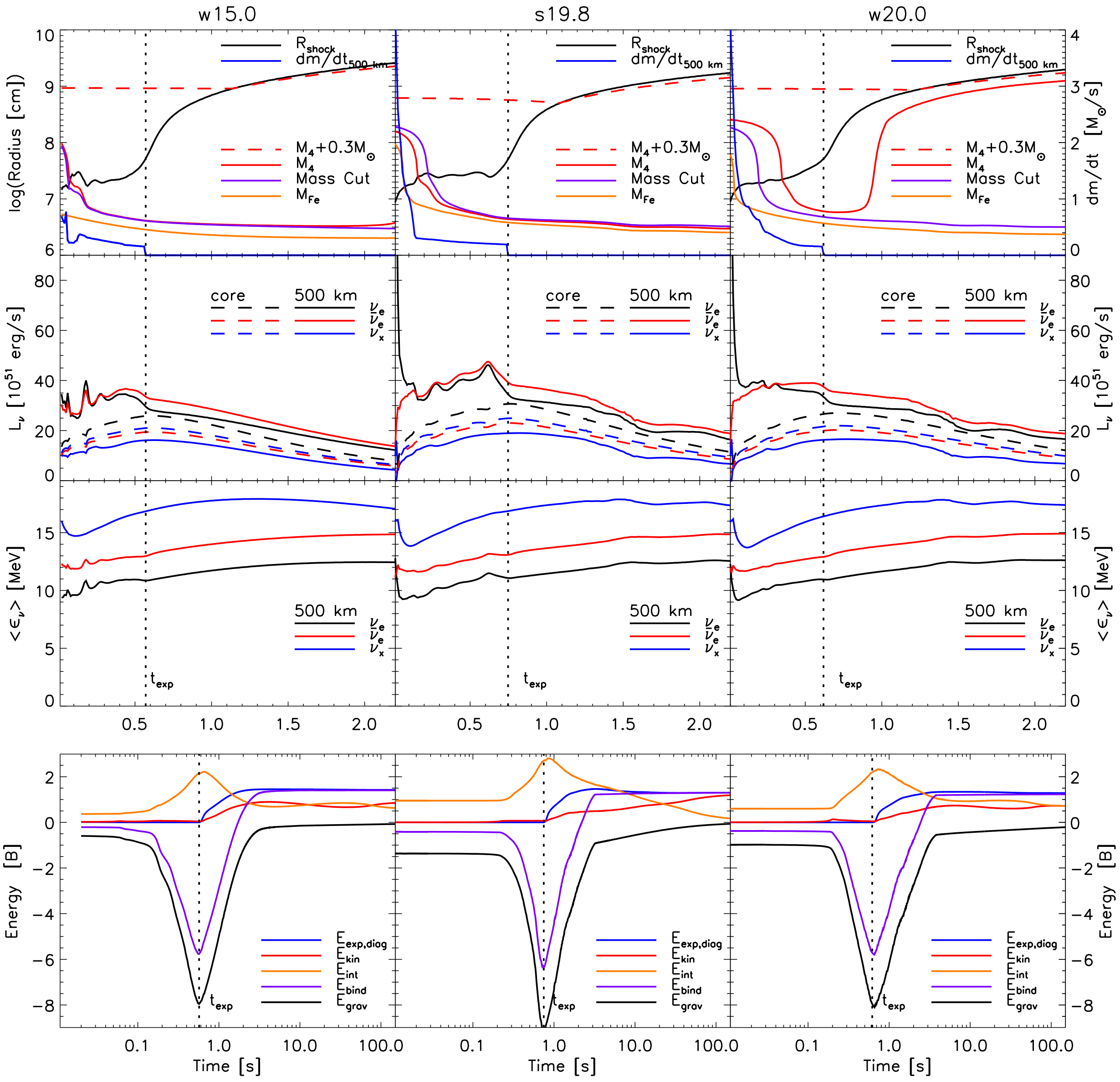

Figure 4.5.: Same as Fig. 4.4, but for w15.0 (*left*), s19.8 (*middle*) and w20.0 (*right*). All of these models are SN 1987A calibration models.

The expansion of the shock radius in model z9.6 reproduces the results of multi-dimensional simulations (Melson et al., 2015b) fairly well, and the diagnostic explosion energy also reaches ~0.1 B after roughly 0.5 s and asymptotes to a final energy of about 0.16 B after several seconds. This energy is in the upper range of estimates for SN 1054 but is still compatible with them (Tominaga et al., 2013, Smith, 2013, Yang & Chevalier, 2015). Also the luminosities and mean energies of electron neutrinos (ν_e) and anti-neutrinos ($\bar{\nu}_e$), which are the crucial agents for driving and powering the explosions, are in the ballpark of results of sophisticated transport calculations for this stellar model (cf. Fig. 12 of Mirizzi et al. 2016). In all displayed runs of Figs. 4.4 and 4.5 the escaping luminosities (solid lines in the second panel from top) for ν_e and $\bar{\nu}_e$ are enhanced compared to the core luminosities (dashed lines) due to the neutrino emission produced by the accretion and mantle cooling of the PNS.

While the z9.6 progenitor explodes relatively quickly (at $t_{\mathrm{exp}} \sim 0.15\,\mathrm{s}$ after core bounce, defined as the time when the outgoing shock passes 500 km), it takes more than 0.5 s for the shocks in w18.0, n20.0, w15.0, s19.8, and w20.0 to expand to 500 km and to accelerate outwards (vertical dashed lines in Figs. 4.4 and 4.5). In all cases the explosion sets in after the mass shell $M_4 = m(s = 4)$, where the progenitor entropy reaches a value of $4\,k_{\mathrm{B}}$ per baryon, has fallen through the shock (see Chap. 5 or Ertl et al. 2016a). All SN 1987A progenitor models behave very similarly concerning their shock trajectories, although the mass-accretion rates show a different time evolution. This is a consequence of the different core parameters found for each model to reproduce nickel nucleosynthesis and explosion energy.

4.1.4. Connection of Crab-Like and SN 1987A-Like Progenitor Models

Modified Core Contraction

Figure 4.6 displays the mass inside of a radius of 3000 km for all considered progenitor stars up to $30\,M_\odot$ at the onset of core collapse. For most appropriate comparison we evolved all models until they had contracted to the same central density of $3 \times 10^{10}\,\mathrm{g\,cm^{-3}}$. The low-mass stars with $M \leq 12.0\,M_\odot$ are clearly separated from the more massive progenitors by smaller enclosed masses $M_{3000} = m(r \leq 3000\,\mathrm{km})$. Since the Crab remnant is thought to have originated from the explosion of a star in the ~9–10 $M_\odot$ range (e.g., Nomoto et al., 1982, Nomoto, 1987, Smith, 2013, Tominaga et al., 2013), we call progenitor models with low M_{3000} cores Crab-like. The other models are termed SN 1987A-like, as we assume them to evolve more like the calibration models for SN 1987A. Our calibration models for SN 1987A possess M_{3000} cores that join with the SN 1987A-like cases (see in Fig. 4.6 the purple star and blue diamond for the w18.0 and n20.0 progenitors, respectively, and the colored symbols for the other calibration models).

Since the value of M_{3000} provides the mass that is located within 3000 km from the center, it correlates with the mass of the PNS that forms in the collapse of the stellar core. In Chap. 2 we showed already that radii of cooling PNS in self-consistent simulations depend on the PNS mass. Less massive PNS contract slower and converge at larger final radii than more massive ones (cf. Fig. 2.2).

Table 4.2 lists the parameter values obtained in our Crab calibration of the z9.6 model. We again use $\Gamma = 3.0$ and $\zeta = 0.65$ as in the w18.0 calibration, but now employ a reduced value of $n = 1.55$ and a larger value of $R_{\mathrm{c,f}} = 7\,\mathrm{km}$, because these values describe a slower contraction of the PNS core to a larger final radius (cf. Eq. 3.28) as as desired.

Model z9.6 for the Crab progenitor is in the extreme corner of the Crab-like sample in terms of mass and M_{3000} (see the blue circle in Fig. 4.6) and the PNS masses in this sample can vary considerably. We therefore determine the values of n and $R_{\mathrm{c,f}}$ for the other Crab-like progenitors (with masses M) by interpolating as function of M_{3000} between the Crab model and the SN1987-like progenitor with the smallest value of M_{3000}, which is the case at $15.2\,M_{\odot}$ in Fig. 4.6. This progenitor is part of the s2014 series with solar metallicity by Sukhbold & Woosley (2014). It was the first series the Crab-like calibration was applied to and is therefore our reference case to distinguish between Crab-like and SN 1987A-like models. On the SN 1987A-like side we use here the SN 1987A calibration values of n and $R_{\mathrm{c,f}}$ for the w18.0 series. Our interpolation functions for $y \equiv n,\ R_{\mathrm{c,f}}$ therefore are:

$$y(x) = y_0 + \frac{y_1 - y_0}{x_1 - x_0}\,(x - x_0)\,, \tag{4.2}$$

with $x = M_{3000}(M)$, $x_0 = M_{3000}(\mathrm{Z9.6})$, $x_1 = M_{3000}(\mathrm{s2014\text{-}15.2})$, $y(x) = X[M_{3000}(M)]$, $y_0 = X[M_{3000}(\mathrm{Z9.6})]$, and $y_1 = X[M_{3000}(\mathrm{SW14\text{-}15.2})]$. For all SN 1987A-like progenitors, we still apply the same values of the model parameters as obtained for the SN 1987A calibration of each series and listed in Table 4.2.

For the $9.0\,M_{\odot}$ progenitor, which has a lower mass M_{3000} than model z9.6, we use the same values of all core-model parameters as for the $9.6\,M_{\odot}$ case. Although we employ z9.6 as our template case for Crab and can also refer to a recent 3D explosion simulation of this model (Melson et al., 2015b) for its parameter calibration, our $9.0\,M_{\odot}$ explosion is equally well compatible with Crab. The computed properties of this explosion (energy around 0.1 B and ^{56}Ni mass below $0.01\,M_{\odot}$) turn out to be fully consistent with the observational limits for Crab.

As a drawback of this modification, the explosions of some of the low-mass progenitors set in rather late [*]. This, however, is basically compatible with the tendency of relatively slow shock expansion and late explosions that are also found in sophisticated multi-dimensional simulations of such stars, which, in addition, reveal long-lasting phases of simultaneous

---

[*] In rare cases one may even obtain failed explosions, e.g. for the primordial metallicity set z2016 (see Sect. 6.4).

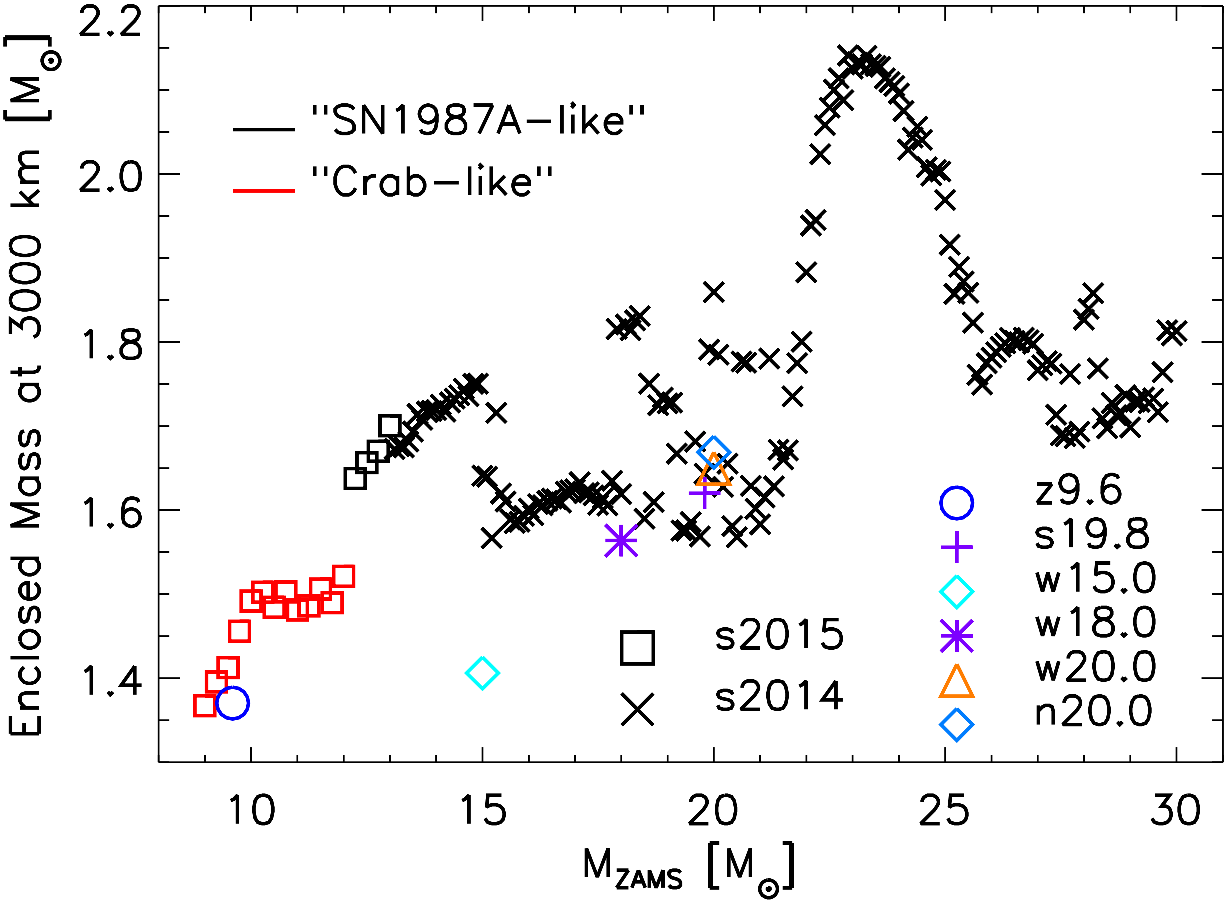

Figure 4.6.: Mass inside a radius of 3000 km for all progenitors up to 30 $M_\odot$ at the time when the central density reaches the same value of $3 \times 10^{10}\,\mathrm{g\,cm^{-3}}$. The black crosses and squares indicate "SN1987-like" cases; the red squares, "Crab-like" ones. Squares are models similar to Woosley & Heger (2015); crosses are similar to those of the Sukhbold & Woosley (2014) progenitor set. The locations of the calibration models are indicated by colored symbols as indicated in the figure legend. While n20.0, w20.0, and s19.8 cluster closely, w15.0 lies far off, because this model has a very steep density gradient outside of the iron core.

accretion and mass ejection after the onset of the explosion (Janka et al., 2012, Müller et al., 2013, Müller, 2015). This extended accretion phase has only moderate consequences for the estimated remnant masses, because the mass-accretion rate of these progenitors reaches a low level of $\lesssim 0.05$–$0.1\,M_\odot\,\mathrm{s}^{-1}$ after a few 100 ms post bounce, and some or even most of the accreted mass is re-ejected in the neutrino-driven wind.

Overall, our results for different progenitor sets and multiple calibration models exhibit features very similar to those discussed in detail by Ugliano et al. (2012), except of course for the improvements of the Crab-like stars in the low-mass regime. We will present these results in chapters 5 and 6. We point out here, that the fallback masses in the low-mass range of progenitors were overestimated by Ugliano et al. (2012) due to an error in the analysis (more discussion will follow in Chap. 6 and is published in an erratum by Ertl et al., 2016b).

ζ-Modification

We will use a slightly different low-mass calibration procedure for the subsequent chapter (Chap. 5). We use it for reasons of simplicity and conformity with the publication by Ertl et al. (2016a), which the subsequent chapter is based on. It is different from the one presented before and not used in Sukhbold et al. (2016) or Chap. 6. The results of the subsequent chapter for the explodability of massive stars are independent of the chosen low-mass calibration.

We reduce the compression parameter of the PNS core model by a linear relation $\zeta' \propto \xi_{1.75,\mathrm{b}}$ (the value of $\xi_{1.75,\mathrm{b}}$ is measured at core bounce) for progenitors with $\leq 13.5\,M_\odot$, i.e., we use the function

$$\zeta' = \zeta \left(\frac{\xi_{1.75,\mathrm{b}}}{0.5} \right) \quad \text{for} \quad M \leq 13.5\,M_\odot\,, \tag{4.3}$$

with ζ being the value determined from the SN 1987A calibration for a considered progenitor model of that supernova. We note that the values of $\xi_{1.75,\mathrm{b}}$ are less than 0.5 for all progenitors below $13.5\,M_\odot$ and close to 0.5 for $M \sim 13.5\,M_\odot$, for which reason Eq. (4.3) connects smoothly to the ζ value applied for stars above $13.5\,M_\odot$ according to the SN 1987A calibration.

The modification of Eq. (4.3) accounts for the reduced burden of the small mass of the accretion layer of these stars with their extremely low compactnesses. Such a modification allows us to reproduce the trend to weak explosions obtained in sophisticated 2D and 3D simulations for low-mass iron-core progenitors (Janka et al., 2012, Melson et al., 2015b, Müller, 2015).

We discard the ζ-modification for Chap. 6, because it is less well motivated in comparison to the modified core contraction (cf. Sec. 2.3).

4.2. Sets of Progenitor Models Across the Stellar Mass Range

The large sets of progenitor models we use as input in Hotb are evolved through their stellar evolution employing 1D stellar evolution codes. These calculations vary initial conditions like zero-age main-sequence (ZAMS) mass, treatment of physics (e.g., convection, number of species being part of the nuclear reaction network) and metallicity. They are followed until the iron-core becomes gravitationally unstable and begins to collapse. Most of the models used in this work are evolved with the stellar evolution code KEPLER by Weaver et al. (1978) with the latest physics as described by Woosley et al. (2002). In addition, the physical modeling, like wind mass-loss rates, nuclear burning and the treatment of convection is different for different codes, but also differs distinct between versions of the same stellar evolution code. Sukhbold & Woosley (2014) showed that this can change the core structure significantly for a star with a certain individual ZAMS mass, but the latter work also showed that the basic tendencies along the stellar mass range largely persist and are only shifted in ZAMS mass. It is therefore crucial to have progenitor models with a fine ZAMS-mass binning to be able to account for the rich core structure and also for the systematic picture of the outcome, BH or NS (see subsequent chapter, Ugliano et al. (2012) and Ertl et al. (2016a)). A question we want to answer is, whether and how the population of SNe changes if the stellar evolution is modeled differently.

We perform collapse and explosion simulations for large progenitor sets of different metallicities, namely: the zero-metallicity z2002 set including 30 models with ZAMS masses of $11.0 - 40.0\,M_\odot$ of Woosley et al. (2002) and a new set of zero-metallicity models z2011 with 124 models between $9.6\,M_\odot$ and $100.0\,M_\odot$ by Heger & Woosley (2010) for the stars above and including $10.3\,M_\odot$ and by (Heger, 2015, private communication) for the star with lower masses. Furthermore we employ one set of low-metallicity (10^{-4} solar) models, which we call u2002 series, composed of 247 models between $11.0\,M_\odot$ and $75.0\,M_\odot$ by Woosley et al. (2002). Finally, we use a variety of models with solar metallicity: the solar-metallicity s2002 series (101 models, 10.8–75.0 $M_\odot$) of Woosley et al. (2002) plus a $10.0\,M_\odot$ progenitor (Woosley, 2007, private communication) and a $10.2\,M_\odot$ progenitor (Heger, 2003, private communication); the solar-metallicity s2014 (151 models, 15.0–30.0 $M_\odot$) and sh2014 series (15 models, 30.0–60.0 $M_\odot$, no mass loss) of Sukhbold & Woosley (2014), supplemented by additional 36 models with 9.0–14.9 $M_\odot$ also called s2014; the solar-metallicity s2007 series (32 models, 12.0–120.0 $M_\odot$) of Woosley et al. (2007); the n2006 series (8 models, 13.0–50.0 $M_\odot$; Nomoto et al. 2006) and the latest set of low-mass models s2015 with 17 models between $9.0\,M_\odot$ and $13.0\,M_\odot$ with the physics described by Woosley & Heger (2015). In total, we employ 767 iron-core progenitor models.

In Table 4.1 and the rest of our study, time-dependent structural parameters of the stars are measured when the stars possess a central density of $5 \times 10^{10}\,\mathrm{g\,cm^{-3}}$, unless otherwise stated. This choice of reference density defines a clear standard for the comparison of stellar profiles of different progenitors (cf. Appendix A of Buras et al., 2006a). Different from the moment of core bounce, which was used in other works, our reference density has the advantage to be still close to the initial state of the pre-collapse models provided by stellar evolution modeling and therefore to yield values of the structural parameters that are more similar to those of the pre-collapse progenitor data. Another advantage is that stellar evolution simulations can reach this central density the need for adding additional physics (e.g., a high-density EOS). Our calibration model w15.0, however, must be treated as an exception. Because pre-collapse profiles of this model are not available any more, all structural quantities for this case are given (roughly) at core bounce.

A compilation of the most important structural properties of the progenitor sets can be found in Appendix A.

5. A Two-Parameter Criterion for the Explodability of Massive Stars

Thus far, judging the fate of a massive star, either a neutron star (NS) or a black hole (BH), solely by its structure prior to core collapse has been ambiguous. Our work and previous attempts find a non-monotonic variation of successful and failed supernovae with zero-age main-sequence (ZAMS) mass, for which no single structural parameter can serve as a good predictive measure. However in this chapter we will present such a predictive measure for the explodability: two parameters computed from the pre-collapse structure of the progenitor, which in combination allow for a clear separation of exploding and non-exploding cases with only few exceptions (∼1–2.5%) in our set of hundreds of investigated stellar models. One parameter is M_4, defining the normalized enclosed mass for a dimensionless entropy per nucleon of $s = 4$, and the other is $\mu_4 \equiv (\mathrm{d}m/M_\odot)/(\mathrm{d}r/1000\,\mathrm{km})|_{s=4}$, being the normalized mass-derivative at this location. The two parameters μ_4 and $M_4\mu_4$ can be directly linked to the mass-infall rate, $\dot{M}$, of the collapsing star and the electron-type neutrino luminosity of the accreting proto-neutron star (PNS), $L_{\nu_e} \propto M_{\mathrm{ns}}\dot{M}$, which play a crucial role in the "critical luminosity" concept for the theoretical description of neutrino-driven explosions as runaway phenomenon of the stalled accretion shock.

The content of this chapter is already published in Ertl et al. (2016a), yet adjusted and updated to fit to the narrative of this work.

5.1. Introduction

Presupernova stars in the mass range above $\sim 9\,M_\odot$ exhibit large variations of their structure with respect to, e.g., their Fe-core and O-core masses, their binding energies, and their density or entropy profiles above the Fe-core (Woosley et al., 2002). These properties vary non-monotonically with the ZAMS mass and can differ considerably even between progenitors with only a small difference of their ZAMS masses (Sukhbold & Woosley, 2014).

Correspondingly, Ugliano et al. (2012) found that the properties of neutrino-driven supernovae (SNe) like explosion energy, nickel mass, and remnant mass change non-monotonically with the ZAMS mass. In particular, for the investigated grid of 101 solar-metallicity progenitors binned in $0.2\,M_\odot$ steps (Woosley et al., 2002), they found islands of non-exploding, black hole (BH) forming cases down to 15 $M_\odot$, alternating with mass-intervals of exploding progenitors. In a few cases individual neighboring progenitors showed opposite behavior.

Ugliano et al. (2012) used a simple, parametric model for the contracting PNS as a neutrino source to trigger neutrino-driven explosions in spherically symmetric (1D) hydrodynamic simulations, but their basic findings were confirmed by other groups working with semi-analytic descriptions in 1D (Pejcha & Thompson, 2015) and approximate neutrino transport in two- and three-dimensional (2D, 3D) hydrodynamic models (Nakamura et al., 2015, Horiuchi et al., 2014). While O'Connor & Ott (2011) suggested that BH formation requires a compactness (normalized enclosed mass-radius ratio) of $\xi_{2.5} > 0.45$ with

$$\xi_M \equiv \frac{M/M_\odot}{R(M)/1000\,\mathrm{km}}\,, \tag{5.1}$$

Ugliano et al. (2012) obtained only explosions for $\xi_{2.5} < 0.15$, explosions or BH formation for $0.15 \leq \xi_{2.5} \leq 0.35$, and only BH formation for $\xi_{2.5} > 0.35$, which implies a larger fraction of BH formation cases for solar-metallicity stars. Horiuchi et al. (2014) pointed out that a critical compactness of $\xi_{2.5} \gtrsim 0.2$ for failed explosions is compatible with a lack of red supergiant Type-IIP SN progenitors above $\sim$16 $M_\odot$ (Smartt et al., 2009) and with a significant excess of the star-formation rate compared to the observed SN rate (Horiuchi et al., 2011). Pejcha & Thompson (2015) showed that their parameterization "case (a)", which yields results similar to those of Ugliano et al. (2012), is close to being optimally compatible with a combination of several observational constraints.

How can the non-monotonicity of the explodability be understood in terms of the pre-supernova properties and in the context of the physics of the neutrino-driven mechanism? Are there characteristic parameters of the pre-supernova star that decide better about success or failure of the explosion than a single value of the compactness or other, similarly useful parameters like the iron-core mass or the binding energy outside of the iron core? While all these measures reflect trends like an enhanced tendency of BH formation for high compactness, large iron-core mass or high exterior binding energy, there are still many outliers that do not obey the correlations. For example, a suitably chosen mass M of the compactness ξ_M allows to correctly predict explosions in <90% of the cases (Pejcha & Thompson, 2015), but the best choice of M is merely empirical and the physical justification of ξ_M as a good diagnostics is unclear.

Here we propose a two-parameter criterion that separates successful explosions from failures with very high reliability. While two compactness values, e.g. $\xi_{1.5}$ and $\xi_{2.5}$, or the iron-core mass and the mean entropy in some suitable mass range begin to show such a disentanglement, we demonstrate that the normalized mass inside a dimensionless entropy per nucleon of $s = 4$,

$$M_4 \equiv m(s=4)/M_\odot\,, \tag{5.2}$$

and the mass derivative at this location,

$$\mu_4 \equiv \left.\frac{\mathrm{d}m/M_\odot}{\mathrm{d}r/1000\,\mathrm{km}}\right|_{s=4}\,, \tag{5.3}$$

both determined from the pre-supernova profiles, allow to predict the explosion behavior successfully in $\gtrsim 97\%$ of all cases and have a direct connection with the theoretical basis of the neutrino-driven mechanism.

We described the numerical realization in detail in Chap. 3, based on a detailed discussion of our modeling methodology in comparison to other approaches in the recent literature in Chap. 2, present our results in the following sections of this chapter, and conclude in Sect. 5.9.

Note that we will apply a different calibration for the low-mass stars in this chapter. For reasons of simplicity and conformity with the publication by Ertl et al. (2016a), we will use the ζ-modification for low-mass stars here. We realize that decreasing the parameter ζ, which scales the compression work exerted on the inner (excised) core of the PNS by the overlying accretion mantle (cf. Eqs. 1–4 in Ugliano et al., 2012, and Sect. 3.4), and by this reducing the wind power in proportionality to the compactness parameter $\xi_{1.75,\mathrm{b}}$, which drops strongly for low-mass progenitors (see Eq. 4.3). This procedure can be justified by the much lighter accretion layers of such stars, which implies less compression of the PNS core by the outer weight. Such a modification reduces the neutrino emission of the high-density core and therefore the mass outflow in the early neutrino-driven wind. As a consequence, the explosion energy falls off towards the low-mass end of the investigated progenitor sets. This can be seen in the upper panel of Fig. 5.1, which should be compared to the upper left panel of Fig. 5 in Ugliano et al. (2012).

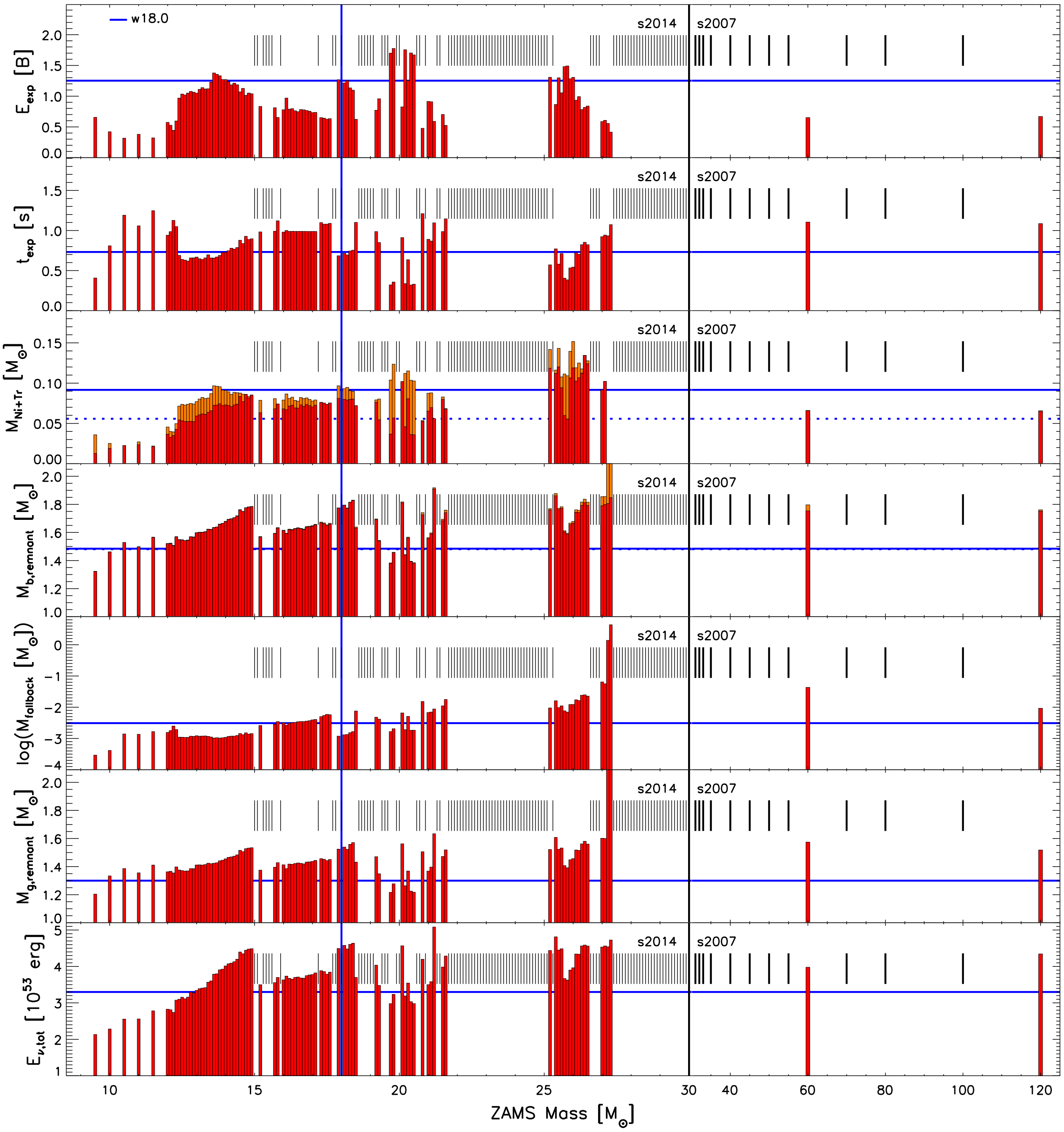
w18.0
s2014
s2007
E_{exp} [B]
2.0
1.5
1.0
0.5
0.0
t_{exp} [s]
1.5
1.0
0.5
0.0
M_{Ni+Tr} [$M_\odot$]
0.15
0.10
0.05
0.00
$M_{b,remnant}$ [$M_\odot$]
2.0
1.8
1.6
1.4
1.2
1.0
log($M_{fallback}$ [$M_\odot$])
0
−1
−2
−3
−4
$M_{g,remnant}$ [$M_\odot$]
2.0
1.8
1.6
1.4
1.2
1.0
$E_{\nu,tot}$ [10^{53} erg]
5
4
3
2
1
10
15
20
25
30
40
60
80
100
120
ZAMS Mass [$M_\odot$]

Figure 5.1.: Explosion properties for models of the s2014 series, the supplementary low-mass progenitors with $M_{\mathrm{ZAMS}} < 15\,M_\odot$, and models with $M_{\mathrm{ZAMS}} > 30\,M_\odot$ from the s2007 series, exploded with the w18.0 calibration. Note that we do not present the w2015 models here, as done in the following chapters. The results of this chapter are independent of the choice of the low-mass progenitors and the employed calibration for the low ZAMS mass limit. A black vertical line marks the boundary between the two progenitor sets. The panels show the final explosion energies, E_{exp} (*top*; $1\,\mathrm{B} = 1\,\mathrm{bethe} = 10^{51}\,\mathrm{erg}$), times of the onset of the explosion, t_{exp} (defined as the moment when the shock expands beyond 500 km; *second from top*), masses of ejected explosively produced ^{56}Ni (red bars) and tracer element (orange bars; *third from top*), baryonic remnant masses with fallback masses indicated by orange sections of the bars (*fourth from top*), fallback masses (plotted logarithmically; *fifth from top*), gravitational remnant masses (Eq. (5.9); *sixth from top*), and total energies radiated in neutrinos, $E_{\nu,\mathrm{tot}}$ (*bottom*). Mass and parameter values of the calibration models are indicated by vertical and horizontal blue lines, respectively, with the dashed horizontal blue line in the middle panel giving the ^{56}Ni mass and the solid horizontal blue line the sum of ^{56}Ni and tracer. Non-exploding cases are marked by short vertical black bars in the upper half of each panel.

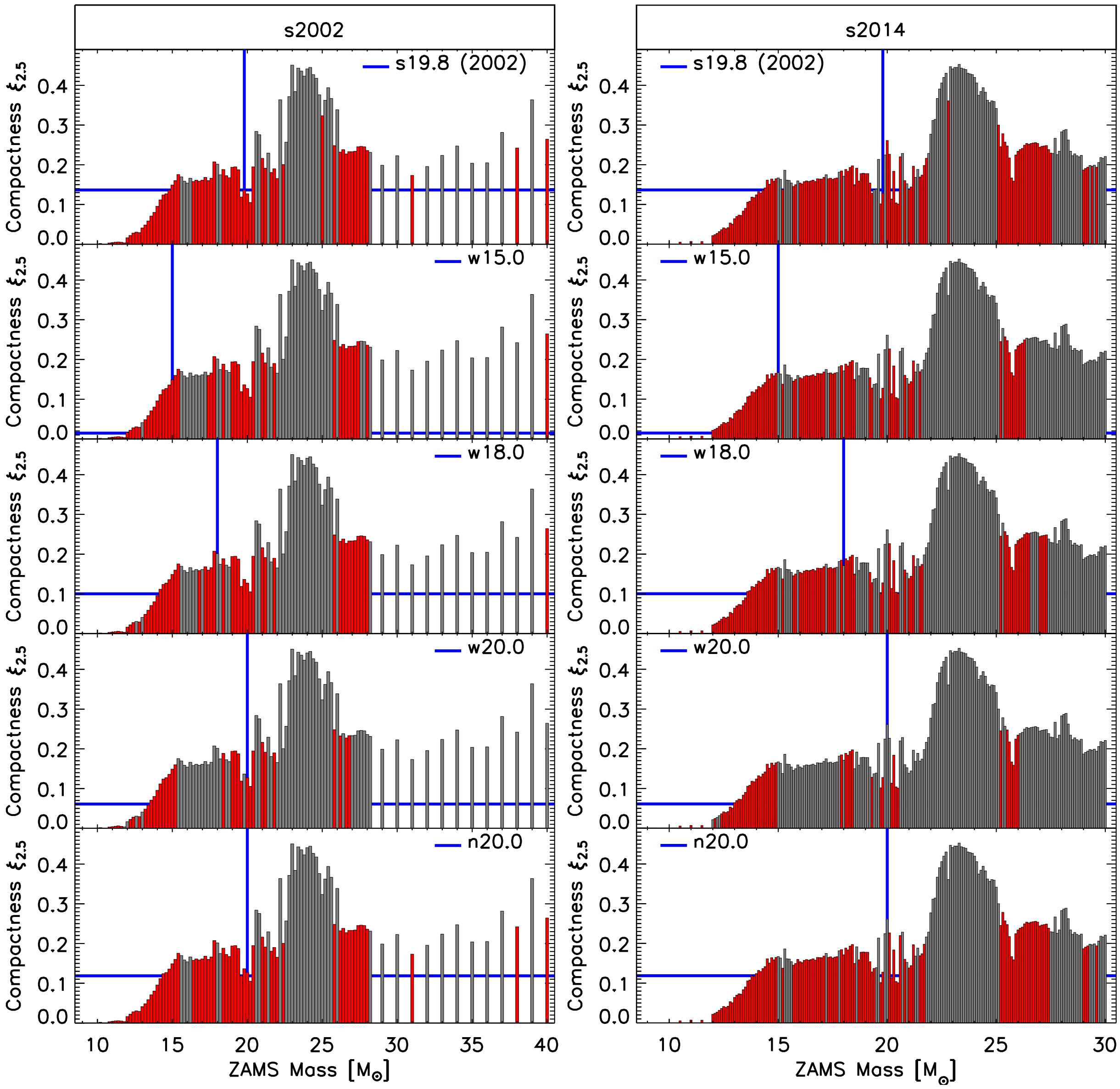

Figure 5.2.: Compactness $\xi_{2.5}$ versus ZAMS mass for the s2002 (*left*) and s2014 progenitor series (plus $M_{\mathrm{ZAMS}} < 15\,M_\odot$ models) with exploding (red bars) and non-exploding (gray bars) cases for all calibrations. The s2002 results for the s19.8 calibration agree well with Ugliano et al. (2012). Blue vertical and horizontal lines indicate the values of the progenitors used for the calibrations.

The ζ-scaling of Eq. (4.3) is introduced as a quick fix in the course of the work we published in Ertl et al. (2016a) and is a fairly ad hoc measure to cure the problem of overestimated explosion energies for low-mass SN progenitors. In Sukhbold et al. (2016) and the following chapters a different approach is taken, in which the final value of the core-radius

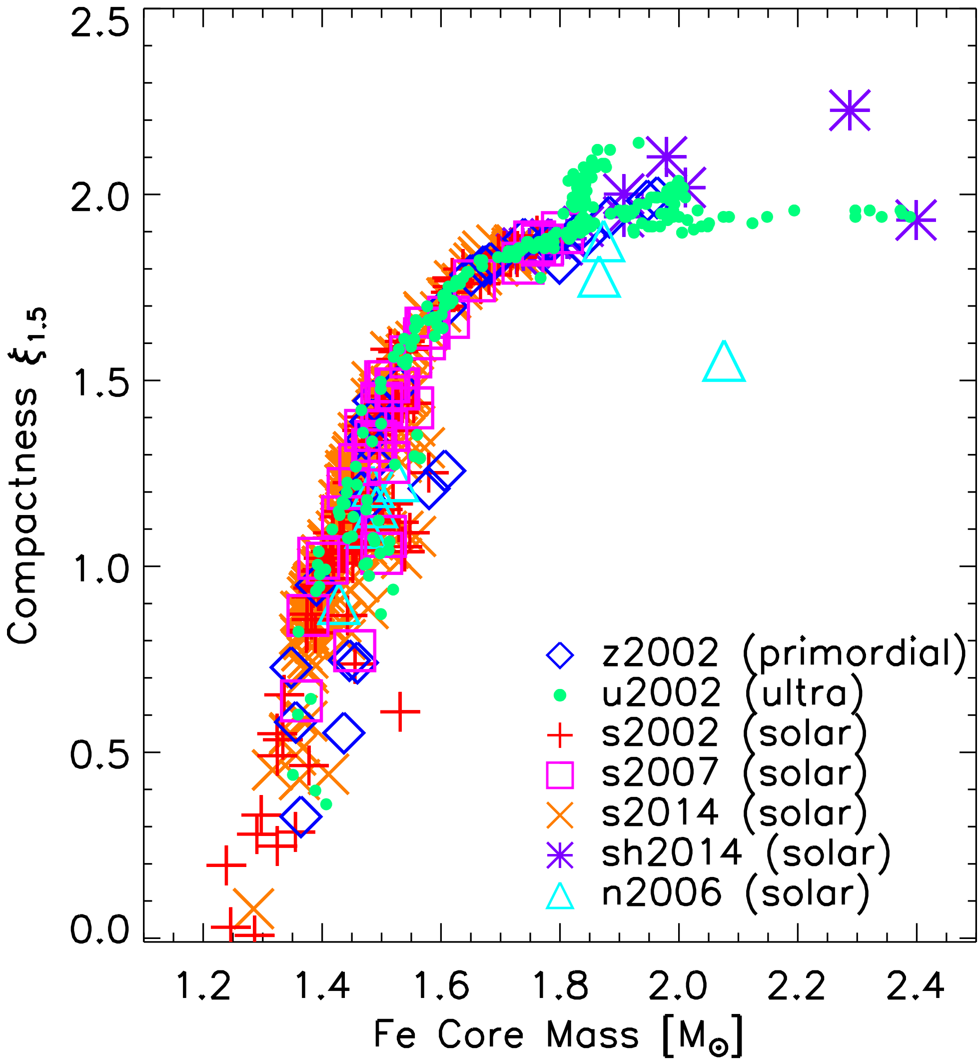

Figure 5.3.: Correlation of iron-core mass, $M_{\rm Fe}$, and compactness $\xi_{1.5}$ for the investigated models of all progenitor series. Note that $M_{\rm Fe}$ is taken from the pre-collapse model while $\xi_{1.5}$ is evaluated for a central density of $5 \times 10^{10}\,\mathrm{g\,cm^{-3}}$.

parameter of the one-zone model describing the supernuclear PNS interior as neutrino source (see Ugliano et al. 2012) is modified. This procedure can directly be motivated by the contraction of the PNS found in self-consistent cooling simulations with microphysical high-density equations of state and detailed neutrino transport. Mathematically, the modification of the core radius has a similar effect on the core-neutrino emission as the ζ-scaling employed here. We emphasize that the consequences for the overall explosion behavior of the low-mass progenitors is very similar for both the ζ-reduction and the core-radius. They lead to considerably lower explosion energies for $M_{\rm ZAMS} \lesssim 12\,M_\odot$ stars and a further drop of the explosion energies below $\sim 9.5\,M_\odot$. All in all, the main results of this chapter are

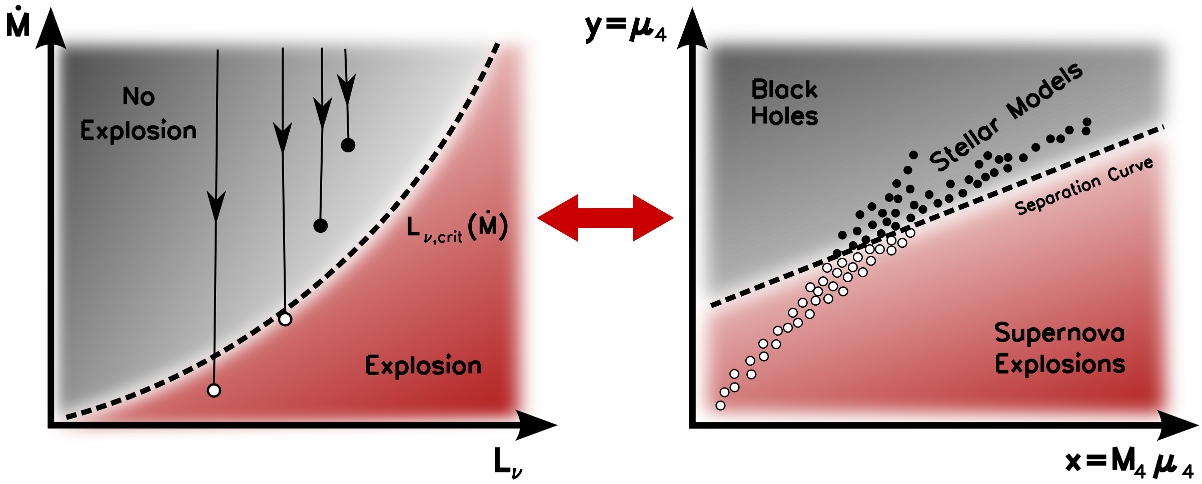

Figure 5.4.: Correspondence of L_ν-$\dot{M}$ plane with critical neutrino luminosity $L_{\nu,\mathrm{crit}}(\dot{M})$ (*left*) and x-y plane with separation curve $y_{\mathrm{sep}}(x)$ (*right*). In the left plot post-bounce evolution paths of successfully exploding models (white circles) and non-exploding models (black circles) are schematically indicated, corresponding to white and black circles for pre-collapse models in the right plot. Evolution paths of successful models cross the critical line at some point and the accretion ends after the explosion has taken off. In contrast, the tracks of failing cases never reach the critical conditions for launching the runaway expansion of the shock. The symbols in the left plot mark the "optimal point" relative to the critical curve that can be reached, corresponding to the stellar conditions described by the parameters $(M_4\mu_4, \mu_4)$ at the $s = 4$ location, which seems decisive for the success or failure of the explosion of a progenitor, because the accretion rate drops strongly outside.

independent of the choice for the low-mass calibration.

5.2. One and Two-Parameter Classifications

Figure 5.2 shows $\xi_{2.5}$ versus ZAMS mass with BH formation cases indicated by gray and explosions by red bars for the s2002 and s2014 series and all calibrations. The irregular pattern found by Ugliano et al. (2012) for the s2002 progenitors is reproduced and appears similarly in the s2014 set. High compactness $\xi_{2.5}$ exhibits a tendency to correlate with BHs. But also other parameters reflect this trend, for example $\xi_{1.5}$, the iron-core mass M_{Fe} (defined as the core where $\sum_{\{i|A_i>46\}} X_i > 0.5$ for nuclei with mass numbers A_i and mass fractions X_i), and the enclosed mass at the bottom of the O-burning shell. All three of them are tightly correlated, see Fig. 5.3 as well as Fig. 4 of Ugliano et al. (2012). Also high values of the binding energy $E_{\mathrm{b}}(m > M_{\mathrm{Fe}})$ outside of M_{Fe} signals a tendency for BH formation, because this energy correlates with $\xi_{2.5}$ (cf. Fig. 4 in Ugliano et al., 2012). However, for none of these single parameters a sharp boundary value exists that discriminates between explosions and non-explosions. For all such choices of a parameter, the BH formation limit tends to vary (non-monotonically) with M_{ZAMS} and in a broad interval of values either explosion or BH formation can happen. Pejcha & Thompson (2015) tried to optimize the choice of M for ξ_M, but even their best case achieved only 88% of correct predictions. Since in the cases of $\xi_{2.5}$ and $E_{\mathrm{b}}(m > M_{\mathrm{Fe}})$, for example, the threshold value for BH formation tends to grow with higher ZAMS mass, one may hypothesize that a second parameter could improve the predictions.

Placing the progenitors in a two-parameter space spanned by $\xi_{1.5}$ and $\xi_{2.5}$ or, equally good, M_{Fe} and $\xi_{2.5}$, begins to show a cleaner separation of successful and failed explosions: SNe are obtained for small values of $\xi_{2.5}$, whereas BHs are formed for high values of $\xi_{2.5}$, but the value of this threshold increases with $\xi_{1.5}$ and M_{Fe}. For given $\xi_{1.5}$ (or M_{Fe}) there is a value of $\xi_{2.5}$ above which only BHs are formed. However, there is still a broad overlap region of mixed cases.

This beginning separation can be understood in view of the theoretical background of the neutrino-driven mechanism, where the expansion of the SN shock is obstructed by the ram pressure of infalling stellar-core matter and shock expansion is pushed by neutrino-energy deposition behind the shock. For neutrino luminosities above a critical threshold $L_{\nu,\mathrm{crit}}(\dot{M})$, which depends on the mass-accretion rate $\dot{M}$ of the shock, shock runaway and explosion are triggered by neutrino heating (see Fig. 5.4, left panel, and, e.g., Burrows & Goshy, 1993, Janka, 2001, Murphy & Burrows, 2008, Nordhaus et al., 2010, Hanke et al., 2012, Fernández, 2012, Pejcha & Thompson, 2012, Janka, 2012, Müller & Janka, 2015, Summa et al., 2016). M_{Fe} (or $\xi_{1.5}$) can be considered as a measure of the mass M_{ns} of the PNS as accretor, which determines the strength of the gravitational potential and the size of the neutrino luminosities. Such a dependence can be concluded from the proportionality $L_\nu \propto R_\nu^2 T_\nu^4$, where R_ν is the largely progenitor-independent neutrinosphere radius and the neutrinospheric temperature T_ν increases roughly linearly with M_{ns} (see Müller & Janka, 2014). On the other hand, the long-time mass-accretion rate of the PNS grows with $\xi_{2.5}$, which is higher for denser stellar cores. For each PNS mass explosions become impossible above a certain value of $\dot{M}$ or $\xi_{2.5}$.

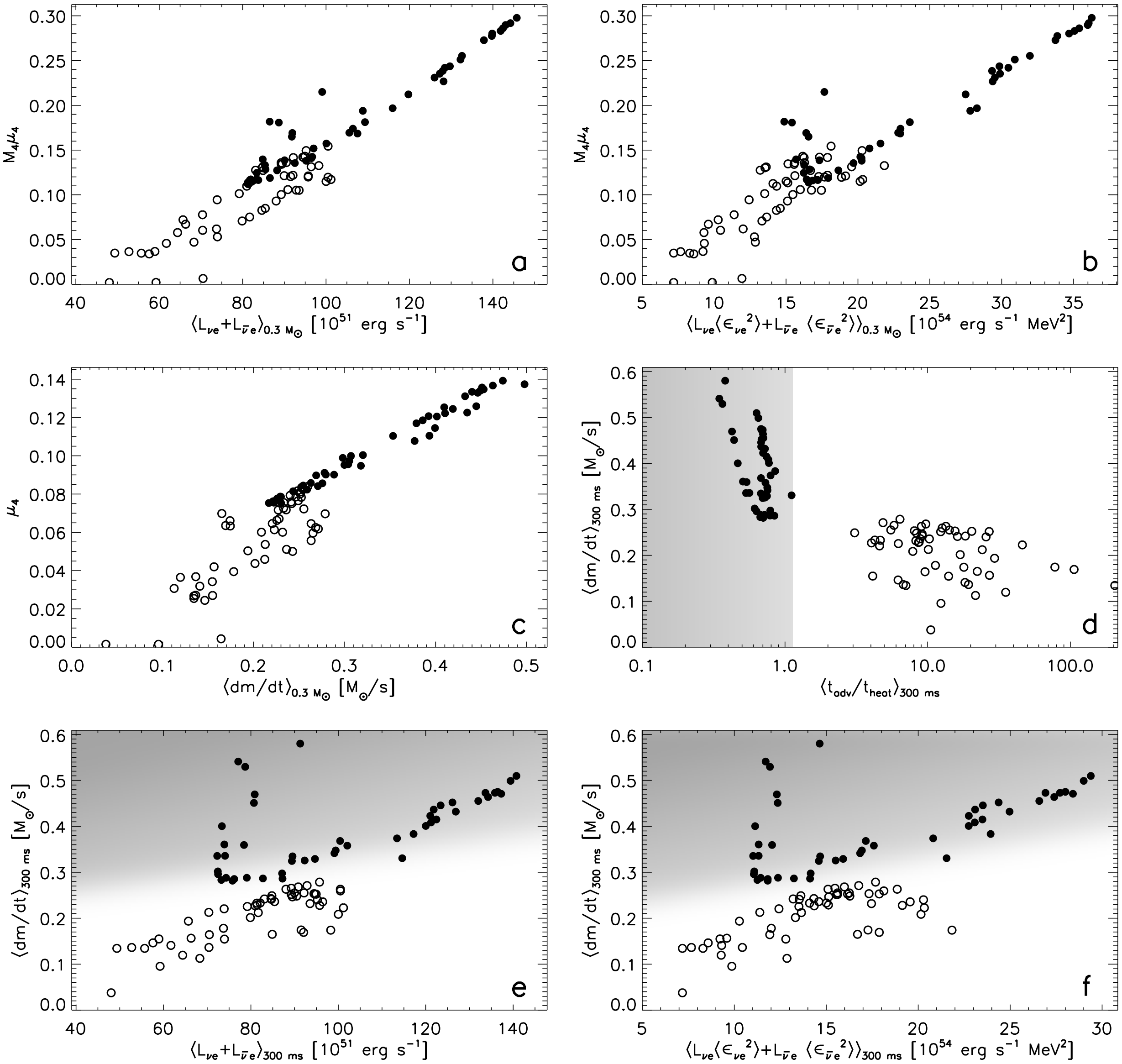
a
$M_4\mu_4$
0.00 0.05 0.10 0.15 0.20 0.25 0.30
40 60 80 100 120 140
$\langle L_{\nu e}+L_{\bar{\nu}e}\rangle_{0.3\,M_\odot}$ [10^{51} erg s^{-1}]
b
$M_4\mu_4$
5 10 15 20 25 30 35
$\langle L_{\nu e}\langle\epsilon_{\nu e}^2\rangle+L_{\bar{\nu}e}\langle\epsilon_{\bar{\nu}e}^2\rangle\rangle_{0.3\,M_\odot}$ [10^{54} erg s^{-1} MeV^2]
c
μ_4
0.00 0.02 0.04 0.06 0.08 0.10 0.12 0.14
0.0 0.1 0.2 0.3 0.4 0.5
$\langle dm/dt\rangle_{0.3\,M_\odot}$ [$M_\odot$/s]
d
$\langle dm/dt\rangle_{300\,ms}$ [$M_\odot$/s]
0.0 0.1 0.2 0.3 0.4 0.5 0.6
0.1 1.0 10.0 100.0
$\langle t_{adv}/t_{heat}\rangle_{300\,ms}$
e
$\langle dm/dt\rangle_{300\,ms}$ [$M_\odot$/s]
40 60 80 100 120 140
$\langle L_{\nu e}+L_{\bar{\nu}e}\rangle_{300\,ms}$ [10^{51} erg s^{-1}]
f
$\langle dm/dt\rangle_{300\,ms}$ [$M_\odot$/s]
5 10 15 20 25 30
$\langle L_{\nu e}\langle\epsilon_{\nu e}^2\rangle+L_{\bar{\nu}e}\langle\epsilon_{\bar{\nu}e}^2\rangle\rangle_{300\,ms}$ [10^{54} erg s^{-1} MeV^2]

Figure 5.5.: End points of the postbounce evolution of exploding (open circles) and non-exploding models (filled circles) in planes spanned by various pairs of parameters. The data correspond to results of the s2002 model series with w18.0 calibration. All symbols represent time-averaged locations because of strong temporal variations of the postshock accretion layer. *Panels a–c* display correlations of our dimensionless progenitor parameters μ_4 and $M_4\mu_4$ with time-averaged values of the preshock mass-accretion rate, $\dot{M} = \mathrm{d}m/\mathrm{d}t$, and the characteristic neutrino-emission properties, respectively, as obtained in our simulations and measured at 500 km. The abscissas of *panels a and b* show the summed luminosities of ν_e and $\bar{\nu}_e$, $L_{\nu_e} + L_{\bar{\nu}_e}$, and the summed products of luminosities and mean squared energies, $L_{\nu_e}\langle\epsilon^2_{\nu_e}\rangle + L_{\bar{\nu}_e}\langle\epsilon^2_{\bar{\nu}_e}\rangle$, of both neutrino species, respectively. For the exploding models the time averaging is performed from the arrival of the $s = 4$ interface at the shock until the explosion sets in (defined by the shock radius reaching 500 km), whereas the averages for non-exploding models cover the time from the $s = 4$ interface passing the shock until $0.3\,M_\odot$ of overlying material have been accreted by the shock. *Panel d* displays the separation of exploding and non-exploding models in the plane spanned by the mass-accretion rate and the ratio of advection to heating timescale. *Panels e and f* demonstrate this separation in the planes spanned by $\dot{M}$ and $L_{\nu_e} + L_{\bar{\nu}_e}$ or $L_{\nu_e}\langle\epsilon^2_{\nu_e}\rangle + L_{\bar{\nu}_e}\langle\epsilon^2_{\bar{\nu}_e}\rangle$, respectively. The time averages of the quantities in *panels d–f* are computed from the passage of the $s = 4$ interface through the shock until 300 ms later for non-exploding models or until the onset of the explosion otherwise. Gray shading in *panels d–f* indicates the regions where explosions fail. (No exact boundary curves are determined for the cases of *panels e and f*.)

5.3. Two-Parameter Classification Based on the Theoretical Concept of the Neutrino-Driven Mechanism

If the initial mass cut at the onset of the explosion develops at an enclosed mass $M = m(r)$ of the progenitor, we can choose $M = m(r)$ as a suitable proxy of the initial PNS mass, M_{ns}. A rough measure of the mass-accretion rate $\dot{M}$ by the stalled shock around the onset of the explosion is then given by the mass-gradient $m'(r) \equiv \mathrm{d}m(r)/\mathrm{d}r = 4\pi r^2 \rho(r)$ at the corresponding radius r. This is the case because $m'(r)$ can be directly linked to the free-fall accretion rate of matter collapsing into the shock from initial radius r according to

$$\dot{M} = \frac{\mathrm{d}m}{\mathrm{d}t_{\mathrm{ff}}} = \frac{\mathrm{d}m(r)}{\mathrm{d}r}\left(\frac{\mathrm{d}t_{\mathrm{ff}}(r)}{\mathrm{d}r}\right)^{-1} = \frac{2m'(r)}{t_{\mathrm{ff}}[(3/r) - m'(r)/m(r)]} \approx \frac{2}{3}\,\frac{r}{t_{\mathrm{ff}}}\,m'(r)\,, \tag{5.4}$$

where $t_{\mathrm{ff}} = \sqrt{r^3/[Gm(r)]}$ is the free-fall timescale (Suwa et al., 2016) and the last, approximate equality is justified by the fact that $(m'/m)^{-1} = \mathrm{d}r/\mathrm{d}\ln(m) \gg r$ outside of the dense stellar core.

Following the critical-luminosity concept now points the way to further improvements towards a classification scheme of explosion conditions: The L_ν-$\dot{M}$ dependence of the neutrino-driven mechanism suggests that the explodability of the progenitors may be classified by the parameters $M = m(r)$ and $\dot{M} \propto m'(r)$, because the accretion luminosity $L_\nu^{\mathrm{acc}} \propto GM_{\mathrm{ns}}\dot{M}/R_{\mathrm{ns}} \propto Mm'(r)$ accounts for a major fraction of the neutrino luminosity of the PNS at the time of shock revival (Müller & Janka, 2014; 2015), and, in particular, it is the part of the neutrino emission that reflects the main progenitor dependence. It is important to note that the time-evolving NS and neutrinospheric radii, $R_{\mathrm{ns}} \sim R_\nu$, are nearly the same for different progenitors and only weakly time dependent when the explosions take place rather late after bounce. This is true for our simulations (where $t_{\mathrm{exp}} \gtrsim 0.5\,\mathrm{s}$ with few exceptions; Fig. 5.1) as well as for self-consistent, sophisticated models (see, e.g., Fig. 3 in Müller & Janka 2014). In both cases the spread of the NS radii and their evolution between $\sim$0.4 s and 1 s after bounce accounts for less than 25% variation around an average value of all investigated models. In Sect. 5.7 we will come back to this argument and give reasons why the NS radius has little influence on the results discussed in this work. Moreover, the neutrino loss from the low-entropy, degenerate PNS core, whose properties are determined by the incompressibility of supranuclear matter, should exhibit a progenitor dependence mostly through the different weight of the surrounding accretion mantle, whose growth depends on $\dot{M}$. Such a connection is expressed by the terms depending on m_{acc} and $\dot{m}_{\mathrm{acc}}$ in the neutrino luminosity of the high-density PNS core in Eq. (4) of Ugliano et al. (2012). We therefore hypothesize, and demonstrate below, a correspondence of the L_ν-$\dot{M}$ space and the Mm'-m' parameter plane and expect that the critical luminosity curve $L_{\nu,\mathrm{crit}}(\dot{M})$

maps to a curve separating BH formation and successful explosions in the Mm'-m' plane*.

In our simulations neutrino-driven explosions set in around the time or shortly after the moment when infalling matter arriving at the shock possesses an entropy $s \sim 4$. We therefore choose M_4 (Eq. 5.2) as our proxy of the PNS mass, $M_4 \propto M_{\mathrm{ns}}$, and $\mu_4 \equiv m'(r)[M_\odot/(1000\,\mathrm{km})]^{-1}|_{s=4}$ (Eq. 5.3) as corresponding measure of the mass-accretion rate at this time, $\mu_4 \propto \dot{M}$. The product Mm' is therefore represented by $M_4\mu_4$. Tests showed that replacing M_4 by the iron-core mass, M_{Fe}, is similarly good and yields results of nearly the same quality in the analysis following below (which points to an underlying correlation between M_4 and M_{Fe}). In practice, we evaluate Eq. (5.3) for μ_4 by the average mass-gradient of the progenitor just outside of $s = 4$ according to

$$\mu_4 \equiv \left.\frac{\Delta m/M_\odot}{\Delta r/1000\,\mathrm{km}}\right|_{s=4} = \frac{(M_4 + \Delta m/M_\odot) - M_4}{[r(M_4 + \Delta m/M_\odot) - r(s=4)]\,/1000\,\mathrm{km}}\,, \tag{5.5}$$

with $\Delta m = 0.3\,M_\odot$ yielding optimal results according to tests with varied mass intervals Δm. With the parameters M_4 and μ_4 picked, our imagined mapping between critical conditions in the L_ν-$\dot{M}$ and Mm'-m' spaces transforms into such a mapping relation between the L_ν-$\dot{M}$ and $M_4\mu_4$-μ_4 planes as illustrated by Fig. 5.4.

Figure 5.5 demonstrates the strong correlation of the mass-accretion rate $\dot{M} = \mathrm{d}m/\mathrm{d}t$ with the parameter μ_4 as given by Eq. (5.5) (panel c) as well as the tight correlations between $M_4\mu_4$ and the sum of ν_e and $\bar{\nu}_e$ luminosities (panel a) and the summed product of the luminosities and mean squared energies of ν_e and $\bar{\nu}_e$ (panel b). It is important to note that the non-stationarity of the conditions requires us to average the quantities plotted on the abscissas over time from the moment when the $s = 4$ interface passes through the shock until the models either explode (i.e., the shock radius expands beyond 500 km; open circles) or until the mass shell $(M_4 + 0.3)\,M_\odot$ has fallen through the shock, which sets an endpoint to the time interval within which explosions are obtained (non-exploding cases marked by filled circles). The time averaging is needed not only because of evolutionary changes of the preshock mass-accretion rate (as determined by the progenitor structure) and corresponding evolutionary trends of the emitted neutrino luminosities and mean energies. The averaging is necessary, in particular, because the majority of our models develops large-amplitude shock oscillations after the accretion of the $s = 4$ interface, which leads to quasi-periodic variations of the neutrino emission properties with more or less pronounced, growing amplitudes (see the examples in Fig. 2.1). Panel d demonstrates that exploding models (open circles) exceed a value of unity for the ratio of advection timescale, t_{adv}, to heating timescale, t_{heat}, in the gain layer, which was considered as a

---

*Since the shock revival is determined by neutrino heating, which depends on $L_\nu\langle\epsilon_\nu^2\rangle$, and since the average squared neutrino energy $\langle\epsilon_\nu^2\rangle \propto T_\nu^2 \propto M_{\mathrm{ns}}^2$ increases with time and PNS mass (Müller & Janka 2014), Müller & Janka (2015) discuss the critical condition for shock revival in terms of $L_\nu\langle\epsilon_\nu^2\rangle$ as a function of $M_{\mathrm{ns}}\dot{M}$. This suggests that an alternative choice of parameters could be M^3m' and Mm' instead of Mm' and m', respectively. Our results demonstrate that the basic physics is already captured by the Mm'-m' dependence.

useful critical threshold for diagnosing explosions in many previous works (e.g., Janka & Keil 1998, Thompson 2000, Janka et al. 2001, Thompson et al. 2005, Buras et al. 2006a, Marek & Janka 2009, Müller et al. 2012b, Fernández 2012, Müller & Janka 2015, Summa et al. 2016). The exploding models also populate the region towards low mass-accretion rates (as visible in panels a–c, too), which confirms our observation reported in Sect. 5.2. In contrast, non-exploding models cluster, clearly separated, in the left, upper area of panel d, where $t_{\mathrm{adv}}/t_{\mathrm{heat}} \lesssim 1$ and the mass-accretion rate tends to be higher. For the calculation of the timescales we follow the definitions previously used by, e.g., Buras et al. (2006a), Marek & Janka (2009), Müller et al. (2012b), Müller & Janka (2015):

$$t_{\mathrm{heat}} = \left(\int_{R_{\mathrm{g}}}^{R_{\mathrm{s}}} (e+\Phi)\rho\,\mathrm{d}V\right)\left(\int_{R_{\mathrm{g}}}^{R_{\mathrm{s}}} \dot{q}_\nu \rho\,\mathrm{d}V\right)^{-1}, \tag{5.6}$$

$$t_{\mathrm{adv}} = \int_{R_{\mathrm{g}}}^{R_{\mathrm{s}}} \frac{1}{|v_r|}\,\mathrm{d}r\,. \tag{5.7}$$

Here, the volume and radius integrals are performed over the gain layer between gain radius R_{g} and shock radius R_{s}. e is the sum of the specific kinetic and internal energies, Φ the (Newtonian) gravitational potential, ρ the density, $\dot{q}_\nu$ the net heating rate per unit of mass, and v_r the velocity of the flow. Again, because of the variations of the diagnostic quantities associated with the time evolution of the collapsing star and the oscillations of the gain layer, the mass-accretion rate and timescale ratio are time-averaged between the moment when the $s = 4$ interface passes the shock until either 300 ms later or until the model explodes (shock radius exceeding 500 km)*. Panels e (and f) lend support to the concept of a critical threshold luminosity in the L_ν-$\dot{M}$ (and $L_\nu\langle\epsilon_\nu^2\rangle$-$\dot{M}$) space mentioned above. The two plots show a separation of exploding (open circles) and non-exploding (filled circles) models in a plane spanned by the time-averaged values of the preshock mass-accretion rate on the one hand and the sum of ν_e and $\bar{\nu}_e$ luminosities (panel e) or the summed product of ν_e and $\bar{\nu}_e$ luminosities times their mean squared energies on the other hand (panel f). Again the same time-averaging procedure as for panel d is applied. After the $s = 4$ progenitor shell passes the shock, the time-averaged conditions of the exploding models reach the lower halfs of these panels, whereas the time-averaged properties of the non-exploding models define the positions of these unsuccessful explosions in the upper halfs. A separation appears that can be imagined to resemble the critical luminosity curve $L_{\nu,\mathrm{crit}}(\dot{M})$ sketched in the left panel of Fig. 5.4.

Because of the strong time dependence of the postshock conditions and of the neutrino emission during the phase of dynamical shock expansion and contraction after the accretion of the $s = 4$ interface, it is very difficult to exactly determine the critical luminosity curve that captures the physics of our exploding 1D simulations. Although we do not consider such an effort as hopeless if the governing parameters are carefully taken into account (cf., e.g., the discussions in Pejcha & Thompson 2015, Müller & Janka 2015, Summa et al.

---

*We tested intervals ranging from 100 ms to 600 ms and observed the same trends for all choices.

2016) and their time variations are suitably averaged, we think that the clear separation of successful and failed explosions visible in panels e and f of Fig. 5.5 provides proper and sufficient support for the notion of such a critical curve (or, more general: condition) in the $L_{\nu,\mathrm{crit}}$-$\dot{M}$ space. Figure 5.4 illustrates our imagined relation between the evolution tracks of collapsing stellar cores that explode or fail to explode in this L_ν-$\dot{M}$ space on the left side and the locations of SN-producing and BH-forming progenitors in the $M_4\mu_4$-μ_4 plane on the right side. The sketched evolution paths are guided by our results in panels e and f of Fig. 5.5. In the following section we will demonstrate that exploding and non-exploding simulations indeed separate in the $M_4\mu_4$-μ_4 parameter space.

5.4. Separation Line of Exploding and Non-Exploding Progenitors

The existence of a separation line between BH forming and SN producing progenitors in the $M_4\mu_4$-μ_4 plane is demonstrated by Fig. 5.6, which shows the positions of the progenitors for all investigated model series in this two-dimensional parameter space. For all five calibrations successful explosions are marked by colored symbols, whereas BH formation is indicated by black symbols. The regions of failed explosions are underlaid by gray. They are bounded by straight lines with fit functions as indicated in the panels of Fig. 5.6,

$$y_{\mathrm{sep}}(x) = k_1 \cdot x + k_2 \,, \tag{5.8}$$

where $x \equiv M_4\mu_4$ and $y \equiv \mu_4$ are dimensionless variables with M_4 and μ_4 computed by Eq. (5.5). The values of the dimensionless coefficients k_1 and k_2 as listed in Table 5.1 are determined by minimizing the numbers of outliers.

Table 5.1.: Bh-sn separation curves for all calibration models

Calibration Model	k_1[a]	k_2[a]	M_4[b]	μ_4[b]	$M_4\mu_4$[b]
s19.8 (2002)	0.274	0.0470	1.529	0.0662	0.101
w15.0[c]	0.225	0.0495	1.318	0.0176	0.023
w18.0	0.283	0.0430	1.472	0.0530	0.078
w20.0	0.284	0.0393	1.616	0.0469	0.076
n20.0	0.194	0.0580	1.679	0.0441	0.074

[a] Fit parameters of separation curve (Eq. 5.8) when x and y are measured for a central stellar density of $5 \times 10^{10}\,\mathrm{g\,cm^{-3}}$.

[b] Measured for a central stellar density of $5 \times 10^{10}\,\mathrm{g\,cm^{-3}}$.

[c] M_4 and μ_4 measured roughly at core bounce, because pre-collapse data are not available.

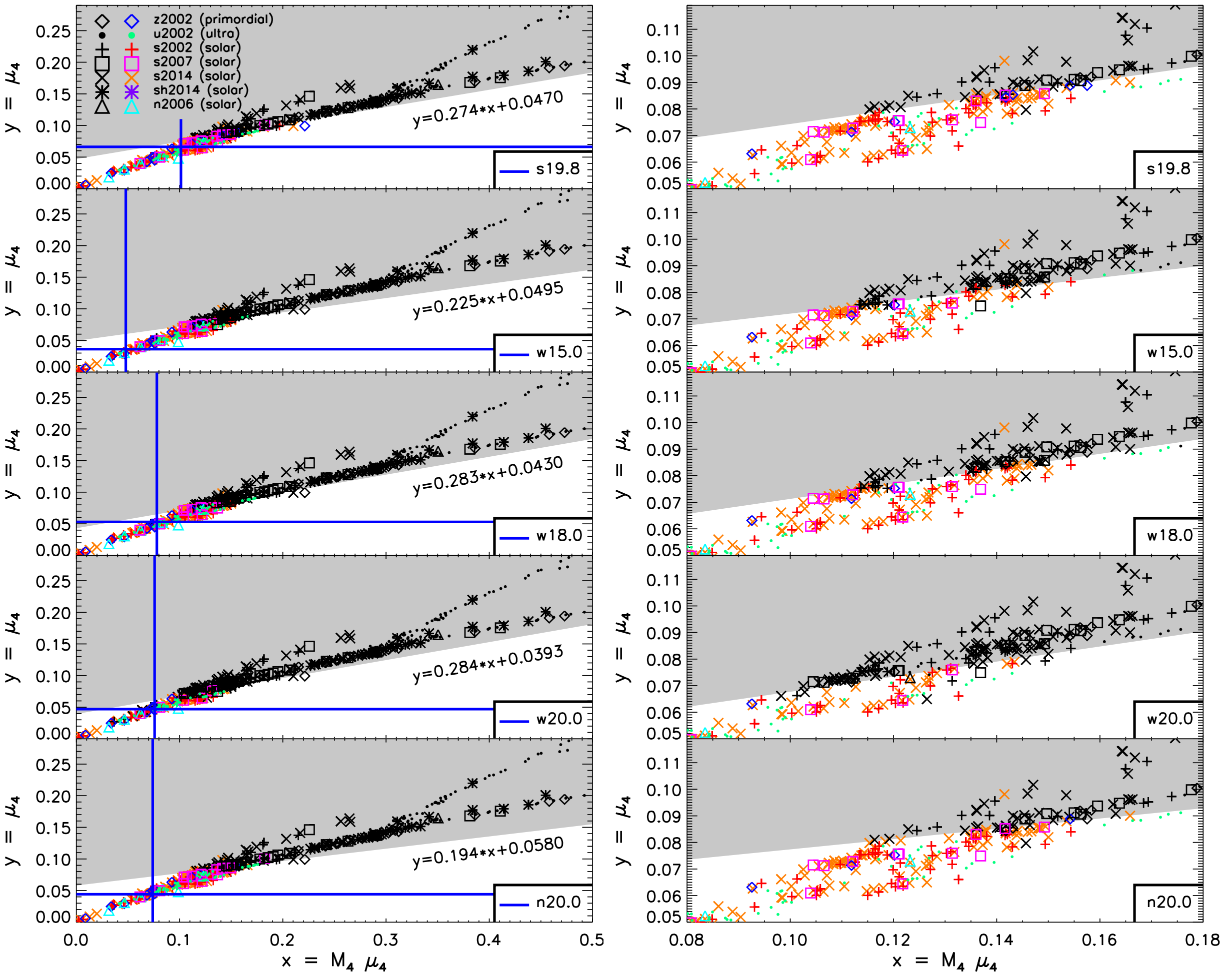

Figure 5.6.: Separation curves between BH formation (gray region, black symbols) and SN explosions (white region, colored symbols) for all calibrations in the plane of parameters $x = M_4\mu_4$ and $y = \mu_4$ (zooms in *right* panels). Note that the left panels do not show roughly two dozen BH-forming models of the u2002 series, which populate the x-range between 0.5 and 0.62 and are off the displayed scale. Different symbols and colors correspond to the different progenitor sets. The locations of the calibration models are also indicated in the left panels by crossing blue lines.

The stellar models of all progenitor sets populate a narrow strip in the x-y plane of Fig. 5.6, left panels. BH formation cases are located in the upper left part of the x-y plane. The inclination of the separation line implies that the explosion limit in terms of μ_4 depends on the value of the $M_4\mu_4$ and therefore a single parameter would fail to predict the right behavior in a large number of cases. Denser cores outside of M_4 with high mass-accretion rates (larger μ_4) prevent explosions above some limiting value. This limit grows for more massive cores and thus higher M_4 because larger mass-accretion rates do not only hamper shock expansion by higher ram pressure but larger core masses and bigger accretion rates also correlate with an increase of the neutrino luminosity of the PNS as expressed by our parameter $M_4\mu_4$. The evolution tracks of successful explosion cases in the left panel of Fig. 5.4 indicate that for higher $L_\nu \propto M_{\rm ns}\dot{M}$ the explosion threshold, $L_{\nu,\rm crit}(\dot{M})$, can be reached for larger values of $\dot{M}$.

Explosions are supported by the combination of a massive PNS, which is associated with a high neutrino luminosity from the cooling of the accretion mantle, on the one hand, and a rapid decline of the accretion rate, which leads to decreasing ram pressure, on the other hand. A high value of M_4 combined with a low value of μ_4 is therefore favorable for an explosion because a high accretion luminosity (due to a high accretor mass $M_{\rm ns} \approx M_4$) comes together with a low mass-accretion rate (and thus low ram pressure and low binding energy) exterior to the $s = 4$ interface (cf. Fig 5.7). Such conditions are met, and explosions occur readily, when the entropy step at the $s = 4$ location is big, because a high entropy value outside of M_4 correlates with low densities and a low accretion rate. M_4 is usually the base of the oxygen shell and a place where the entropy changes discontinuously causing (or resulting from) a sudden decrease in density due to burning there. This translates into an abrupt decrease in $\dot{M}$ when the mass M_4 accretes. Figure 14 of Sukhbold & Woosley (2014) shows a strong correlation between compactness $\xi_{2.5}$ and location of the oxygen shell. The decrease of the mass-accretion rate is abrupt only if the entropy change is steep with mass, for which μ_4 at M_4 is a relevant measure.

Progenitors with $M_{\rm ZAMS} \lesssim 22\,M_\odot$ that are harder to explode often have relatively small values of M_4 and an entropy ledge above $s = 4$ on a lower level than the entropy reached in more easily exploding stars. The lower neutrino luminosity associated with the smaller accretor mass in combination with the higher ram pressure can prohibit shock expansion in many of these cases. Corresponding to the relatively small values of M_4 and relatively higher densities outside of this mass, these cases stick out from their neighboring stars with respect to the binding energy of overlying material, namely, non-exploding models in almost all cases are characterized by *local* maxima of $E_{\rm b,4} = E_{\rm b}(m/M_\odot > M_4)$ (see Fig. 5.7).

In view of this insight it is not astonishing that exploding and non-exploding progenitors can be seen to start separating from each other in the two-parameter space spanned by M_4 and the average entropy value $\langle s\rangle_4$ just outside of M_4 (Fig. 5.8). Averaging s over the mass interval $[M_4, M_4 + 0.5]$ turns out to yield the best results. Exploding models cluster towards the side of high $\langle s\rangle_4$ and low M_4, while failures are found preferentially for low values of $\langle s\rangle_4$. The threshold for success tends to grow with M_4. However, there is still a broad band where both types of outcomes overlap. The disentanglement of SNe and BH-formation events is clearly better achieved by the parameter set of $M_4\mu_4$ and μ_4, which, in addition, applies correctly not only for stars with $M_{\rm ZAMS} \geq 15\,M_\odot$ but also for progenitors with lower masses.

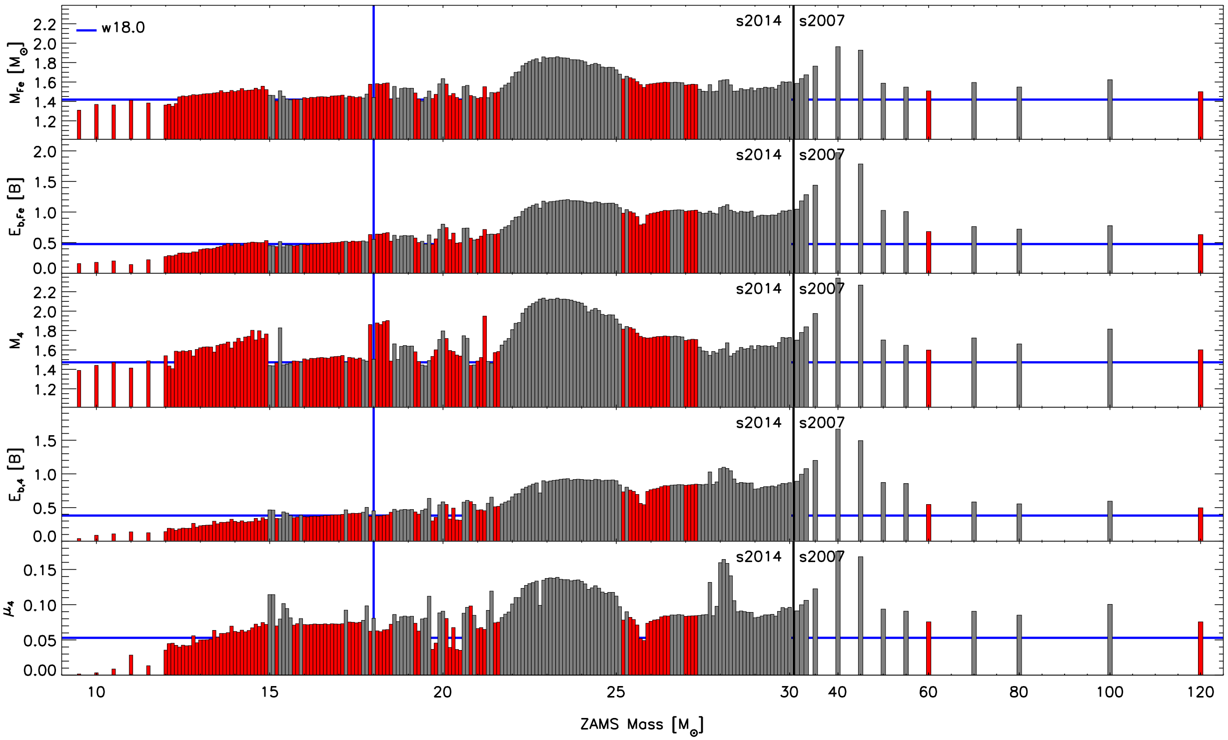
w18.0
s2014
s2007
M_{Fe} [$M_\odot$]
$E_{b,Fe}$ [B]
M_4
$E_{b,4}$ [B]
μ_4
10
15
20
25
30
40
60
80
100
120
ZAMS Mass [$M_\odot$]

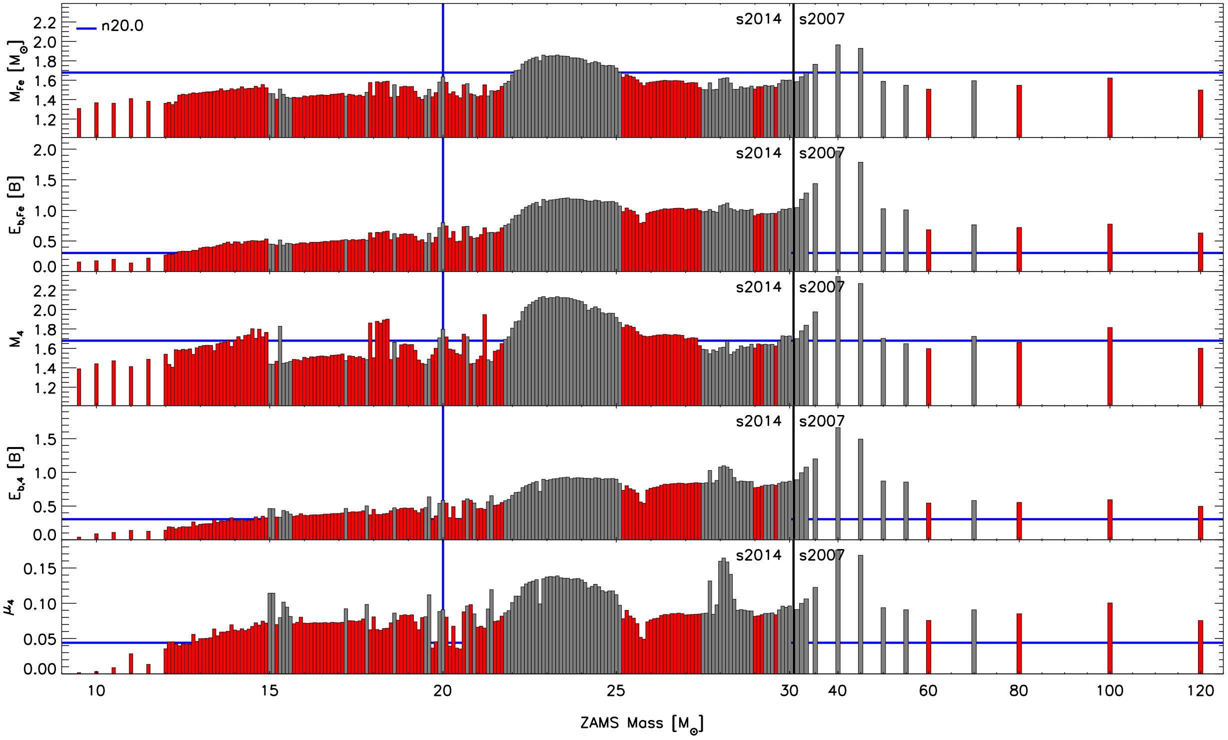
n20.0
s2014
s2007
M_{Fe} [$M_\odot$]
$E_{b,Fe}$ [B]
M_4
$E_{b,4}$ [B]
μ_4
10
15
20
25
30
40
60
80
100
120
ZAMS Mass [$M_\odot$]

Figure 5.7.: Iron-core masses M_{Fe} (*top panel*), exterior binding energies ($E_{\mathrm{b,Fe}} = E_{\mathrm{b}}(m > M_{\mathrm{Fe}})$; *second panel*), normalized masses M_4 (*third panel*), exterior binding energies ($E_{\mathrm{b},4} = E_{\mathrm{b}}(m/M_\odot > M_4)$; *fourth panel*), and μ_4 (*fifth panel*), for models of the s2014 series, the supplementary low-mass progenitors with $M_{\mathrm{ZAMS}} < 15\,M_\odot$, and models with $M_{\mathrm{ZAMS}} > 30\,M_\odot$ from the s2007 series. A black vertical line marks the boundary between the two progenitor sets. Red bars indicate exploding cases and gray bars non-exploding ones. All quantities are measured when the central density of the collapsing stellar iron core is $5 \times 10^{10}\,\mathrm{g\,cm^{-3}}$. The *upper five panels* correspond to the w18.0 calibration, the *lower five panels* to the n20.0 calibration. Mass and parameter values of the calibration models are indicated by vertical and horizontal blue lines, respectively. In the region of $M_{\mathrm{ZAMS}} \lesssim 22\,M_\odot$ non-exploding cases, with very few exceptions, correlate with local minima of M_4 and pronounced local maxima of μ_4 and $E_{\mathrm{b},4}$. A high value of M_4 combined with a low value of μ_4 is typically supportive for an explosion because a high accretion luminosity (due to a high accretor mass $M_{\mathrm{ns}} \approx M_4$) comes together with a low mass-accretion rate (and thus low ram pressure and low binding energy) exterior to the $s = 4$ interface. The iron-core masses and their exterior binding energies show a similar tendency, but significantly less pronounced.

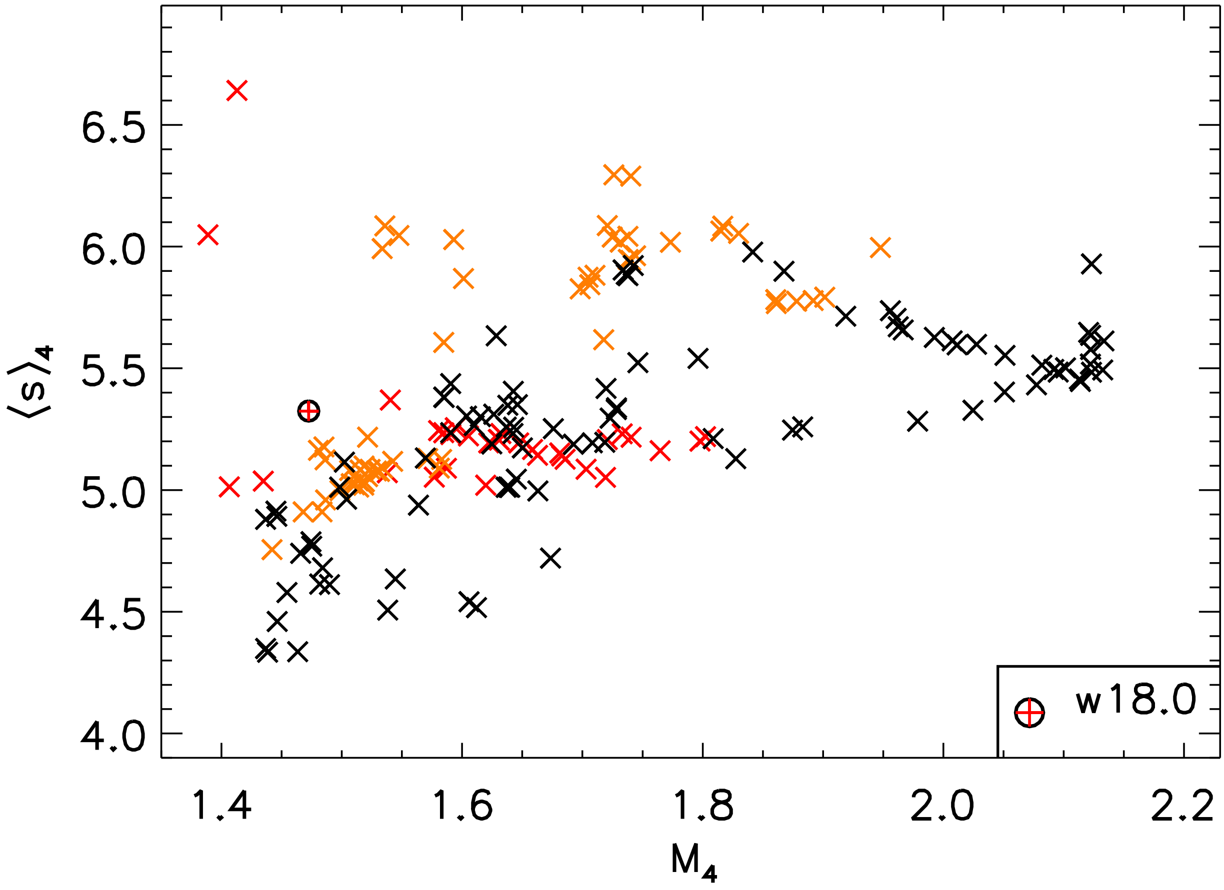

Figure 5.8.: Two-parameter plane spanned by $M_4 = M(s = 4)$ and mean entropy of overlying matter, $\langle s \rangle_4$, averaged over a mass intervall of $0.5\,M_\odot$. The locations of progenitors from the s2014 series and the supplementary low-mass set with $M_{\rm ZAMS} < 15\,M_\odot$ are marked by crosses. Black crosses indicate BH formation cases and tend to concentrate towards the lower and right half of the panel, i.e., towards low values of $\langle s \rangle_4$ for given M_4. Orange crosses mean successful SN explosions of the s2014 models with the w18.0 calibration, and red crosses are explosions for the $M_{\rm ZAMS} < 15\,M_\odot$ progenitors. While high entropies outside of the $s = 4$ location signal a tendency of success for the stars of the s2014 set (although the separation from BH-formation cases is not sharp), the successfully exploding $M_{\rm ZAMS} < 15\,M_\odot$ models mix completely with BH forming events.

5.5. Stellar Outliers

Out of 621 simulated stellar models for the s19.8, w15.0, w18.0, w20.0, and n20.0 calibrations only 9, 14, 16, 11, and 9 models, respectively, do not follow the behavior predicted by their locations on the one or the other side of the separation line in the $M_4\mu_4$-μ_4 plane (see the zooms in the right column of Fig. 5.6). But most of these cases lie very close to the boundary curve and their explosion or non-explosion can be affected by fine details and will certainly depend on multi-dimensional effects. A small sample of outliers is farther away from the boundary line. The w20.0 calibration is the weakest driver of neutrino-powered explosions in our set and tends to yield the largest number of such more extreme outliers.

These cases possess unusual structural features that influence their readiness to explode. On the non-exploding side of the separation line, model s20.8 of the s2014 series with $(M_4\mu_4, \mu_4) \approx (0.142, 0.0981)$ is one example of a progenitor that blows up with all calibrations except w20.0, although it is predicted to fail (see Fig. 5.6). In contrast, its mass-neighbor s20.9 with $(M_4\mu_4, \mu_4) \approx (0.123, 0.085)$ as well as its close neighbor in the $M_4\mu_4$-μ_4 space, s15.8 of the s2002 series with $(M_4\mu_4, \mu_4) \approx (0.140, 0.096)$, both form BHs as expected. The structure of these pre-supernova models in the $s = 4$ region is very similar with $M_4 = 1.45, 1.45, 1.46$ for s20.8, s20.9, s15.8, respectively. Although s20.8 reaches a lower entropy level outside of $s = 4$ than the other two cases and therefore is also predicted to fail, its explosion becomes possible when the next entropy step at an enclosed mass of $1.77\,M_\odot$ reaches the shock. This step is slightly farther out (at $1.78\,M_\odot$) in the s20.9 case and comes much later (at $\sim$1.9 $M_\odot$) in the s15.8 model. Both the earlier entropy jump and the lower preceding entropy level enable the explosion of s20.8, because the associated higher density maintains a higher mass-accretion rate and therefore higher neutrino luminosity until the entropy jump at $1.77\,M_\odot$ falls into the shock. The abnormal structure of the progenitor therefore prevents that the explosion behavior is correctly captured by our two-parameter criterion for the explodability.

On the exploding side, model s15.3 of the s2014 series with $(M_4\mu_4, \mu_4) \approx (0.146, 0.0797)$ is expected to blow up according to the two-parameter criterion, but does not do so for all calibrations (Fig. 5.6). Similarly, s15.0 of the s2007 series with $(M_4\mu_4, \mu_4) \approx (0.137, 0.0749)$ fails with the w15.0 and w20.0 calibrations although success is predicted. We compare their structure with the nearby successful cases of s25.4 (s2014 series, $(M_4\mu_4, \mu_4) \approx (0.150, 0.0820)$), and s25.2, s25.5 (both from the s2014 series), and s25.8 (s2002 series), all of which group around $(M_4\mu_4, \mu_4) \approx (0.143, 0.0783)$. The successfully exploding models all have similar entropy and density structures, namely fairly low entropies ($s \lesssim 3$) and therefore high densities up to 1.81–1.82 $M_\odot$, where the entropy jumps to $s \gtrsim 6$. The high mass-accretion rate leads to an early arrival of the $s = 4$ interface at the shock ($\sim$300 ms after bounce) and high accretion luminosity. Together with the strong decline of the accretion rate afterwards this fosters the explosion. In contrast, the two models that blow up less easily have higher entropies and lower densities so that the $s = 4$ mass shells (at $\sim$1.8 $M_\odot$ in s15.0 and at $\sim$1.82 $M_\odot$ in the s15.3) arrive at the shock much later (at $\sim$680 ms and $\sim$830 ms post bounce, respectively), at which time accretion contributes less neutrino luminosity. Moreover, both models have a pronounced entropy ledge with a width of $\sim$0.05 $M_\odot$ (s15.0) and $\sim$0.08 $M_\odot$ (s15.3) before the entropy rises above $s \sim 5$. This ledge is much narrower than in the majority of non-exploding models, where it stretches across typically 0.3 $M_\odot$ or more. The continued, relatively high accretion rate prohibits shock expansion and explosion. This is obvious from the fact that model s15.0 with the less extended entropy ledge exhibits a stronger tendency to explode and for some calibrations indeed does, whereas s15.3 with the wider ledge fails for all calibrations. Our diagnostic parameter μ_4 to measure the mass derivative in an interval of $\Delta m = 0.3\,M_\odot$, however, is dominated by the high-entropy level (low-density region) above the ledge and therefore underestimates the mass-accretion rate in the ledge domain, which is relevant for describing the explosion conditions. Again the abnormal structure of the s15.0 and s15.3 progenitors prevents our two-parameter classification from correctly describing the explosion behavior of these models.

5.6. Systematics of Progenitor and Explosion Properties in the Two-Parameter Plane

In Fig. 5.9 colored symbols show the positions of the progenitors of the s2014 series and those of the supplementary low-mass models with $M_{\mathrm{ZAMS}} < 15\,M_\odot$ in the x-y-plane relative to the separation lines $y_{\mathrm{sep}}(x)$ of exploding and non-exploding cases. In the upper panel the color coding corresponds to M_{ZAMS}, in the middle panel to the iron-core mass, M_{Fe}, and in the bottom panel to the binding energy of matter outside of the iron core. M_{Fe} is taken to be the value provided by the stellar progenitor model at the start of the collapse simulation in order to avoid misestimation associated with our simplified nuclear burning network and with inaccuracies from the initial mapping of the progenitor data. Since we use the pressure profile of the progenitor model instead of the temperature profile, slight differences of the derived temperatures can affect the temperature-sensitive shell burning and thus the growth of the iron-core mass.

While low-mass progenitors with small iron cores and low binding energies populate the region towards the lower left corner with significant distance to the separation curve, stars above $20\,M_\odot$ with bigger iron cores and high binding energies can be mostly found well above the separation curve. However, there are quite a number of intermediate-mass progenitors above the line and higher-mass cases below. In particular, a lot of stars with masses between $\sim\!25\,M_\odot$ and $30\,M_\odot$ cluster around $y_{\mathrm{sep}}(x)$ in the $x \sim 0.13$–0.15 region. These stars are characterized by $M_{\mathrm{Fe}} \sim 1.4$–$1.5\,M_\odot$ and high exterior binding energies. Some of them explode but most fail (cf. Fig. 5.7). The ones that group on the unsuccessful side are mostly cases with smaller iron cores, whose neutrino luminosity is insufficient to create enough power of neutrino heating to overcome the ram pressure of the massive infall.

Figure 5.10 displays the BH-formation cases of the s2014 series without associated SNe by black crosses in the x-y-plane. Successful SN explosions of this series plus additional $M_{\mathrm{ZAMS}} < 15\,M_\odot$ progenitors are shown by color-coded symbols, which represent, from top to bottom, the final explosion energy (E_{exp}, with the binding energy of the whole progenitor taken into account), the explosion time (t_{exp}, measured by the time the outgoing shock reaches 500 km), the gravitational mass of the remnant (with fallback taken into account),

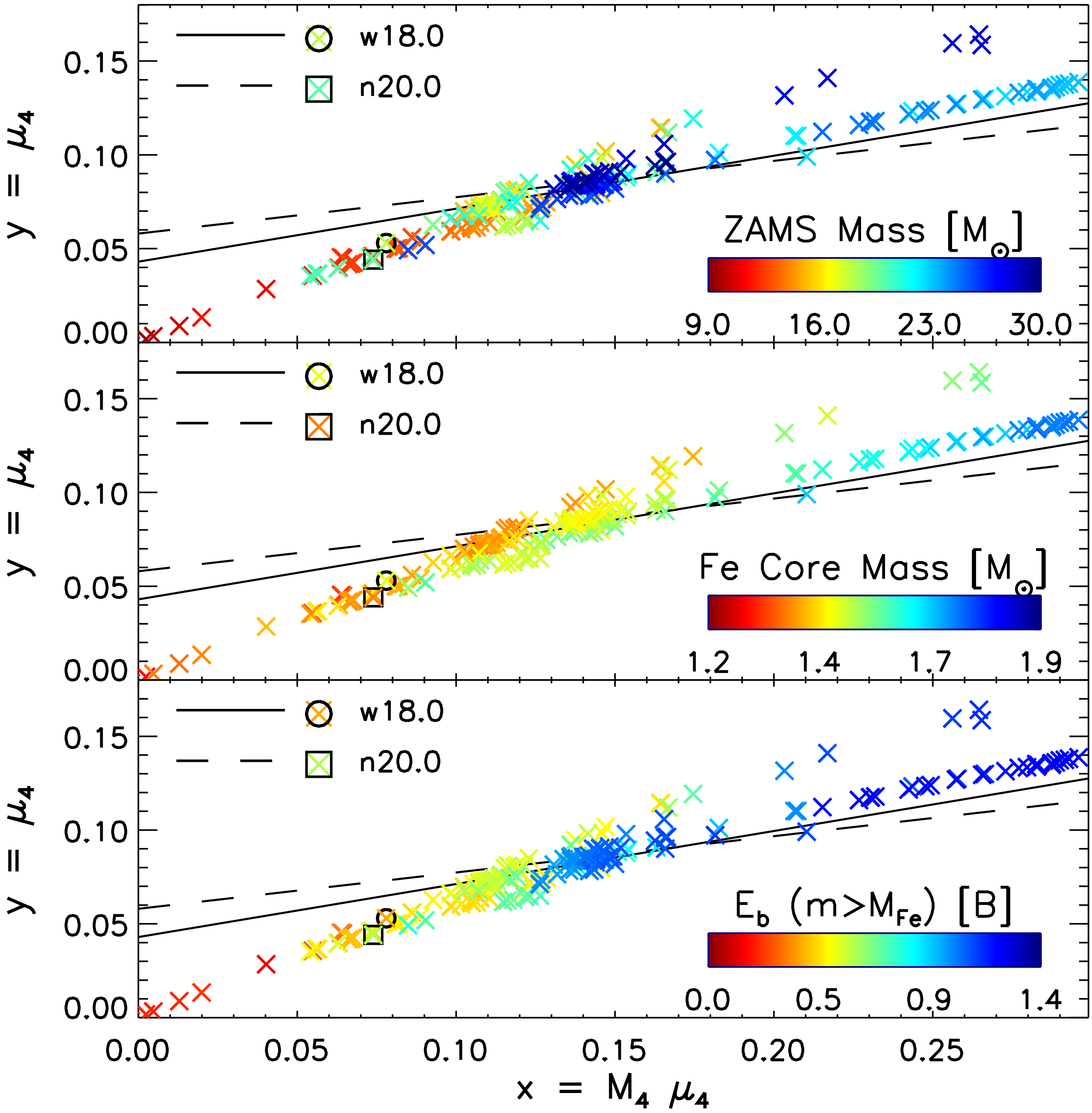

Figure 5.9.: ZAMS masses, iron-core masses, M_{Fe}, and binding energies outside of the iron core, $E_{\mathrm{b}}(m > M_{\mathrm{Fe}})$, (*from top to bottom*) of the s2014 series and the supplementary low-mass progenitors with $M_{\mathrm{ZAMS}} < 15\,M_{\odot}$ in the x-y parameter plane. The solid and dashed lines mark the separation curves $y_{\mathrm{sep}}(x)$ for the w18.0 and n20.0 calibration models (different symbols as given in the legend), respectively.

the ejected mass of ^{56}Ni plus tracer element (see Sect. 3.4.3; fallback also taken into account), and the fallback mass. The left plot shows the results of our w18.0 calibration, the

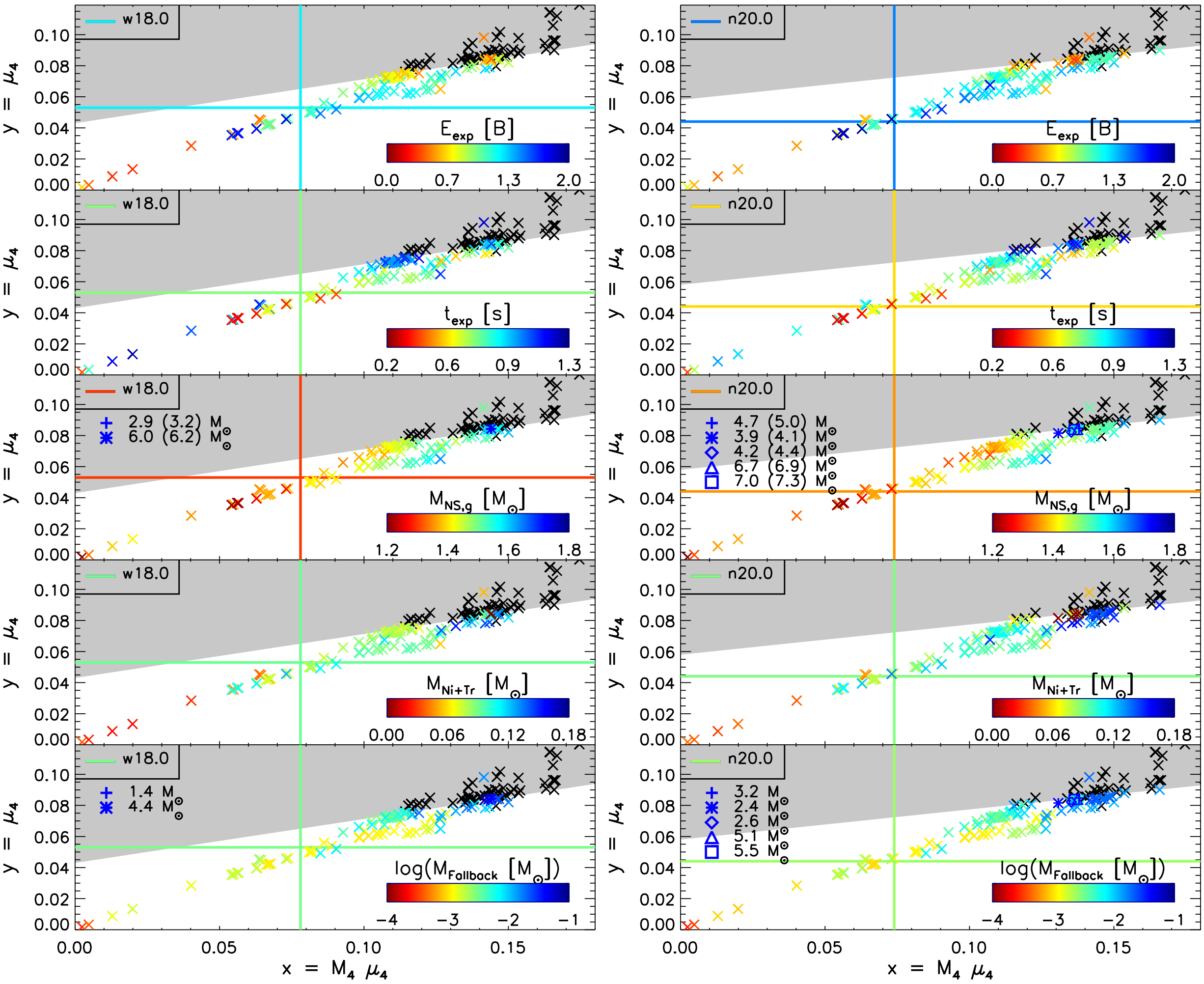

Figure 5.10.: Explosion energies (1 B = 1 bethe = 10^{51} erg), post-bounce explosion times, gravitational neutron-star masses ($M_{\mathrm{ns,g}} = M_{\mathrm{ns,b}} - E_{\nu,\mathrm{tot}}/c^2$), ejected iron-group material (i.e., ^{56}Ni plus tracer masses), and fallback masses (*from top to bottom*) of the s2014 series and the supplementary low-mass progenitors with $M_{\mathrm{ZAMS}} < 15\,M_\odot$ for calibration models w18.0 (*left*) and n20.0 (*right*) in the x-y parameter plane. Black crosses correspond to BH formation cases, colored crosses to successful explosions. In the middle and bottom panels, the blue (partly overlapping) symbols correspond to fallback SNe with estimated BH masses (baryonic masses in parentheses) and fallback masses as listed in the legends. The horizonal and vertical lines mark the locations of the calibration models with the colors corresponding to the values of the displayed quantities.

right plot for the n20.0 calibration. The gravitational mass of the NS remnant, $M_{\mathrm{ns,g}}$, is estimated from the baryonic mass, $M_{\mathrm{ns,b}}$, by subtracting the rest-mass equivalent of the total neutrino energy carried away in our simulations:

$$M_{\mathrm{ns,g}} = M_{\mathrm{ns,b}} - \frac{1}{c^2} E_{\nu,\mathrm{tot}} \,. \tag{5.9}$$

Our estimates of NS binding energies, $E_{\mathrm{ns,b}} = E_{\nu,\mathrm{tot}}$, are roughly compatible with Lattimer & Yahil (1989) fit of $E_{\mathrm{ns,b}}^{\mathrm{LY}} = 1.5 \times 10^{53}\,(M_{\mathrm{ns,g}}/M_\odot)^2\,\mathrm{erg} = 0.084\,M_\odot c^2\,(M_{\mathrm{ns,g}}/M_\odot)^2$. Blue symbols in the middle and bottom panels mark fallback BH formation cases, for which gravitational and baryonic masses (the latter in parentheses) are listed in the panels. We ignore neutrino-energy losses during fallback accretion for both NS and BH-forming remnants.

Progenitors in Fig. 5.10 that lie very close to the separation line tend to produce weaker explosions that set in later than those of progenitors with a somewhat greater distance from the line. Moreover, there is a tendency of more massive NSs to be produced higher up along the x-y-band where the progenitors cluster, i.e., bigger NS masses are made at higher values of $x = M_4\mu_4$. Also the largest ejecta masses of ^{56}Ni and ^{56}Ni plus tracer are found towards the right side of the displayed progenitor band just below the boundary of the BH formation region.

Fallback masses tend to decrease towards the lower left corner of the x-y-plane in Fig. 5.10, far away from the separation curve, where predominantly low-mass progenitors are located, besides five progenitors around 20 $M_\odot$, which lie in this region because they have extremely low values of $E_{\mathrm{b}}(m > M_4)$, see Fig. 5.7, and exceptionally small values of μ_4 (Fig. 5.9), and develop fast and strong explosions with small NS masses, large masses of ejected ^{56}Ni plus tracer, and very little fallback. Closer to the separation line the fallback masses are higher, but for successfully exploding models they exceed $\sim$0.05 $M_\odot$ only in a few special cases of fallback SNe (cf. Fig. 5.1), where the fallback mass can amount up to several solar masses. We point out that the fallback masses in particular of stars below $\sim$20 $M_\odot$ were massively overestimated by Ugliano et al. (2012). The reason was an erroneous interpretation of the outward reflection of reverse-shock accelerated matter as a numerical artifact connected to the use of the condition at the inner grid boundary. The reverse shock, which forms when the SN shock passes the He/H interface, travels backward through the ejecta and decelerates the outward moving matter to initially negative velocities. This inward flow of stellar material, however, is slowed down and reflected back outward by the large negative pressure gradient that builds up in the reverse-shock heated inner region. With this outward reflection, which is a true physical phenomenon and not a boundary artifact, the matter that ultimately can be accreted by the NS is diminished to typically between some $10^{-4}\,M_\odot$ and some $10^{-2}\,M_\odot$ of early fallback (see Fig. 5.1).

In a handful of high-mass s2014 progenitors (s27.2 and s27.3 for the w18.0 calibation and s27.4, s29.0, s29.1, s29.2, and s29.6 for the n20.0 set) the SN explosion is unable to unbind a large fraction of the star so that fallback of more than a solar mass of stellar matter is likely to push the NS beyond the BH formation limit. Such fallback SN cases cluster in the vicinity of $x \sim 0.13$–0.14 and $y \sim 0.080$–0.081 on the explosion side of the separation line.

In the ZAMS-mass sequence they lie at interfaces between mass intervals of successfully exploding and non-exploding models, or they appear isolated in BH-formation regions of the ZAMS-mass space (see Figs. 5.2 and 5.7). Their fallback masses and estimated BH masses are listed in the corresponding panels of Fig. 5.10. Naturally, they stick out also by their extremely low ejecta masses of ^{56}Ni and tracer elements, late explosion times (around one second post bounce or later), and relatively low explosion energies (∼0.3–0.5 B).

5.7. Influence of the Neutron Star Radius

Basically, the accretion luminosity, which is given by $L_\nu^{\mathrm{acc}} \propto G M_{\mathrm{ns}} \dot{M} / R_{\mathrm{ns}}$, does not only depend on the PNS mass, M_{ns}, and the mass-accretion rate, $\dot{M}$, but also on the PNS radius, R_{ns}. One may wonder whether our two-parameter criterion is able to capture the essential physics although we disregard the radius dependence when using $x = M_4\mu_4$ as a proxy of the accretion luminosity.

For this reason, we tested a redefinition of $x = M_4\mu_4$ by including a factor $\langle R_{\mathrm{ns}}\rangle^{-1}_{300\,\mathrm{ms}}$, i.e., using $\tilde{x} \equiv M_4\mu_4\langle R_{\mathrm{ns}}\rangle^{-1}_{300\,\mathrm{ms}}$ instead*. Doing so, we found essentially no relevant effects on the location of the boundary curve. In fact, the separation of exploding and non-exploding models in the $\tilde{x}$-y-plane is even slightly improved compared to the x-y-plane, because $\langle R_{\mathrm{ns}}\rangle^{-1}_{300\,\mathrm{ms}}$ for most non-exploding models is larger than for the far majority of exploding ones. As a consequence, the non-exploding cases tend to be shifted to the left away from the boundary line, whereas most of the exploding cases are shifted to the right, also increasing their distances to the boundary line. This trend leads to a marginally clearer disentanglement of both model groups near the border between explosion and non-explosion regions. A subset of the (anyway few and marginal) outliers can thus move to the correct side, while very few cases can become new, marginal outliers. It might therefore even be possible to improve the success rate for the classification of explodability by a corresponding (minor) relocation of the boundary curve. The improvement, however, is not significant enough to justify the introduction of an additional parameter into our two-parameter criterion in the form of $\langle R_{\mathrm{ns}}\rangle_{300\,\mathrm{ms}}$, which has the disadvantage of not being based on progenitor properties and whose exact, case-dependent value cannot be predicted by simple arguments.

Because the line separating exploding and non-exploding models did not change in our test, the criterion advocated in this chapter captures the basic physics, within the limitations of the modeling. While we report here this marginal sensitivity of our two-parameter criterion to the NS radius as a result of the present study, a finally conclusive assessment

---

*The radius R_{ns} of the PNS is defined by the radial position where the density is $10^{11}\,\mathrm{g\,cm^{-3}}$. As in panels d–f of Fig. 5.5, the time-averaging for $\langle R_{\mathrm{ns}}\rangle^{-1}_{300\,\mathrm{ms}}$ is performed from the passage of the $s = 4$ interface through the shock until the onset of the explosion for successful models and from the infall of the $s = 4$ interface until 300 ms later for non-exploding models. We also employ a normalization factor of 70 km to recover (roughly) the same range of values for $\tilde{x}$ as in the case of x.

of this question would require to repeat our set of model calculations for different prescriptions of the time-dependent contraction of the inner boundary of our computational grid. The chosen functional behavior of this boundary movement with time determines how the PNS contraction proceeds during the crucial phase of shock revival. In order to avoid overly severe numerical time-step constraints, which can become a serious handicap for our long-time simulations with explicit neutrino transport over typically 15 seconds, we follow Ugliano et al. (2012) in using a relatively slow contraction of the inner grid boundary. It would be highly desirable to perform model calculations also for faster boundary contractions, which is our plan for future work. In view of this caveat the arguments and test results discussed in this section should still be taken with a grain of salt.

On grounds of the discussion of our results in the x-y-plane one can actually easily understand why the definition of the separation curve of exploding and non-exploding models presented in this chapter did not require us to take into account a possible dependence of the accretion luminosity on the NS radius. Instead, we could safely ignore such a dependence when we coined our ansatz that $L_\nu \propto Mm'(r) \propto M_4\mu_4$. There are two reasons for that. On the one hand, the separation line in the $M_4\mu_4$-μ_4 plane is fairly flat. A variation of the NS radius corresponds to a horizontal shift of the location of data points in the x-y plane. However, with the contraction behavior of the neutron stars obtained in our simulations, only for (relatively few) points in the very close vicinity of the separation curve such a horizontal shift is sufficiently big to potentially have an influence on whether the models are classified as non-exploding or exploding. On the other hand, the models near the separation line typically blow up fairly late ($t_\mathrm{exp} \gtrsim 0.6\,\mathrm{s}$), and the NS masses lie in a rather narrow range between roughly $1.4\,M_\odot$ and $1.6\,M_\odot$ for the gravitational mass (see Fig. 5.10). For such conditions the variation of the NS radius is of secondary importance (cf. Fig. 3 in Müller & Janka 2014). Low-mass progenitors with less massive NSs, whose radius (at the same time) can be somewhat larger (Fig. 3 in Müller & Janka 2014), however, are located towards the lower left corner of the x-y plane and therefore far away from the separation curve (compare Figs. 5.9 and 5.10). An incorrect horizontal placement of these cases (due to the omission of the dependence of the neutrino luminosity on the NS radius) does not have any relevance for the classification of these models.

5.8. Brief Comparison to Previous Works

Our result of a complex pattern of NS and BH forming cases as function of progenitor mass was previously found by Ugliano et al. (2012), too, and was confirmed by Pejcha & Thompson (2015). Aside from differences in details depending on the use of different progenitor sets and different SN 1987A calibration models, the main differences of the results presented here compared to those of Ugliano et al. (2012) are lower explosion energies for progenitors with $M \lesssim 13\,M_\odot$ (see discussion in Sect. 2.3) and lower fallback masses as mentioned in Sect. 5.6. Based on simple arguments (which, however, cannot account for the complex dynamics of fallback), Pejcha & Thompson (2015) already expected (in particular for their parameterization (a)) that cases with significant fallback —in the sense that the remnant masses are significantly affected— should be rare for solar-metallicity progenitors. Our results confirm this expectation, although the ZAMS masses with significant fallback are different and less numerous than in the work by Pejcha & Thompson (2015). As pointed out by these authors, fallback has potentially important consequences for the remnant mass distribution, and the observed NS and BH masses seem to favor little fallback for the majority of SNe.

As discussed in detail by Ugliano et al. (2012), our explosion models (as well as parameterization (a) of Pejcha & Thompson 2015) predicts many more BH formation cases and more mass intervals of non-exploding stars than O'Connor & Ott (2011), who made the assumption that stars with compactness $\xi_{2.5} > 0.45$ do not explode. Roughly consistent with our results and those of Ugliano et al. (2012), Horiuchi et al. (2014) concluded on the basis of observational arguments (comparisons of the SN rate with the star formation rate; the red supergiant problem as a lack of Type-IIP SNe from progenitors above a mass of $\sim 16\,M_\odot$) that stars with an "average" compactness of $\xi_{2.5} \sim 0.2$ should fail to produce canonical SNe (cf. Fig. 15 in Sukhbold et al. 2016).

A correlation of explosion energy and ^{56}Ni mass as found by Pejcha & Thompson (2015) and Nakamura et al. (2015) (both, however, without rigorous determination of observable explosion energies at infinity) and as suggested by observations (see Pejcha & Thompson 2015 for details) is also predicted by our present results (but not by Ugliano et al. 2012 with their erroneous estimate of the fallback masses, see Sect. 6.2.3 or Ertl et al. 2016b, and the overestimated explosion energies of low-mass progenitors, see Sect. 2.3 and Sect. 4.1). Our models yield low explosion energies and low nickel production towards the low-mass side of the SN progenitors (see also Sukhbold et al. 2016). In contrast, the modeling approach by Pejcha & Thompson (2015) predicts a tendency of lower explosion energies and lower ^{56}Ni masses towards the high-mass side of the progenitor distribution (because of the larger binding energies of more massive stars), although there is a large mass-to-mass scatter in all results. This difference could be interesting for observational diagnostics. The modeling approach by Pejcha & Thompson (2015) seems to yield neutrino-driven winds that are considerably stronger, especially in cases of low-mass SN progenitors, than those obtained in the simulations of Ugliano et al. (2012) and, in particular, than those found in current, fully self-consistent SN and PNS cooling models, whose behavior we attempt to reproduce better by the Crab-motivated recalibration of the low-mass explosions used in the present work. Moreover, for the ^{56}Ni-E_{exp} correlation reported by Pejcha & Thompson (2015), a mass interval between $\sim 14\,M_\odot$ and $\sim 15\,M_\odot$ with very low explosion energies and very low Ni production, which does not exist in our models, also plays an important role. Nakamura et al. (2015) found a positive correlation of the explosion energy and the ^{56}Ni mass with compactness $\xi_{2.5}$. We can confirm this result for the nickel production but not for the explosion energy (cf. Sukhbold et al. 2016, Fig. 15 there). A possible reason for this discrepancy could be the consideration of "diagnostic" energies by Nakamura et al.

(2015) at model dependent final times of their simulations instead of asymptotic explosion energies at infinity, whose determination requires seconds of calculation and the inclusion of the binding energy of the outer progenitor shells (see Fig. 5.1 and Sukhbold et al. 2016, Fig. 6, for the evolution of the energies in some exemplary simulations).

A comprehensive discussion of explosion properties like explosion energies, nickel production, neutrino signal, etc. will be subject of the next chapter (Chap. 6). We will discuss the properties of the compact remnants thereafter in Chap. 7. For the same reason we also refrain here from more extended comparisons to the progenitor-dependent explosion and remnant predictions of other studies, in particular those of O'Connor & Ott (2011), Nakamura et al. (2015), Pejcha & Thompson (2015) and Müller et al. (2016a). A detailed assessment of the different modeling methodologies and their underlying assumptions would be needed to understand and judge the reasons for differences of the results and to value their meaning in the context of supernova predictions based on the neutrino-driven mechanism. Such a goal reaches beyond the scope of this work.

5.9. Conclusions

We performed 1D simulations of SNe for a large set of progenitors of different masses and metallicities, including the solar-metallicity s2002 series (Woosley et al., 2002) previously investigated by Ugliano et al. (2012) and the new s2014 models of Sukhbold & Woosley (2014) with their fine griding of $0.1\,M_\odot$ in the ZAMS mass.

In order to obtain SN explosions in spherical symmetry, we adopt the methodology of Ugliano et al. (2012), using 1D hydrodynamics and approximate neutrino transport and a PNS-core neutrino source, but with improvements in a number of modeling aspects (e.g., a nuclear high-density EOS and a fully self-consistent implementation of nuclear burning through a small network, cf. Sect. 3.2). Explosions are triggered by a neutrino luminosity that is sufficiently large to overcome the critical threshold condition for shock runaway. This luminosity is fed by a progenitor-dependent accretion component during the post-bounce shock-stagnation phase as well as a component from the high-density core of the nascent NS. The core emission is also progenitor-dependent, because it scales with the mass of the hot accretion mantle that assembles around the cooler high-density core of the PNS during the pre-explosion evolution. The conditions for an explosion are thus tightly coupled to the progenitor structure, which determines the post-bounce accretion history.

Our approach contains a number of free parameters, whose values are calibrated by reproducing observational properties (explosion energy, ^{56}Ni mass, total neutrino energy and signal duration) of SN 1987A with suitable progenitor models of this SN. We consider five different such progenitors for our study, namely besides the s19.8 star of the s2002 model series of Woosley et al. (2002), which was used by Ugliano et al. (2012) as calibration model, also 15, 18, and 20 $M_\odot$ of Woosley and collaborators as well as a 20 $M_\odot$ model from Shigeyama & Nomoto (1990) (see Sect. 4.1).

Because 1D simulations cannot properly reproduce the period of continued accretion and simultaneous outflow that characterizes the early expansion of the revived shock in multi-dimensional simulations and delivers the explosion energy, our 1D models exhibit an extended episode of accretion that is followed by a strong early wind phase. The overestimated mass loss during the latter phase compensates for the enhanced preceding accretion, and the associated recombination energy yields the dominant contribution to the power supply of the beginning explosion. A detailed discussion of our methodology can be found in Chap. 2.

Non-exploding cases tend to correlate with *local* maxima of the compactness $\xi_{2.5}$, of the total binding energy outside of the iron core, $E_\mathrm{b}(m > M_\mathrm{Fe})$, and, most significantly, *local* maxima of the total binding energy $E_\mathrm{b}(m/M_\odot > M_4)$ outside of the mass coordinate $M_4 = m(s = 4)/M_\odot$, where the dimensionless entropy per nucleon reaches a value of 4. Many (but not all) non-exploding progenitors below $\sim$22 $M_\odot$ also coincide with local minima of M_Fe and, in particular, with minima of M_4. However, there are no fix threshold values of any of these characteristic parameters of the pre-collapse progenitor structure that could be used to discriminate favorable from non-favorable conditions for an explosion.

Guided by such insights we propose a two-parameter criterion to classify the explodability of progenitor stars by the neutrino-heating mechanism in dependence of the pre-collapse properties of these stars. The two structural parameters that turn out to yield the best separation of successful and unsuccessful cases are M_4 and the mass derivative $\mu_4 = \mathrm{d}m/\mathrm{d}r[M_\odot/(1000\,\mathrm{km})]^{-1}|_{s=4} = m'(s = 4)[M_\odot/(1000\,\mathrm{km})]^{-1}$ just outside of the $s = 4$ location, which we combine to a parameter $x \equiv M_4\mu_4$. The parameters x and $y \equiv \mu_4$ are tightly connected to the two crucial quantities that govern the physics of the neutrino-driven mechanism, namely the mass-accretion rate of the stalled shock, $\dot{M}$, and the neutrino luminosity L_ν. The former determines the ram pressure that damps shock expansion and can be mathematically linked to the mass derivative m' (see Eq. 5.4). The latter is a crucial ingredient for the neutrino heating that is responsible for shock revival and is dominated by the accretion luminosity and the PNS-mantle cooling emission during the crucial phase of shock revival. Both of these scale with $\dot{M}$ and/or the accretor mass (i.e., the PNS mass) so that $L_\nu \propto M_\mathrm{ns}\dot{M}$ expresses the leading dependence. Since the neutrino-driven explosions in our simulations set in shortly after the entropy interface and density jump around $s = 4$ have fallen through the shock (Fig. 2.1), M_4 can be taken as a good proxy of M_ns as the accretor mass, and μ_4 can serve as a measure for the mass-accretion rate $\dot{M}$ of the PNS.

Higher values of M_4 tend to be favorable for an explosion as shown by Fig. 5.7, where many non-exploding cases (dark gray) correlate with local minima of M_4. The reason is that the neutrino luminosity scales (roughly) with $x = M_4\mu_4$ (the actual sensitivity of the neutrino-energy deposition to M_4 is even steeper). Therefore higher M_4 imply greater neutrino luminosities and stronger neutrino heating. In contrast, the influence of $y = \mu_4$

is ambivalent. On the one hand a high value of μ_4 increases the neutrino luminosity, on the other hand it also causes a large ram pressure that has to be overcome by neutrino heating. The effect of these competing influences is that a higher value of M_4 in association with a lower value of μ_4 favors explosions. Reversely, non-exploding cases in Fig. 5.7 are correlated with local minima of M_4 and maxima of μ_4. Visually, this means that explosion cases are preferentially located toward the lower right of the $M_4\mu_4$-μ_4 parameter space (cf. Figs. 5.4, 5.6, 5.10).

The parameters x and y therefore span a plane in which successful explosions and failures with BH formation are clearly separated. The progenitor stars populate an astonishingly narrow band that stretches from the lower left corner with the lightest stars to the upper right direction of the x-y-plane, where the massive progenitors with the biggest iron cores and highest binding energies of overlying material are located (see Fig. 5.9). While SNe can be found in the region of low values of y, i.e., for low mass-accretion rate, the non-exploding cases inhabit the domain of high y, but the limiting value of the mass-accretion rate that prevents the success of the neutrino-driven mechanism grows with the value of x. Both sectors in the x-y plane are separated by a boundary line that can be well represented by a linear function $y_{\mathrm{sep}}(x)$ (Eq. 5.8) with increasing slope. (The values of the dimensionless coefficients of this linear relation are listed for all calibration models in Table 5.1.) Because of the physical meaning of the parameters x and y, there is a close correspondence between the separation line $y_{\mathrm{sep}}(x)$ and the critical threshold luminosity $L_{\nu,\mathrm{crit}}(\dot{M})$ that has to be exceeded to trigger runaway expansion of the accretion shock by neutrino heating. The rising slope of the separation curve in this context means that for each value of the neutrino luminosity, respectively x, there is an upper limit of the mass-accretion rate, respectively y, up to which neutrino-driven explosions are possible, and that this BH-formation threshold value of y grows with x. The parameters x and y, computed from the progenitor profiles before collapse, allow one to judge whether a considered star is able to overcome the threshold neutrino luminosity for an explosion, or, in other words, whether its mass accretion rate stays below the critical limit above which the onset of the explosion is prevented.

Only ∼1–3% of all investigated progenitors do not follow this discrimination scheme in their final fate but lie on the wrong side of the separation curve. These outliers are characterized by pathologies of their entropy and density profiles that describe the composition-shell structure in the Si-O-layers. Such special conditions lead to unusual combinations of mass-accretion rate and PNS masses. Our two-parameter criterion expressed by the separation line $y_{\mathrm{crit}}(x)$ therefore enables one, with a very high significance, to predict the explodability of progenitor stars via the neutrino-driven mechanism by referring to the properties of these stars as captured by the pair of parameters x and y.

Clausen et al. (2015) explore the interesting possibility that the death of massive stars in NS vs. BH formation may be better captured by a probabilistic description. The non-monotonic variations of explosion vs. non-explosion with ZAMS mass or compactness might be interpreted as stochasticity in the explosion behavior. However, by considering the problem in a more appropriate two-parameter space, our two-parameter criterion unmasks these putatively random variations as actually deterministic phenomenon. Clausen et al. (2015), in contrast, suggest a variety of factors besides ZAMS mass and metallicity, e.g. rotation, binarity, the strength of magnetic fields, stochastic differences in the pre-collapse structure or even in the explosion mechanism, that might introduce a randomness such that a star of given mass might not form either a NS or a BH but both with a certain probability. If such a diversity in the stellar destiny depends on a causal process, for example the presence of different amounts of spin, a deterministic description could still apply but would require an extension to a parameter space of more than the two dimensions combined by our current criterion, e.g., by adding extra dimension(s) that capture the role of rotation in the explosion mechanism. If, in contrast, truly stochastic effects like turbulent processes or chaotic fluctuations in the progenitor, decide about the stellar fate, a deterministic criterion for explodability would be ruled out and a probabilistic description would be indispensable.

Our study employs pre-collapse models that emerge from 1D stellar evolution calculations of single, non-rotating SN progenitors with prescribed mass-loss histories. The results of our study naturally depend on the post-bounce accretion properties of the collapsing stars. The (iron and low-entropy) core masses as well as the entropy and density jumps at the composition-shell interfaces play an important role in setting the conditions for the neutrino-heating mechanism, which is obvious from the definition of our parameters x and y. It is conceivable that multi-dimensional hydrodynamics could lead to considerable changes of the stellar properties as functions of the progenitor mass (e.g., Arnett et al., 2015), and that asymmetries and perturbations in the shell-burning layers of the pre-collapse core might have important consequences for the development of SN explosions by the neutrino-driven mechanism (e.g., Arnett & Meakin, 2011, Couch & Ott, 2013; 2015, Müller & Janka, 2015, Couch et al., 2015). We are hopeful that the basic insights of our study, in particular the existence of a two-parameter criterion for the explodability —expressed by a SN-BH separation line $y_{\mathrm{crit}}(x)$ in the x-y-space and the tight connection between this curve and the critical luminosity condition $L_{\nu,\mathrm{crit}}(\dot{M})$ of the neutrino-driven mechanism— possess more general validity. The explosion properties of the progenitor stars as functions of the ZAMS mass, however, do not only depend (moderately) on the considered SN 1987A progenitor models but will probably also change once multi-dimensional stellar evolution effects will be accounted for in the pre-supernova conditions.

6. Properties of the Explosive Outflow

We analyze the properties of the explosive outflow in this chapter for large sets of progenitor models provided by stellar evolution. We will postpone the discussion of the compact remnants to the subsequent chapter. The most important observable signatures connected to core-collapse supernovae (CCSNe) will be determined and compiled to gain a systematic picture. This chapter overlaps with the content of the work by Sukhbold et al. (2016), where we analyzed a set of progenitor models with solar metallicity for the different core-model calibrations (cf. Chap. 4). We will begin with this set of models, before we continue by adding further progenitor sets. An overview of the findings and conclusions by Sukhbold et al. (2016) is given in Sect. 6.1. The subject of the next section will be the previous study by Ugliano et al. (2012). The latter work employed an older version of HOTB and applied it to simulate the s2002 set. The calibration was performed with the $19.8\,M_\odot$ model of the same set. We will compare our findings to theirs in Sect. 6.2, and elaborate on an erroneous interpretation of the hydrodynamic results for the late-time fallback onto the compact remnant. After that we will broaden our input-parameter space by adding further progenitor models, starting with additional sets of stars with solar metallicity in Sect. 6.3. Then we will discuss sets with sub-solar metallicity in Sect. 6.4. This allows for analyzing of the dependencies of supernova (SN) outcomes on metallicity.

We will restrict ourselves mainly to the w18.0 and the n20.0 calibration, but the detailed results for the other calibration models are provided in the Appendix B. We will focus on the sets with the finest zero-age main-sequence (ZAMS) mass binning available for each metallicity. These are the z2011 series for primordial stars (no metal enrichment at birth), the u2002 set for ultra-metal poor stars (10^{-4} solar), and a compilation of progenitor models with solar metallicity. Nevertheless, all further model sets listed in Chap. 4 will be compared to as well and their results are also available in the Appendix B.

The content of this chapter is in parts already published in Ertl et al. (2016a) and Sukhbold et al. (2016), yet only the author's contribution to the latter publication was taken.

6.1. Combined Set of Solar-Metallicity Models

This section is guided by the work by Sukhbold et al. (2016) and can be envisioned as a summary of the latter. We simulated a very dense grid of progenitor models with solar metallicity for this work, which we composed of three different sets of progenitor models. The resulting collection of models covers the lowest zero-age main-sequence (ZAMS) masses that undergo iron-core collapse, starting at 9.0 $M_\odot$up to a cut-off mass of 120 $M_\odot$. KEPLER by Weaver et al. (1978) is one of the most advanced stellar evolution codes and especially designed for the late stages of massive star evolution, with convective core and shell-burning phases. The low-mass progenitor models ($\lesssim$ 13 $M_\odot$) were evolved with the latest improvements of the physical modeling as described by Woosley & Heger (2015) (termed "s2015" in this work). The intermediate mass models from 13 $M_\odot$ up to 30 $M_\odot$ are described in Sukhbold & Woosley (2014) (we term them "s2014"). We use the models from the s2007 set for the high-mass regime above 30 $M_\odot$ based on Woosley & Heger (2007). The latter set has a coarse ZAMS-mass binning, but this is not problematic for the most massive stars, because they are less common according to the Salpeter initial mass function (Salpeter, 1955, Chabrier, 2003).

6.1.1. Observable Signatures and Their Correlations

The general features of the results for the combined set are similar to the results obtained by Ugliano et al. (2012) for a different progenitor set. They are identical to those discussed in Chap. 5 and (Ertl et al., 2016a) for stars with ZAMS masses $M_{\rm ZAMS}$ greater than 13 $M_\odot$. In the mass range $M_{\rm ZAMS} \leq 13\,M_\odot$ the results presented here do not only employ updated progenitor models, the s2015 models, but use a more elaborate treatment based on an additional calibration anchor, the SN 1054, in contrast to the (seemingly ad hoc) ζ-reduction. The new low ZAMS-mass treatment is applied to Crab-like models (i.e., of cases $M_{\rm ZAMS} \leq 12.0\,M_\odot$).

Figure 6.1 gives an overview of the outcome of the combined set for each employed calibration. The massive stars either form a NS and explode, collapse to a BH without successful shock revival, or form a BH by late-time fallback (FBH) with explosive outflow. Each outcome channel is realized in our combined solar set, but the FBH SNe contribute only sub-dominantly. We will postpone the discussion of the compact remnants, their masses, and the formation channels to Chap. 7. Note that we separated the Crab-like progenitor models (labeled with "z9.6") from the other calibration models. We will use the same parameter choice for the low-mass stars each, when we combine it with the SN 1987A-like calibrations.

Figures 6.2 and 6.3 provide an overview of the explosion and remnant properties of the combined solar set. We display the results for simulations calibrated with w18.0 and n20.0, each of them supplemented with the low-mass calibration based on the z9.6 model for SN 1054 (cf. Chap. 4). The final kinetic energy (or explosion energy) $E_{\rm exp}$ is evaluated as well as the time the explosion sets in after core-bounce $t_{\rm exp}$, i.e. $R_{\rm shock}$ reaches 500 km. The two properties correlate to some extent, because later explosion times typically result

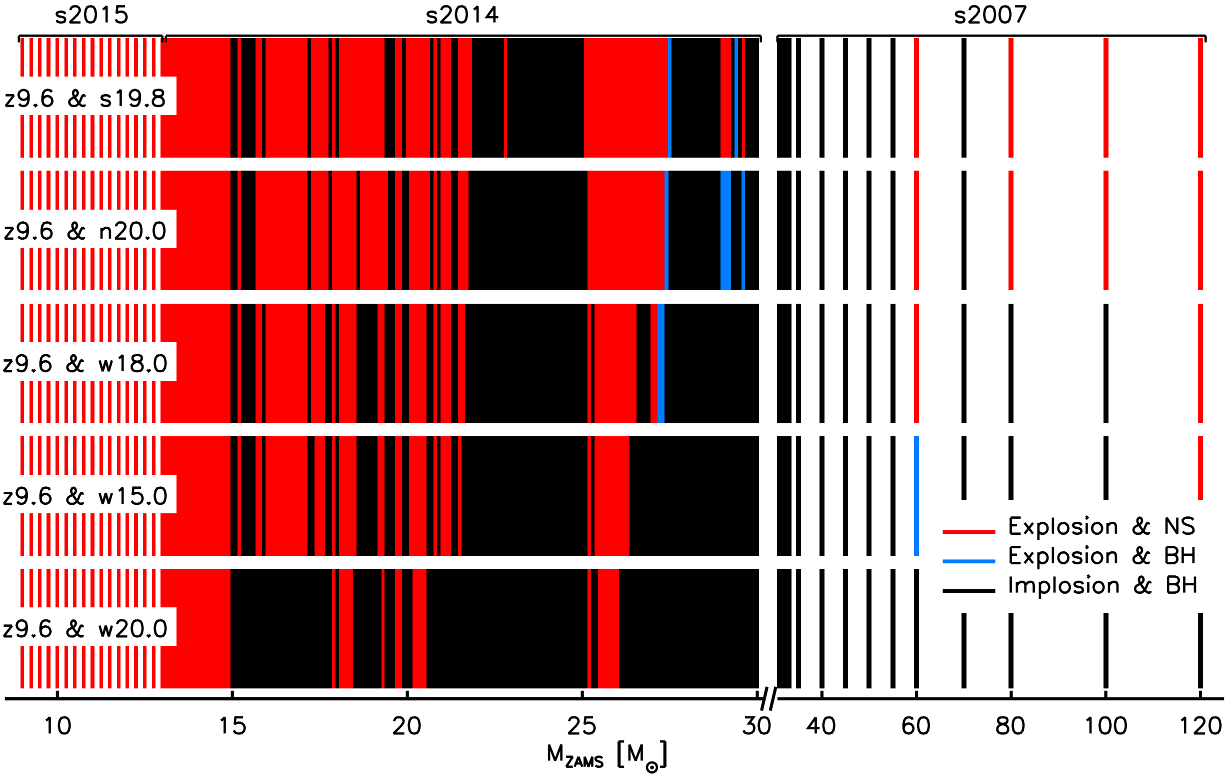

Figure 6.1.: Outcome systematics for the combined set of progenitor models with solar metallicity, which is composed of the s2015, the s2014, and the s2007 set. Each row depicts the results for a certain calibration and they are sorted by the number of explosions starting with the one that yielding the most at the top. Unsuccessful cases, without revival of the stalled shock, are marked by a black bar, while cases of successful shock-revival forming a NS or a BH are by a red and a blue line, respectively. The ZAMS-mass interval for the progenitor models is $0.25\,M_\odot$ starting at $9.0\,M_\odot$ up to $13.0\,M_\odot$, $0.1\,M_\odot$ up to $30.0\,M_\odot$, $1.0\,M_\odot$ up to $35.0\,M_\odot$, $5.0\,M_\odot$ up to $60.0\,M_\odot$, and $20.0\,M_\odot$ up to the cut-off mass of $120.0\,M_\odot$.

in less energetic explosions. This can be understood by the decaying power of cooling core reducing the power of the neutrino-driven wind with time.

Furthermore, we evaluate the amount of ^{56}Ni ejecta mass of the models and add the mass of ejected tracer material to it. The tracer nucleus can be envisioned as an error bar of the nickel ejecta mass in exploding simulations. In a more sophisticated simulation, some of the tracer will be ^{56}Ni, but some of it will form other iron-group elements. On the one hand we use an gray neutrino-transport scheme with an approximative electron fraction only, which in turn is found to influence the ^{56}Ni-nucleosynthesis critically (Thielemann et al., 1996). Another factor is the α-burning network of HOTB, which is restricted to symmetric α-nuclei and cannot account for electron fractions different from 0.5. Due to both deficiencies, we produce the tracer instead of ^{56}Ni, whenever the electron fraction is below $Y_e < 0.49$.

Note that no nickel is ejected in the cases with massive fallback, because the innermost mass shells retreat onto the compact remnant. The innermost mass shells, which are initially ejected contain the largest fraction of the explosively burned nickel as well as the contribution synthesized in the neutrino-driven wind. In axial-symmetry or without symmetry constraint, some of the nickel might mix outwards and survive (for multi-dimensional models see Wongwathanarat et al., 2013; 2015).

The correlation between the nickel ejecta mass and the explosion energy is interesting since both can be potentially observed (Hamuy, 2003, Spiro et al., 2014). We find an increasing nickel ejecta mass with increasing explosion energy (Fig. 17 in Sukhbold et al., 2016). A closer look reveals that the Crab-like models follow a clear trend with more energetic explosions ejecting larger amounts of nickel. The SN 1987A-like models, in contrast, produce relatively constant ^{56}Ni-ejecta with explosion energy of around $0.07\,M_{\odot}$, but only if the tracer material is not included. Adding the full amount of the ejected tracer material reveals a much cleaner correlation for all explosions with Crab-like and SN 1987A-like models. This is a clear indicator that a major fraction of the explosion energy is added by the neutrino-driven wind. The electron fraction in the wind is typically below 0.5, and therefore a site for tracer production.

6.1.2. Systematics of the Calibration Model

Figure 6.2 and 5.1 in comparison demonstrate that the ζ-modification used in Chap. 5 leads to the same overall explosion results as our present Crab-like calibration for the low-mass progenitors. This can be understood by the mathematical structure of the core luminosity as given by Eq. (3.25), where a similar effect on $L_{\nu,\mathrm{c}}$ can be achieved by either a reduction of the absolute value of S (by decreasing ζ) or an increase of R_{c} through a larger value of $R_{\mathrm{c,f}}$. As already discussed, the explosions of these stars set in fairly late after an extended phase of accretion, and the explosion is powered by a relatively massive and energetic neutrino-driven wind. This seems to be compatible with the recent result of multi-dimensional simulations by Müller (2015), who found a long-lasting phase of simultaneous accretion and mass ejection after the onset of the explosion for stars in the mass range between $11\,M_{\odot}$ and $12\,M_{\odot}$.

While supernovae near the low-mass end of the investigated mass range tend to explode with the lowest energies and smallest production of ^{56}Ni, our results exhibit a moderately strong correlation of these explosion parameters as a function of ZAMS mass. Overall, our results appear compatible with the observational data collected by Poznanski (2013), in particular in view of the weakness of the M-E_{exp} correlation concluded from a critical assessment of the observational analysis by Pejcha & Thompson (2015).

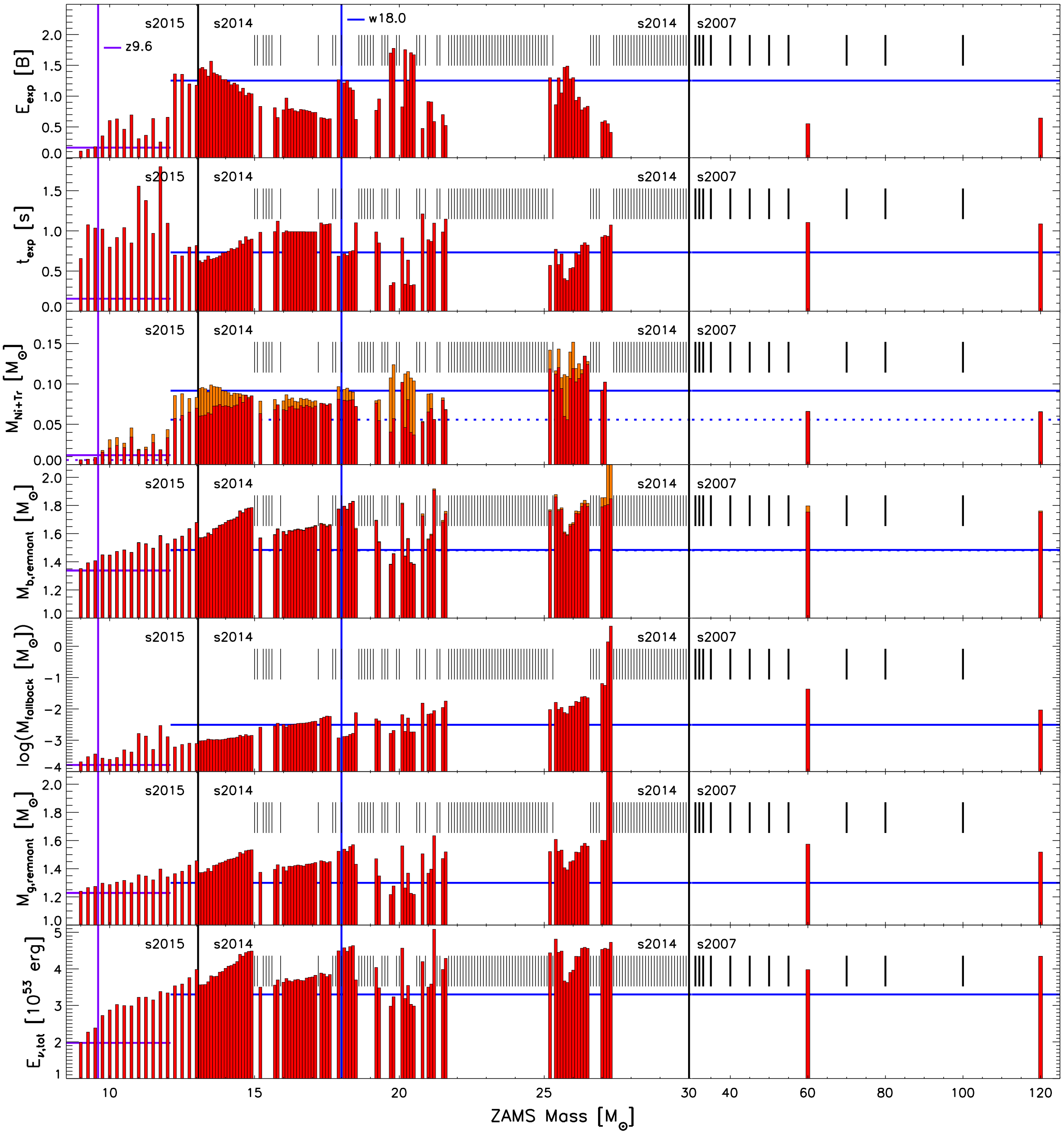

Figure 6.2.: Explosion properties for all models exploded with the z9.6 and w18.0 calibrations. Black vertical lines mark the boundaries between the different progenitor sets of our model sample is composed of. The panels, *from top to bottom*, show the final explosion energy, E_{exp}, in units of $1\,\mathrm{B} = 1\,\mathrm{Bethe} = 10^{51}\,\mathrm{erg}$, the time of the onset of the explosion, t_{exp}, the mass of finally ejected, explosively produced ^{56}Ni (red bars) and tracer element (orange bars), the baryonic mass of the compact remnant with the fallback mass indicated by orange sections on the bars, the fallback mass, the gravitational mass of the compact remnant, and the total energy radiated in neutrinos, $E_{\nu,\mathrm{tot}}$. The masses of the calibration models are indicated by vertical blue lines, and the corresponding results by horizontal solid or dashed blue lines, which extend over the mass ranges that are considered to have Crab-like or SN1987A-like progenitor properties, respectively. Non-exploding cases are marked by short vertical black bars in the upper half of each panel.

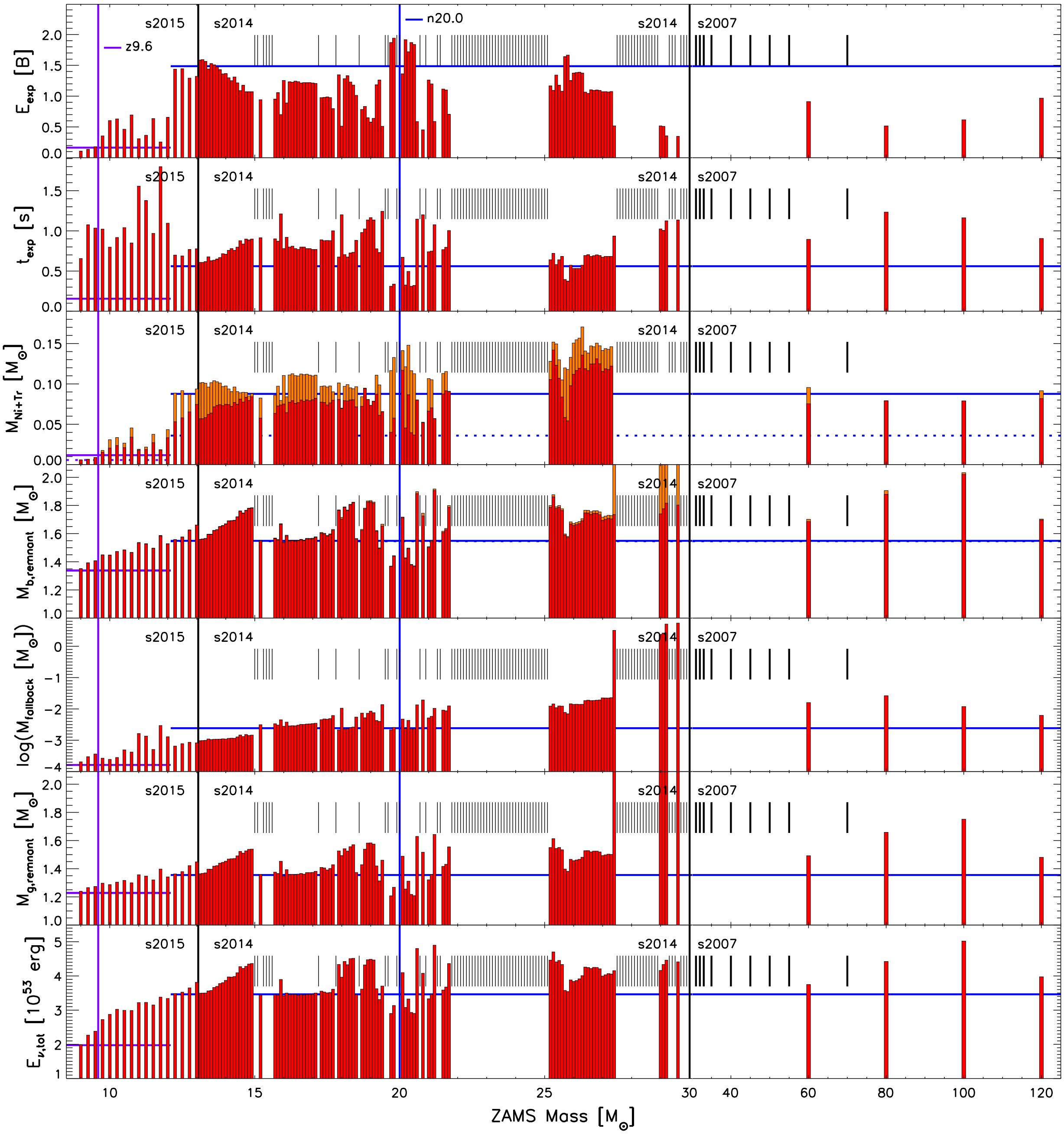

Figure 6.3.: Same as Fig. 6.2, but for simulations with the z9.6 and n20.0 calibrations.

Among the SN 1987A models, w15.0 has both, an unusually low compactness parameter (Table 4.1) and an extremely low value of M_{3000} (Fig. 4.6), a structure more Crab-like than SN1987A-like. Nevertheless, we found that w15.0, calibrated to fit SN 1987A, is almost as successful as w18.0, n20.0, and s19.8 powering explosions. In contrast, w20.0 is not special with respect to its compactness value or M_{3000} core, but turned out to be the weakest engine, i.e. the largest number of failed explosions.

The behavior of w15.0 can be understood in terms of the two parameters M_4 and μ_4 that determine neutrino-driven explosions as discussed in Chap. 5. M_4 is the stellar mass enclosed by the radius where the entropy per baryon is $s = 4\,k_\mathrm{B}$ and μ_4 the gradient dM/dr just outside of this location. w15.0 has much lower values of both M_4 and μ_4 than all the other calibration models. For this reason w15.0 has a low accretion component (see Fig. 4.5) of the neutrino luminosity. In order to explode the w15.0 model with sufficiently high energy fitting SN 1987A requires that the parameters of the core-cooling model provide a sufficiently powerful explosion on their own to compensate the low accretion component. With such a strong core component of the neutrino emission, w15.0 also acts as a strong engine for other progenitor stars.

The largest fraction of BH formation cases is obtained with the w20.0 calibration model, a $20\,M_\odot$ SN 1987A progenitor of Woosley et al. (1997), which explodes relatively easily and reproduces the SN 1987A ^{56}Ni yield with a fairly low ratio of explosion energy to ejecta mass of $(E_\mathrm{exp}/M_\mathrm{ej})$ of 0.7 only. The core neutrino source is correspondingly weak and enables successful SNe in a smaller subset of progenitors.

This shows that not every calibration model is suitable for SN 1987A, but the success rate of w15.0, w18.0, s19.8, n20.0 are fairly similar, which is an indicator for the robustness of our approach. Many models simulated with the w20.0 calibration on the other hand fail to explode. The nucleosynthesis products of these non-exploding massive stars are consumed by the BH rather than ejected. As a consequence, such a weak engine would fail to reproduce the solar abundance-pattern of the light s-process elements (Brown & Woosley, 2013). Furthermore, the fact that the red supergiant s19.8 and the blue supergiant n20.0 result in very similar explosion patterns demonstrates that our approach is dominated by the core structure rather than the outer layers of the star. The core structure in turn was found to fluctuate significantly in the mass regime of the progenitor star of SN 1987A (Sukhbold & Woosley, 2014).

Other modeling approaches by Pejcha & Thompson (2015) or by Müller et al. (2016a) find a qualitatively similar behavior of explosions and non-explosions with ZAMS mass, although their modeling is based on different assumptions and techniques.

6.1.3. Explosive Nucleosynthesis and Light Curves by Post-Processing with Kepler

Kepler has two advantages in comparison to Hotb, which can be used to obtain additional observable signatures for our models. On the one hand, Kepler has a large nuclear-reaction network (~2000 isotopes) for detailed nucleosynthesis calculations. On the other hand, it incorporates flux-limited radiative diffusion allowing for calculating approximate bolometric light curves, which are powered by the radioactive decay of ^{56}Ni and ^{56}Co (Woosley & Heger, 2007). These capabilities were previously employed to study population nucleosynthesis driving the explosions of models of massive stars by a piston (Woosley & Weaver, 1995, Woosley et al., 2002, Woosley & Heger, 2007, Zhang et al., 2008). The energy of the explosion and the initial location of the piston were prescribed and not a result of the simulation. The piston boundary is moved along a specified trajectory in time. These kinds of studies have some caveats: They do not rely on any explosion mechanism for the death of a massive star and, consequently, the details of the energy deposition are different for a piston-driven explosion in comparison to the energy deposition by neutrinos (see Chap. 4 of Ugliano, 2012). Furthermore, one cannot decide whether a star explodes or whether it does not, which can change the nucleosynthesis yields dramatically.

We overcome some of the problems of piston-driven explosions by calibrating the piston to the simulation results with Hotb. We extracted mass-shell trajectories for successful explosions. A mass coordinate of the shell was chosen lying above the neutrino-driven wind (see Fig. 10 in Sukhbold et al., 2016). The mass shell is the inner boundary of the piston-driven explosion and all mass within this boundary is neglected. We therefore purposely neglect the neutrino-driven wind contribution, because Kepler does not have a physical model for neutrino interactions, which would influence nucleosynthesis (see Thielemann et al., 1996, for an example) by varying the electron fraction. The piston location corresponds approximately to the mass which is enclosed by the shock right before the onset of the explosion in the simulations with Hotb. The piston-boundary movement for the mass coordinate was then tuned to reproduce explosion energy and the bulk nucleosynthesis, i.e. the ^{56}Ni ejecta mass (see Figs. 11 and 12 in Sukhbold et al., 2016).

This approach resulted in detailed explosive nucleosynthesis (but neglecting the neutrino-driven wind) and bolometric light curves for all explosions. The piston-driven simulations were conducted with Kepler for the Crab-like models and the models exploded with the w18.0 and the n20.0 calibration.[*] We will restrict ourself to the discussion of the main conclusions drawn from these results, but more details are presented in the publication by Sukhbold et al. (2016).

The nucleosynthesis yields were integrated with the Salpeter initial mass function (IMF; Salpeter, 1955) to get production factors of the elements for a population of stars. This cannot replace a detailed galactic chemical-evolution simulation, but it tells us which elements might be overproduced or where there might be a deficiency. The stars up to 12 $M_\odot$ contribute only little to the overall nucleosynthesis, although they make up roughly half of the SN explosions in our study. Their abundance patterns are solar-like or supersolar. The nucleosynthesis of the low-mass stars can still be interesting when analysing SN remnants.

The more massive stars between 12 $M_\odot$ and 30 $M_\odot$ are responsible for most of the nucleosynthesis output of CCSNe. The abundance pattern is consistently solar and there is a deficiency of iron-group elements in comparison to the solar abundance patterns (Lodders, 2003). The deficiency is also found for the low-mass stars and actually desired to allow for a contribution by Type-Ia SNe. Above 30 $M_\odot$ only a few explosions were found, but

---

[*] Conducted by the Santa Cruz group, Tuguldur Sukhbold, S. E. Woosley, and Justin M. Brown

still these stars add the mass of their winds during stellar evolution to the nucleosynthesis yields even if they form a BH. The entire range from 9 to 120 $M_\odot$resembles the solar abundance pattern well and also shows similarities to the earlier survey by Woosley & Heger (2007). The exceptions of the resemblance allow for drawing some conclusions about stellar evolution, e.g. that the mass-loss rates might be too high.

The typical SN in our simulations results in a light curve of Type IIP with hydrogen in the spectra and a plateau in the time evolution of the bolometric luminosity. This is expected, because most of the stars in our combined set are red supergiants with a massive hydrogen envelopes. The exploding models above 30 $M_\odot$ produce a variety of Type Ibc SNe, because they lost their hydrogen due to mass loss during their evolution. But the resulting light curves of these stars are too faint and too broad if compared to observed light curves. These stars do not pose the common class of Ibc SNe, either because we missed exploding stars between 30 and 40 $M_\odot$, or stars with lower ZAMS-mass lost their hydrogen envelopes by binary interaction. The latter is more likely as an explanation (Dessart et al., 2011, Eldridge et al., 2013).

6.2. Comparison to Ugliano et al. (2012)

Here, we will compare our results to the previous study of Ugliano et al. (2012), who employed an earlier version of HOTB. The code was updated in a few aspects in our work: A high-density equation of state, the L&S by Lattimer & Swesty (1991) was implemented to achieve a more realistic behavior of the PNS. We also implemented the deleptonization scheme (see Sect. 3.3.1) enabling us to follow the core collapse of a progenitor model up to core bounce. We can now use HOTB for all phases of the explosion, from the onset of iron-core collapse beyond the point of shock break-out through the surface of the star. Before these improvements were available, calculations of core collapse were run with a different code (PROMETHEUS-VERTEX by Rampp & Janka, 2002).

For the comparison, we assess the same set of progenitor models, the s2002 set by Woosley et al. (2002), and the same calibration model for SN 1987A, a red supergiant with a ZAMS mass of 19.8 $M_\odot$. We had to re-calibrate our core-cooling model to obtain the observable signatures of SN 1987A for the improved physical modeling. The same core parameters as in the previous study would yield under-energetic explosions (Ertl, 2012).

6.2.1. Zero-Age Main-Sequence Mass Outcome Pattern

Fig. 6.4 shows our results for the calibration models s19.8 and z9.6. The results of all other calibration models are available in Sect. B.2. A compilation of the results of Ugliano et al. (2012) is displayed in Fig. 5 of their work.

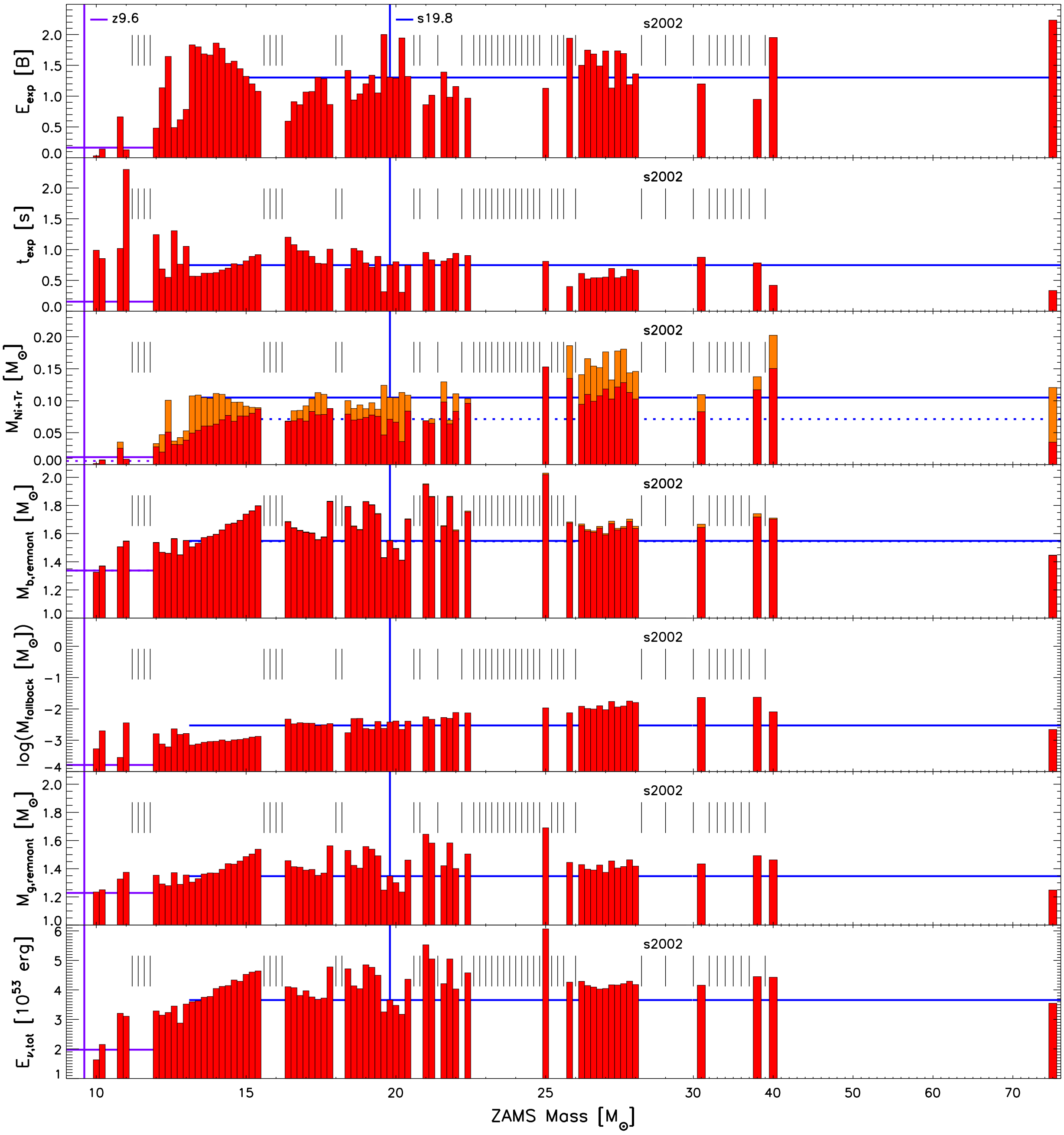

Figure 6.4.: Same as Fig. 6.2, but for the model set s2002 simulated with the s19.8 calibration combined with the z9.6 calibration for low-mass stars.

Overall, our results confirm the ZAMS-mass dependent explosion behavior that was found by Ugliano et al. (2012). For the same explosion calibration, this progenitor set and the newer s2014 models have basic features in common. Moreover, for all calibration cases we observe the same patterns of successful explosions alternating with BH formation events above $\sim 15\,M_\odot$.

Concerning FBH SNe, the previous study found a single case, the 37 $M_\odot$ model. The same model does not explode in our updated setup. Nevertheless, we find some FBH cases in our setup for some calibrations either above 30 $M_\odot$ for the n20.0 and at the edge of the explosion region around 28 $M_\odot$ for the w18.0 and w15.0. We find FBH SNe in a similar ZAMS-mass regions in the combined set of progenitor models assessed in the previous section. Furthermore, we find fewer successful explosions in the regime above 30 $M_\odot$ for all calibrations in comparison to the previous study. The reason might be, either a more powerful engine resulting from the calibration procedure of the previous study or the systematic perturbation of the progenitor models. The perturbation of the progenitor models results in an altered mass-accretion rate compared to our simulations. A transient phenomenon is the consequence, which is connected to the different physics used in PROMETHEUS-VERTEX and Ugliano's version of HOTB (see Sect. 3.4 in Ertl, 2012, for details). Still some stars explode above 30 $M_\odot$. For example the 40 $M_\odot$ explodes robustly with all calibrations except for the w20.0. The solar models of the combined set discussed in the last section do not show explosions in this mass range (part of the s2007 set). The different outcomes are connected to the systematically different core structures of the models in this regime. A comparison of the differences of the two model sets are given by Sukhbold & Woosley (2014). Fig. 1 of the latter work compares the compactness parameter evaluated for the innermost 2.5 $M_\odot$ of both sets (see Eq. 5.1 in Sect. 5.1). It shows that the s2002 model set has more compact cores, which is different from the s2007 model set in this regime and is also true for higher masses. The 75 $M_\odot$ model explodes robustly with all calibrations in our setup, although it shows a high compactness value (see Chap. 5). In consequence there is no high-mass boundary for BH formation and successful explosions in the s2002 set. Note that the 75 $M_\odot$ model was not studied by Ugliano et al. (2012).

6.2.2. Low-Mass Progenitor Models

The low-mass progenitors are simulated here employing the interpolation between Crab-like and SN 1987A-like models. We apply the low-mass calibration for models below 13.0 $M_\odot$ and find that they yield lower explosion energies and nickel ejecta masses in comparison to the previous study. This is the desired behavior and it follows what is found by observations and self-consistent simulations (see Sects. 2.3 and 4.1.4). We also find that some of these low-mass models might not explode at all. Progenitors in the mass range from 11.2 to 11.8 $M_\odot$ implode and form BHs. The 11.2 $M_\odot$ model, most prominently, was also explored by self-consistent simulations in axial symmetry (2D) and without symmetry constraints (3D) (Tamborra et al., 2014, and references therein). The 2D simulations revealed explosions, while the 3D equivalent did not show successful revival of the stalled shock. This demonstrates that the low-mass models are possibly ambiguous in their outcome and also that they are at the brink of explosion. A slightly increased energy deposition by neutrinos behind the shock might explode these stars.

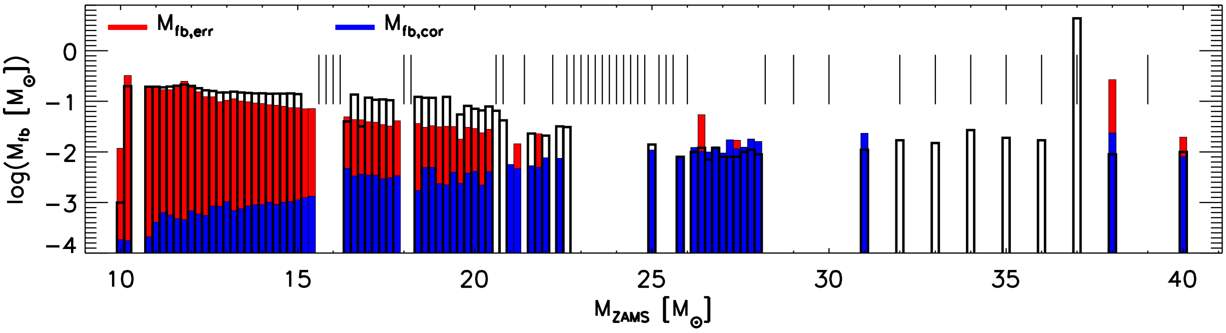

Figure 6.5.: Fallback masses for all progenitors investigated by Ugliano et al. (2012). The white histogram bars display the results of Ugliano et al. (2012). The red bars show our results from simulations with modeling improvements in various aspects (but with the same $19.8\,M_\odot$ red supergiant model for the SN 1987A calibration case), also applying the incorrect fallback estimate of Eq. (6.1). The blue histogram bars display the fallback masses as computed with the correct fallback determination according to Eq. (6.2). The vertical lines in the upper part of the plot indicate non-exploding cases obtained with the improved modeling by Ertl et al. (2016a). Note that for better comparison with Ugliano et al. (2012) the models reported in this plot do *not* include the calibration of the low-mass explosions with the Crab-like progenitor.

6.2.3. Late-Time Fallback*

A further difference between our study and the one by Ugliano et al. (2012) is the mass that implodes after the neutrino-driven wind ceases, the so-called fallback mass. In the previous study, an erroneous interpretation of the hydrodynamical results led to an incorrect determination of the mass. This also affects the neutron star masses provided in that study, but only to a minor extent. The problem was already addressed and corrected in the follow-up works by Ertl et al. (2016a) and Sukhbold et al. (2016). We will present the differences of the old and new fallback results in detail and explain the origin of the mistake in the original analysis by Ugliano et al. (2012).

The fallback masses obtained by Ugliano et al. (2012) are displayed in Fig. 6.5 by white histogram bars. The red bars show the fallback masses determined for the same progenitor set with our improved modeling and the same *incorrect* fallback criterion as applied by Ugliano et al. (2012). The results basically agree, and a tendency of higher fallback masses for lower-mass progenitors is present in both data sets. The quantitative differences are a consequence of improvements of some modeling aspects and the re-calibration of the core-cooling model for the s19.8. The blue histogram bars represent the fallback masses as determined with a *correct* evaluation of the fallback for our models. The correct values are

---

*This section is already published in Ertl et al. (2016b), yet updated and adjusted to fit to the narrative of this work.

considerably smaller in particular for progenitors below $\sim 20\,M_\odot$. The trend of increasing fallback masses for less massive stars is inverted to the opposite behavior.

The reason for the error in the fallback analysis by Ugliano et al. (2012) can be understood from the dynamics plotted in Fig. 6.6. After the subsiding of the neutrino-driven wind (on a timescale of 10–20 seconds after bounce), gas in the inner regions of the exploding star is decelerated by the gravitational pull of the neutron star and flows back inwards. This leads to fallback with a rate that peaks at some ten seconds post bounce and decreases afterwards according to a power law ($\propto t^{-5/3}$).

On a timescale of days to weeks, the reverse shock created when the supernova shock passes the helium-hydrogen interface, propagates towards the center of the exploding star. Moving backward through the inner layers of the star, the reverse shock accelerates the inward motion of the gas. At the same time, it compresses and the shock heats the gas, raising its pressure by $2-3$ orders of magnitude. When the reverse shock leaves the computational domain through the inner grid boundary, which is treated as an open (outflow) boundary with a radial location of typically 10^{10} cm during these late stages of the evolution, the gas has negative (supersonic) velocities in a large volume of the star (Fig. 6.6). Shortly afterwards, however, the inflow of the stellar matter is reversed and a strong outward moving shock develops.

Ugliano et al. (2012) calculated the fallback mass by taking the sum of all gas mass that had fallen through the inner grid boundary at this “reflection time”, t_r, plus an estimate of additional fallback that will be added later from the mass that has been accelerated inward by the reverse shock. For this latter contribution they took the arithmetic average of the mass at time t_r with negative velocities and the mass with velocities smaller than the escape velocity v_esc (in all cases these two masses were nearly identical):

$$M_\mathrm{fb,err} = \int_0^{t_\mathrm{r}} \mathrm{d}t\,\dot{M}_\mathrm{ib}(t) + 0.5\,\left[M_{v<0}(t_\mathrm{r}) + M_{v<v_\mathrm{esc}}(t_\mathrm{r})\right]\,. \tag{6.1}$$

The values of the fallback mass thus obtained are close to the local, late-time maxima of the red lines in the upper two panels of Fig. 6.6. Applying this recipe, Ugliano et al. (2012) erroneously assumed that the dynamical evolution as computed for $t > t_\mathrm{r}$ is not trustworthy, because they interpreted the outward going wave as a consequence of a reflection of the reverse shock at the inner grid boundary and therefore as a numerical artifact caused by the presence of this boundary.

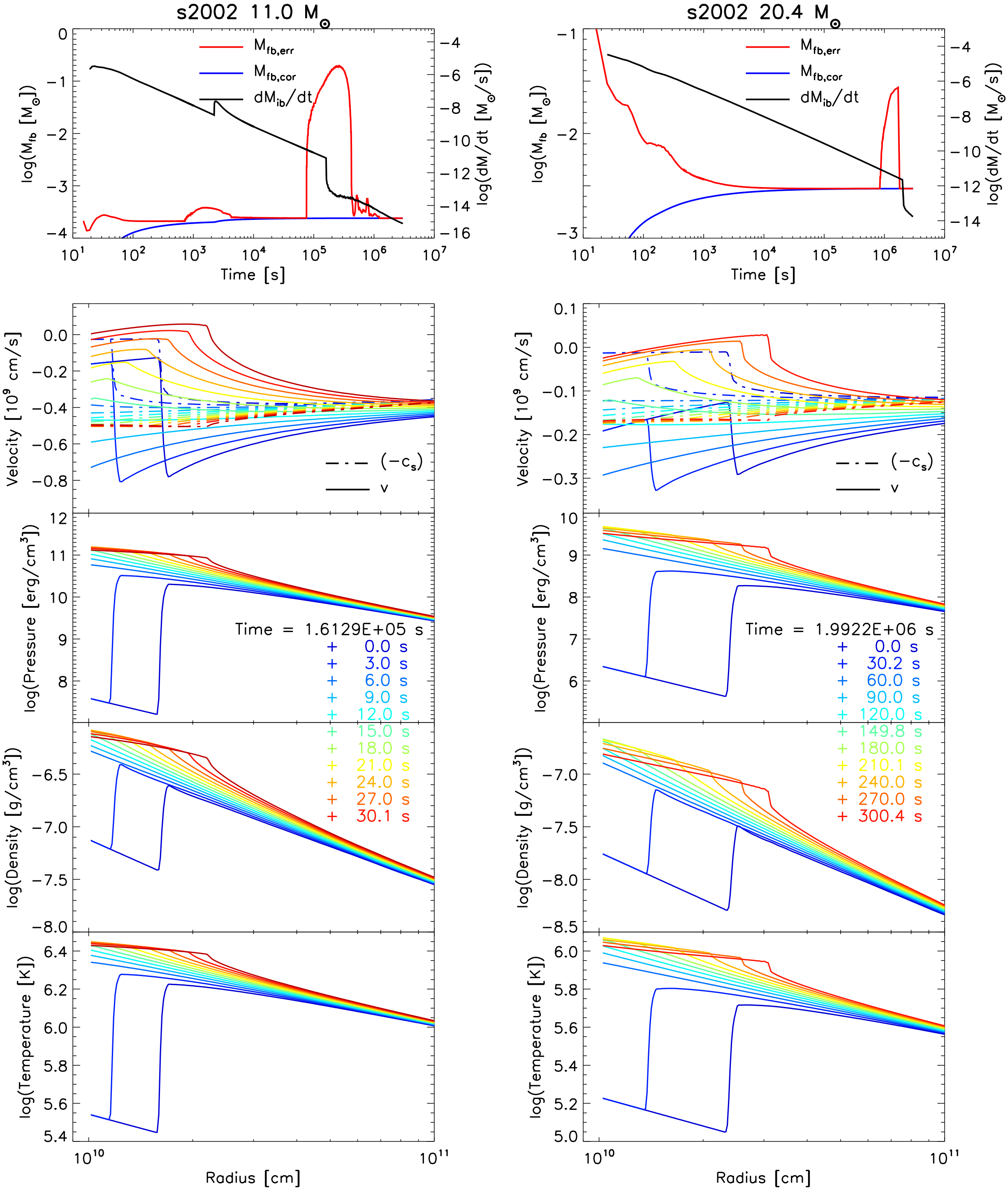
s2002 11.0 M$_\odot$
s2002 20.4 M$_\odot$
M$_{fb,err}$
M$_{fb,cor}$
dM$_{ib}$/dt
log(M$_{fb}$ [M$_\odot$])
log(dM/dt [M$_\odot$/s])
Time [s]
Velocity [10^9 cm/s]
(−c$_s$)
v
log(Pressure [erg/cm^3])
Time = 1.6129E+05 s
0.0 s
3.0 s
6.0 s
9.0 s
12.0 s
15.0 s
18.0 s
21.0 s
24.0 s
27.0 s
30.1 s
Time = 1.9922E+06 s
0.0 s
30.2 s
60.0 s
90.0 s
120.0 s
149.8 s
180.0 s
210.1 s
240.0 s
270.0 s
300.4 s
log(Density [g/cm^3])
log(Temperature [K])
Radius [cm]
10^{10}
10^{11}

Figure 6.6.: Fallback and dynamical evolution of two exemplary explosion simulations for an $11.0\,M_\odot$ progenitor (*left*) and a $20.4\,M_\odot$ case (*right*). The *upper panels* display the total fallback mass as a function of time. The red line gives the incorrect result applying the rhs of Eq. (6.1) at all times. The "reflection time", t_r, is at about the instant of the late, local maximum of the red curve. The previous, incorrect estimate of the fallback mass (Eq. 6.1) corresponds to a value close to this maximum. The rising blue line shows the correct evaluation according to Eq. (6.2), the black line with the decaying trend depicts the corresponding mass-accretion rate, $\dot{M}_\mathrm{ib}$. The temporary increase of $\dot{M}_\mathrm{ib}$ in the $11.0\,M_\odot$ model at $\sim$2000 s is connected to the inward acceleration of matter by the first reverse shock that is created when the supernova shock passes the carbon-helium interface. The sets of *lower panels* display velocity (v; solid lines), adiabatic sound speed (c_s; dash-dotted lines), pressure, density, and temperature profiles (*from top to bottom*) for selected points in time around the "reflection time".

A detailed, time-dependent analysis, however, reveals that this interpretation was not correct (see Fig. 6.6). The infalling reverse-shock heated matter is decelerated because of the steepening of the negative pressure gradient ceased by the geometrically focussing. The deceleration produces a wave that begins to move outwards again and steepens into a shock front when the expansion velocity exceeds the local sound speed. This happens well after the reverse shock has left the grid, at which time no numerical artifact is created (in fact, such an artifact would not be able to travel into the computed volume because the postshock flow streams to the boundary with supersonic speed). The "reflection wave" is therefore *not* a numerical artifact but a physical phenomenon, in which the contracting stellar mass itself reverses its infall. Tests with smaller radii for the location of the inner grid boundary (e.g., 5×10^8 cm or 10^9 cm) show exactly the same dynamical behavior. The correct evaluation of the fallback is therefore a simple time integral of the mass flow rate through the inner boundary:

$$M_{\mathrm{fallback}} \equiv M_{\mathrm{fb,cor}} = \int_0^\infty \mathrm{d}t\, \dot{M}_{\mathrm{ib}}(t)\,. \tag{6.2}$$

6.3. Further Sets with Solar Metallicity

s2007

We did not only simulate the high-mass end of the s2007 as part of the combined model set (see Sect. 6.1) but the full provided ZAMS-mass range (see Figs. B.10 − B.14 in the Appendix B). The stellar evolution of the models is calculated with Kepler and should be similar to the s2014 set, both employing the latest physics. The ZAMS masses range from 12 to 120 $M_\odot$ with a very coarse binning of at least 1 $M_\odot$. The 12 $M_\odot$ model is the only progenitor star where we apply a reduced core contraction based on the Crab-like calibration. The coarse ZAMS-mass binning obscures the irregular pattern of explosions and implosions, which is clearly visible for the finer-binned s2014 set. This model set demonstrates that a fine ZAMS-mass binning is crucial to get a comprehensive picture of the possible outcomes with ZAMS mass.

n2006

The n2006 (Nomoto et al., 2006) models are the only set of progenitors that are not evolved with Kepler through their stellar evolution, which makes them very interesting. Unfortunately, there are only eight progenitor models between 13 and 50 $M_\odot$ with solar metallicity. None of the models is a Crab-like model. In consequence, we only applied the SN 1987A engines. The results are displayed in Figs. B.16 − B.20 in the Appendix B. The set of models shows cases of successful explosions up to 25 $M_\odot$ for all calibrations except for the w20.0, where we find explosions only up to 20 $M_\odot$. In the high-mass regime, the 50 $M_\odot$ progenitor is the only exploding model, but it explodes robustly with all calibrations and it forms a BH by late-time fallback for the w18.0, w15.0, and w20.0 calibration. Again, the most massive star of the set is an exploding model as already found in the s2002 and s2007 series and it also proves that FBH SNe are not a peculiarity of KEPLER models and occur in other model sets as well. We cannot conclude on whether the modeling approach by Nomoto et al. (2006) shows a continuous behavior of the outcome with ZAMS mass or whether the ZAMS-mass grid is too coarse to see an irregular, KEPLER-like outcome pattern.

6.4. Sets of Models with Sub-Solar Metallicities

Why are sub-solar metallicities interesting? Stars in the LMC have metallicities less than solar and the SN 1987A was hosted by this galaxy. Also SNe observed in distant galaxies, occurred earlier in the history of the universe and they are therefore likely less metal-enriched. The argument is different for metal-free stars, because they are not produced in the present universe (nothing is metal-free) and, consequently, cannot be observed directly. These stars were the first population of stars (Pop III) and also the first stars to pollute the universe with heavy elements, which is a possible observable signature, e.g. in the spectra of very metal-poor stars.

Only a few model sets with sub-solar metallicity are available and can be employed in the work at hand. We will focus on the z2011 set of metal-free stars, because it has a dense ZAMS-mass binning (down to 0.1 $M_\odot$) and it includes the latest physics (Heger & Woosley, 2010). Furthermore, we will employ the u2002 set for ultra-metal poor (10^{-4} solar) stars, because it is the only set available with a metallicity between solar and metal-free. The u2002 has also a sufficiently fine ZAMS-mass grid with progenitor models at every 0.2 $M_\odot$ up to 60.0 $M_\odot$and an additional model at 75.0 $M_\odot$.

The main effect of metallicity is that it drives the mass-loss of a star by a wind from its surface* reducing its mass compared to its birth mass. Consequently, stars with solar metallicity show strong mass loss, while metal-poor or metal-free stars roughly conserve their ZAMS mass (Woosley et al., 2002). In a simple understanding of stellar evolution, metallicity influences stellar evolution processes and, in turn, determines the structure of a massive star when it dies. The most prominent structural signature (apart from the final mass) is the color of the star. Solar-metallicity stars die as red supergiants, while most of the metal-poor and metal-free stars are blue supergiants at the onset of collapse. Due to the lack of mass-loss in low-metallicity stars, the binding energy of the outer shells above the iron core increases linearly with increasing ZAMS mass. In contrast, the binding energy

---

[*] There are other processes of mass loss like pulsations (the only case is the 100 $M_\odot$ of z2011), binary evolution, and rotation, which are not considered by the work at hand.

outside the iron core of solar-like stars is limited by mass loss (cf. Fig. 19 in Woosley et al., 2002).

This massive mass-loss is the main reason why we cannot find a ZAMS-mass limit for BH formation for the solar-metallicity stars. Even the 120 $M_\odot$ model of the combined solar set explodes robustly except for the w20.0 calibration. This is also true for all the other solar-metallicity model sets: the 75 $M_\odot$ model of the s2002 explodes as well as the 50 $M_\odot$ model from the n2006 sample (although most of the times as FBH SN).

In contrast to the solar-metallicity stars, we can determine a boundary for BH formation of the sub-solar sets. If we take a look at the outcome pattern displayed in Fig. 6.7 for the ultra-metal poor stars of the u2002 series, we can determine a robust ZAMS-mass boundary for BH formation of $\sim 27\,M_\odot$ with exception of the weak w20.0 engine. The metal-free stars behave slightly different concerning their outcome systematics, which is displayed in Fig. 6.8. But we can still identify a limit for successful explosions in a ZAMS-mass interval of $26 - 27\,M_\odot$. The limit for successful explosions clearly correlates with the strength of the engine. Yet, if we are concerned with a BH-formation boundary, we have to consider cases of massive late-time fallback, which turn successful explosions with a NS formed into BHs. The BH boundary is therefore around a ZAMS mass of $\sim 27\,M_\odot$ for the strongest engines, s19.8 and n20.0, $\sim 26\,M_\odot$ for the intermediate engines, w18.0 and w15.0, and only $\sim 19\,M_\odot$ for the w20.0 calibration model.

Figures 6.9 and 6.10 show the results for the u2002 and the z2011 sets, respectively. These figures are similar to Fig. 6.2 for the combined solar series. The results displayed in all of the mentioned figures are for the w18.0 calibration and we will use this calibration for the comparison of the three metallicities – solar, ultra-metal poor, and primordial. The explosion energies up to $15 - 16\,M_\odot$ show a similar trend, they increase initially up to $\sim 15\,M_\odot$ (with exceptional cases) and decreases again up to a BH-formation boundary. What follows up to around $\sim 23\,M_\odot$ is a region of strong fluctuations due to the similarly fluctuating core structure. As a side note, this is the reason why Heger & Woosley (2010) increased the ZAMS-mass binning for the z2011 series in the regions with high fluctuations of the core structure prior to collapse. In the mentioned regime, high explosion energies ($\sim 2\,$B) follow cases with low explosion energies or failed cases within narrow ZAMS-mass intervals. This behavior can be found in all sets regardless of the metallicity, although the u2002 series contains more successful explosions with typically higher energies (compare the ZAMS-mass range between 16.0 and 17.0 $M_\odot$). For z2011, we find the opposite. The metal-poor models result in the least energetic explosions of all sets. For higher ZAMS mass, we find an “island of explodability” around $25 - 27\,M_\odot$ for all metallicities, following a region of nearly pure BH formation. The “island” is slightly smaller for the primordial stars.

The nickel ejecta masses are correlated with the explosion energy and show similar trends, although the large fallback masses in the z2011 remove all of the nickel of many successful explosions. All in all, the ultra-metal poor series behaves like the combined solar set up

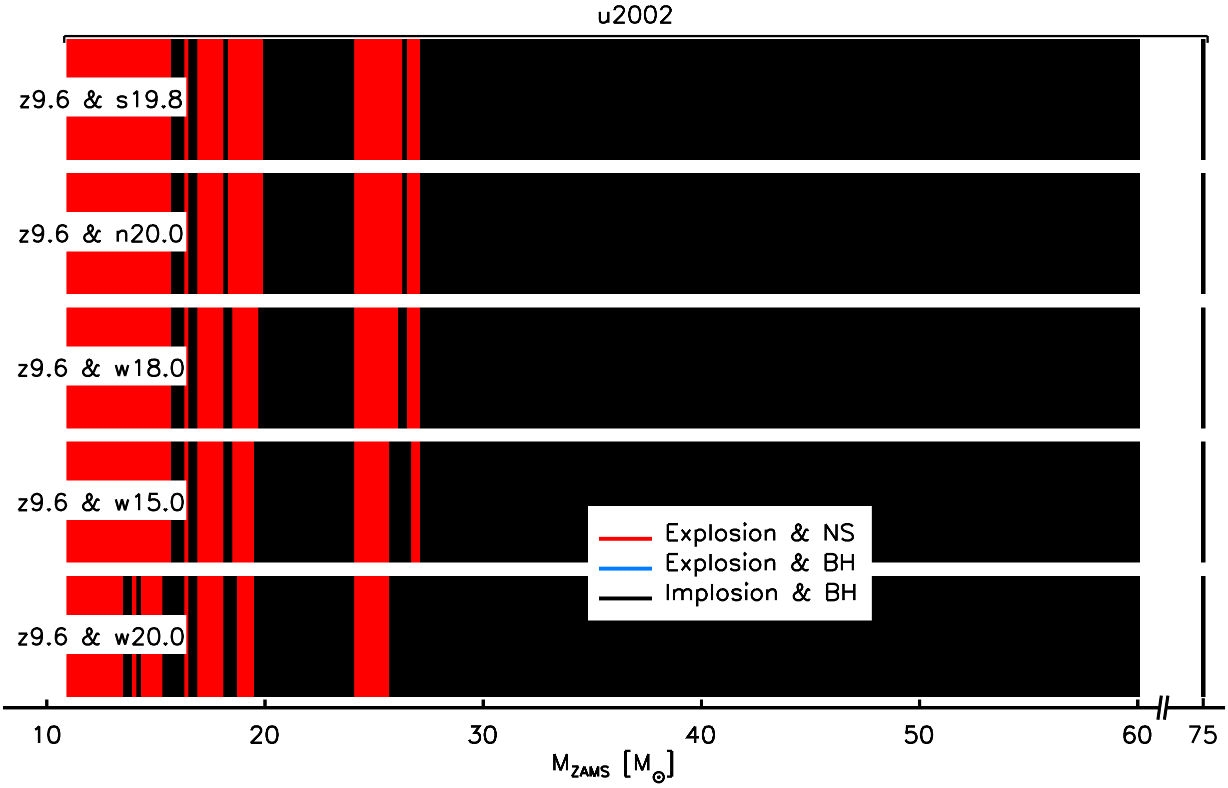

Figure 6.7.: Outcome systematics for the ultra metal-poor progenitor models of the u2002 series. Each row depicts the results for a certain calibration and they are sorted by the number of explosions starting with the one that yielding the most at the top. Unsuccessful cases, without revival of the stalled shock, are marked by a black bar, while cases of successful shock-revival forming a NS or a BH are by a red and a blue line, respectively. The ZAMS-mass interval of the progenitor models is $0.2\,M_\odot$ starting at $11.0\,M_\odot$up to the cut-off mass of $75\,M_\odot$, but with a gap between $60.0\,M_\odot$ and $75.0\,M_\odot$. Note that we do not find any cases of BH formation by late-time fallback (FBH SNe) regardless of the employed calibration in this set.

to $\sim 27\,M_\odot$. Above this ZAMS mass, strong mass-loss of the solar models yields further successful explosions, while all sub-solar models form BHs. This is a behavior already expected by stellar-evolution studies based on the high binding energies of the outer layers (e.g., Woosley et al., 2002). The argument is slightly different for our simulations, because the high-mass models of the sub-solar sets do not even show successful shock-revival due to their core structure. These stars can be found to the upper right corner of the cloud of models in the two-parameter plane way above the separation line (left panel of Fig. 5.6).

After the assessment of the combined solar set and its low-mass Crab-like models, we conclude that interpolating between the w18.0 and the z9.6 is sufficient to capture the systematics of the outcome of these stars. All stars exploded and the calibration only affects the low ZAMS-mass end, $M_{\mathrm{ZAMS}} < 12\,M_\odot$. The s2002 series already revealed

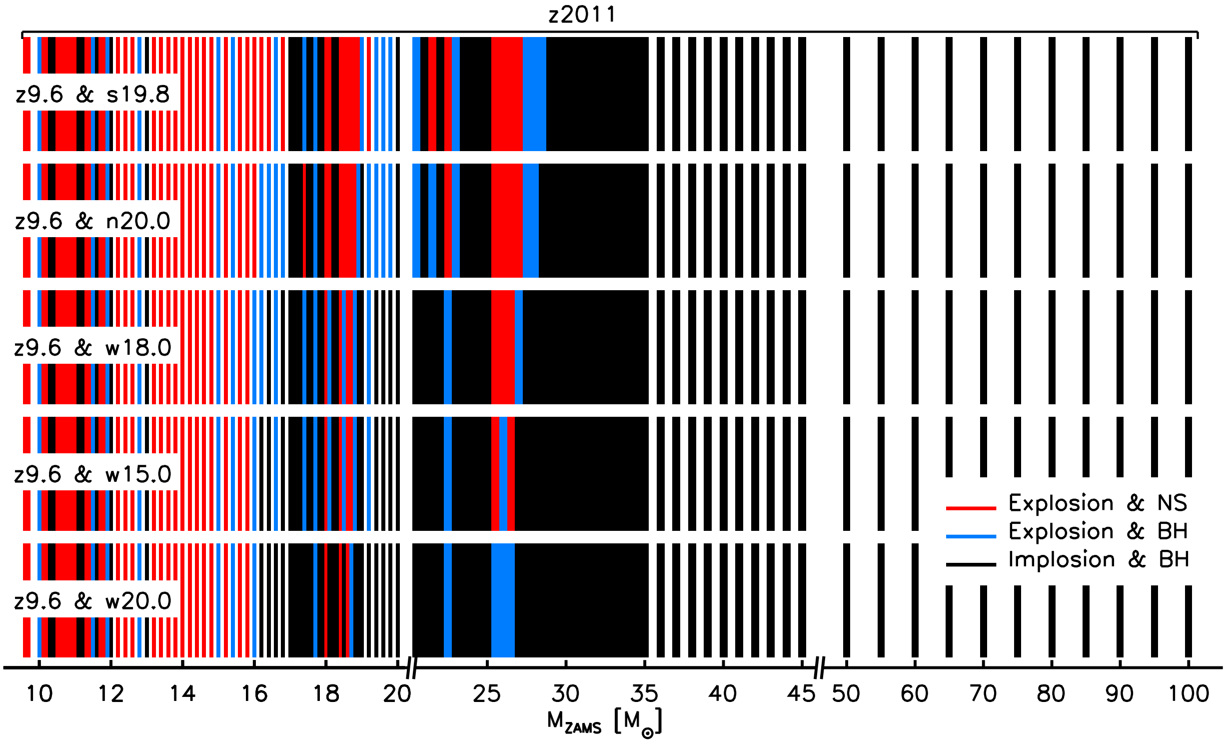

Figure 6.8.: Outcome systematics for the primordial stars of the u2002 series. Each row depicts the results for a certain calibration and they are sorted by the number of explosions starting with the one that yielding the most at the top. Unsuccessful cases, without revival of the stalled shock, are marked by a black bar, while cases of successful shock-revival forming a NS or a BH are by a red and a blue line, respectively. The ZAMS-mass intervals of the progenitor models are 0.1 $M_\odot$ starting at 9.6 $M_\odot$ up to 12.0 $M_\odot$, 0.2 $M_\odot$ up to 17.0 $M_\odot$, 0.1 $M_\odot$ up to 19.0 $M_\odot$, again 0.2 $M_\odot$ up to 20.0 $M_\odot$, 0.5 $M_\odot$ up to 35.0 $M_\odot$, 1.0 $M_\odot$ up to 45.0 $M_\odot$, and 5.0 $M_\odot$ up to the cut-off mass of 100.0 $M_\odot$.

that some of the Crab-like models might not explode at all (see Sect. 6.2). The z2011 set now demonstrates that FBH SNe are possible and that additional models with higher masses (15.2, 15.4, and 15.6 $M_\odot$) have Crab-like M_{3000} cores. Future work should therefore interpolate separately for each SN 1987A calibration in case of the low-mass models.

One might argue that the combined solar set as well as the primordial set z2011 are evolved with the latest physics, while the ultra-metal poor set is not. But if we recall the comparison of the solar set s2002 with the combined solar set, we find little qualitative differences in their behavior with exception of the 30−40 $M_\odot$ mass range (see Sect. 6.2). Concerning the FBH SNe, we find that s2002 as well as the combined set show such cases for masses $M_{\mathrm{ZAMS}} > 27\,M_\odot$.

For the metal-free models, we find a very similar pattern, if we compare z2002 (see Figs. B.30 − B.34 in the Appendix B) and the recent set of primordial stars z2011. The

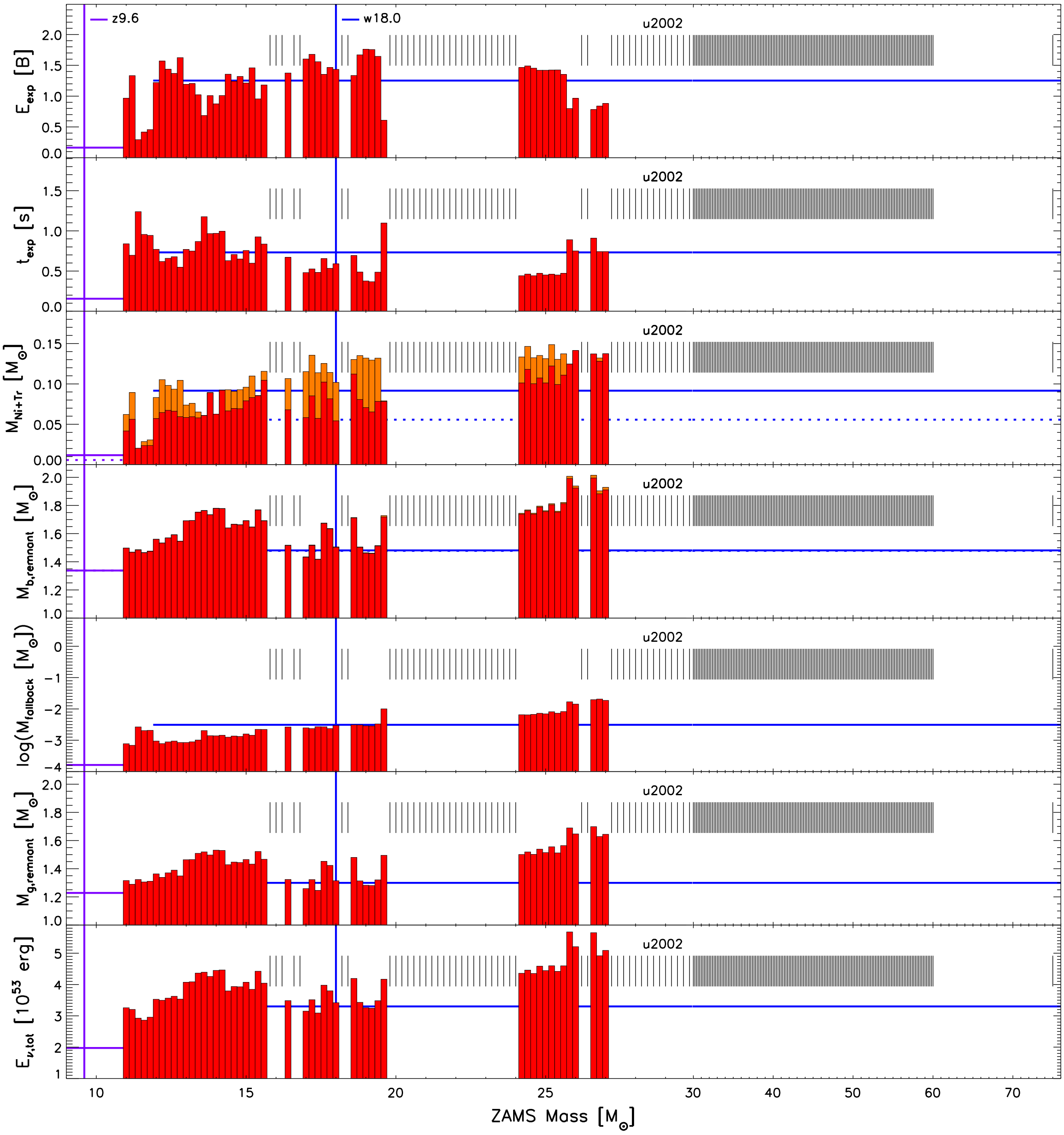

Figure 6.9.: Same as Fig. 6.2. The model series is u2002 with 10^{-4} solar metallicity, simulated with the z9.6 and n20.0 calibrations. The z9.6 calibration is applied up to and including the 11.8 $M_\odot$ star.

coarse grid of z2002 with its 1 $M_\odot$ binning might be problematic for comparing the two sets, but we find a high number of FBH SNe in z2002 and they are also similarly distributed as in the z2011 set. We can conclude that the z2002 series behaves similar compared to the more recent z2011 series. One would expect that the same is true for a new ultra-metal

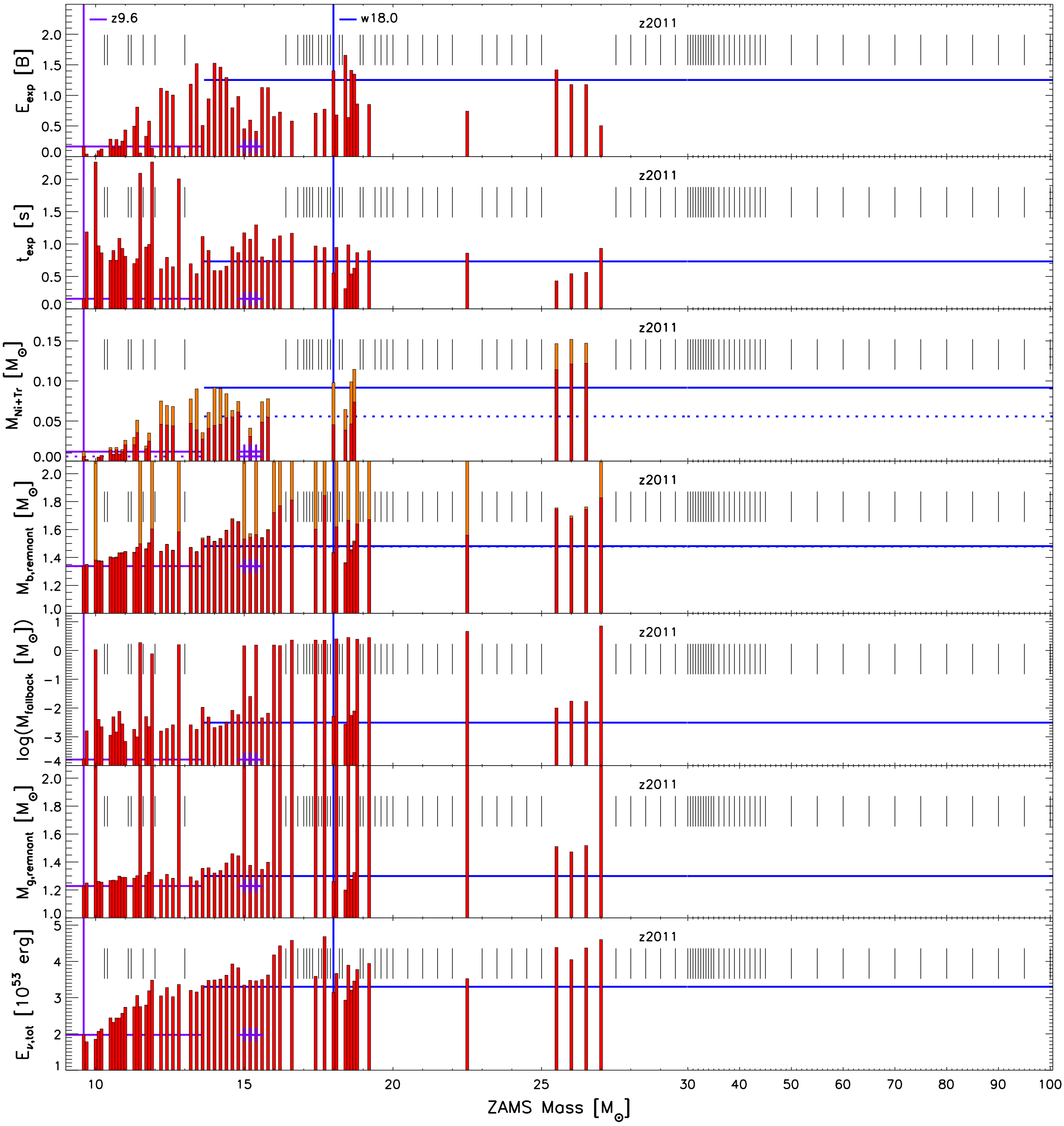

Figure 6.10.: Same as Fig. 6.2. The model series is z2011 with primordial metallicity, simulated with the z9.6 and w18.0 calibrations. A violet cross marks models that are also simulated with the z9.6 calibration, but are separated in ZAMS mass from the continuum of the low-mass models.

poor set if it were recomputed with the latest physical modeling.

6.5. Conclusions

Firstly we discussed the findings that were already published in the collaborative work Sukhbold et al. (2016). We analyzed the explosion systematics of a combined set of massive stars with solar metallicity. The progenitor models were selected to obtain a dense ZAMS-mass binning and were evolved employing the latest physical modeling (Woosley et al., 2002, Sukhbold & Woosley, 2014, Woosley & Heger, 2015). The set of progenitors was simulated with the approach discussed in Chaps. 2 and 3. All available calibration models were employed, the z9.6 for the Crab-like stars and w15.0, w18.0, w20.0, n20.0, and s19.8 for the SN 1987A-like stars, while only the latter of the SN 1987A calibration models is a red supergiant and all others are blue supergiants. Details on the calibration procedure can be found in Chap. 4.

The different calibrations resulted in a different number of exploding stars, with the following ordering for their strength: s19.8 was the strongest engine, followed by n20.0, w18.0, w15.0, and w20.0. Nevertheless, all calibration models except w20.0 showed only little variability in the outcome, which is an indicator for the robustness of the calibration procedure as well as the fact that the pre-SN structure dominates. A similar outcome pattern was also found by Pejcha & Thompson (2015) and Müller et al. (2016a), but for other sets of solar-metallicity models simulated with Kepler. Our w20.0 calibration, on the other hand, demonstrates that a model can fit well with the observational constraints imposed by SN 1987A and its progenitor star, but fails as an engine. The reason is that it explodes easily resulting in a weak core-model contribution. The small number of exploding models would underproduce especially the light s-process elements (Brown & Woosley, 2013) or would require a higher SN rate than observed. Qualitatively, we find that the outcome depends more on the pre-SN structure than on the employed central engine.

The systematics of explosions and non-explosions revealed continuous NS formation up to around $\sim 15\,M_\odot$, followed by a high variability. Energetic explosions can follow BH formation cases even within narrow ZAMS-mass intervals. Furthermore, we cannot determine a ZAMS mass above which all stars form BHs, but rather "island of explodability in a sea of BH formation" (Sukhbold et al., 2016). We also point out that this is true for all of the investigated sets with solar metallicity and simulated with almost all engines.

Our simulations tool, Hotb, is capable of calculating bulk nucleosynthesis by a fully-coupled α-reaction network. The obtained nickel ejecta masses for all stars correlate roughly with the explosion energies, and we find an even better correlation if we add the tracer material. The explosion energies range from 0.1 B to 2.3 B and the combined ejecta of the nickel and the tracer peak at $\sim 0.15\,M_\odot$. Exploding cases without nickel ejecta correspond to cases where all nickel is consumed by the BH that forms due to massive fallback. There are only a few such cases in the set.

We also added light curves and detailed isotopic explosive nucleosynthesis by post-processing our results with Kepler, but neglecting the neutrino-driven wind contribution. Our study certainly improves earlier piston-driven studies, because we get explosion energies and mass cuts from the simulations with HOTBbased on the core structure, rather than having them as free parameters. We find that some parts of the solar-abundance pattern of elements are not well reproduced, pointing towards inadequate nuclear-reaction rates, mass-loss recipes, or calibrations. The light curves are mostly of typical Type IIP, while the Type Ibc light curves are too broad and faint compared to data reported in the literature. This is an indicator that we should find more explosions in the $30-40\,M_\odot$ range, but more likely that stars with lower ZAMS masses loose their envelopes by binary interaction.

Recently, Müller et al. (2016a) conducted a similar study with an even denser solar-metallicity set. They employed a purely analytical approach complementary to ours, where they followed the different phases of a CCSN: core collapse, the stalled accretion-shock, the onset of the explosion, and the shock expansion phase by the solution of simple ordinary differential equations. The free parameters of their approach were set either by results of numerical simulations or by physical intuition, but also varied to show robustness. They did not calibrate their approach to any observation as we do, but they still find similar trends: For stars in the mass range of $15-20\,M_\odot$ they find considerable variability of the outcome as well as stars that could fit SN 1987A in their explosion energy and nickel ejecta masses. They find the “island of explodability” after many BH formation cases around $\sim 25\,M_\odot$, where we find such an island as well. Unlike us, they find many cases of massive fallback in their set of stars with solar metallicity. We will postpone this discussion to the subsequent chapter, where we will elaborate the fallback question.

We expanded our work and included more progenitor sets with solar metallicity, especially the model series s2002, which was already employed by Ugliano et al. (2012). The latter work conducted their progenitor survey with a previous version of HOTB. A comparison is therefore certainly interesting and led to some critical improvements in the modeling and the analysis of our results. Firstly, we found good agreement of the variety of explosion properties – explosion energies, nickel ejecta masses, and neutrino properties. Also the irregular pattern of explosions and failed SNe persists, which is qualitatively similar to the pattern found in the combined solar set of Sukhbold et al. (2016). SNe with large late-time fallback masses that turn the initially formed NS into a BH (FBH SNe) were found as well in both studies and in all solar sets that we studied. Nevertheless, there was an error connected to the evaluation of the fallback mass by Ugliano et al. (2012). We discussed this issue in Sect. 6.2.3 and the erratum by Ertl et al. (2016b). It originated from an erroneous interpretation of the hydrodynamical results by Ugliano et al. (2012), but was already corrected for in Ertl et al. (2016a) and Sukhbold et al. (2016). The high energetic results for the low-mass stars were the basis for adopting SN 1054 as a second calibration anchor. Now we find decreasing explosion energies and nickel yields towards the low ZAMS-mass end, but this correction also resulted in non-exploding cases in this mass range. Whether the non-exploding cases are problematic is undecided, because results of self-consistent simulations are also ambiguous concerning shock-revival (Tamborra et al., 2014, and references therein).

As already mentioned, we find no boundary mass above which all stars collapse to a BH in any of our solar-metallicity sets. The reason is mass loss, which prohibits the core growth of the most massive stars, allowing for a favorable core structure for shock-revival coinciding with loosely bound envelopes. When we evaluated the simulations for sub-solar metallicity, the model sets show a clear boundary for BH formation, which is typically around $\sim 27\,M_\odot$ and $\sim 26\,M_\odot$ for the ultra-metal poor (u2002) and metal-free stars (z2002 or z2011), respectively. Models with ZAMS masses below the BH-formation limit show a very similar irregular outcome pattern very much like the solar-metallicity models, although we find that the u2002 series results in slightly more energetic explosions, while the z2011 shows the other trend with a lot of weak explosions. The primordial stars, regardless of the employed model set, z2011 or z2002, both show weaker explosions and in addition a high number of FBH SNe. The discussion of this phenomenon is postponed to the next chapter (Chap. 7).

Pejcha & Thompson (2015) applied a semi-analytic approach to determine the onset of the explosion and used analytic arguments to estimated the explosion properties. They employed their modeling approach to the s2002, the u2002, and the z2002 set by Woosley et al. (2002). Their progenitor models are identical to a subset of the progenitor models we employed and they also cover the full metallicity range available: solar, 10^{-4} solar, and metal-free. The latter study is therefore a candidate for comparison. A caveat is certainly that they do not calculate the full hydrodynamical evolution of the shock as it propagates through the star, but they rely on analytic arguments and neutrino-luminosities from 1D simulations of accreting PNSs. The left panel of their Fig. 12 for "parameterization (a)" shows the outcome systematics for the different metallicities. The main differences are that they obtain explosions above $30\,M_\odot$ for non solar-metallicity stars. Based on an analytic argument, they find a similar number of FBH SNe for the metal-poor and the metal-free set. This does not agree with our findings showing no such cases in the metal-poor set, but many in the metal-free set. The stars with solar metallicity behave very much like ours concerning the number of successful explosions and cases with significant fallback (FBH). Other observational properties, explosion energies and nickel masses, of the solar set agree well with Ugliano et al. (2012) as as discussed by the study of Pejcha & Thompson (2015). The low ZAMS-mass progenitors show high explosion energies in their work, even higher than found by Ugliano et al. (2012). Unfortunately, these properties are not provided for the sub-solar model sets.

7. Compact Remnants

We are now going to elaborate on the question, what is left behind by the death of a massive star – a neutron star (NS) or a black hole (BH). The mass and type of the compact remnant is one of the main observables connected to CCSNe. Their masses can be measured if they are part of binary systems, single or double pulsar binaries (see Özel & Freire, 2016, for a recent compilation) and binary systems with one BH (see Wiktorowicz et al., 2014, for a recent compilation). Typically, the observed objects cannot be directly connected to their progenitor stars, because the event that led to their formation happened long ago and the remnant has faded away. We are left with a mass distribution of NSs and BHs largely disentangled from their progenitor systems. The connection between massive stars and compact remnants is therefore ambiguous.* Here we address the question, whether the current massive-star models, provided by stellar evolution calculations and exploded by the neutrino-driven mechanism, are compatible with the observed population of compact objects.

There are three channels for the formation of the compact remnant in our modeling approach: in case of successful shock-revival, a proto-neutron star (PNS) is formed initially in the center of the star. The PNS will cool and constitute the final remnant of the supernova, unless the explosion is not powerful enough (see Sect. 7.2) to unbind most of the envelope of the star. Substantial fallback of material at late times turns the initially-formed NS into a BH (we term these cases "FBH"). Note, that although a BH is formed, some of the envelope is ejected resulting in an observable signature. We can simulate the formation of the late-time fallback by hydrodynamic simulations of the shock expanding through the star and beyond the break-out through the surface for $\sim 3 \times 10^6\,\mathrm{s}$ (for the description of the setup see Sec. 3.4.3).

Apart from these two formation scenarios for a compact remnant, the accretion shock that forms after core bounce might not be revived at all. The outer layers continue to implode, which adds mass to the PNS pushing it beyond the limit for BH formation, which is theoretically unknown, but above $2\,M_\odot$ (Demorest et al., 2010, Antoniadis et al., 2013). The final mass of the BH in this unsuccessful case depends on the structure of the star prior to collapse. If the envelope is only loosely bound, it might be ejected due to the reduction of the gravitational potential by neutrino losses from the core as formulated by Nadezhin (1980). The phenomenon was recently only revisited by Lovegrove & Woosley (2013) with

---

*This is not entirely true, because the binary companion can contain some information about the progenitor of the compact object, e.g. the metallicity.

numerical simulations. We do not conduct numerical simulations of this phenomenon for our models sets is and leave this to future work. In this study, we only consider the two extreme cases for mass ejection alongside BH formation: the complete implosion of the progenitor star without mass ejection resulting in the pre-SN mass being the BH mass. The gravitational mass would needed to be corrected for the neutrino emission of the PNS until it tuns into a BH, which is also left for future work. The other extreme case is the complete ejection of the hydrogen envelope. The ejection of parts of the helium shell is unlikely (Lovegrove & Woosley, 2013), because of its much higher gravitational binding energies. Which of the cases is more realistic, depends on the unknown BH mass limit and the binding energy of the hydrogen shell, which can vary significantly with lower values for red than blue supergiants.

There is another formation channel for BHs, which we cannot realize in our spherical symmetric (1D) simulations: In axis-symmetric (2D) and simulations without symmetry constraint (3D) some material still streams towards the PNS after the explosion is on its way. It is accreted and feeds a neutrino-driven wind. Müller et al. (2016a), for instance, pointed out that these continuous downflows of matter can add mass to the PNS pushing it beyond the BH mass limit after the onset of the explosion alongside inefficient re-ejection. This would also lead to an explosion accompanied by BH formation early on, maybe resulting in different BH masses than the ones found in our simulations. Simulations in full geometry (3D) are indispensable for answering the question, whether this formation channel is possible in nature or solely an artifact of axial-symmetric simulations (2D).

The efficiency of the re-ejection by a neutrino-driven wind is unknown, but Müller et al. (2016a) tried to account for it in their semi-analytical approach. Our spherical symmetric (1D) models cannot follow this phenomenon. Downflows can never accompany outflows. We therefore have to imitate these two simultaneous processes found in self-consistent simulations by two consecutive phases: an extended phase of accretion followed by a strong neutrino-driven wind after the onset of the explosion. Our massive winds add a major constituent of the explosion energy, but this only imitates what continued accretion might do in self-consistent simulations after the onset of the explosion. The final remnant mass,

$$M_{\mathrm{remnant,final}} = M_{\mathrm{NS,t=t_{exp}}} - M_{\mathrm{NS-wind}} + M_{\mathrm{Fallback}}, \tag{7.1}$$

is the initial PNS mass at the onset of the explosion, $M_{\mathrm{NS,t=t_{exp}}}$, reduced by the mass of the neutrino-driven wind, $M_{\mathrm{NS-wind}}$, and finally determined by adding the mass of the late-time fallback. We define an initial mass of the remnant $M_{\mathrm{remnant,initial}} = M_{\mathrm{NS,t=t_{exp}}} - M_{\mathrm{NS-wind}}$, which will be convenient for the following discussion.

7.1. IMF-Weighted Remnant Distributions

The compact remnants of massive stars with solar metallicity have already been discussed in Sukhbold et al. (2016). We will build on the analysis of the latter work by adding the ultra-metal poor set u2002 and the primordial set z2011, thus covering the parameter space in metallicity as well. We will analyze the masses and types of the compact remnants, but restrict the discussion to the calibrations with w18.0 and n20.0.

For the mass distribution of the compacts remnants, we weight their ZAMS masses by the Salpeter initial mass function (IMF; Salpeter, 1955),

$$\mathrm{d}N \propto M^{-\alpha}\mathrm{d}M, \tag{7.2}$$

for each model series where the number of stars in the interval dN and born in a certain mass interval dM is scaled by the mass of the star M to the negative power of the dimensionless parameter α. We will adopt 2.35 for α, the original value given by Salpeter (1955). While the review of Chabrier (2003) argues for a range of values around 2.3.

Table 7.1.: IMF-weighted fractions for the three outcome channels

Calibration	solar[a]			10^{-4} solar[b]			primordial[c]		
Model	NS[d]	BH[e]	FBH[f]	NS[d]	BH[e]	FBH[f]	NS[d]	BH[e]	FBH[f]
z9.6+s19.8	0.736	0.262	0.002	0.589	0.411	0.000	0.598	0.293	0.109
z9.6+n20.0	0.730	0.265	0.005	0.589	0.411	0.000	0.558	0.304	0.138
z9.6+w18.0	0.669	0.329	0.002	0.571	0.429	0.000	0.520	0.383	0.097
z9.6+w15.0	0.644	0.341	0.015	0.554	0.446	0.000	0.513	0.398	0.089
z9.6+w20.0	0.554	0.446	0.000	0.471	0.529	0.000	0.496	0.425	0.079

[a] Combination of s2015 ($M_{\mathrm{ZAMS}} = 9.0 - 13.0\,M_\odot$), s2014 ($M_{\mathrm{ZAMS}} = 13.1 - 30.0\,M_\odot$), and s2007 ($M_{\mathrm{ZAMS}} = 30.0 - 120.0\,M_\odot$). [b] u2002 ($M_{\mathrm{ZAMS}} = 11.0 - 75.0\,M_\odot$). [c] z2011 ($M_{\mathrm{ZAMS}} = 9.6 - 100.0\,M_\odot$). [d] Explosion & neutron star. [e] Implosion & black hole. [f] Explosion & black hole by late-time fallback (FBH).

We list the resulting rates for the three channels for the outcome in Table 7.1. The rate of successful explosions (including FBH cases) is highest for solar metallicity with 55−73 % depending on the calibration, followed by the primordial stars with 51−70 %, and 47−59 % for the metal-poor stars. If we only considered the NS formation rate, the metal-free and the metal-poor would be very similar, and only the solar-metallicity stars would have a higher rate by about ~10 %. The number of FBH cases is small for progenitors with solar metallicity accounting for maybe only one percent of all SNe, while they constitute a large fraction of up to ~10 % in metal-free stars. The reason is that substantial fallback occurs already for very small ZAMS masses (~10 $M_\odot$) in the primordial set, while only stars with masses above ~27 $M_\odot$ show this at solar metallicity.

7.1.1. Neutron Stars

In our modeling approach the neutrino-driven mechanism almost always results in an initial remnant mass, $M_{\mathrm{remnant,initial}}$, below $2.0\,M_\odot$, which can only be increased by fallback. Two types of fallback can be distinguished in our study, visible by a large gap in the obtained fallback masses, M_{Fallback}. There is either little fallback, well below $0.1\,M_\odot$, or massive fallback ranging from $\sim 0.5\,M_\odot$ to $\sim 10\,M_\odot$. The latter cases are FBH SNe, because massive fallback turns the initially formed NS into a BH. We will analyze the mechanism for both types of fallback in the subsequent section, but we will now focus on the consequences for the remnant masses and their distribution.

For the discrimination of the two types of compact remnants, NSs and BHs, we adopt a baryonic mass of $3\,M_\odot$ as crude discriminator. The BH mass limit is theoretically unknown but a lower limit is given by the most massive observed NSs with a gravitational mass of about $\sim 2\,M_\odot$ (Demorest et al., 2010, Antoniadis et al., 2013). Nevertheless, the discrimination between NSs and BHs in our simulations is unambiguous for most compact remnants, because their baryonic mass is either below $2\,M_\odot$ or well above $3\,M_\odot$.

Observations suggest a gap between the most massive NSs (gravitational mass of $\sim 2\,M_\odot$) and the least massive BHs ($\sim 5\,M_\odot$) (Özel et al., 2010, Valentim et al., 2011, Farr et al., 2011, Kreidberg et al., 2012,e.g.,). The studies by Belczynski et al. (2012), Fryer et al. (2012), Pejcha & Thompson (2015), and Müller et al. (2016a) argue in favor of a gap. Ugliano et al. (2012) as well as our work naturally produce the mass gap in the remnant distribution without any further assumptions. The mass gap is connected to the neutrino-driven mechanism by which CCSNe are thought to explode, because shock-revival is only possible as long as the PNS exists and emits neutrinos. Our simulations show that solar-metallicity stars as well as ultra-metal poor stars do not populate the gap , because their fallback masses are either too little or sufficiently large to bridge the gap. In metal-free stars, some cases emerge where massive fallback provides roughly half a solarmass of material, resulting in a small population of compact remnants in the mass gap. We also find some peculiar cases though (low ZAMS-mass non-exploding models), which have low-mass helium cores, e.g. the Crab-like model of the s2002 series with a ZAMS mass of $11.2\,M_\odot$ and a helium-core mass of $2.8\,M_\odot$. If such stars lost all of their hydrogen by the Nadezhin-Lovegrove mechanism their remnant masses would be lower than our baryonic mass limit for BH formation of $3.0\,M_\odot$.

Fig. 7.1 shows the mass distribution of the gravitational NS masses for the different metallicities employing the w18.0 and n20.0 calibration, each supplemented by the Crab-like models. To obtain the gravitational mass of a NS rather than its baryonic mass, we need to correct for the emission of neutrinos. Unlike Sukhbold et al. (2016), we do not adopt the simple, radius-dependent corrections by Lattimer & Prakash (2001), but use the results of our simulations for the properties of the emitted neutrinos. Based on Eq. (5.9), the mass equivalent of the total radiated neutrino energy, $E_{\nu,\mathrm{tot}}$, needs to be subtracted from the baryonic mass of the NS to obtain its gravitational mass. In order to depict the dependency of the mass distribution on the fallback mass, we corrected the baryonic masses of the final remnant, $M_{\text{remnant,final}}$ (black line), as well as the initial remnant mass before fallback, $M_{\text{remnant,inital}}$ (red line, Eq. 7.1), for the neutrino losses. A small inaccuracy is connected to the gravitational masses, because we do not assume any neutrino-losses from the late-time accretion of matter onto the NS. The upper row of the Fig. 7.1 is similar to Fig. 20 of Sukhbold et al. (2016), yet corrected with the formula of Lattimer & Prakash (2001). The figure demonstrates how the NS mass distribution is affected by fallback at late times for each metallicity. The ultra-metal poor stars are basically unaffected and only slightly shifted to higher masses, because there is not a single FBH case (see Table 7.1). The mass distribution for the solar-metallicity set is slightly more affected by fallback, because some stars bridge the gap from NSs and BHs by massive late-time fallback. For the primordial stars though, the effect of fallback is significant on distribution of NS masses, because of the large fraction of FBH SNe. The primordial stars even populate the mass gap by a small fraction. The baryonic masses of BHs resulting from large amounts of fallback range from 2.4 to $\sim 13\,M_{\odot}$and from 3.2 to $7.3\,M_{\odot}$ for star with solar metallicity. All in all, the initial mass distributions before fallback agree quite well with each other and also with the observational data, e.g. comparing masses of the peaks in each distribution. We overlayed the observational data by Özel & Freire (2016) simply by dividing by the total number of observed NSs and summing over bins. Note that we did not correct the observational data for any potential bias, like error bars of the measurements or the fact that all measured NS are part of binaries while our progenitors are single stars. Observationally, one cannot distinguish between young and old NSs. The latter might have accreted mass since their birth in a CCSN and this is a possible explanation for the excess of observed NSs with masses larger than $\sim 1.7\,M_{\odot}$.

7.1.2. Black Holes

BHs are assumed to form in our simulations, if the shock is not revived within $\sim 3\,\text{s}$. Experiments for some sets have shown that revival of the stalled shock does not occur later than $\sim 2.5\,\text{s}$. Fig. 7.2 is similar to Fig. 7.1, but displays the baryonic BH masses instead of gravitational NS masses. The difference of the baryonic mass of a BH and its gravitational mass is given by the energy of the emitted neutrinos until the PNS that exists temporarily has collapsed within its event horizon. The mass difference is unlikely to exceed the binding energy of the maximum-mass NS, which is about $0.3\,M_{\odot}$ (O'Connor & Ott, 2011, Steiner et al., 2013). We can safely neglect this mass difference, especially because the mass ejection connected to the Nadezhin-Lovegrove mechanism is uncertain and potentially amounts to the whole mass of the hydrogen envelope. The eventual ejection of the hydrogen shell is accounted for by differently colored solid lines, with black being the distribution for full ejection and red being the full pre-SN mass of the star collapsing to a BH.

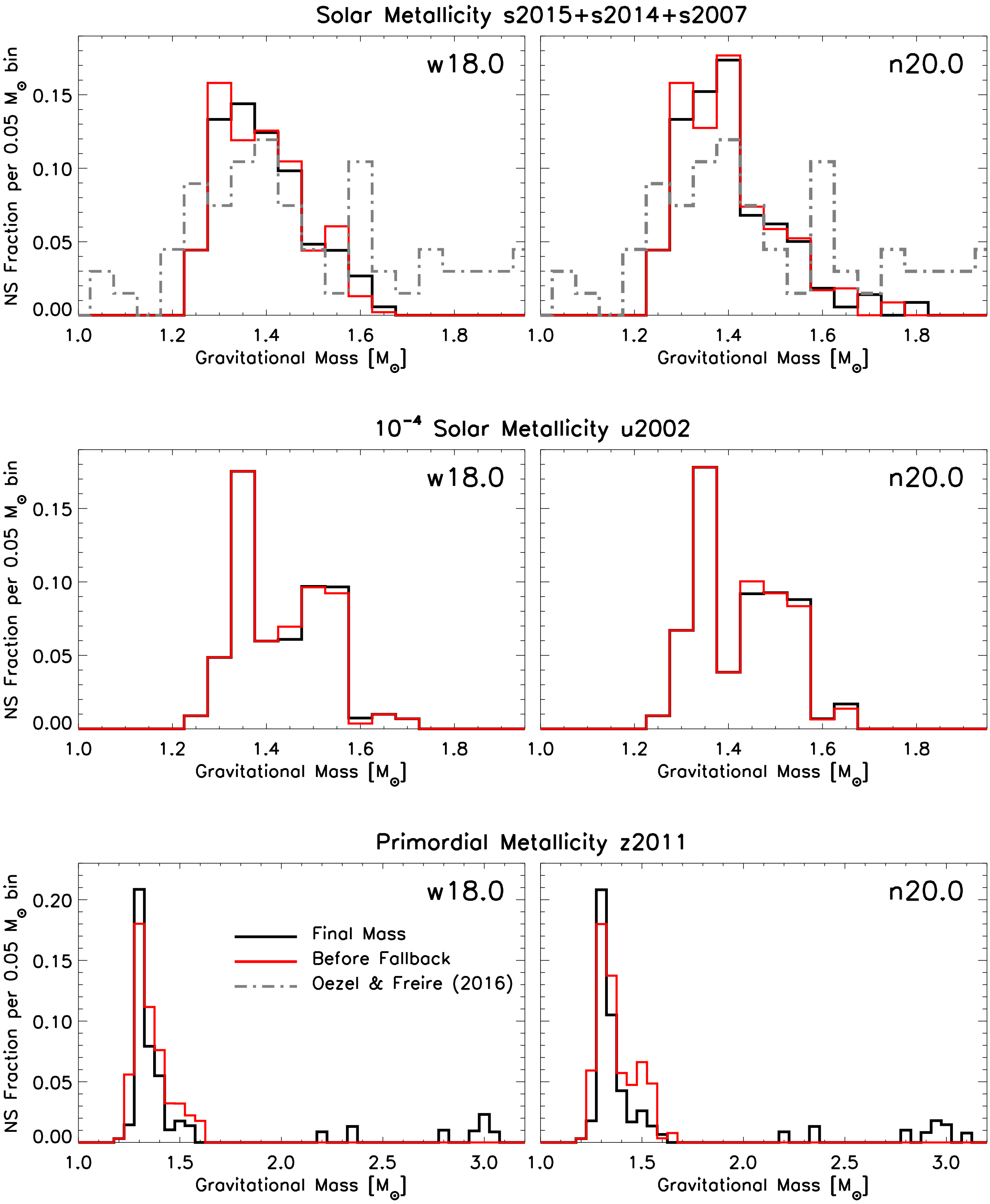

Figure 7.1.: Gravitational NS masses weighted by the Salpeter IMF for the calibration models w18.0 (*left column*) and n20.0 (*right column*) each supplemented with the Crab-like models. The initial masses of the remnants, $M_{\mathrm{remnant,inital}}$ (Eq. 7.1), right after the neutrino-driven wind has ceased, are displayed in *red* and the final remnant mass including fallback, $M_{\mathrm{remnant,inital}}$ (Eq. 7.1), in *black*. The gravitational mass is obtained by subtracting the energy of the neutrino emission, $E_{\nu,\mathrm{tot}}$, from the baryonic mass of the neutron star. Overlayed as *dashed gray lines* is the compilation of observed NS masses by Özel & Freire (2016). Note that the observations are not weighted in any sense (binary evolution, metallicity, observational bias, or error bars).

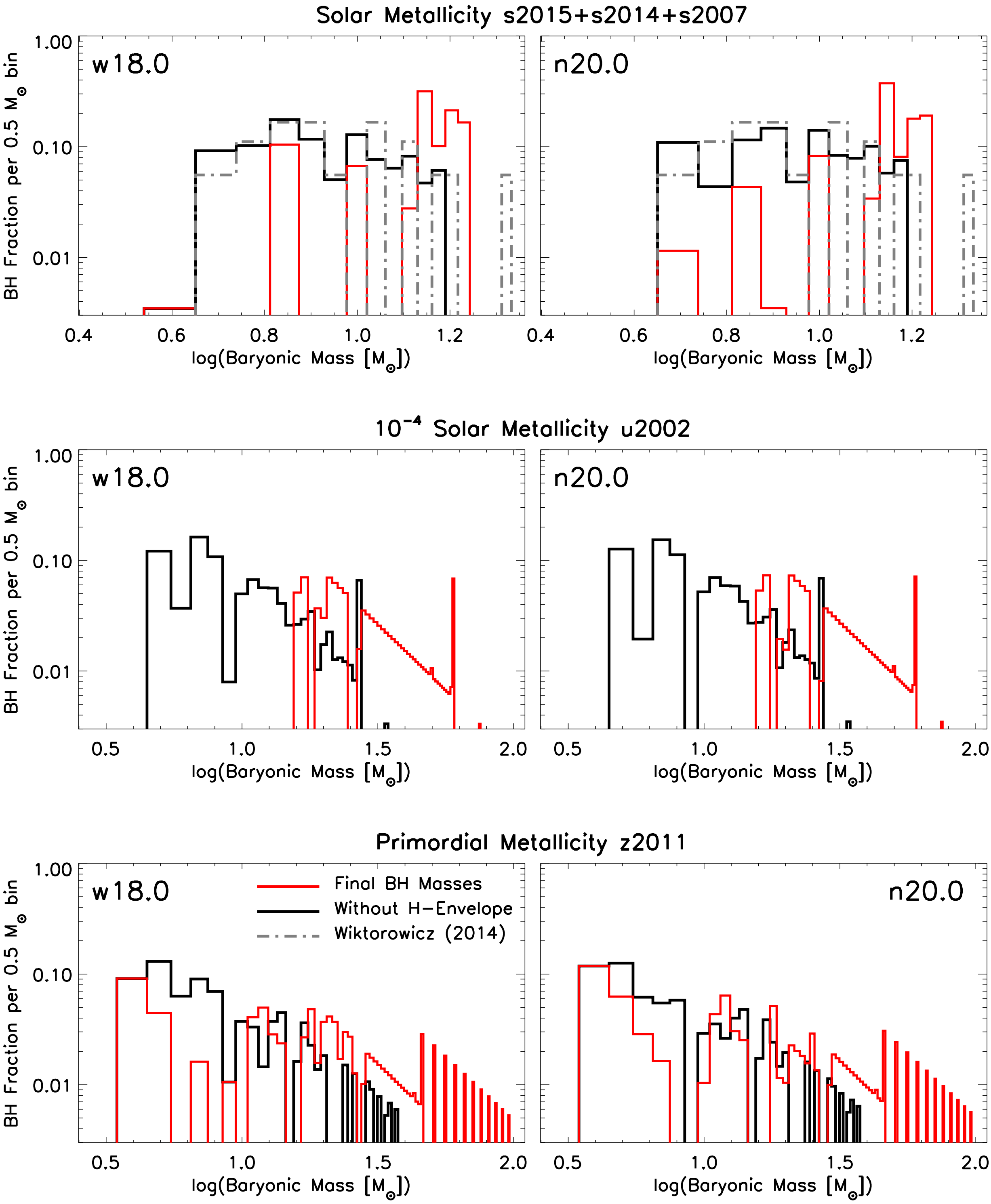

Figure 7.2.: Baryonic BH masses weighted by the Salpeter IMF for the calibration models w18.0 (*left column*) and n20.0 (*right column*) each supplemented with the Crab-like models. The masses of the remnants for all BH forming progenitor stars are displayed, either formed by fallback (FBH) or by unsuccessful revival of the shock. For the latter group, the pre-SN mass of the star is displayed in *red* and without hydrogen envelope in *black*. Overlayed as *dashed gray lines* is a compilation of observed BH masses by Wiktorowicz et al. (2014). Note that the observations are not weighted in any sense (binary evolution, metallicity, observational bias, or error bars).

Our simulation data are again overlayed with the observational data but for X-ray binary systems composed by Wiktorowicz et al. (2014). The comparison here is more problematic, because the observations might be strongly biased by the fact that the observed systems are binaries. Binary stellar evolution can shed mass from the star, especially its extended hydrogen envelope. We cannot conclude, whether the Nadezhin-Lovegrove mechanism is the reason for the good agreement of the observations with the BH mass being the helium core mass or mass-loss by binary evolution. The number of observed BH masses is also very small and amounts to only 18 systems.

If we assume our sample to be unbiased, we see that the helium core is a good measure for the BH mass, better than the pre-SN mass, especially concerning low-mass BH below $10\,M_\odot$. The primordial stars, though, demonstrate that massive fallback can also produce these BHs. The BH formation is still not understood concerning its mechanism(s). Only recently, a new way of observing the BH masses opened up by the observation of gravitational waves from a binary BH merger (Abbott et al., 2016). The BH masses were $36^{+5}_{-4}\,M_\odot$ and $29{\pm}4\,M_\odot$. Our findings demonstrate that BHs with masses of $\sim 30\,M_\odot$ are possible at sub-solar metallicities even if the hydrogen envelope is ejected. Future work should asses the question, how BHs form and how their final mass is determined.

7.2. Metallicity Dependence of BH Formation by Late-Time Fallback

As we pointed out in the previous section (Sect. 7.1), we find that BH formation by late-time fallback (FBH) is more common for primordial stars. In this section we will try to answer, why we find so few FBH cases in the solar sets and not a single case for the metal-poor stars. What follows are attempts to explain the phenomenon, but a final proof of our analysis needs more analysis and extended simulations. Fallback and its consequences has been studied by Chevalier (1989) and with piston-driven simulations for example by (Zhang et al., 2008).

7.2.1. Energy Budget

There are two possibilities for why FBH SNe are more common in metal-free stars. These either stars have a systematically different core structure resulting in weaker explosions or a systematically different stratification of the outer shells, which would be harder to eject.

We begin with the most obvious reasoning: The primordial stars that show a successful revival of the stalled shock have tighter-bound outer shells in comparison to the other sets. In consequence more energy would be needed to unbind the outer layers. Fig. 7.3 displays the binding energy outside of the iron core for the different metallicities as a function of

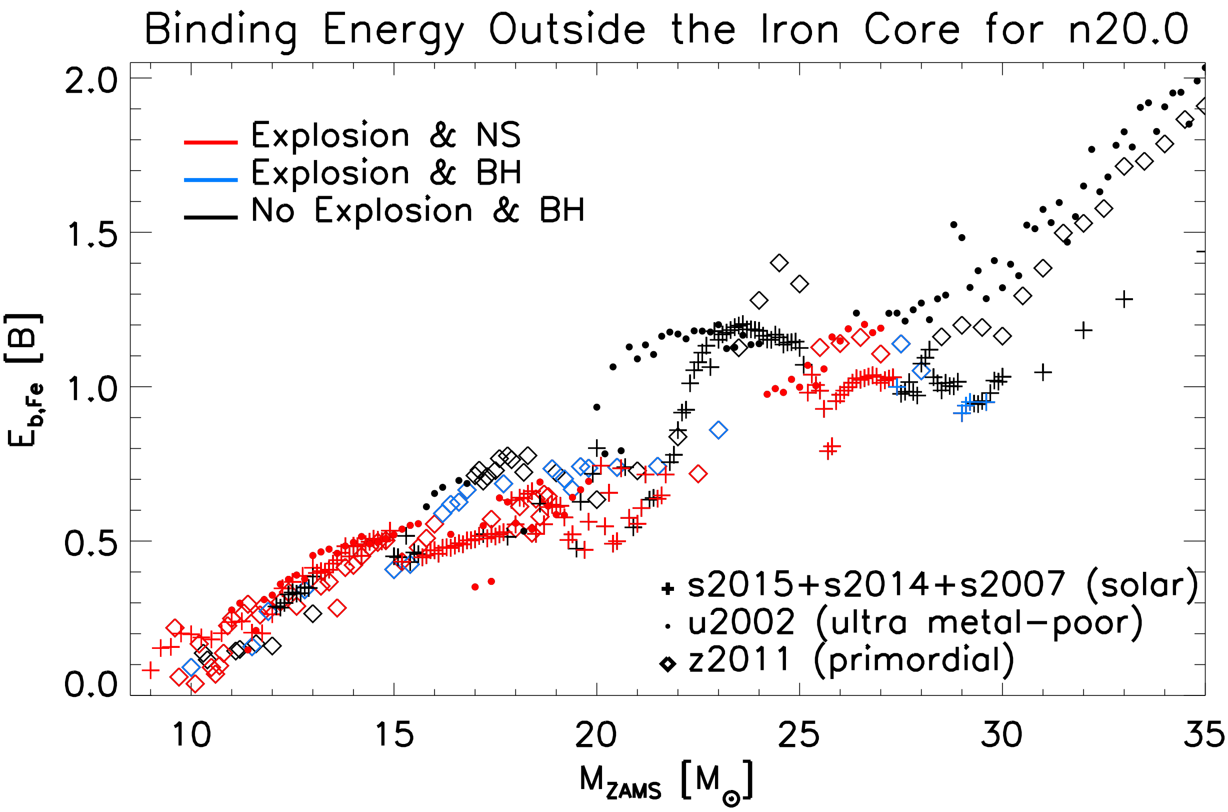

Figure 7.3.: Total binding energy outside of the iron core, $E_\mathrm{b}(m > M_\mathrm{Fe})$ as function of ZAMS mass. Colors depict the outcome with the n20.0 calibration supplemented by the Crab-like models. Explosions forming a NS or a BH are marked *red* and *blue*, respectively, while *black* symbols denote BH-formation cases without an explosion. Different symbols correspond to the different progenitor sets: crosses for the combined solar set, s2015+s2014+s2007, filled circles for the ultra-metal poor model set, u2002, and diamonds for the primordial set, z2016.

ZAMS mass. Most of the stars of the u2002 and z2016 series have very similar binding energies outside of the iron core. We find that the two sets lie on top of each other, while the solar-metallicity progenitors are typically less tightly bound. The FBH cases are marked in blue. They correlate with local maxima in binding energy, but this is not globally true. We also find the inverse, where they are correlated with local minima.

The underlying reason for the higher binding energies of the sub-solar stars is that they are mostly blue supergiants, while the models of the combined solar set are red supergiants (e.g., Zhang et al., 2008, Woosley, 2010). Red supergiants are much more extended in radius compared to their blue counterparts. The question of the late-time fallback seems to be unrelated to whether the star dies as a red or as a blue supergiant, because the ultra-metal poor and primordial stars show opposite behavior regarding the number of FBH cases. On the other hand most BH-formation cases occur by late-time fallback in our set occur, when the star is blue and not red. The least massive star exploding as a FBH

SN is the Crab-like model with $10.0\,M_\odot$ of the z2011 series (see Fig. 6.10), which happens to be a blue supergiant. In contrast, the least massive red supergiant forming a BH by late-time fallback is the $27.0\,M_\odot$ model of the s2014 set exploded with the w15.0 engine (see Fig. 6.10).

If we recall the results of Sect. 6.4, the z2011 progenitors typically resulted in weaker explosions, while the ones for the ultra-metal poor progenitors were more energetic. This behavior poses another possibility for the origin of the excessive number of FBH cases in the primordial models. They tend to launch weaker explosions for some reason, which is not enough to unbind the outer shells.

Such behavior should be connected to a systematically different core structure. Fig. 7.4 depicts the combined solar set, the ultra-metal poor progenitor models, u2002, and the primordial models, z2011, in the two-parameter plane (cf. Chap. 5). The models marked by a black symbol are BH cases without explosion, the red symbols show cases where a NS is the final remnant, and the FBH cases have blue symbols. We cannot conclude that the primordial models cluster in any particular region of the two-parameter plane, or that there is a higher density of these models in any region of the plane. The cores, therefore, do not seem to be structurally different from the other two sets with 10^{-4} solar metallicity or solar metallicity. We find that the u2002 models tend to be at the lower boundary of the “cloud” of models and typically further away from the separation line. But still, the models show large variations and some overlap for all sets.

The FBH cases in our findings are close to the separation line, which corresponds to the edges of islands of explodability in ZAMS mass. Massive fallback correlates with cases that are at the boundary of exploding and non-exploding. Locally in the two-parameter plane, some models might result in a FBH case, while models even closer to the line do not yield massive fallback. If we compare Fig. 7.4 with Fig. 3 of Müller et al. (2016a), we see that their fallback cases cluster close to their separation line as well. But in contrast to clustering, our FBH cases are randomly distributed across the full length of the intersection of the progenitor models with the separation line. Their cases of massive fallback are also close to the separation line but cluster towards the right upper corner in the two-parameter plane (high values of the parameter $M_4\mu_4$). They also find a higher total number of cases in comparison to our combined solar-metallicity set, but this might be connected to the fact that their separation line follows the cloud of progenitor models with a larger fraction of models close to the separation line. In addition, they employ about ten times more progenitor models. More models near the separation line result in a higher number of fallback cases. Another reason might be given by the bottom panel of Fig. 5.9. If we follow the progenitor models diagonally to the upper right corner in the two-parameter plane, the binding energy outside of the iron core increases and, consequently, also the amount of energy needed to overcome it. In our simulations, we would expect to find more FBHs if we tune our core-model to reproduce their separation line intersecting with a higher fraction of the cloud of progenitor models with typically higher binding energies.

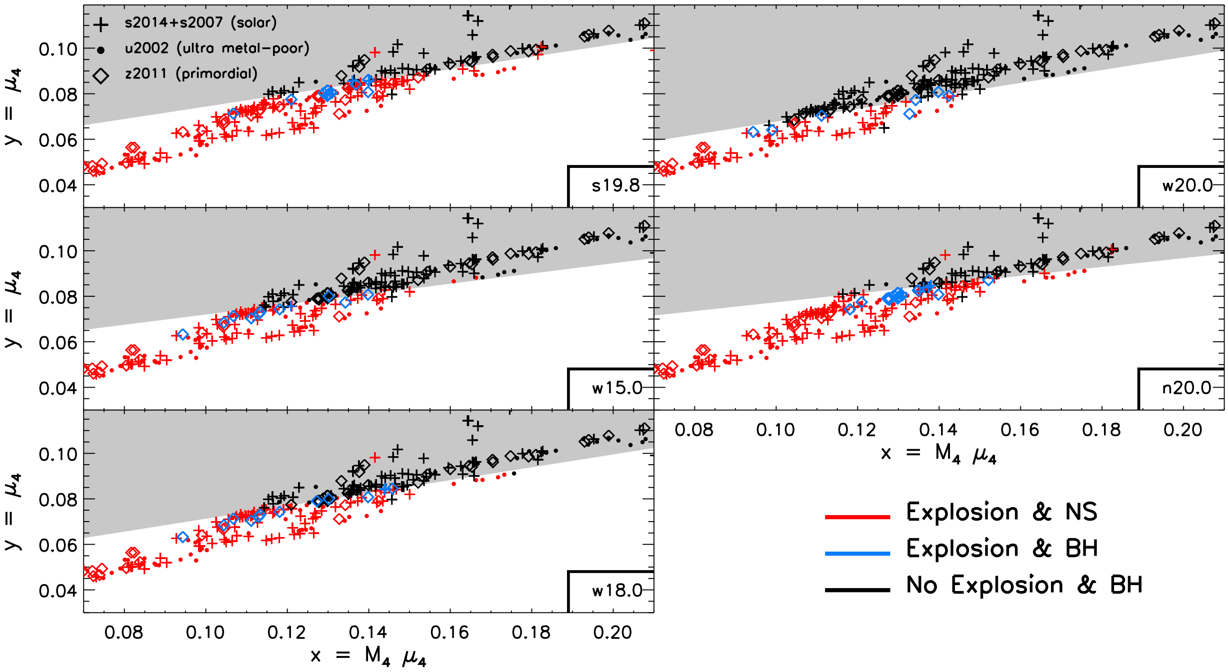

Figure 7.4.: Separation curves between BH formation (gray region, black symbols) and SN explosions (white region, red symbols) for all calibrations in the plane of parameters $x = M_4\mu_4$ and $y = \mu_4$ (cf. Chap. 5). Models where a BH forms by late-time fallback are marked by blue symbols. Different symbols correspond to the different progenitor sets, crosses for the combined solar set, s2014+s2007, filled circles for ultra-metal poor model set, u2002, and diamonds for the primordial set, z2016. Note that the Crab-like models are not displayed, because they do not necessarily obey the same separation line.

Another more important difference between our study and Müller et al. (2016a) is the criterion for FBH SNe: if the energy released by the mechanism is less than the binding energy of the outer layers, they assume massive fallback. A similar reasoning is also the basis for the criterion by which Pejcha & Thompson (2015) decide about "significant fallback" for their models. These criteria are certainly valid as demonstrated by piston-driven explosions (e.g., Zhang et al., 2008) and a simple argument based on energy conservation. But they only pose a lower bound for the real number of FBH SNe, because we find these cases although the criterion is never met in our simulations. To validate this statement, we need to determine the amount of energy the neutrino-driven mechanism provides and compare it with the binding energy of the outer layers. The binding energy of the progenitor,

$$E_{\mathrm{bind}}^{\mathrm{prog}} = -\int_{M_{\mathrm{NS,t=texp}}}^{M_*} \mathrm{d}V\ \rho e_{\mathrm{tot,prog}}, \tag{7.3}$$

is integrated starting with the mass coordinate of the PNS at the onset of the explosion,

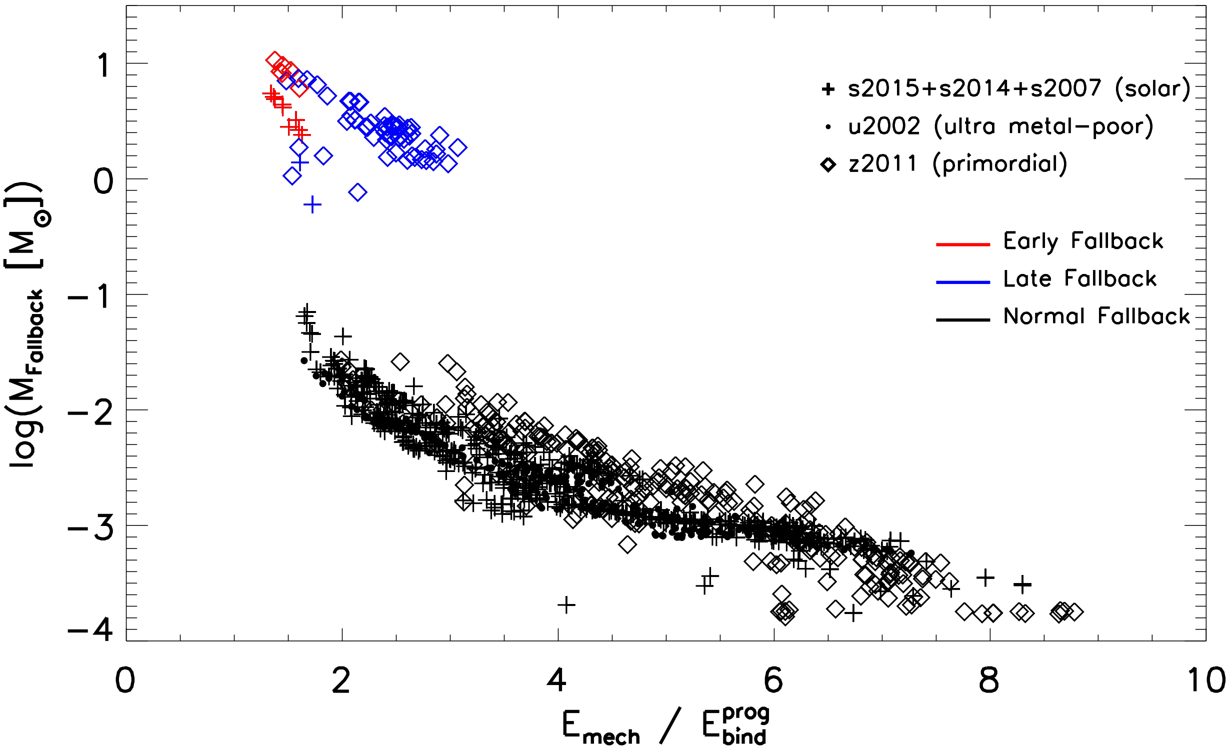

Figure 7.5.: Ratio of the energy provided by the neutrino-driven mechanism, E_mech (Eq. 7.5), and the binding energy of the progenitor, $E_\mathrm{bind}^\mathrm{prog}$ (Eq. 7.3), as functions of the fallback mass. The models of the combined solar set, s2015+s2014+s2007, the ultra-metal poor set, u2002, and the primordial set, z2011, are displayed for *all* calibrations. Colored symbols mark FBH SNe, while we distinguish between early cases (*red*) and late cases (*blue*), either if there is substantial fallback ($> 1\,M_\odot$) before or after 10^4 s, respectively. Black symbols are cases with a NS as remnant and a low fallback ($< 0.1\,M_\odot$).

$M_{\mathrm{NS,t=t_{exp}}}$ (Eq. 7.1) up to the surface of the star M_*. ρ denotes the density and

$$e_\mathrm{tot} = \epsilon + \frac{1}{2}|\boldsymbol{v}|^2 + \Phi, \tag{7.4}$$

the total specific energy of the progenitor model, which in turn is the sum of the specific internal energy ϵ, the specific kinetic energy $\frac{1}{2}|\mathbf{v}|^2$, and the gravitational potential Φ . The total energy provided by the mechanism is defined as follows:

$$E_\mathrm{mech} = \int_{e_\mathrm{tot}>0, t=t_\mathrm{wind}} \mathrm{d}V\ \rho e_\mathrm{tot} - \int_{M_\mathrm{NS}, t=t_\mathrm{exp}}^{M_\mathrm{shock}, t=t_\mathrm{wind}} \mathrm{d}V\ \rho e_\mathrm{tot,prog}\,, \tag{7.5}$$

with the first term being the diagnostic explosion energy and the second term being the binding energy of the progenitor integrated over the mass, which was unbound by the mechanism at the time of evaluation. These quantities are measured at time t_wind when the neutrino-driven wind has ceased (at $\sim 15\,\mathrm{s}$), which corresponds to the time the mechanism has deposited its full energy.

Fig. 7.5 depicts how the ratio of E_{mech} and $E_{\mathrm{bind}}^{\mathrm{prog}}$ correlates with the fallback mass, M_{Fallback}, for our simulations. To recall, a FBH case in the modeling approaches by others (Müller et al., 2016a, Pejcha & Thompson, 2015) is assumed if the mechanism provides a smaller amount of energy than needed to unbind the outer shells, i.e. an energy ratio below unity. This criterion for massive fallback is never met in our simulations, but we still find substantial fallback that turns a NS into a BH. These cases (colored symbols) can be easily discriminated from the "normal" cases (black symbols) by a gap in the fallback mass between $0.1-0.5\,M_{\odot}$. Nevertheless, for both types, a clear correlation is visible. Increasing energy provided by the mechanism compared to the binding energy results in a decreasing fallback mass. Our simulations suggest a value of ~ 1.5 being a better criterion for FBH SNe than unity, but there is also a region where both types of fallback are realized at the same time. The overlap region extends to energy ratios of up to ~ 3.0. Red and blue colors in Fig. 7.5 discriminate cases where the fallback mass amounts to $1\,M_{\odot}$ before $10^4\,\mathrm{s}$ or after this time, respectively. The color scheme will be important for the discussion that follows.

7.2.2. Fallback by Deceleration of the Shock

Our findings suggest that something is missing in the analysis by Müller et al. (2016a) or Pejcha & Thompson (2015) for massive fallback. Their criteria are based solely on the energy budget, while our simulations follow the propagation of the shock through the outer layers of the star. Energy is (re-)distributed hydrodynamically resulting in some mass being bound and falling back.

To understand this hydrodynamic mechanism one needs to know how the movement of the SN shock is influenced by the structure of the star. This can be described based on the analytic blast-wave solution by Sedov (1959): an increasing value of ρr^3 coincides with the deceleration of the shock and, consequently, the matter behind it. Layers of increasing values of ρr^3 are regions of shock deceleration, which can lead to the formation of a reverse shock. The reverse shock propagates inwards and decelerates material. However, matter is also heated and can accelerate again (cf. Sect. 6.2.3). The structure of the star plays the crucial role for the strength of the reverse shock, which decelerates matter and might induce massive fallback (Chevalier, 1989, Zhang et al., 2008).

The uppermost panel of Fig. 7.6 depicts radial progenitor profiles of ρr^3 for all exploding cases with the n20.0 calibration. The different sets for the various metallicities are marked by different colors, black for solar, red for the ultra-metal poor, and blue for the primordial models. Our systematic analysis of the temporal evolution of the fallback mass, M_{Fallback}, showed that the mass increases rapidly if massive fallback arrives at the boundary. The time evolution of the fallback masses of the FBH cases is displayed in the bottom panel of the figure. Massive fallback happens earlier for the solar-metallicity models, while it occurs typically much later in the metal-free stars. We decided to place an arbitrary time criterion, $t_{\mathrm{sep}} = 10^4\,\mathrm{s} \sim 3\,\mathrm{h}$, which roughly separates “early” and “late” cases. The second panel shows the radial profiles, where massive fallback arrives early. The third panel shows the remaining cases where massive fallback occurs late. Each maximum visible in the radial profile can be envisioned as a measure for the resistivity of a progenitor model towards shock propagation. For the interpretation of the ρr^3-profiles, we can divide them into two parts, the helium core and the hydrogen shell. The dividing line is easily identified by the local minimum of ρr^3 above a radius of $\sim 10^{10}\,\mathrm{cm}$ (Fig. 3.3 of Ugliano, 2012, shows an example marking the shells). Now the structural differences between the sets for different metallicities becomes apparent: We find early fallback in cases where there is a high peak in the helium core with a steeply rising ρr^3-profile. This is the case for some solar-metallicity models as well as some metal-free stars and coincides with the time, when massive fallback occurs. The helium-core peaks of the ultra-metal poor series, in contrast, are typically less pronounced.

For the late cases of massive fallback, we find that the primordial stars show a pronounced rising and high radial peak in the hydrogen shell. The second peak is located further inwards, and again the late fallback cases arise for the stars with a high peak-value in the hydrogen shell. The ultra-metal poor models have more extended hydrogen shells and show structural features between the solar and the metal-free series. The helium-core peaks in the ρr^3-profiles are typically smaller for exploding models and the peaks in the hydrogen shell have lower values and are located at larger radii. Nevertheless, if we try to correlate the sum of the peak values of ρr^3 with the energy ratio of E_{mech} and $E_{\mathrm{bind}}^{\mathrm{prog}}$, a clear separation of FBH cases and normal fallback is visible, but only for each progenitor set separately. We conclude, that the deceleration of the shock and the underlying material either occurs in the inner core, the carbon-oxygen shell or helium shell, resulting in early fallback or later in the much more extended hydrogen shell.

Based on this qualitative picture, one would assume that there is a quantitative measure deducible from the structure of the star in correlation with the energy ratio by which a clear separation of the two types of fallback is possible. This could be the basis for a better understanding of the gap in the fallback masses and help predicting the amount of fallback. We can list measures that show tendencies within a set, but not for all sets simultaneously. We correlated the mass of the hydrogen envelope, the mass of the helium core, and the mass of the carbon-oxygen core, and their binding energies with the energy ratio.

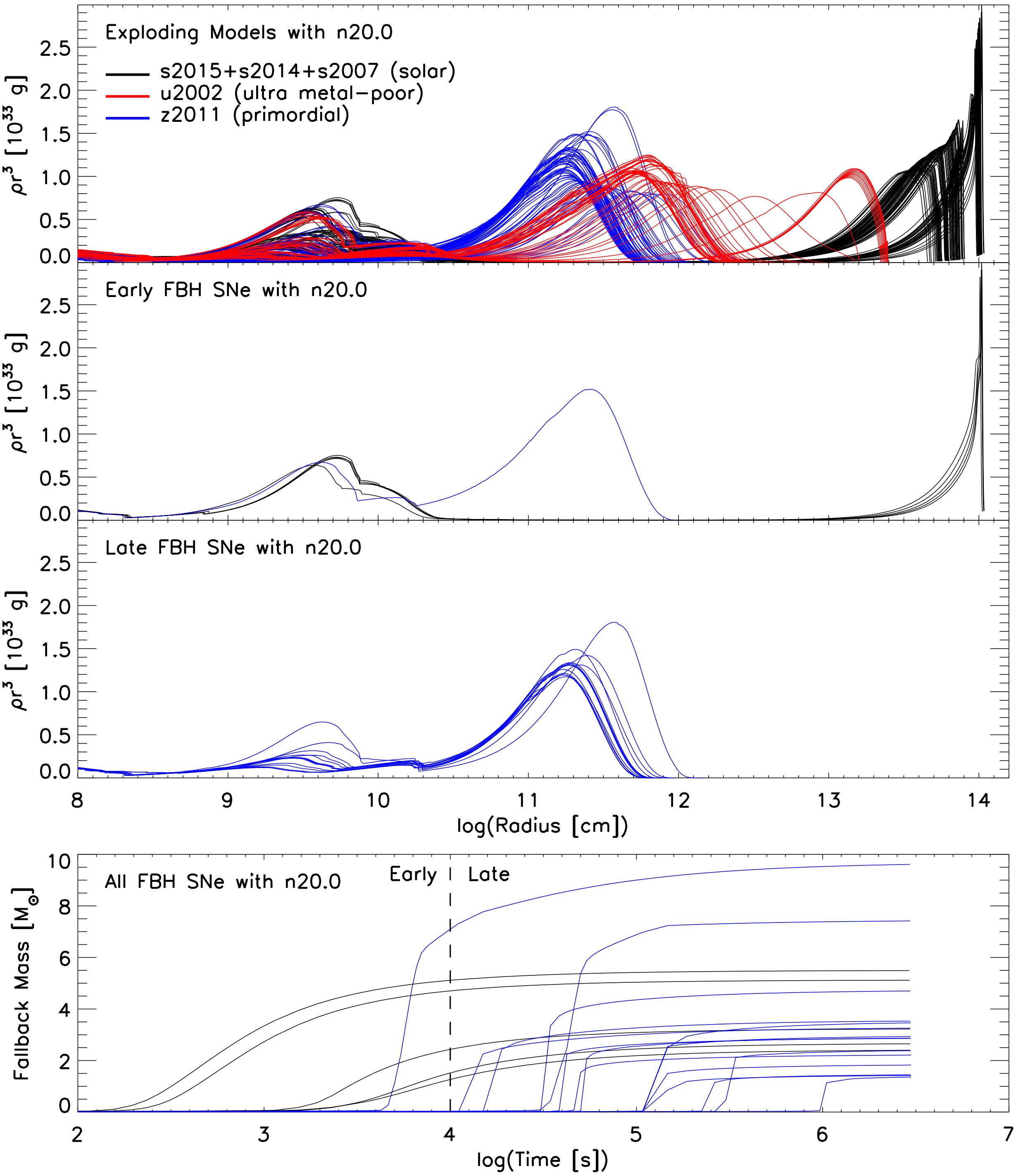

Figure 7.6.: ρr^3 as a function of the radius in the upper group of panels. The progenitor models of the combined solar set, s2015+s2014+s2007, are marked in *black*, the ultra-metal poor set, u2002, in *red*, and the primordial set, z2011, in *blue*. The first panel depicts all models that explode with the n20.0 calibration model, the second panel depicts all *early* FBH SNe ($> 1\,M_\odot$ of fallback before 10^4 s), while the third panel contains the *late* FBH cases. The evolution of the fallback mass with time is shown for all FBH cases in the bottom panel.

7.3. Conclusions

The degenerate remnants in our study can be formed by three channels: an explosion forming a NS, a FBH SN where late-time fallback collapses the NS to a BH, and the complete implosion without shock-revial creating a BH. We found that the FBH channel exists for stars with solar metallicity but only sub-dominantly. Furthermore, that no metal-poor star evolves through this channel, and that a large number of primordial models end this way. If we convolve these results with the Salpeter initial mass function (Salpeter, 1955), we see that 8−14 % depending on the calibration of the metal-free stars result in FBH cases, while only about ~ 1 % of the solar-metallicity stars end up as such cases, and none for metal-poor stars. The integration also revealed that the supernova rate, the ratio of successful explosion and BH forming cases, is highest for solar-like stars with 55−74 %, and ranges from 47 to 60 % (FBH cases are not included) for all sub-solar stars.

The IMF-integrated distribution of NS masses is in good agreement with the observed mass distribution regardless of the metallicity or calibration with exception of the metal-poor stars, which produce more massive NSs. The potential mass gap between the lowest BH masses and most massive NSs results naturally from our approach, modeling the neutrino-driven mechanism. Others already argued that the mass gap is the natural consequence of the neutrino-driven mechanism (Belczynski et al., 2012, Fryer et al., 2012, Pejcha & Thompson, 2015, Müller et al., 2016a), but only if there is no fallback of the order of $\sim 1\,M_{\odot}$. For some of the metal-free stars, we find fallback of this magnitude and the resulting remnants populating the mass gap. All other sets (solar-metallicity or metal-poor stars) so not show a population within the mass gap, because the fallback is either small or large enough to bridge the gap.

The obtained BH mass distribution is only in good agreement if the hydrogen envelope is lost from the system. A potential mechanism by which this is possible is based on the work by Nadezhin (1980) and revisited by Lovegrove & Woosley (2013). Temporarily, depending on the mass-accretion rate, a hot PNS forms, which emits a large fraction of the binding energy of the former iron core in the form of neutrinos, before its mass reaches the BH formation limit. By this, the gravitational potential of the massive star is reduced, which might lead to the ejection of parts of the loosely-bound hydrogen envelope. We analyzed both extreme cases, full ejection and no mass-ejection of the hydrogen envelope. The agreement of the observations and the helium-core constituting the final BH mass are striking, while the full pre-SN mass would result in a population of BH masses being too massive. In case of no or reduced mass-loss during stellar evolution, for single metal-poor or metal-free stars, respectively, the pre-SN mass would yield an even more massive population. The helium-core mass fits better with the observations. Nevertheless, we cannot conclude, that the Nadezhin-Lovegrove mechanism is responsible for the mass ejection, because the observations might be biased. All observed systems are binaries and this might have affected stellar evolution. The hydrogen envelope could have been removed by binary interaction. A third possibility is demonstrated by the metal-poor stars. A lack of BHs with low masses could be compensated by a larger number of SNe that form BHs by fallback. Our simulations might also result in more FBH SNe, already for solar-metallicity stars, if we calibrate our core-model differently. Müller et al. (2016a) obtained more such cases based, although their criterion for fallback only poses a lower limit for the number of cases.

The latter study as well as Pejcha & Thompson (2015) employed a simple argument based on the energy budget of the SN for the decision about substantial fallback. If the energy provided by the explosion mechanism is lower than the binding energy of the outer shells (or the ratio of the two contributions below unity), massive fallback is assumed. Such a simple criterion is not enough to explain all cases of BH formation by late-time fallback in our sample, and the real origin is connected to a hydrodynamical mechanism. We demonstrated that a pure energy criterion is not enough to quantify fallback in CCSNe and that such a criterion only poses a lower bound on the number of cases with massive fallback. Our results revealed that massive fallback is possible even if the energy ratio is ~ 3. Based on our simulations, we can formulate an even stricter energy criterion: If the ratio of the energy provided by the mechanism and the binding energy outside of the initial mass-cut at the onset of the explosion is lower than ~ 1.5, we expect massive fallback. Furthermore, if the ratio has a high value and the star is a compact blue supergiant, it is very likely that the fallback mass is large ($> 0.1\,M_{\odot}$).

It is one of the main surprises, that a large fraction of the primordial stars lead to FBH SNe across a large part of the ZAMS-mass range from $10\,M_{\odot}$ to $\sim 29\,M_{\odot}$, while the slightly metal-enriched stars (10^{-4} solar) do not result in such a case. This is surprising, because they are nearly exclusively blue supergiants, which are more compact than red supergiants and thought to yield more massive fallback (e.g., Chevalier, 1989, Zhang et al., 2008). Even more puzzling is that stars with solar metallicity again show cases of BH-formation by late-time fallback. We identified several reasons for this behavior: The stars of the ultra-metal poor set tend to lead to more energetic explosion and are at the same time radially more extended compared to the metal-free stars. Another more important reason is their structure concerning ρr^3, because its slope poses a measure for the resistivity of shock propagation. If the value is increasing, the shock decelerates, and vice versa. In the ultra-metal poor stars, the shock in the ultra-metal poor stars encounters less resistive inner shells (carbon-oxygen shell and helium shell) compared to models with different metallicity, solar or metal-free. The stars with high peak-values in either the helium core or the hydrogen shell together with a low energy ratio time are the cases that yield FBH SNe. The peak in the hydrogen shell of ρr^3 is typically higher and is positioned at lower radii.

We can conclude, that the metal-poor stars are structurally somewhere between the solar and metal-free stars. The metal-poor stars result in a more compact hydrogen shell than the stars with solar metallicity, but are not as compact as the metal-free stars. At the same time, the peak of the quantity ρr^3 in the helium core in metal-poor stars is lower than for solar-like stars. Either the stars with a similar peak value in the helium shell do not explode or the metal-poor stars do not show such high peak values. Unfortunately, we could not find a quantitative measure for dividing the two classes of fallback. The amount of fallback in each of the classes scales roughly with the ratio of the energy provided by the mechanism and the binding energy of the progenitor. A very similar conclusion is drawn by Zhang et al. (2008). Their piston study finds that the amount of fallback scales with the prescribed energy, but that at least the hydrogen envelope is ejected even for the lowest imposed energy of 0.3 B. These events are supernova-like, but maybe without any radioactive heating by ejected nickel, which is part of the matter that falls back and is consumed by the BH.

Based on the analysis of the new model sets, z2011 and u2002, we cannot exclude that our results are finally converged, although we continued some progenitor models to later times to check for convergence. Fallback might set in much later when the ejected material gets decelerated. Future work needs to extend these simulations in time and radius. The massive fallback found in the primordial models, z2002 and z2011, by the deceleration of the second peak of ρr^3 in the hydrogen envelope happens quite late in some cases. Sometimes massive fallback occurs right before we stop the simulation around 10^6 s (e.g. the $25.5\,M_\odot$ star of the z2011 exploded with the w20.0 calibration). Future work is required to extend the simulations to later times and larger radii to check for convergence. In addition, further analysis of the FBH cases is needed to confirm that the separation of FBH cases and "normal" ones is robust.

8. Summary and Conclusions

Large surveys in the recent years have provided detailed observational signatures of the population of core-collapse supernovae (CCSNe). The systematic identifications of the progenitor stars of Type-IIP SNe (Smartt et al., 2009, Smartt, 2015) have suggested a lack of high-mass stars exploding as SNe. Compilations of mass measurements of black holes (BHs) and neutron stars (NSs) in binary systems have provided a first sketch of the mass distributions of compact remnants (e.g., Özel & Freire, 2016, Wiktorowicz et al., 2014, and references therein). The elemental abundance patterns (for the sun see Lodders, 2003) pose a mixed imprint of all the sources of heavy elements including the contribution by CCSNe. All of the latter observations have provided an observational insight on the progenitor-remnant and the progenitor-explosion connection. Therefore, studies of CCSNe, however, have barely tapped these observational resources and a converged theoretical picture has not yet emerged.

The understanding of the explosion mechanism(s) of massive stars is still incomplete, although considerable progress has been made in recent years with the first successful self-consistent explosions in full geometry (3D; Melson et al., 2015b;a, Lentz et al., 2015). However, computational power restricts evolving these simulations for sufficiently long time to gain converged observable signatures and also a large number of models is computationally unaffordable. Nevertheless, any successful explosion mechanism needs to be able to explode a star in a self-consistent simulation as well as to reproduce the observed population of SNe and their remnants. The delayed neutrino-driven mechanism is the best candidate for a mechanism and certainly the most elaborate.

With the study at hand, we investigated the properties of the progenitor stars and their SN explosions by a *systematic parameter approach*. We explicitly assumed the neutrino-driven mechanism in its current understanding to be the universal explosion mechanism of massive stars and connected state-of-the-art stellar evolution calculations with the best established scenario for this mechanism. The method we employed is computationally efficient and thereby allows for the exploration of the landscape of the progenitor-explosion and progenitor-remnant connection. This study adds a new way of probing the explosion mechanism of massive stars and provides a link to already existing observational constraints connected to the population of CCSNe.

We simulated the final stage of massive-star evolution, the iron-core collapse and the eventual revival of the accretion shock by neutrinos leading to a SN explosion. If successfully revived, we followed the propagation of the shock through the star and beyond break-out through the surface.

Computationally, we simulate the stellar fluid by employing Eulerian hydrodynamics in spherical symmetry (1D) coupled with an approximate gray neutrino-transport scheme. The heart of our modeling approach is the excision of the inner core of the proto-neutron star (PNS) and replacing it by an analytic core-cooling model with physically-motivated parameters (Ugliano et al., 2012). The placement of the parameters is guided by the still existing theoretical uncertainties with respect to high-density physics and neutrino interactions. We calibrate the set of free parameters to the observations of the two well-constrained SNe – SN 1987A and the Crab SN of the year 1054 – and models for their progenitor stars. The progenitor of the Crab SN is believed to be a low-mass star of $8{-}10\,M_{\odot}$resulting in a low-energetic explosion of only $\sim 0.1\,\mathrm{B} = 10^{50}$ erg (Tominaga et al., 2013, Smith, 2013, Yang & Chevalier, 2015), while SN 1987A was a more energetic and therefore more generic SN with ~1.5 B (Arnett et al., 1989, Utrobin et al., 2015). These two SNe are our observational anchors for the theoretical survey. The obtained parameters are then applied to many hundred iron-core progenitor models (762 to be precise) with zero-age main-sequence (ZAMS) masses of $9 - 120\,M_{\odot}$, metallicities ranging from solar to metal-free, and different modeling approaches towards stellar evolution (cf. Chap. 4).

The first question one might ask is which stars explode and which implode, and how is this correlated with their birth masses. This is not only interesting because it is the endpoint of stellar evolution of massive stars, but also for further theoretical studies of galactic chemical evolution or any study employing SN-feedback. Observationally, recent efforts in identifying progenitor stars in archival pre-SN images have suggested that stars more massive than $\sim 18 M_{\odot}$ die quietly forming BHs (Smartt et al., 2009, Smartt, 2015). This is based on theoretical modeling of the stellar evolution in order to connect the color and the luminosity of the progenitor to its ZAMS mass. The latter study further assumes that a certain ZAMS mass exists below which stars exclusively explode, while the more massive ones above form BHs. We find no such ZAMS-mass limit for BH formation in our simulations. Our simulations resulted in continuous explosions up to $\sim 15\,M_{\odot}$, while more massive models showed explosions and failed cases (BHs) interspersed with each other even within narrow ZAMS-mass intervals. This behavior is described by Sukhbold et al. (2016) as "islands of 'explodability' in a sea of BH formation" (see Fig. 6.1). Already previous attempts found a non-monotonic variation of successful and failed supernovae with ZAMS mass (Ugliano et al., 2012, Pejcha & Thompson, 2015, Nakamura et al., 2015, Horiuchi et al., 2014). We used five different progenitor models for the calibration to SN 1987A and our modeling approach resulted in an irregular outcome pattern regardless of the employed core-parameter choice, which is a clear indicator that the core structure dominates the outcome and not the calibration. Still, some calibration models yielded more successful explosion than others. Furthermore, each set of solar-metallicity models provided by stellar evolution shows such irregularities (except the ones with a too coarse ZAMS-mass grid) and we cannot determine a boundary for BH formation for any of them.

On the contrary, we even obtain successful explosions for the most massive stars of each model series. Our findings are only by a first glance in conflict with the study by Smartt (2015), because if weighted with the Salpeter initial mass function, successful explosions of the high-mass models can be compensated by a lack of low-mass explosions between 15 and $18\,M_\odot$. We can conclude that the statistical argument of the latter study which is based on the assumption of successful explosions up to a certain BH boundary, can also be fulfilled by an irregular explosion pattern.

We further extended our study by progenitors with sub-solar metallicities, ultra metal-poor stars (10^{-4} solar) and primordial stars (metal-free at birth). These sets of models show a similar irregular outcome systematic with ZAMS mass as the solar models, but only up to $\sim 27\,M_\odot$ (cf. Figs. 6.7 and 6.8). More massive stars, however, show a regular pattern of non-explosions, which therefore poses a boundary for BH formation. The reason why we obtain a BH boundary for sub-solar metallicities and not for the solar metallicity is connected to stellar evolution. Larger mass loss for solar-metallicity stars during their evolution leads to smaller cores and lower binding energies of the outer shells being favorable for successful explosions. A qualitatively similar result was obtained by Pejcha & Thompson (2015) for the metallicity dependence of the outcomes, but by a different modeling approach. Their study used a scaling law for the critical neutrino luminosity deduced from 1D simulations and analytic arguments to estimate observable properties.

We also investigated the underlying reason for the irregular outcome pattern with ZAMS mass. We assessed the behavior in Chap. 5, where we identified a structural measure for the *explodability* of a massive star. Thus far, judging the fate of a massive star, either a NS or a BH, solely by its structure prior to core collapse has been ambiguous. No single structural parameter can serve as a good predictive measure for the explodability of massive stars, yet some show tendencies (see Ertl et al., 2016a, or Chap. 5). For example the compactness parameter by O'Connor & Ott (2011), which is used extensively in the literature, shows tendencies for the explodability, but does not predict the outcome, explosion or not, robustly. The same is true for other structural measures, like the iron-core mass, the binding energy outside of the iron core, and others. However, we derived such a predictive measure for the explodability: two parameters computed from the pre-collapse structure of the progenitor, which in combination allow for a clear separation of exploding and non-exploding cases with only few exceptions in our set of hundreds of investigated stellar models. One parameter is M_4, defining the normalized enclosed mass for a dimensionless entropy per nucleon of $s = 4$, and the other is $\mu_4 \equiv (\mathrm{d}m/M_\odot)/(\mathrm{d}r/1000\,\mathrm{km})|_{s=4}$, being the normalized mass derivative at this location. The location of $s = 4$ is chosen because it is a good measure for the interface between the Si and Si/O shells, where the mass-accretion rate, $\dot{M}$, typically shows a steep decline when accreted by the shock. The two parameters $y = \mu_4$ and $x = M_4\mu_4$ can be directly linked to the mass-accretion rate, $\dot{M}$, of the collapsing star and the electron-type neutrino luminosity of the accreting proto-neutron star (PNS), $L_{\nu_e} \propto M_{\mathrm{ns}}\dot{M}$, which play a crucial role in the "critical luminosity" concept (Burrows & Goshy, 1993) for the theoretical description of neutrino-driven explosions as runaway phenomenon of the stalled accretion shock. We demonstrated the connection of our two parameters to the theoretical concept of the "critical luminosity" for our models (cf. Sect. 5.3).

The two parameter x and y span a plane where the cloud of progenitor models can be divided into two distinct groups by a staight line, $y_{\mathrm{sep}}(x)$, for each of the employed calibrations. The line clearly separates exploding and non-exploding cases with only ~1−2.5 % of all of our models misassigned. The misassignments are either very close to the separation line or show pathologies in their structure.

The study by Müller et al. (2016a) demonstrates that our criterion for the explodability works equally well for their completely different approach. They solve a large set of ordinary differential equations and scaling laws for the different components of CCSNe and also the question of successful shock revival. Their approach is guided by a set of self-consistent simulations and numerical experiments for the different phases of the explosion. They argue that our two-parameter criterion only captures successful shock revival rather than successful SN explosions, because they assume that a lot of cases will turn into BH due to the large binding energy of the outer shells and the weak energy contribution by the neutrino-driven mechanism. Nevertheless, also these cases should result in some explosive outflow and therefore a faint explosion. Piston-driven simulations, where a Lagrangian boundary is moved to artificially explode a star with prescribed final explosion energy, show exactly this behavior even if the explosion energy is small (e.g., Zhang et al., 2008).

Clausen et al. (2015) bring forward the argument that CCSNe are better captured by a probabilistic description. The non-monotonic ZAMS-mass variations and one-parameter approaches (e.g., compactness) might suggest something like that. However, our two-parameter space demonstrates that the phenomenon can be captured by one criterion unambiguously and the outcome is actually deterministic. Nevertheless, there is some justification for a stochastic picture, because we cannot capture all physical phenomena, like rotation, magnetic fields, binary effects, etc. and the measurements also allow for some range of interpretation by their error bars.

The question of shock revival can be answered within the first seconds after core bounce, but we can continue our simulations after the onset of the explosion and follow them even beyond the shock-breakout from the surface of the star. We are thus able to determine the most important observational signatures, which are the explosion energy, the time of the onset of the explosion, the radiated neutrino energy, bulk nucleosynthesis in the form of approximate nickel ejecta mass, and mass and type of the compact object. The explosion energies range from 0.1 to 2.3 B, while the weakest explosions were found for progenitors below $12\,M_{\odot}$. The more massive stars resulted in more energetic explosions, because of their larger accretion component to the neutrino luminosity. The nickel ejecta masses ranged from none to $0.15\,M_{\odot}$, because some cases showed substantial fallback and the nickel was thus removed from the ejecta. If we were not constrained by spherical symmetry, mixing could have been possible and some nickel might have survived even in these cases (Wongwathanarat et al., 2013; 2015). All in all, these results agree well with the previous study by Ugliano et al. (2012) as well as the studies by Müller et al. (2016a) and Pejcha & Thompson (2015).

Furthermore, we were able to deduce light curves and detailed explosive nucleosynthesis for one of the progenitor sets with solar metallicity. These results are already reported in a collaborative work (Sukhbold et al., 2016). We found good agreement with the solar elemental abundance pattern (Lodders, 2003), but were also pointed towards some deficiencies. Nevertheless, we certainly improved on previous piston-driven studies (e.g., Woosley & Heger, 2007) by initiating the explosions more realistically. The conclusions drawn from our study set showed deficiencies connected to the assumed mass-loss rates during stellar evolution and suggested more explosions for high-mass stars. Most SNe in our simulations resulted in light curves of Type IIP with typical shapes. Only a few Type Ibc were found and the few cases obtained were too faint and broad. The reason for the low number of Type-Ibc SNe and their peculiar shapes maybe found in missing explosions between 30 and $40\,M_\odot$, but it is more likely that stars with lower masses loose their hydrogen by binary interaction which is not included in the stellar evolution calculations.

Prolonging the simulations beyond shock break-out allows for the determination of the mass that is bound at late times and falls back towards the degenerate remnant. With the mass of the fallback, we were able to determine the final mass and type of the compact remnant (depending to some extent on the theoretically unknown NS mass limit). Ugliano et al. (2012) and also the work at hand find that the neutrino-driven mechanism leads to a gap between the highest obtained baryonic NS mass ($\sim 2\,M_\odot$) and the least massive BH ($\sim 4\,M_\odot$). Observations of binary systems with NSs or BHs also show a similar gap in the measured mass distribution of compact objects (Özel et al., 2010, Valentim et al., 2011, Farr et al., 2011, Kreidberg et al., 2012,e.g.,). Our findings as well as other studies demonstrate that the gap to occurs naturally for the neutrino-driven mechanism, because neutrino heating is connected to the hot PNS and shuts down as soon as a BH forms (Belczynski et al., 2012, Fryer et al., 2012, Pejcha & Thompson, 2015, Müller et al., 2016a).

We can distinguish three channels for the formation of the compact remnant: BH formation without shock revival, an explosion forming a NS, and an explosion alongside forming a BH by late-time fallback (termed "FBH"). The only possibility for populating the mass gap between NSs and BHs is by late-time fallback in our simulations.* Only a few cases of massive late-time fallback occur in our simulations for stars with solar metallicity. A similarly low number of cases was found by Ugliano et al. (2012). No FBH case resulted for the ultra-metal poor stars (10^{-4} solar) regardless of the employed calibration, but a large number was found in primordial stars. These metal-free stars were the only ones in our study with remnant masses populating the mass gap. Still, the total IMF-weighted

---

*Müller et al. (2016a) describes another possibility in which the stalled shock is revived, but continuous downflows push the mass of the NS beyond its limit and turning it into a BH early on. Such cases are out of reach with our 1D modeling approach. However, these cases might be an artifact of very asymmetric explosions in axially symmetric simulations.

probability of the population within the gap is low and also the observations are biased by metallicity and do not reflect the remnant masses resulting from primordial stars.

The reason for the obtained bimodal distribution is a gap in the fallback masses. The bound mass that falls back is either tiny or large enough to bridge the mass gap. These two classes of fallback do not obey a simple energy criterion, where massive fallback results from a weak energy input by the neutrino-driven mechanism outweighed by the binding energy of the outer shells. In fact an inefficient distribution of energy is found, because massive fallback even occurs when the ratio of the two energies (energy provided by the central engine divided by the binding energy of the outer shells) is ~ 3. Up to a energy ratio of ~ 1.5 our simulations result purely in FBH SNe. We were further able to connect this behavior to the structure of the stars which show pronounced maxima in their ρr^3-profiles. A rising ρr^3-profile with radius can be envisioned as resistivity for the shock propagation (Sedov, 1959). We demonstrated that a high peak-value in either the hydrogen shell or the helium core alongside a small value of the energy ratio leads to massive fallback. Unfortunately, we could not determine a quantitative measure that clearly separates FBH SNe and "normal" fallback robustly. Nevertheless, we showed that the energy criteria by Müller et al. (2016a) and Pejcha & Thompson (2015) only pose a lower bound for the number of FBH cases.

In case of BH formation without shock revival, the PNS emits a large fraction of the binding energy of the former iron-core in the form of neutrinos before it turns into a BH. Based on this energy loss, Nadezhin (1980) argued that the loosely bound envelope can be ejected by the reduced gravity. The phenomenon was only recently revisited with hydrodynamical simulations by Lovegrove & Woosley (2013). The extreme cases for the BH masses are either provided the whole pre-SN mass of the star without mass ejection or only by its helium core ejecting the whole hydrogen enevelope. Our results show that regardless of metallicity, the helium-core mass fits the mass measurements of X-ray binaries (Wiktorowicz et al., 2014) much better than the pre-SN mass. However, mass from the system can also be removed by binary interaction and this certainly plays a role for some of the observed systems. There is a further possibility for the formation of BHs with masses less than their pre-SN mass, which is demonstrated by the primordial stars. The BHs formed by massive fallback result in masses lower than the helium-core mass. However, we cannot draw the conclusion that the mass is shed by the Nadezhin-Lovegrove mechanism, binary evolution, or weak SN explosions with massive fallback. The question of BH mass loss is unsolved and left for future work, especially whether the Nadezhin-Lovegrove mechanism is capable of ejecting mass from compact blue supergiants.

There are some caveats connected to the study at hand. Without self-consistent 3D explosion simulations for large sets of progenitor stars being possible yet, our study refers to a 1D modeling approach, in which not only the neutrino description is approximated in many aspects, but also the explosions have to be triggered artificially. Such a modeling approach is indispensable at the moment, although there has been progress in 2D and 3D modeling and in particular also through improvements in the treatment of the crucial neutrino physics and transport in collapsing stellar cores (see, e.g., Janka et al., 2012, Janka, 2012, Burrows, 2013, Mezzacappa et al., 2015, Melson et al., 2015b;a, Lentz et al., 2015,and references therein). A parametric study like ours has to keep up with these advancements and model them somehow, e.g., the post-shock turbulence or a model for simultaneous downflows and outflows after shock-revival.

Although the elements of this approximate approach appear qualified to capture the essence of the neutrino-heating mechanism in dependence of the progenitor-specific post-bounce accretion evolution (cf. Chapter 2 for details), confirmation by fully self-consistent, multi-dimensional SN calculations is ultimately unavoidable. Stellar evolution also lacks important physics, because the models employed in this study are purely 1D, without magnetic fields or rotation, and single stars without the inclusion of binary effects. It is also evident that our study, which is only concerned with neutrino-driven explosions, cannot yield any information about the possibility and implications of other mechanisms to explode stars, for example magnetorotational explosions of rapidly rotating stellar cores, which might be a consequence of magnetar or BH formation and could be associated with hypernovae and gamma-ray burst SNe (see, e.g., Mazzali et al., 2014) as well as ultra-luminous SNe (Woosley, 2010, Kasen & Bildsten, 2010, Sukhbold et al., 2016).

A. Appendix to Chapter 4 – Calibration and Progenitor Models

For completeness we will append the properties of all progenitor models here. An overview of all employed progenitor models is given in Chap. 4. The model sets presented in this appendix are grouped by metallicity.

A.1. Combined Set of Solar-Metallicity Progenitors

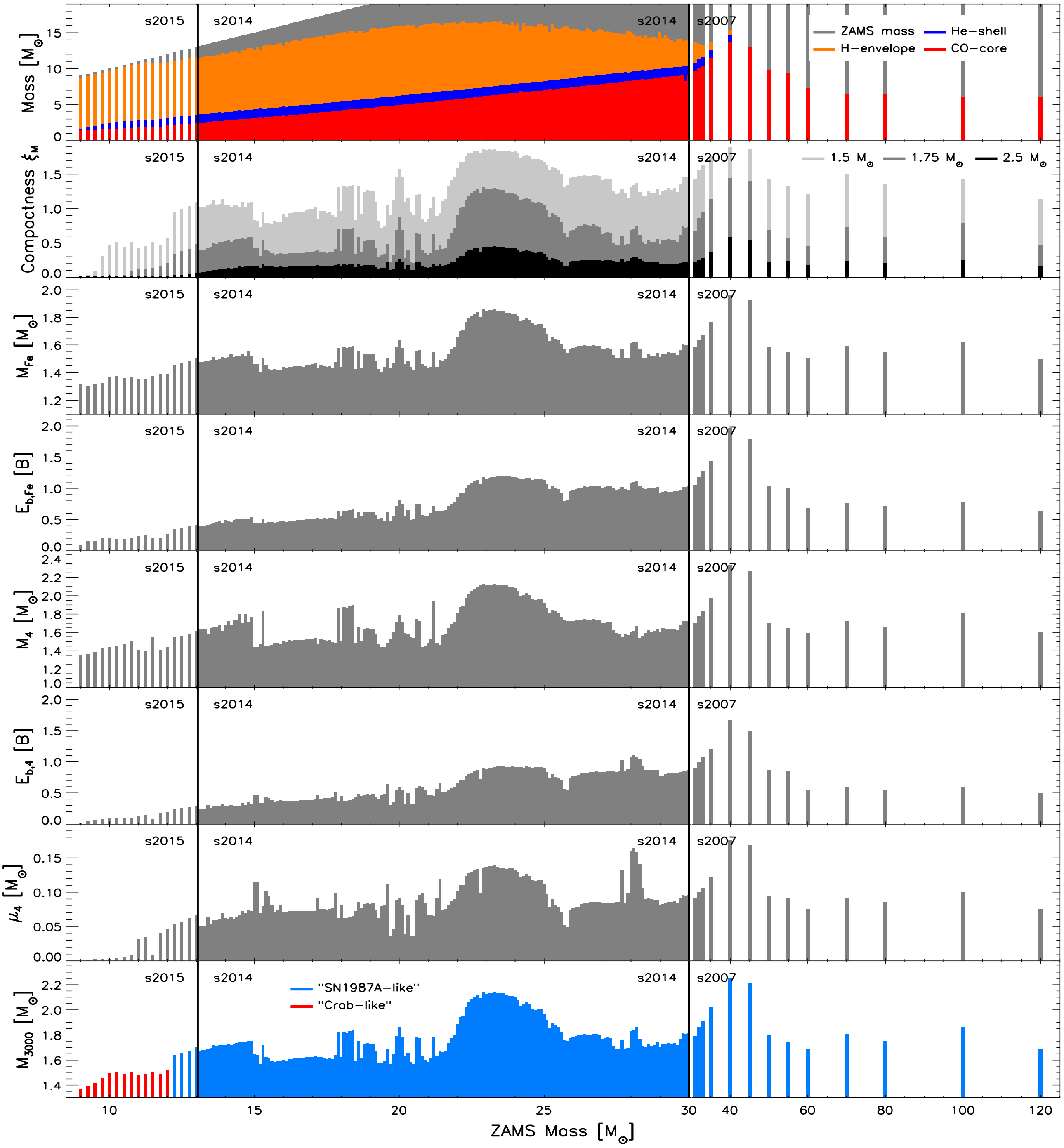

Figure A.1.: Progenitor properties of the combined set with solar metallicity (s2015, s2014, and s2007) as a function of zero-age main-sequence (ZAMS) mass. The *uppermost panel* shows the masses of the outer shells with the ZAMS mass marked in *gray*, the hydrogen-envelope mass in *orange*, the mass of the helium shell in *blue*, and the CO-core mass in *red*. Each shell boundary, H/He and He/CO, are defined as the point where the respective mass fraction of the overlying shell drops below 20 %. The core structure is displayed in the subsequent panels by a variety of measures: the compactness parameters (Eq. 5.1) for the mass coordinates $1.5\,M_\odot$, $1.75\,M_\odot$, and $2.5\,M_\odot$ (*second panel*), iron-core masses M_{Fe} (*third panel*), exterior binding energies ($E_{\mathrm{b,Fe}} = E_{\mathrm{b}}(m > M_{\mathrm{Fe}})$; *fourth panel*), normalized masses M_4 (Eq. 5.2; *fifth panel*), exterior binding energies ($E_{\mathrm{b,4}} = E_{\mathrm{b}}(m/M_\odot > M_4)$; *sixth panel*), μ_4 (Eq. 5.5; *seventh panel*), and the masses enclosed by the innermost 3000 km (M_{3000}; *bottom panel*). The “Crab-like” and “SN 1987A-like” models are marked in the latter panel by *red* and *blue* color, respectively. All progenitor properties are evaluated for a central density of $5 \times 10^{10}\,\mathrm{g\,cm^{-3}}$.

A.2. Solar-Metallicity Set s2002

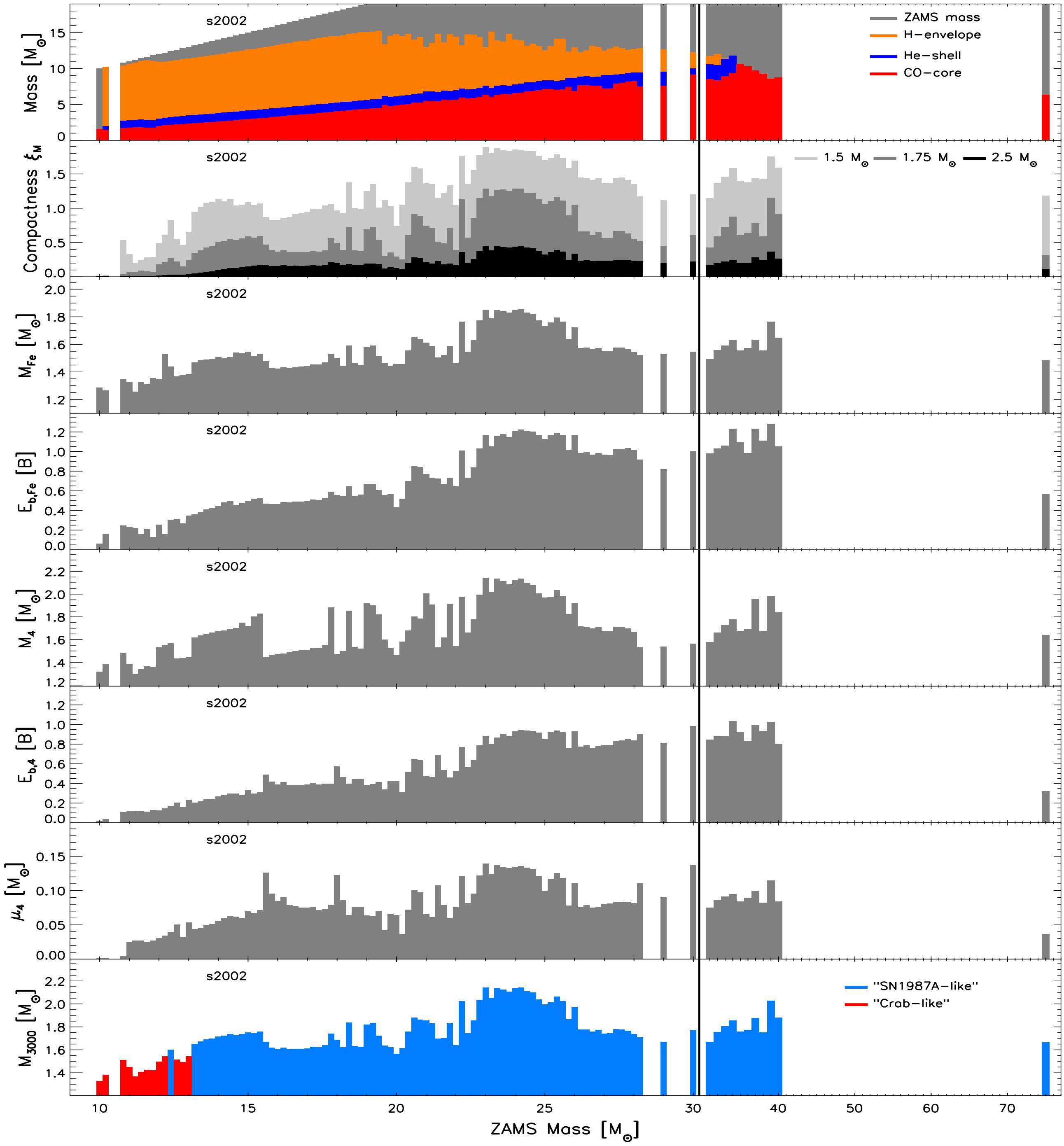

Figure A.2.: Same as Fig. A.1, but for the model set s2002.

A.3. Solar-Metallicity Set s2007

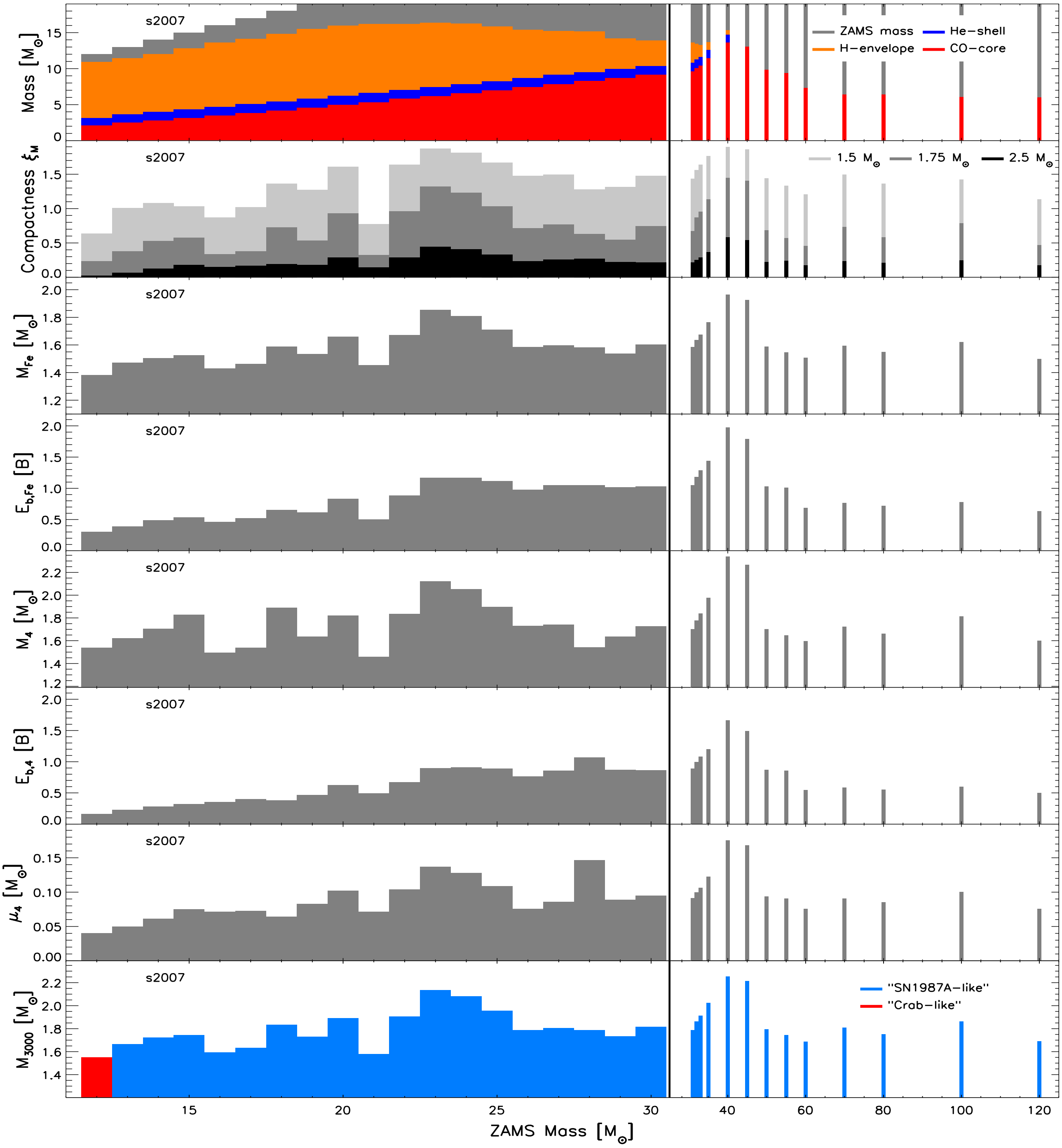

Figure A.3.: Same as Fig. A.1, but for the model set s2007.

A.4. Solar-Metallicity Set n2006

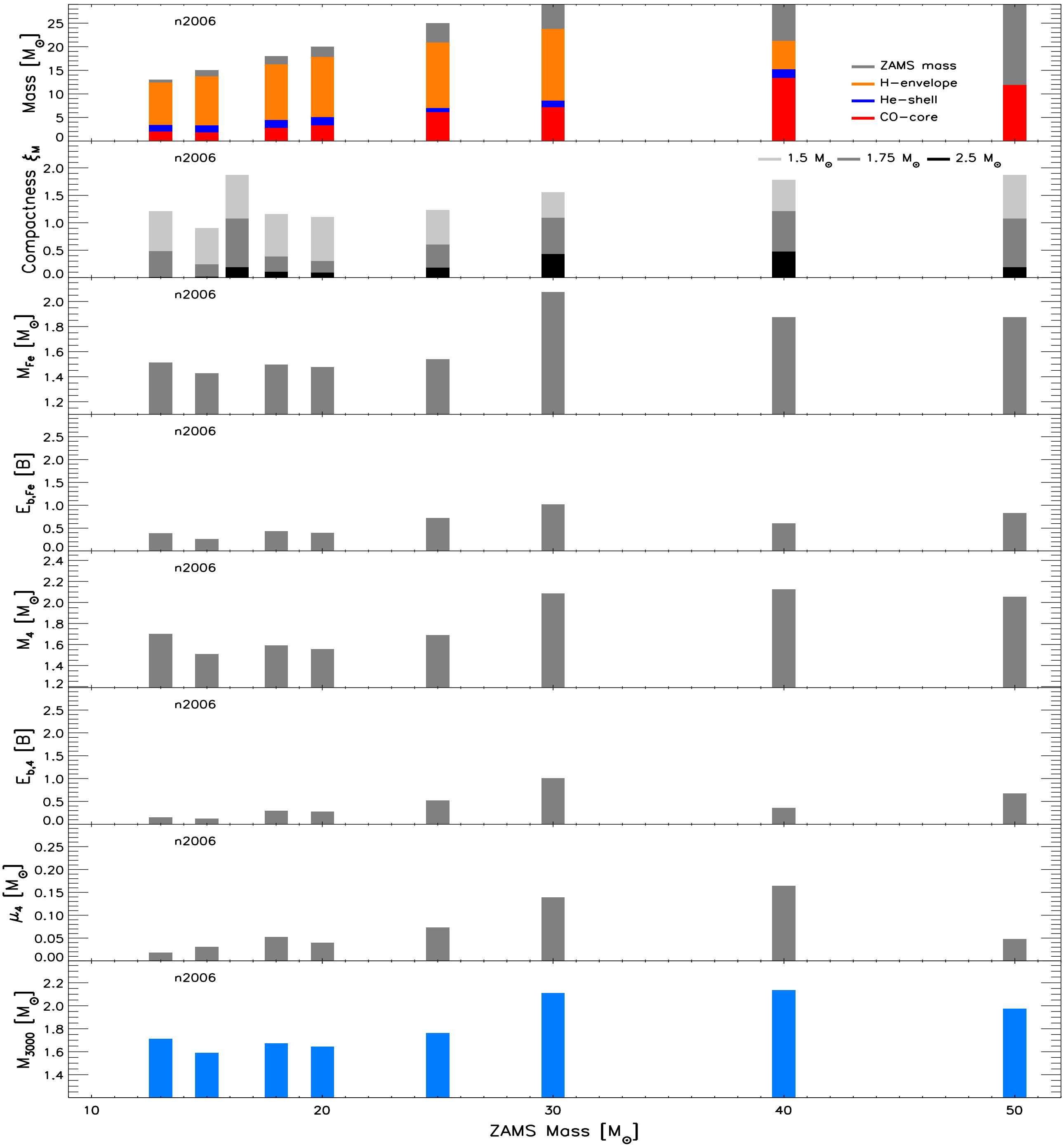

Figure A.4.: Same as Fig. A.1, but for the model set n2006.

A.5. Ultra Metal-Poor Set u2002

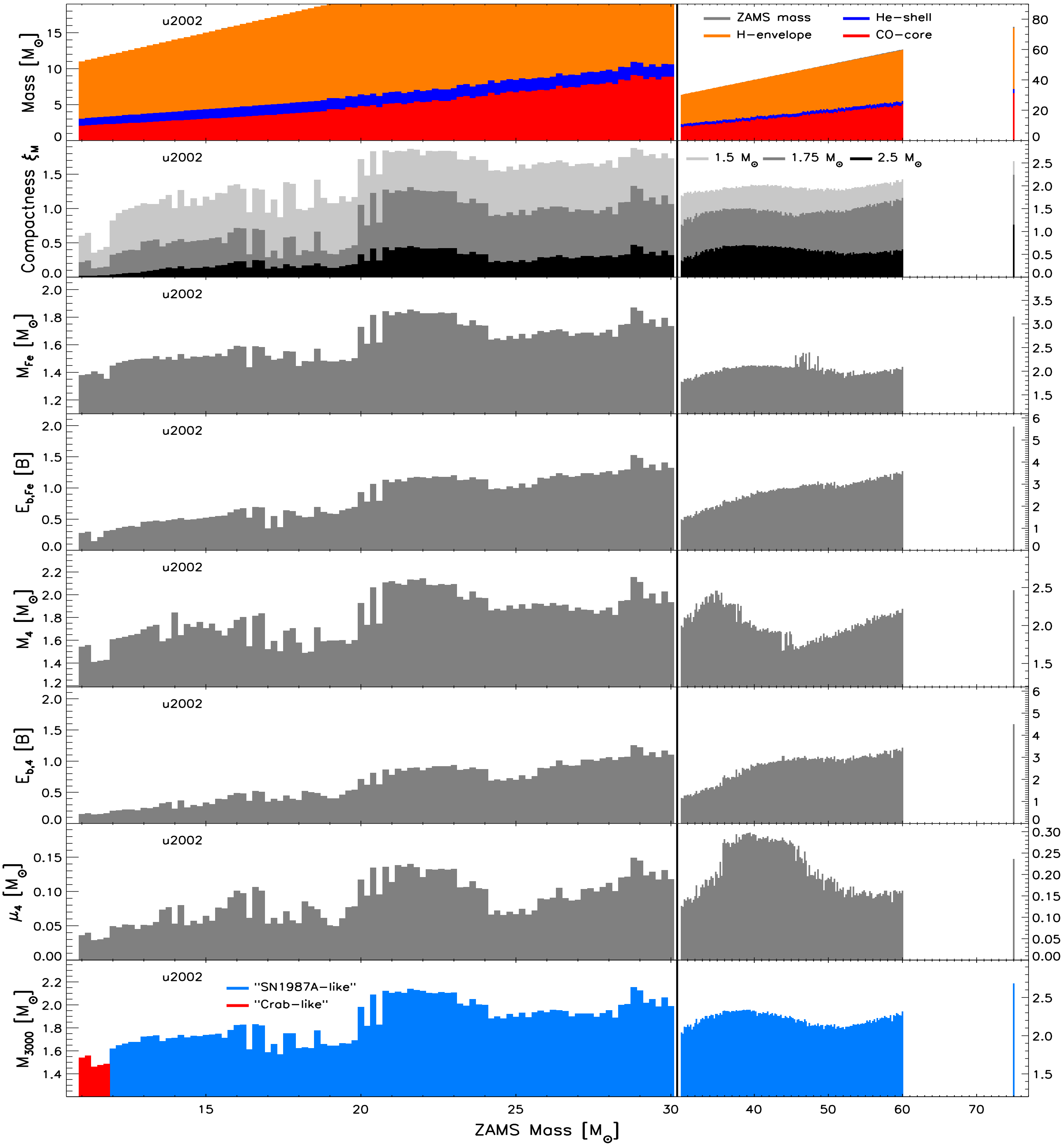

Figure A.5.: Same as Fig. A.1, but for the model set u2002 (10^{-4} solar). Note the different scale for the high-mass models ($> 30\,M_\odot$).

A.6. Metal-Free Set z2011

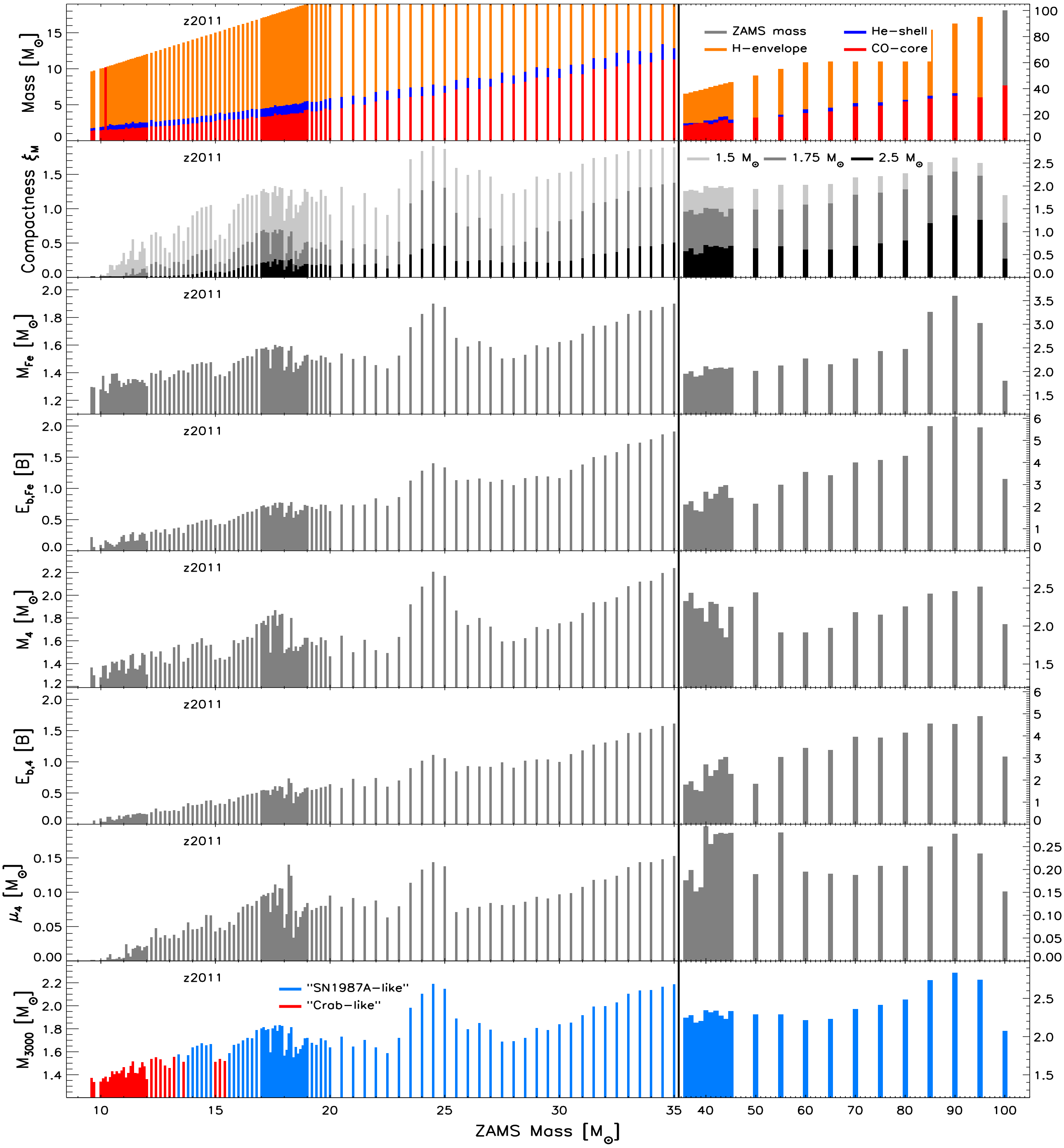

Figure A.6.: Same as Fig. A.1, but for the model series z2011 with primordial metallicity. Note the different scale for the high-mass models ($> 35\,M_\odot$).

A.7. Metal-Free Set z2002

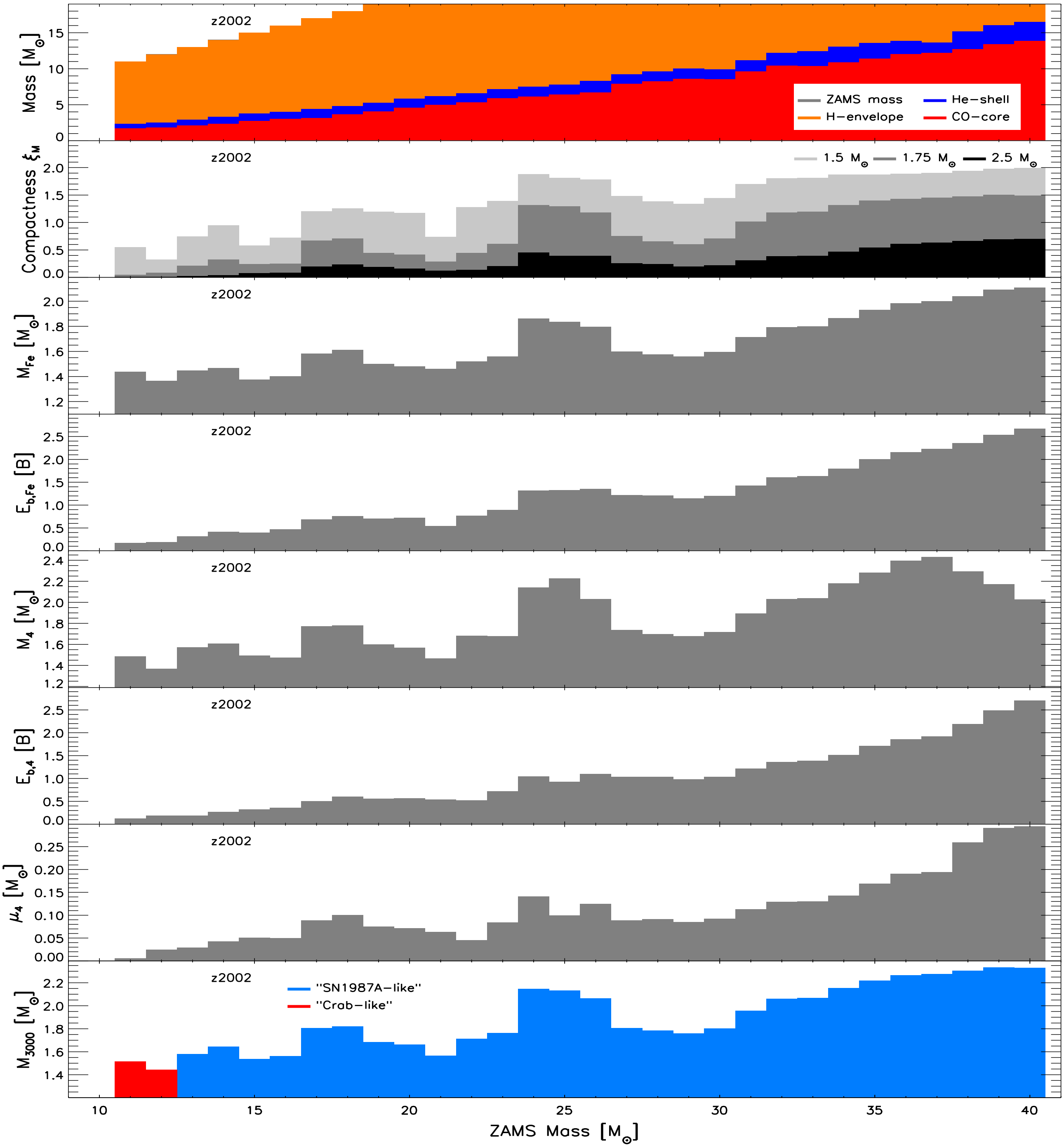

Figure A.7.: Same as Fig. A.1, but for the model set z2002 with primordial metallicity.

B. Appendix to Chapter 6 – Properties of the Explosive Outflow

For completeness we will append all simulated model sets which have not been presented before. We will display the explosion results and remnant properties, but will not discuss them. An overview of all employed progenitor models is given in Chap. 4. The explosion and remnant properties are discussed in Chaps. 6 and 7,respectively. The model sets presented in this appendix are grouped by metallicity and model set, and then sorted by the strength of the core-model calibration, which is equal to the number of successful explosions. The main trend for the strength of the core-model calibration persist through all model sets, and is sorted as follows, starting with the calibration yielding most explosions: s19.8, n20.0, w18.0, w15.0, and w20.0.

B.1. Combined Set of Solar-Metallicity Progenitors

Here we present all missing results for the combined set of solar metallicity models. The outcome systematics for all calibrations can be found in Fig. 6.1 of the main body of this work as well as the detailed results for the calibrations n20.0 and w18.0 in Figs. 6.2 and 6.3, respectively.

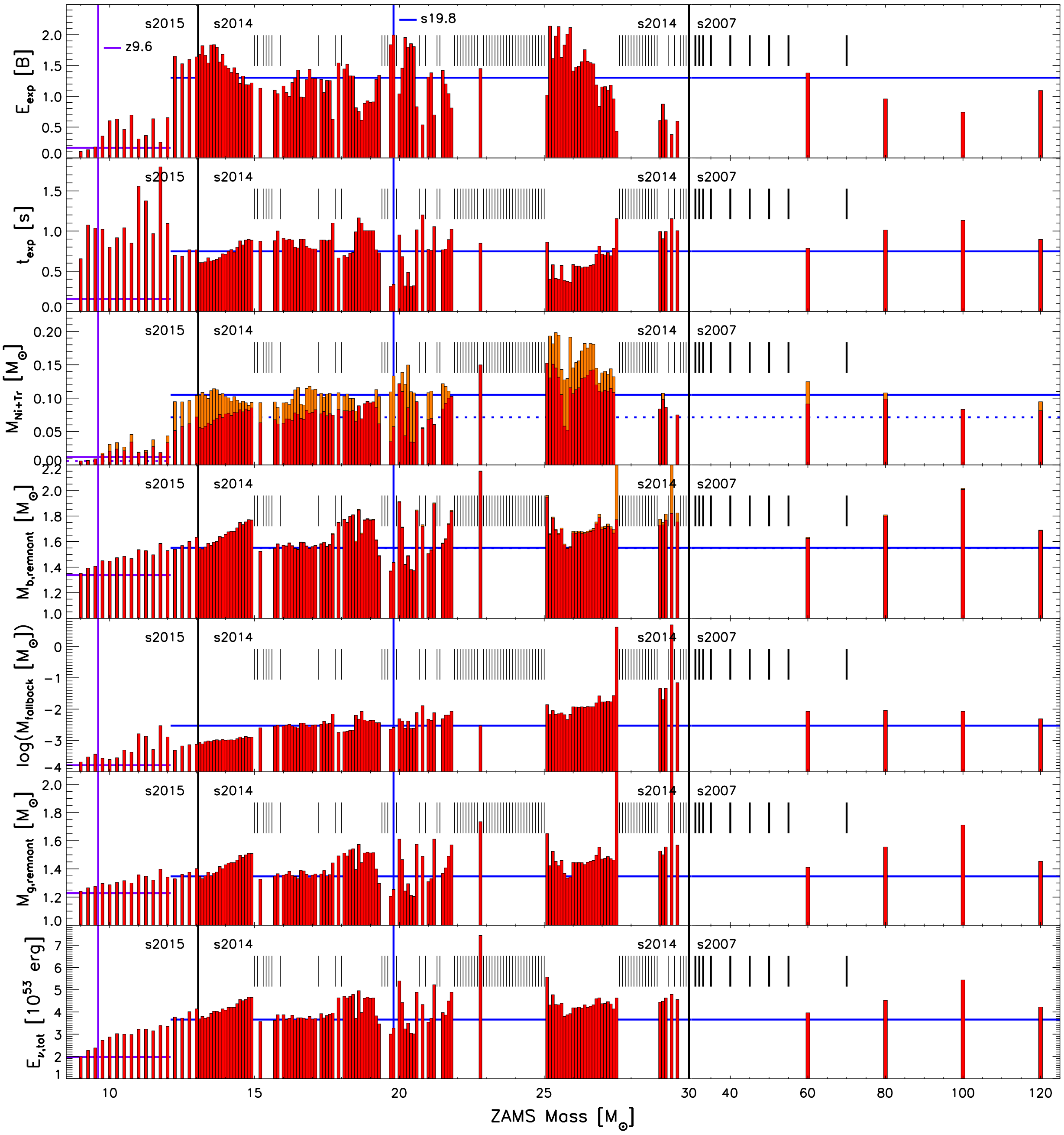
s2015
s2014
s2014
s2007
z9.6
s19.8
E_{exp} [B]
0.0
0.5
1.0
1.5
2.0
t_{exp} [s]
0.0
0.5
1.0
1.5
M_{Ni+Tr} [$M_\odot$]
0.00
0.05
0.10
0.15
0.20
$M_{b,remnant}$ [$M_\odot$]
1.0
1.2
1.4
1.6
1.8
2.0
2.2
log($M_{fallback}$ [$M_\odot$])
−4
−3
−2
−1
0
$M_{g,remnant}$ [$M_\odot$]
1.0
1.2
1.4
1.6
1.8
2.0
$E_{\nu,tot}$ [10^{53} erg]
1
2
3
4
5
6
7
10
15
20
25
30
40
60
80
100
120
ZAMS Mass [$M_\odot$]

Figure B.1.: Explosion properties for all models exploded with the z9.6 and s19.8 calibrations. Black vertical lines mark the boundaries between the different progenitor sets of our model sample is composed of. The panels, *from top to bottom*, show the final explosion energy, E_{exp}, in units of $1\,\mathrm{B} = 1\,\mathrm{Bethe} = 10^{51}\,\mathrm{erg}$, the time of the onset of the explosion, t_{exp}, the mass of finally ejected, explosively produced ^{56}Ni (red bars) and tracer element (orange bars), the baryonic mass of the compact remnant with the fallback mass indicated by orange sections on the bars, the fallback mass, the gravitational mass of the compact remnant, and the total energy radiated in neutrinos, $E_{\nu,\mathrm{tot}}$. The masses of the calibration models are indicated by vertical blue lines, and the corresponding results by horizontal solid or dashed blue lines, which extend over the mass ranges that are considered to have Crab-like or SN1987A-like progenitor properties, respectively. Non-exploding cases are marked by short vertical black bars in the upper half of each panel.

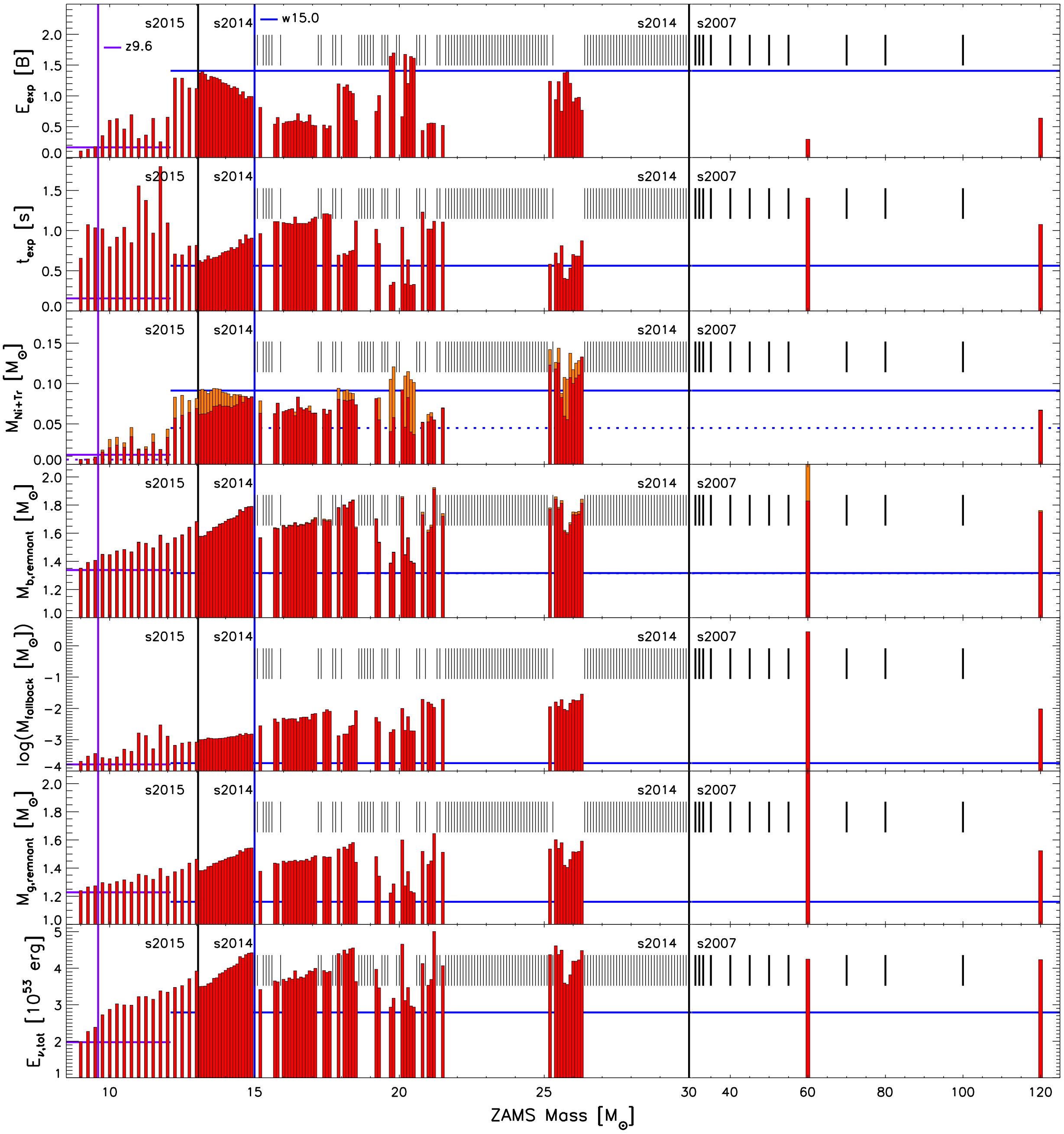

Figure B.2.: Same as Fig. B.1, but for simulations with the w15.0 calibration combined with the z9.6 calibration for low-mass stars.

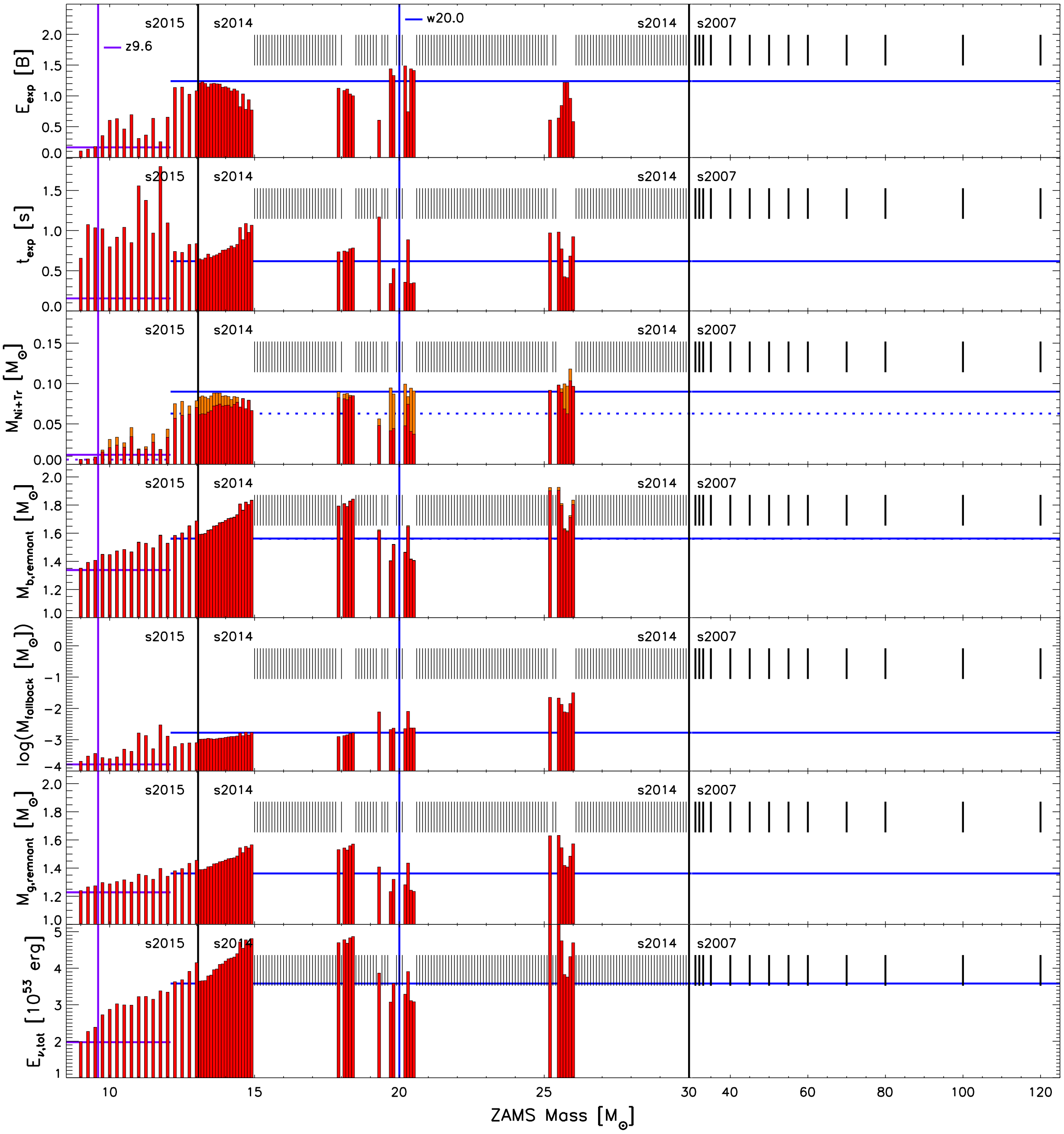

Figure B.3.: Same as Fig. B.1, but for simulations with the w20.0 calibration combined with the z9.6 calibration for low-mass stars.

B.2. Solar-Metallicity Set s2002

All results of the s2002 model series are presented here with exception of the s19.8 calibration, which is present in Fig. 6.4.

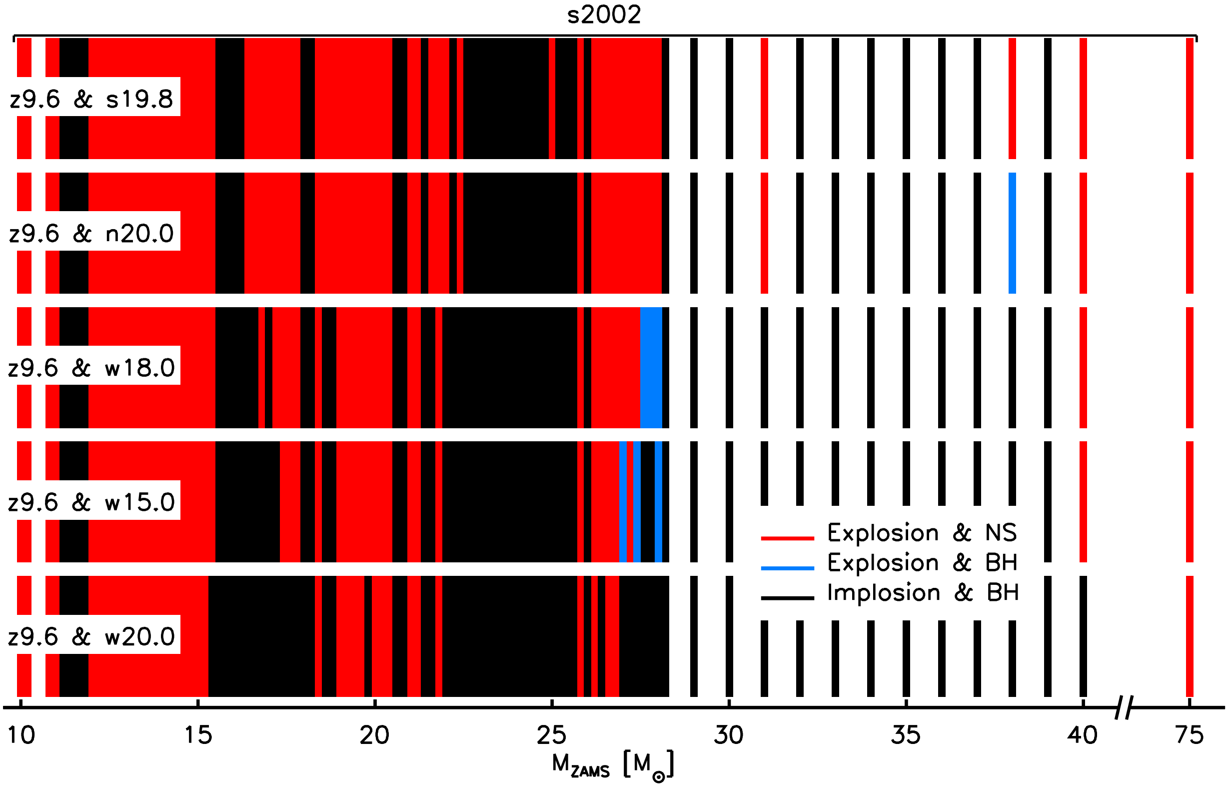

Figure B.4.: Outcome systematics for the solar-metallicity progenitor models of the s2002 series. Each row depicts the results for a certain calibration and they are sorted by the number of explosions starting with the one that yielding the most at the top. Unsuccessful cases, without revival of the stalled shock, are marked by a black bar, while cases of successful shock-revival forming a NS or a BH are by a red and a blue line, respectively. The ZAMS-mass interval of the progenitor models is 0.2 $M_\odot$ starting at 11.0 $M_\odot$ up to 28.2 $M_\odot$, 1.0 $M_\odot$ from 29.0 $M_\odot$ up to 40.0 $M_\odot$. There are further models at masses of 10.0 $M_\odot$, 10.2 $M_\odot$, and 75.0 $M_\odot$.

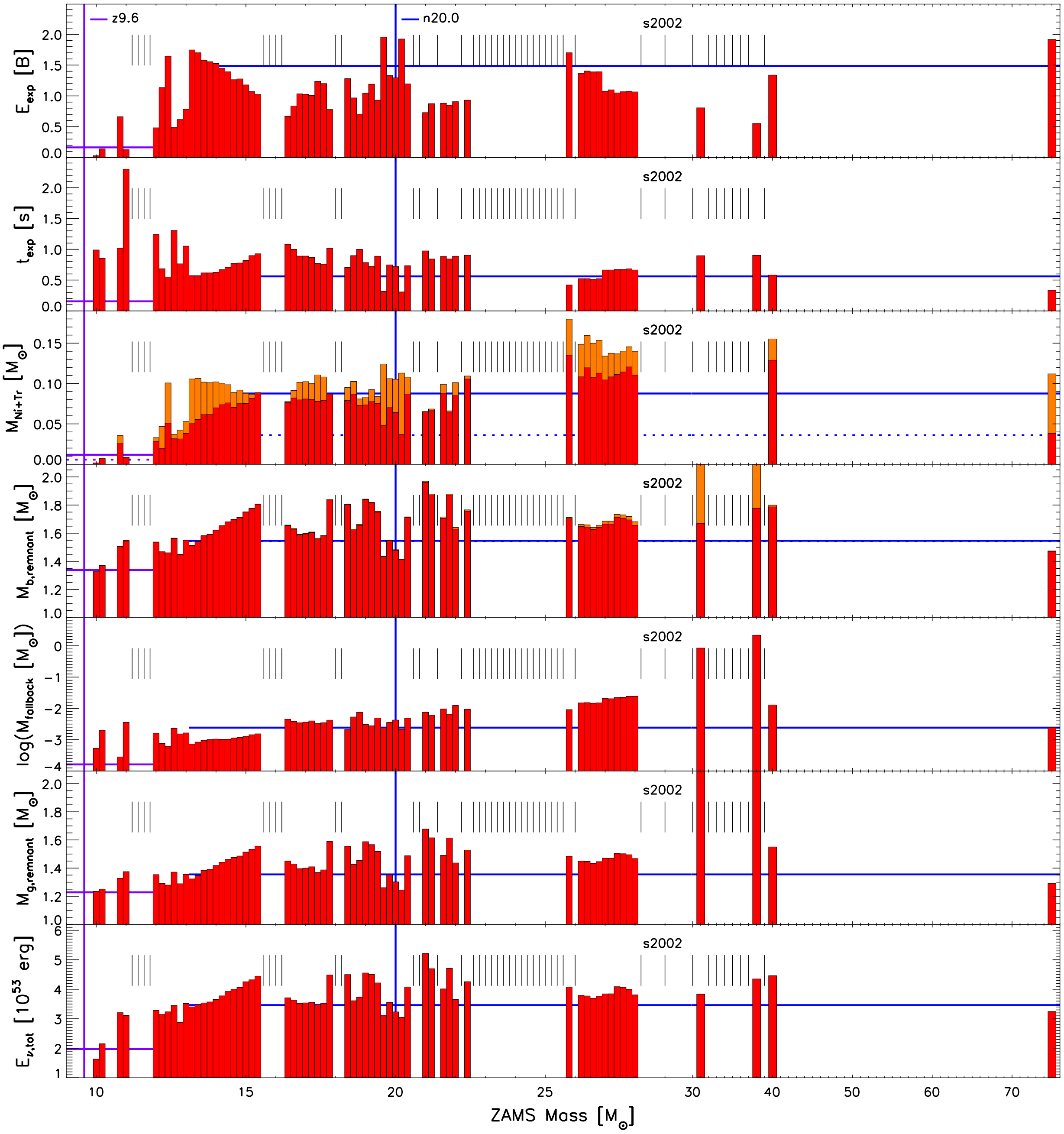

Figure B.5.: Same as Fig. B.1, but for the model set s2002 simulated with the n20.0 calibration combined with the z9.6 calibration for low-mass stars.

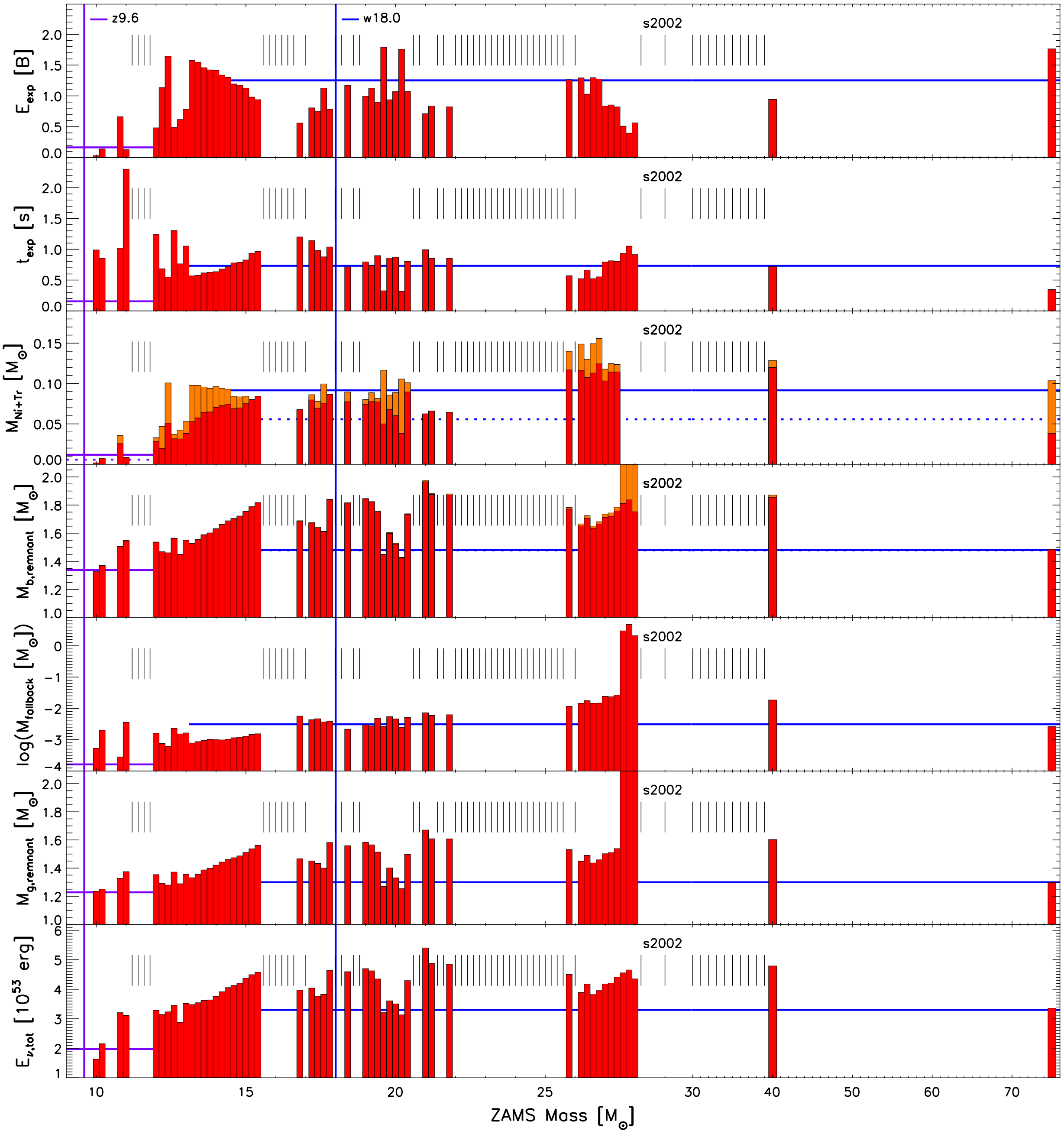

Figure B.6.: Same as Fig. B.1, but for the model set s2002 simulated with the w18.0 calibration combined with the z9.6 calibration for low-mass stars.

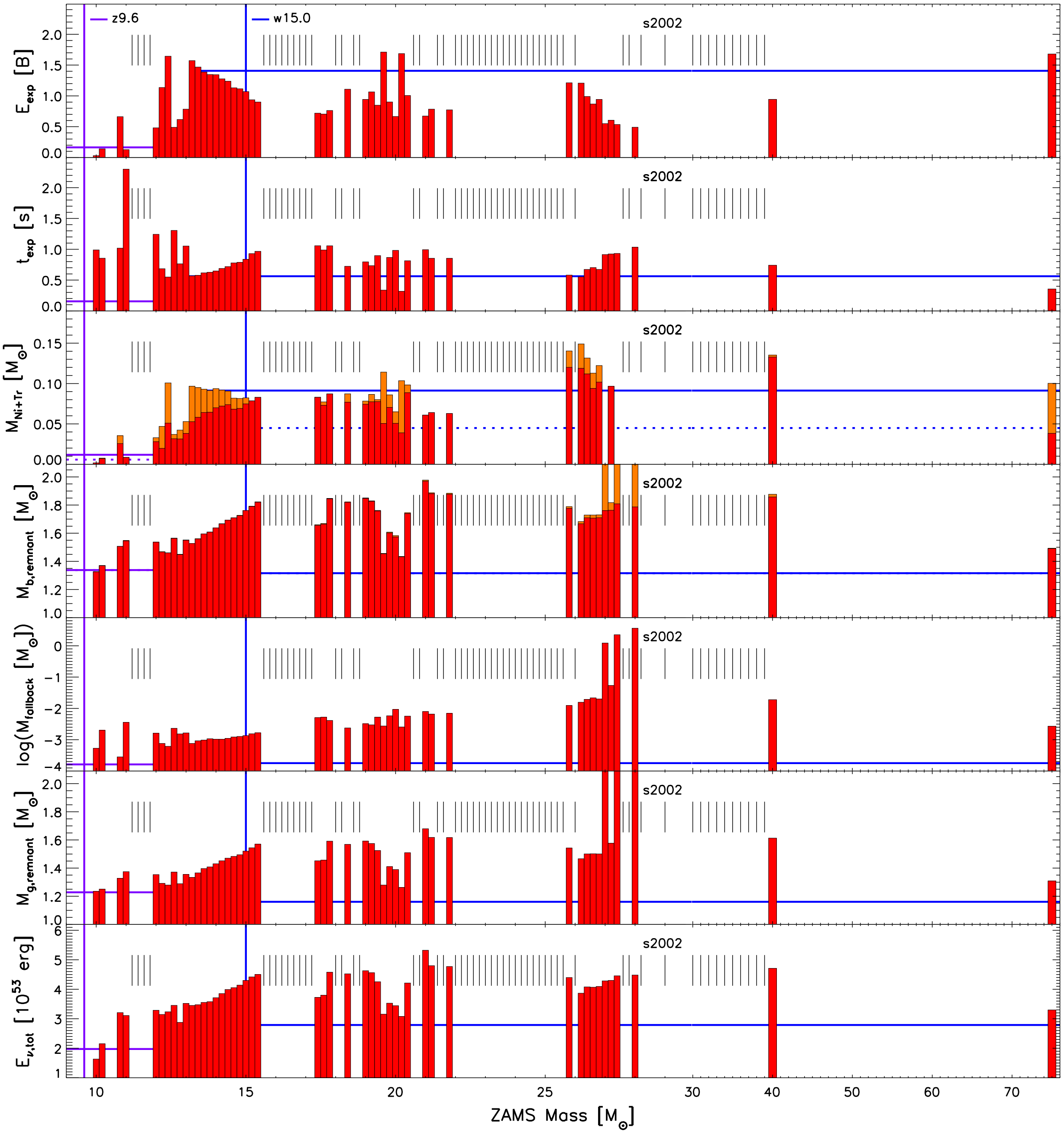

Figure B.7.: Same as Fig. B.1, but for the model set s2002 simulated with the w15.0 calibration combined with the z9.6 calibration for low-mass stars.

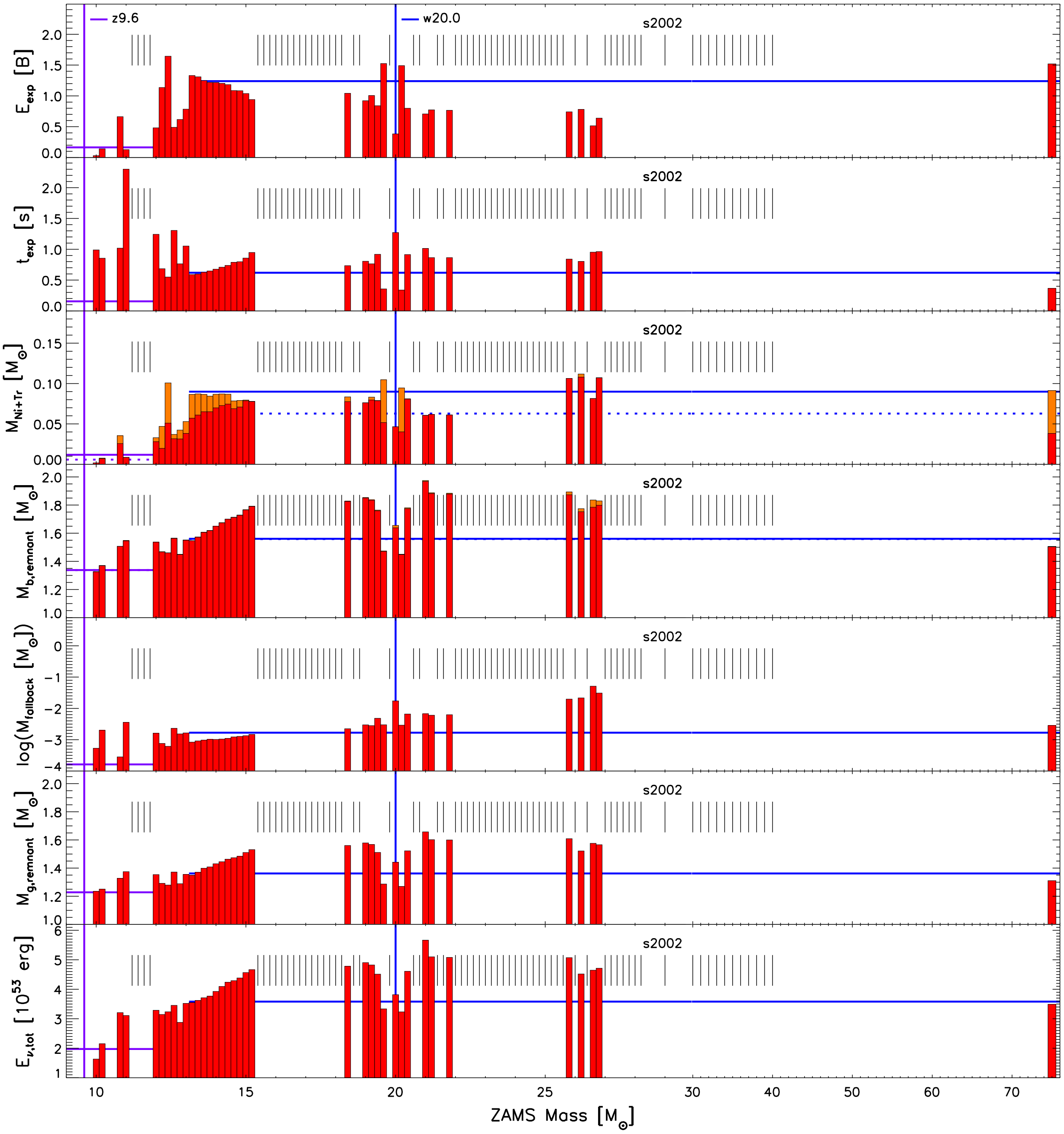

Figure B.8.: Same as Fig. B.1, but for the model set s2002 simulated with the w20.0 calibration combined with the z9.6 calibration for low-mass stars.

B.3. Solar-Metallicity Set s2007

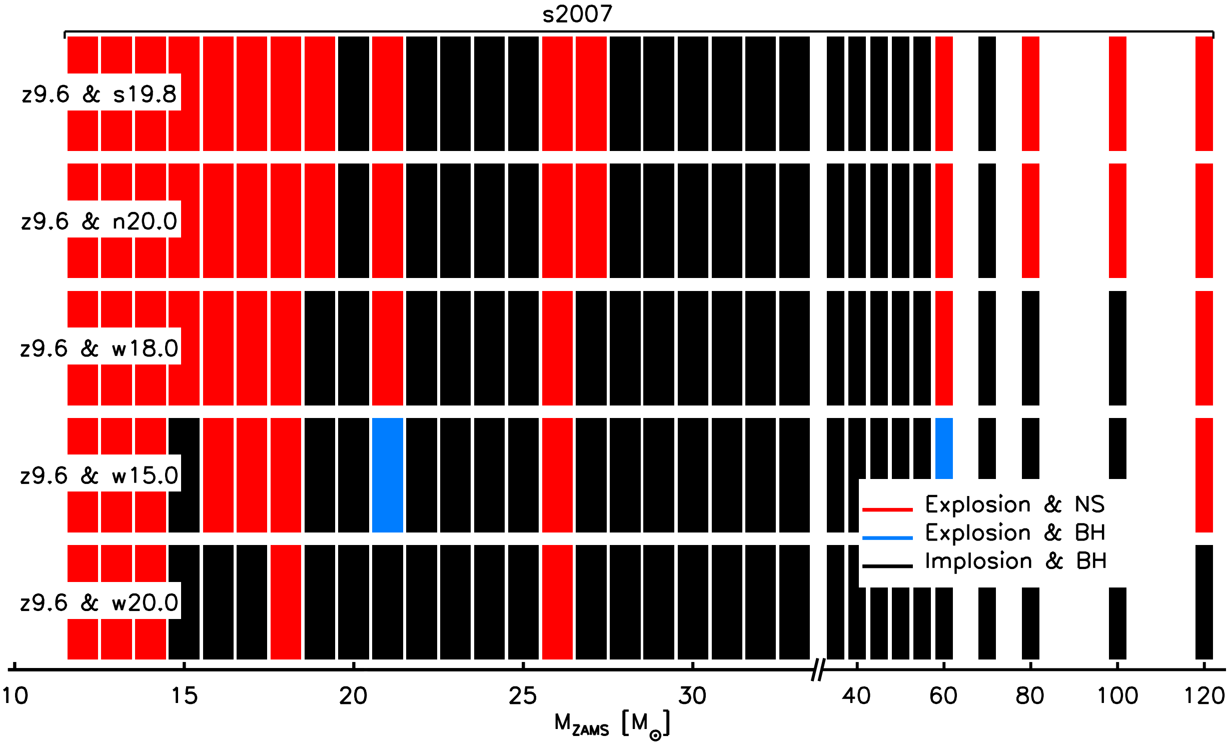

Figure B.9.: Outcome systematics for the solar-metallicity progenitor models of the s2007 series. Each row depicts the results for a certain calibration and they are sorted by the number of explosions starting with the one that yielding the most at the top. Unsuccessful cases, without revival of the stalled shock, are marked by a black bar, while cases of successful shock-revival forming a NS or a BH are by a red and a blue line, respectively. The ZAMS-mass interval of the progenitor models is $1\,M_\odot$ starting at $12\,M_\odot$ up to $33\,M_\odot$, $5\,M_\odot$ from $35\,M_\odot$ to $60\,M_\odot$, $10\,M_\odot$ up to $80\,M_\odot$, and $20\,M_\odot$ to a cut-off mass of $120\,M_\odot$.

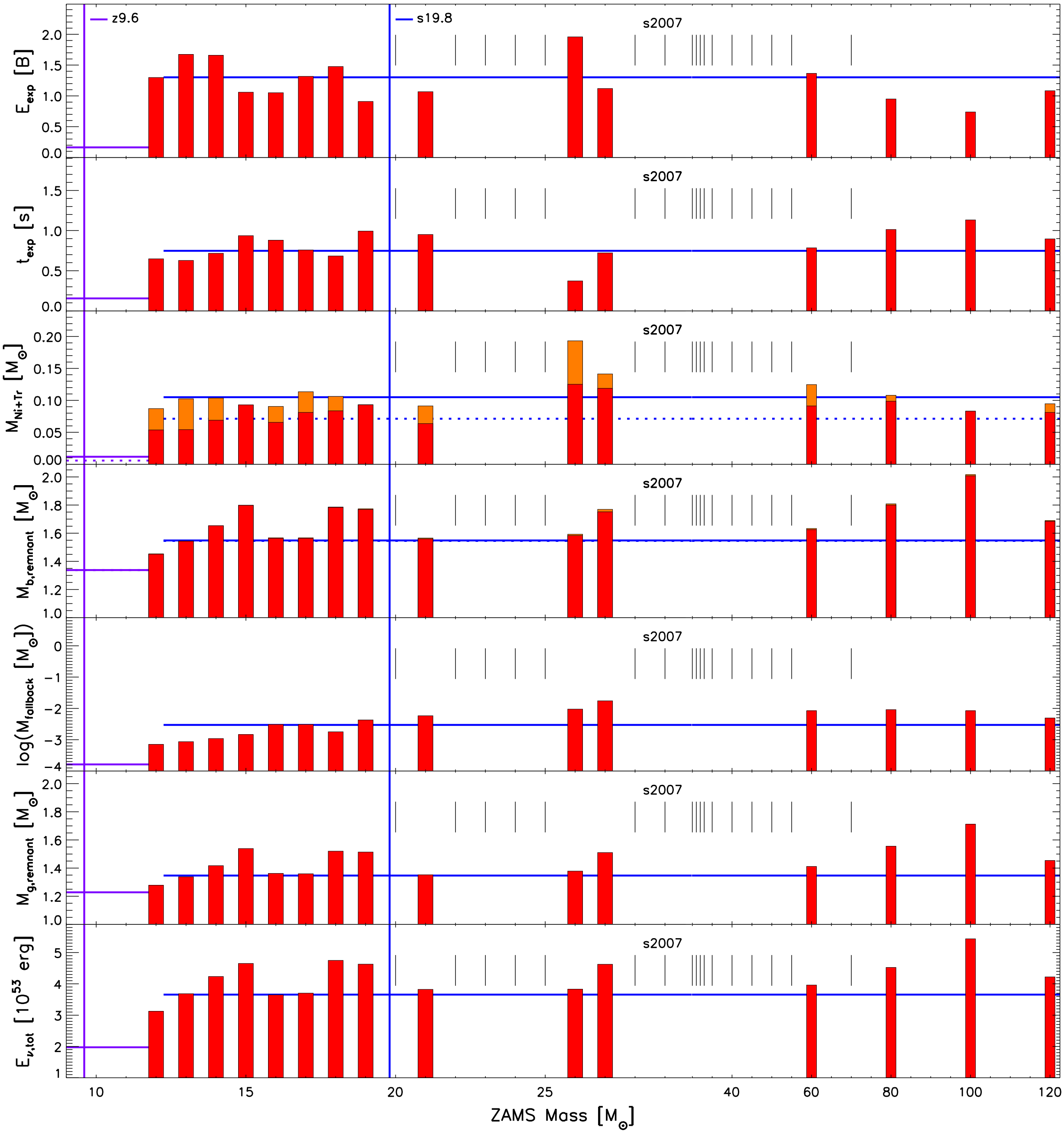

Figure B.10.: Same as Fig. B.1, but for the model set s2007 simulated with the s19.8 calibration combined with the z9.6 calibration for low-mass stars.

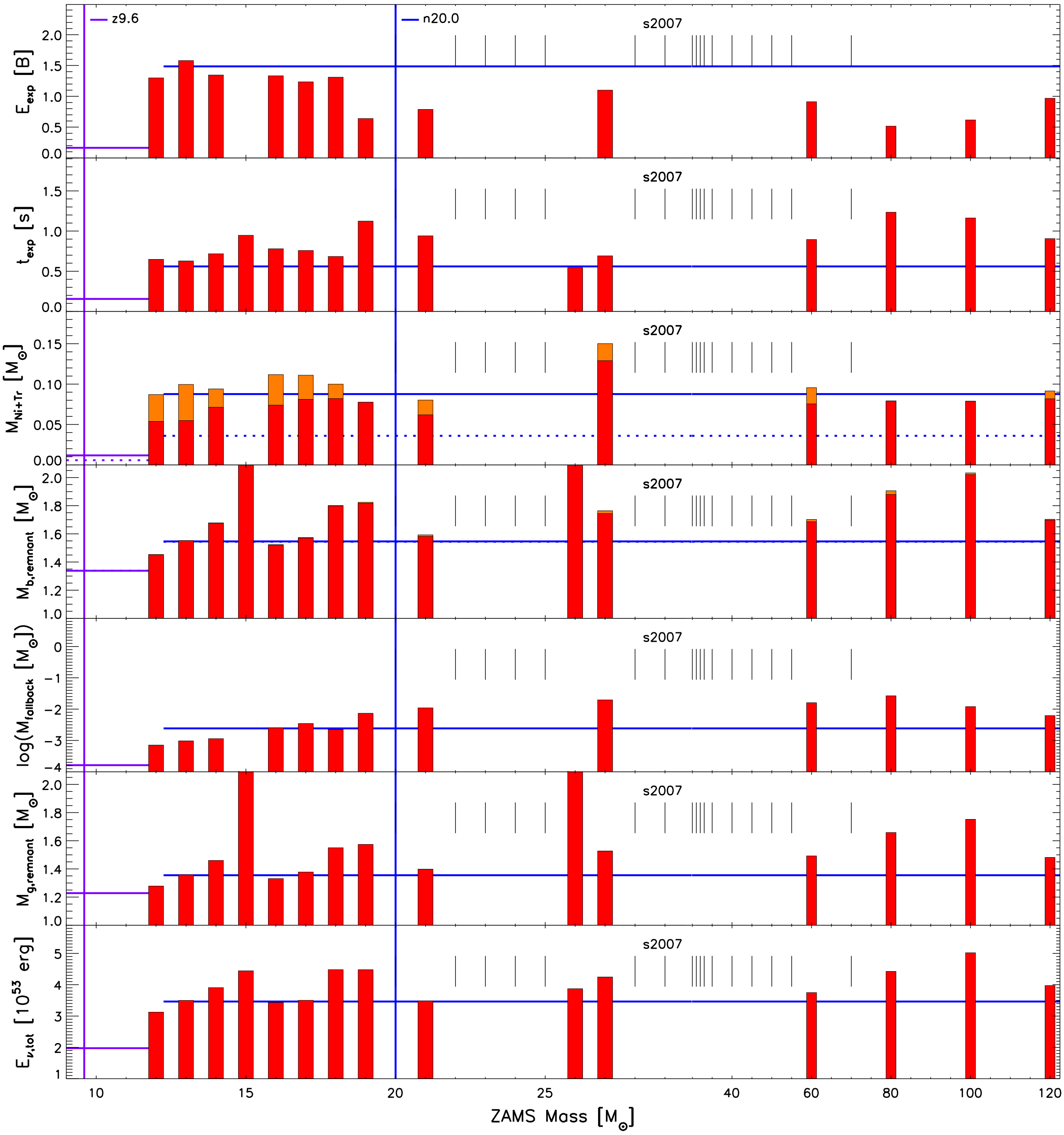

Figure B.11.: Same as Fig. B.1, but for the model set s2007 simulated with the n20.0 calibration combined with the z9.6 calibration for low-mass stars. Note that the 20 $M_\odot$ model is a non-exploding case, which might be only hardly visible in a printed version.

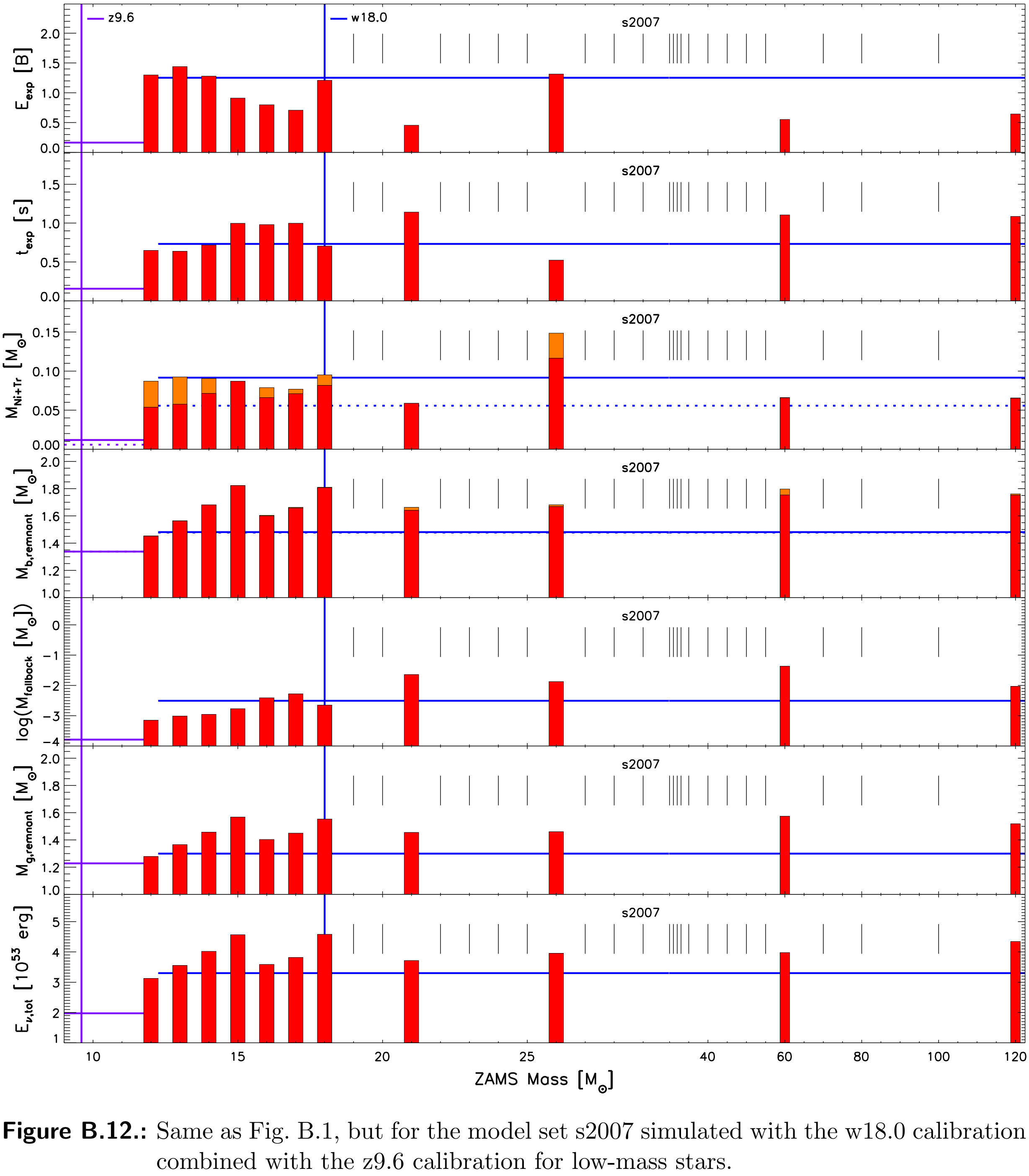

Figure B.12.: Same as Fig. B.1, but for the model set s2007 simulated with the w18.0 calibration combined with the z9.6 calibration for low-mass stars.

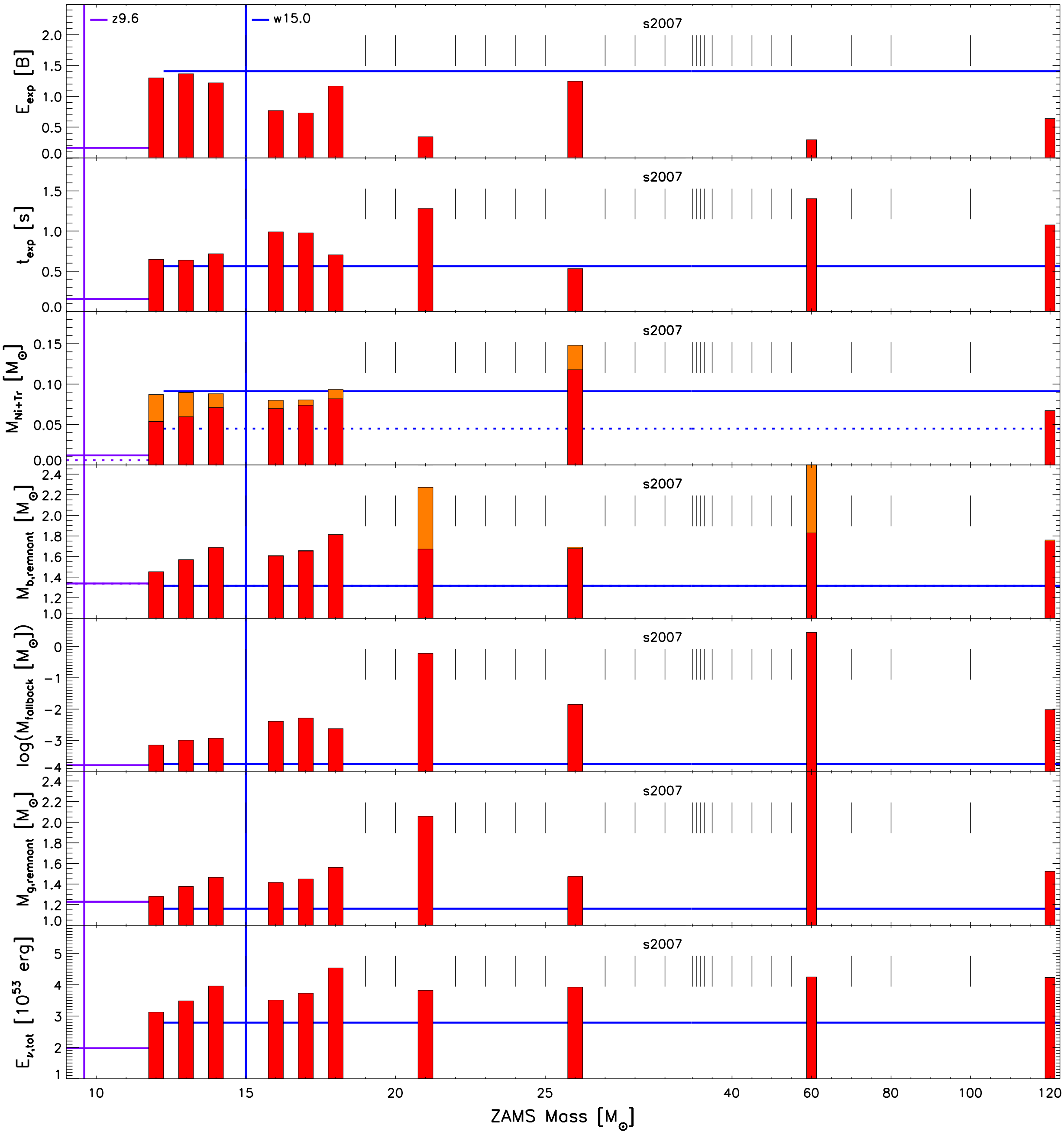

Figure B.13.: Same as Fig. B.1, but for the model set s2007 simulated with the w15.0 calibration combined with the z9.6 calibration for low-mass stars. Note that the 15 $M_\odot$ model is a non-exploding case, which might be only hardly visible in a printed version.

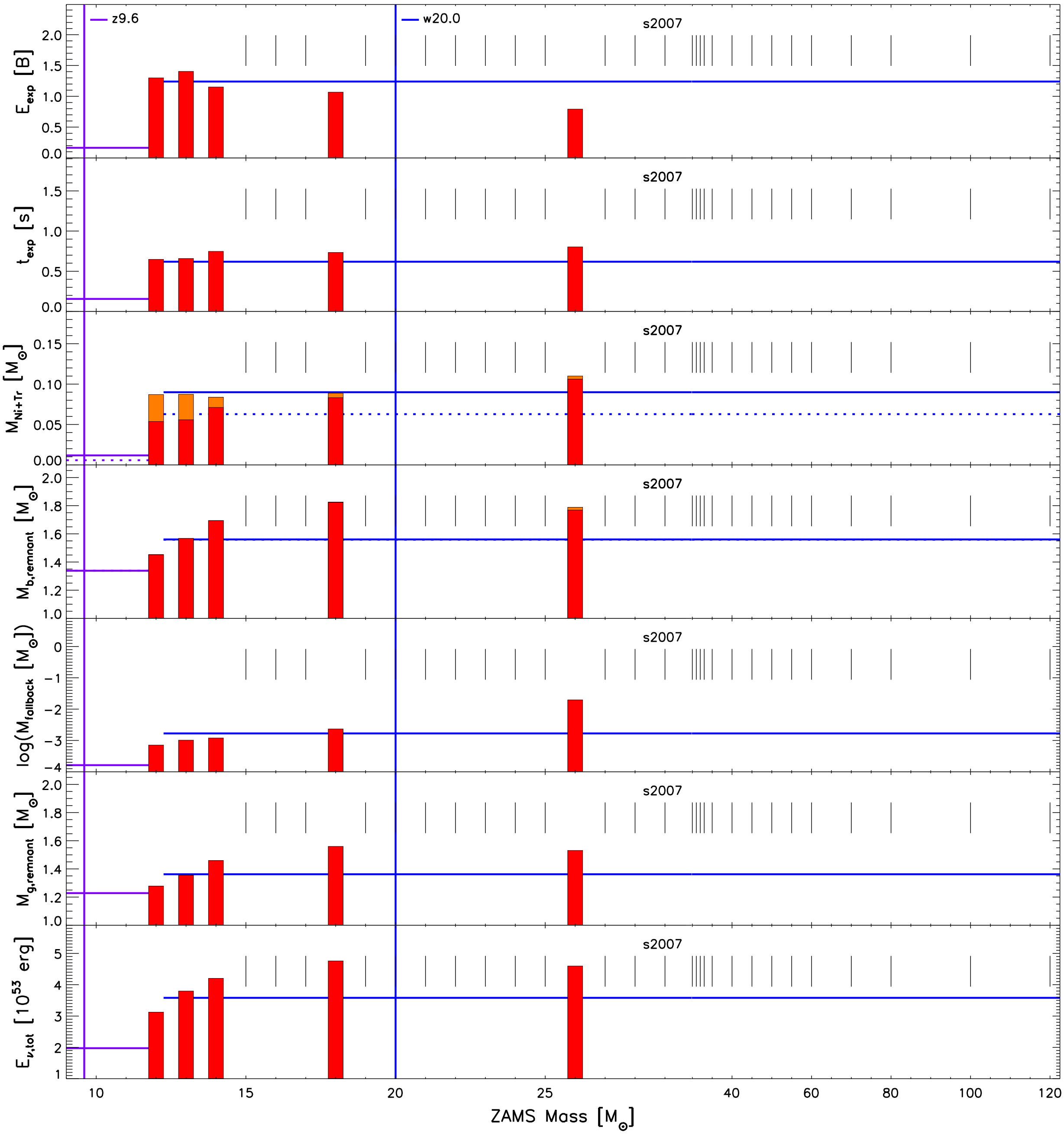

Figure B.14.: Same as Fig. B.1, but for the model set s2007 simulated with the w20.0 calibration combined with the z9.6 calibration for low-mass stars. Note that the 20 $M_\odot$ model is a non-exploding case, which might be only hardly visible in a printed version.

B.4. Solar-Metallicity Set n2006

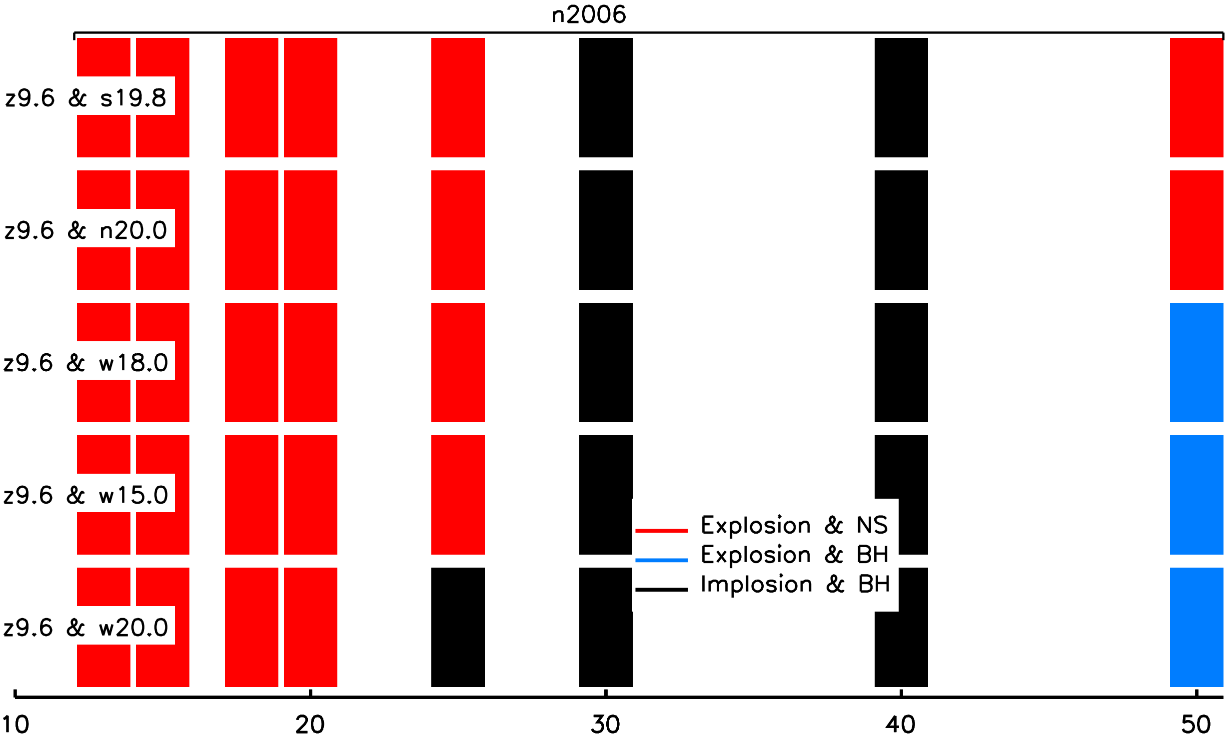

Figure B.15.: Outcome systematics for the solar-metallicity progenitor models of the n2006 series. Each row depicts the results for a certain calibration and they are sorted by the number of explosions starting with the one that yielding the most at the top. Unsuccessful cases, without revival of the stalled shock, are marked by a black bar, while cases of successful shock-revival forming a NS or a BH are by a red and a blue line, respectively. The ZAMS masses of the models are 13 $M_\odot$, 15 $M_\odot$, 18 $M_\odot$, 20 $M_\odot$, 25 $M_\odot$, 30 $M_\odot$, 40 $M_\odot$, and 50 $M_\odot$.

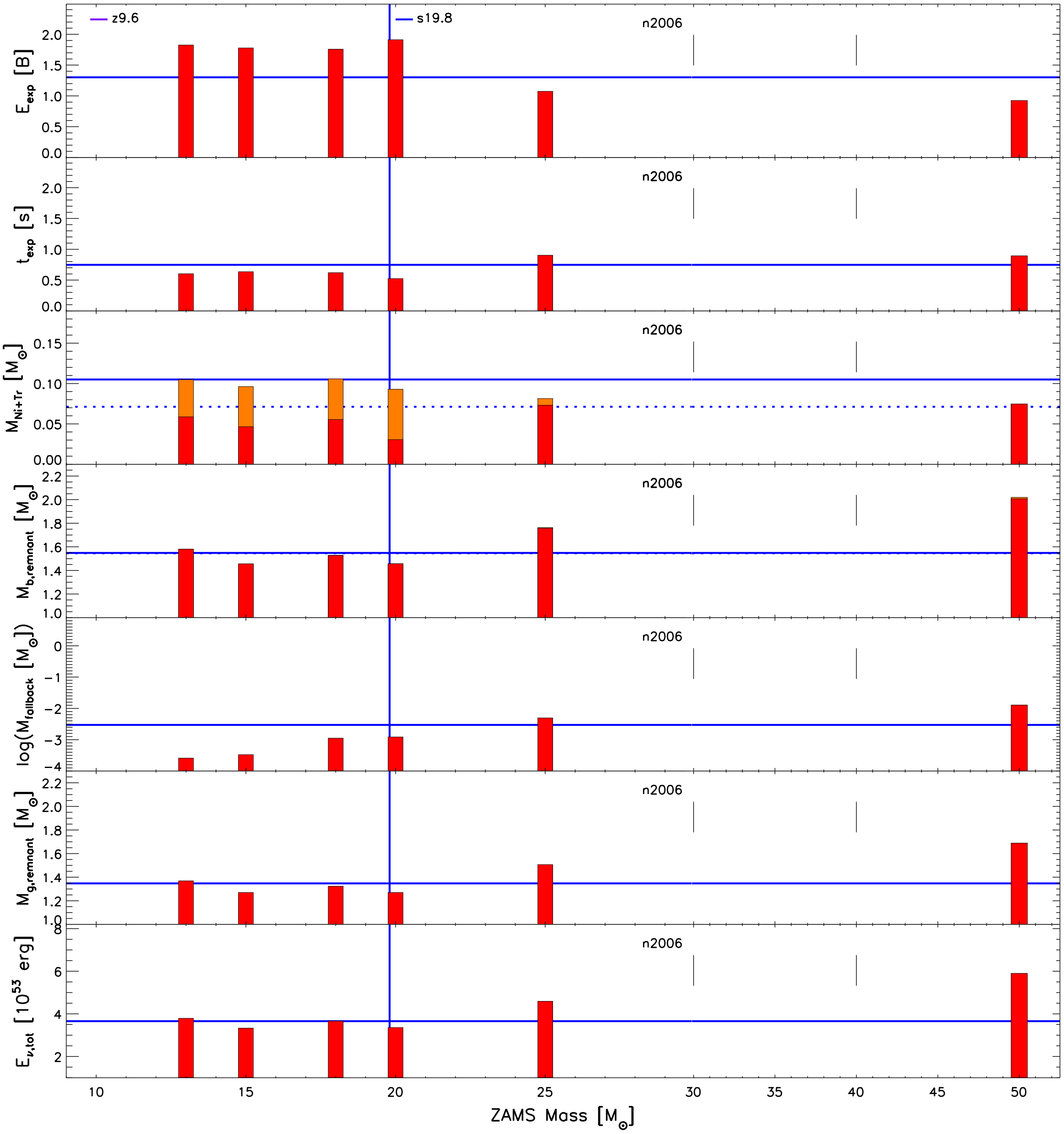

Figure B.16.: Same as Fig. B.1, but for the model set n2006 simulated with the s19.8 calibration combined with the z9.6 calibration for low-mass stars.

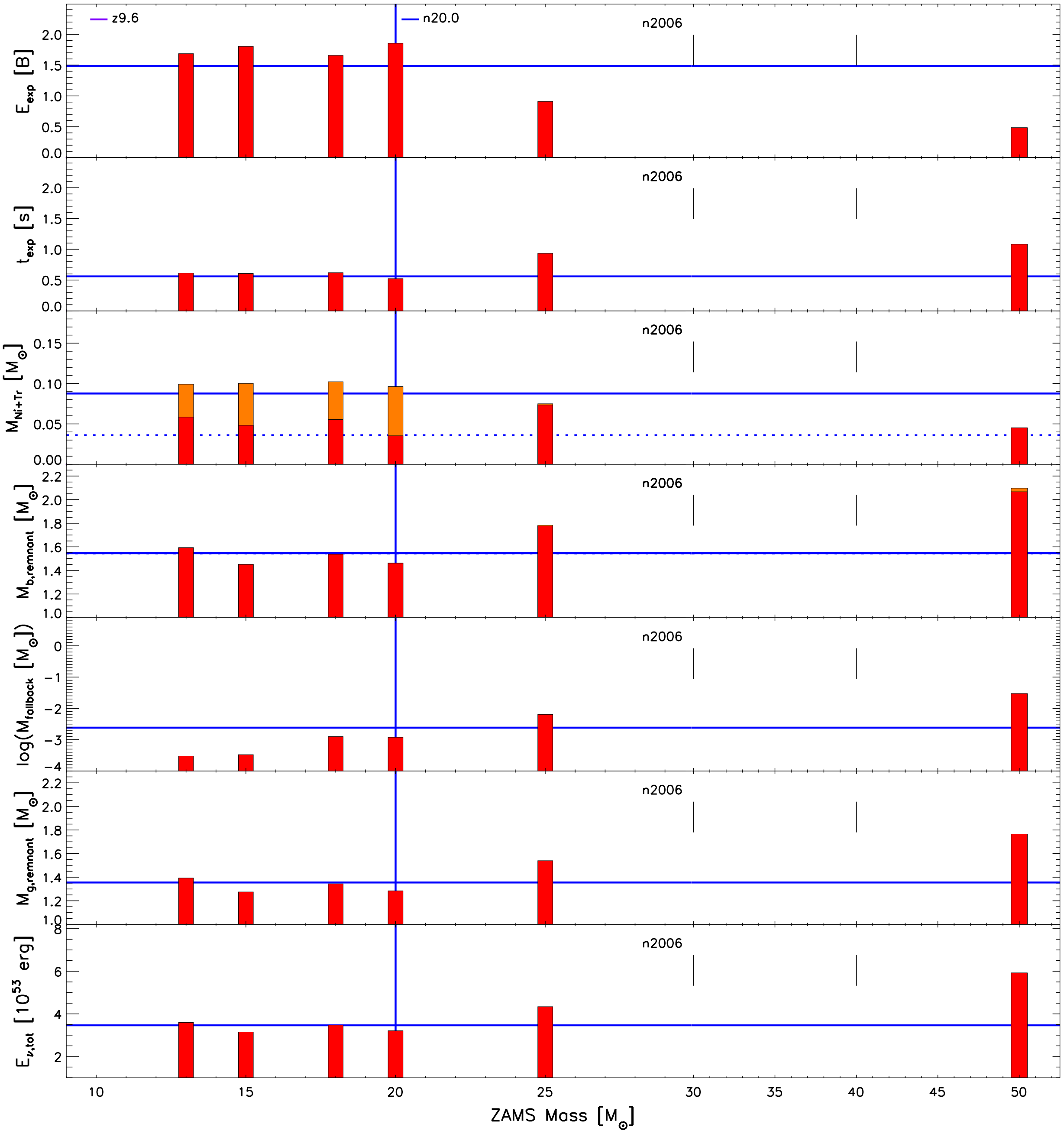

Figure B.17.: Same as Fig. B.1, but for the model set n2006 simulated with the n20.0 calibration combined with the z9.6 calibration for low-mass stars.

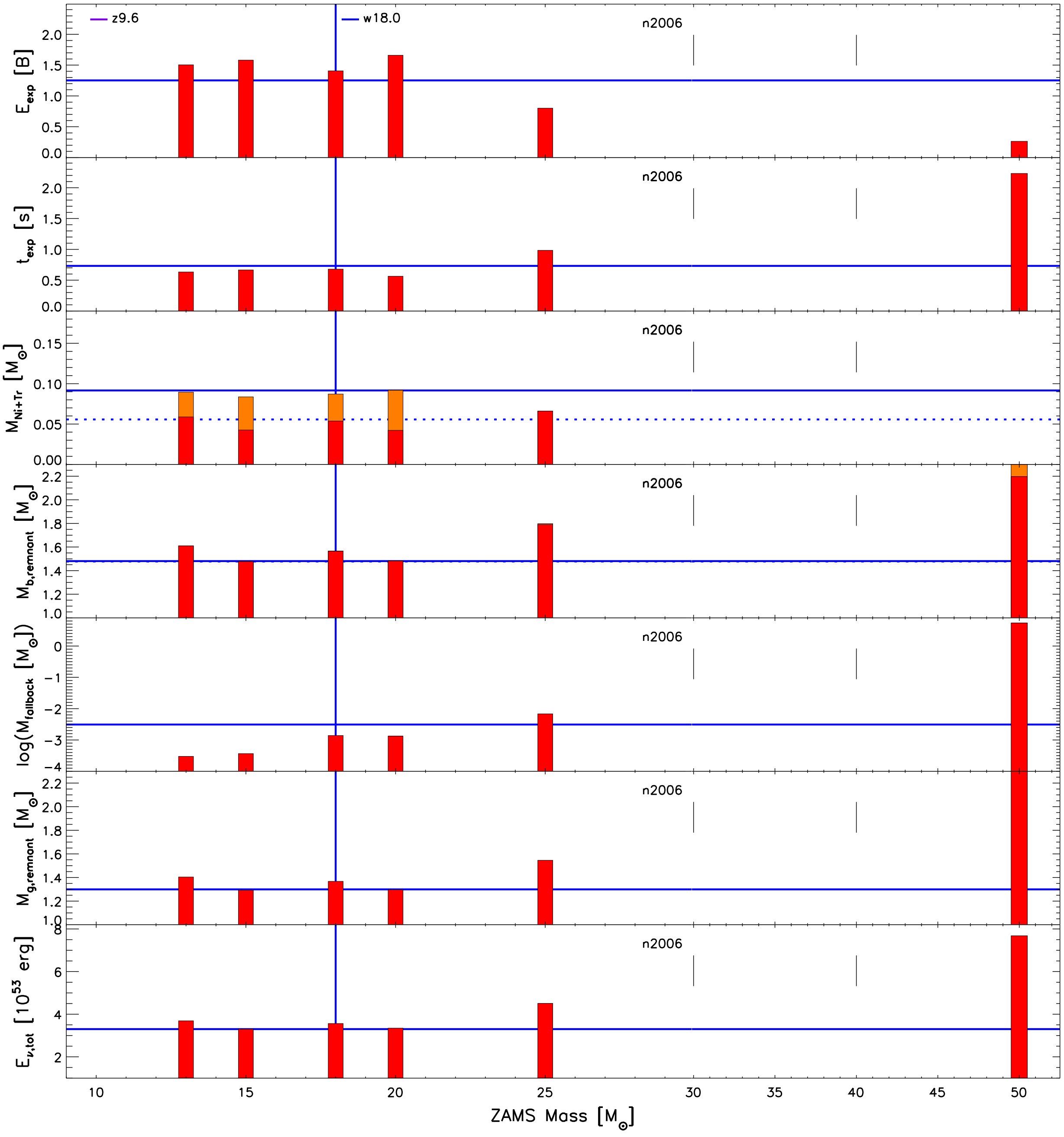

Figure B.18.: Same as Fig. B.1, but for the model set n2006 simulated with the w18.0 calibration combined with the z9.6 calibration for low-mass stars.

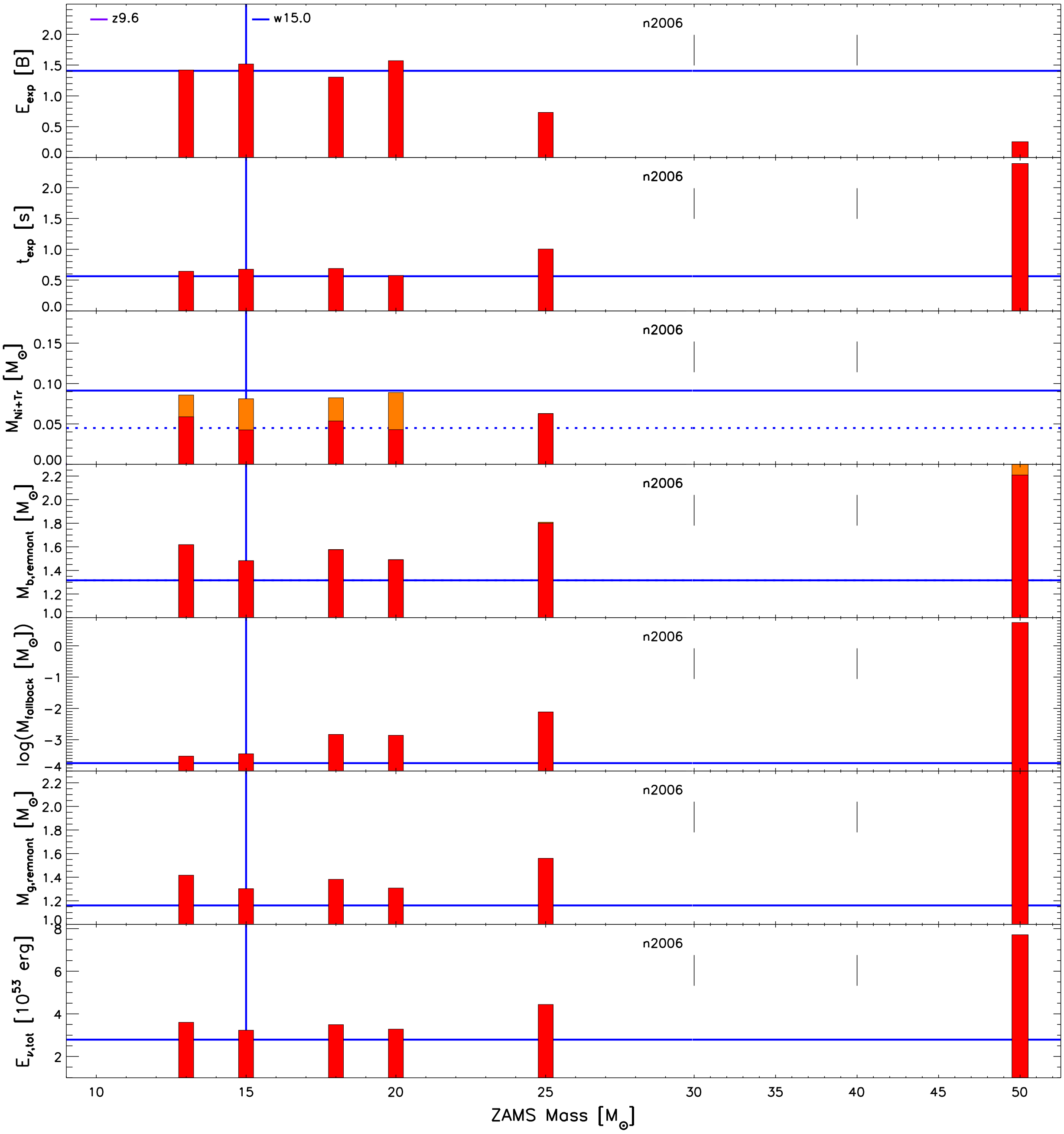

Figure B.19.: Same as Fig. B.1, but for the model set n2006 simulated with the w15.0 calibration combined with the z9.6 calibration for low-mass stars.

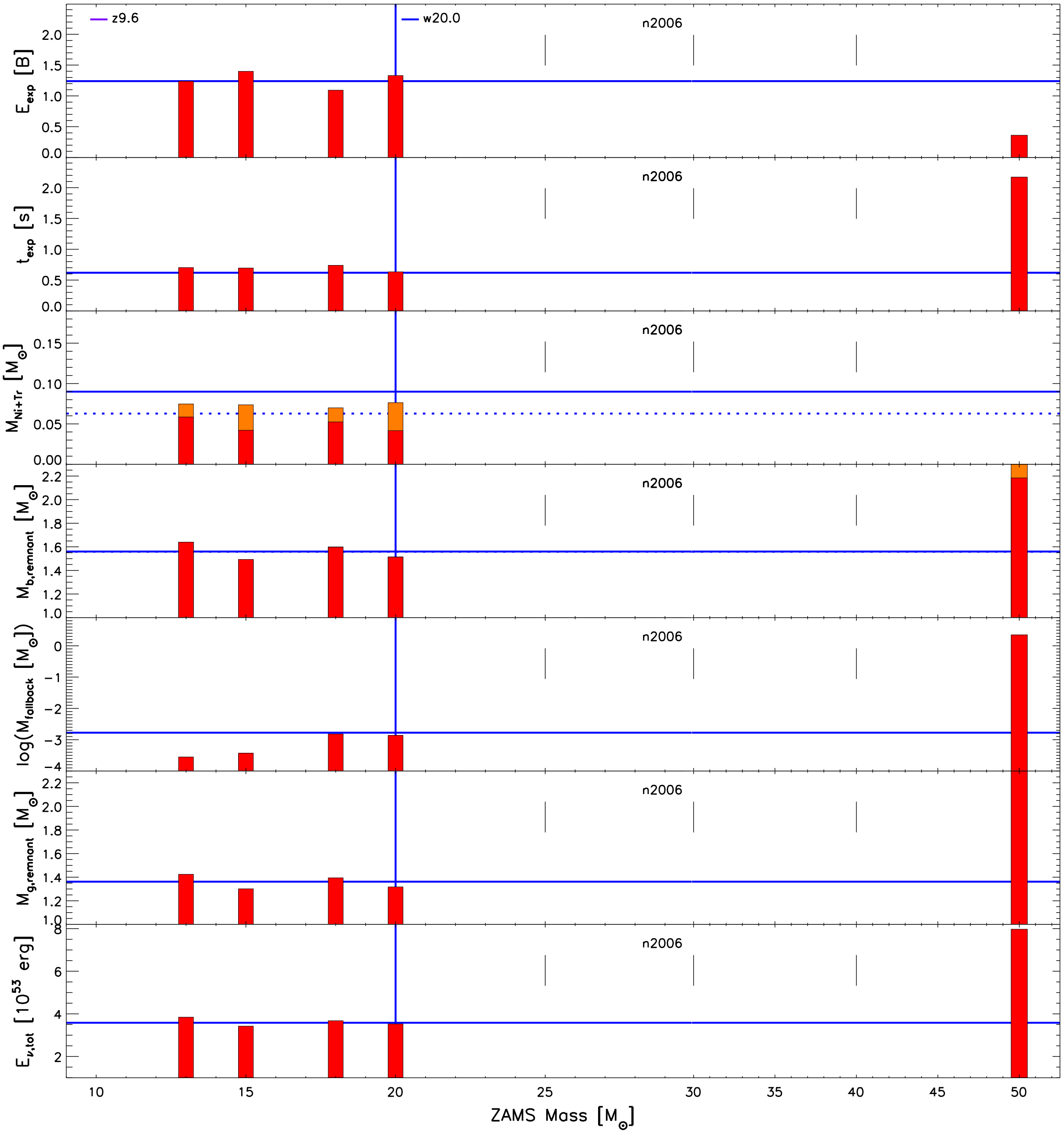

Figure B.20.: Same as Fig. B.1, but for the model set n2006 simulated with the w20.0 calibration combined with the z9.6 calibration for low-mass stars.

B.5. Ultra Metal-Poor Set u2002

Note that the outcome systematics and the w18.0 calibration are already presented in the Figs. 6.7 and 6.9, respectively.

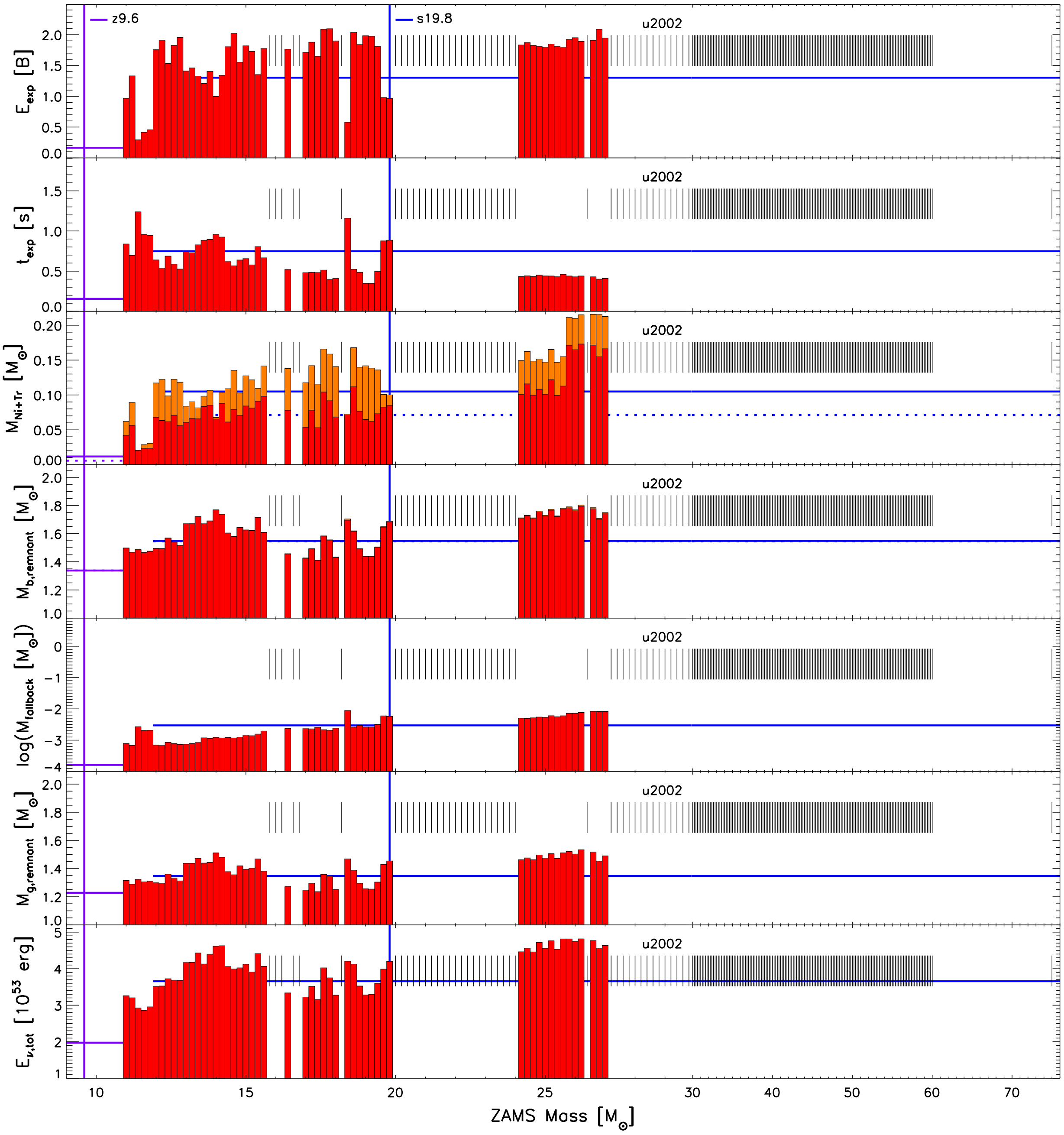

Figure B.21.: Same as Fig. B.1. The model series is u2002 with 10^{-4} solar metallicity, simulated with the z9.6 and s19.8 calibrations. The z9.6 calibration is applied up to and including the 11.8 $M_\odot$ star.

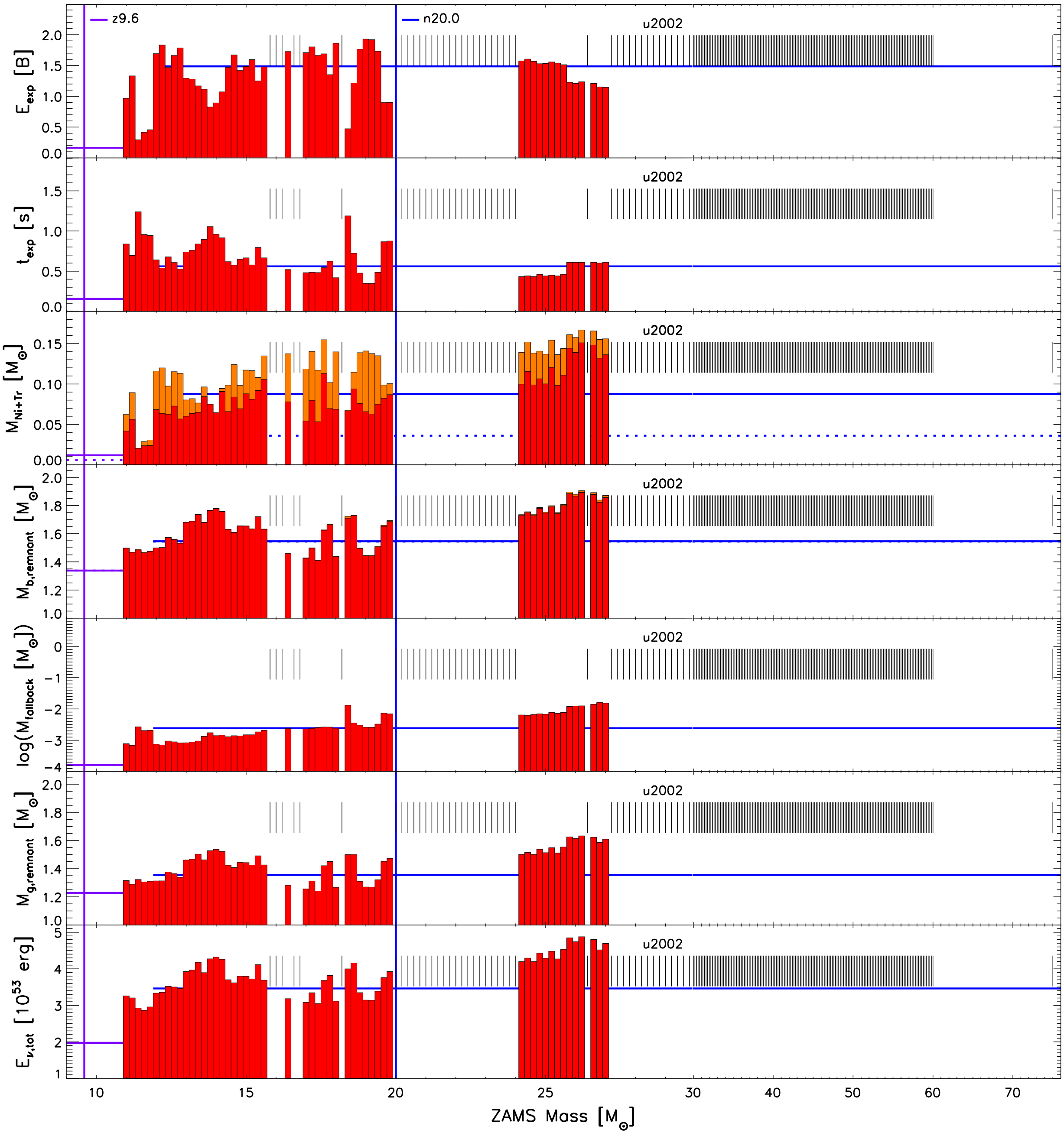

Figure B.22.: Same as Fig. B.1. The model series is u2002 with 10^{-4} solar metallicity, simulated with the z9.6 and n20.0 calibrations. The z9.6 calibration is applied up to and including the $11.8\,M_{\odot}$ star.

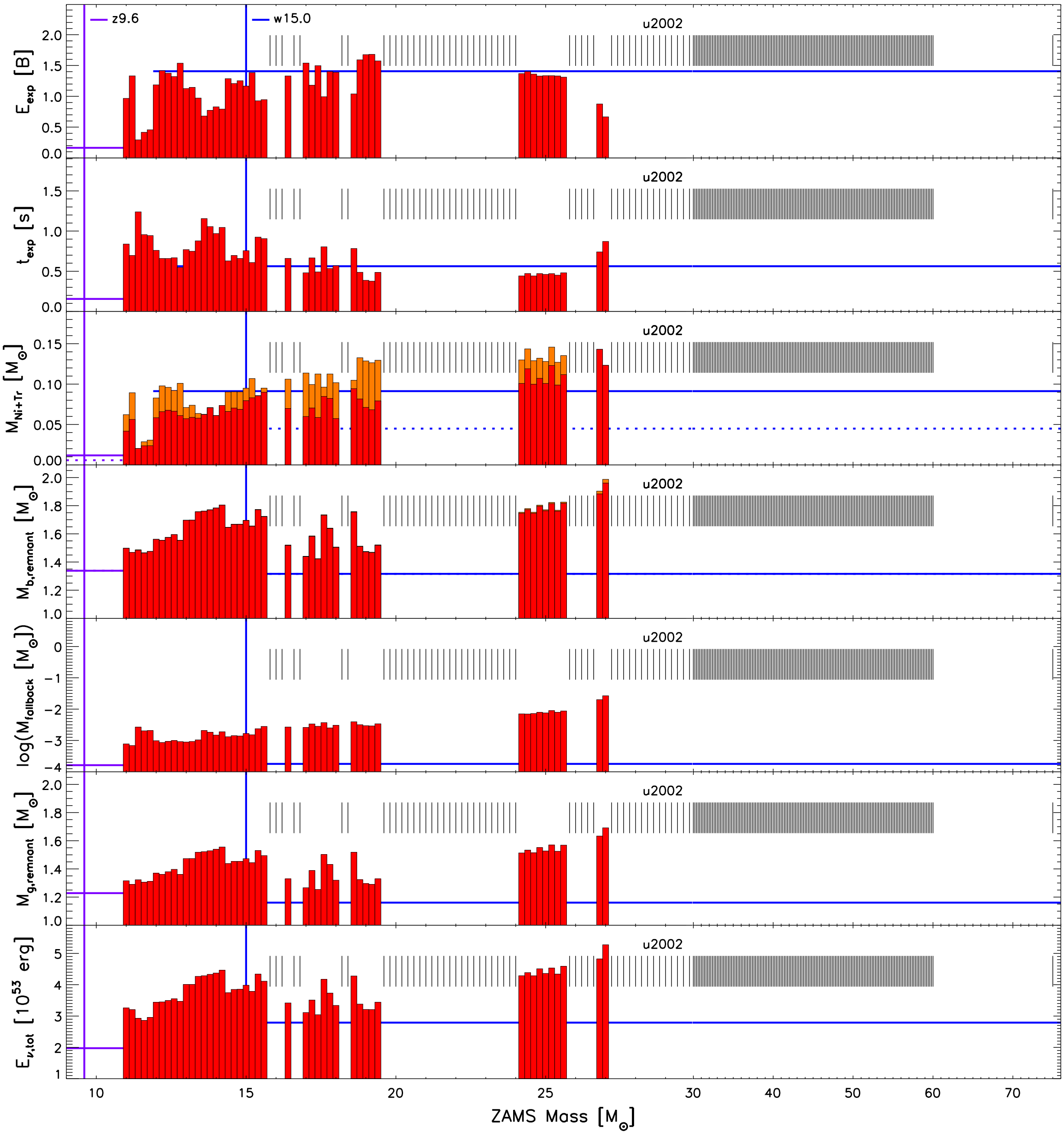

Figure B.23.: Same as Fig. B.1. The model series is u2002 with 10^{-4} solar metallicity, simulated with the z9.6 and w15.0 calibrations. The z9.6 calibration is applied up to and including the 11.8 $M_\odot$ star.

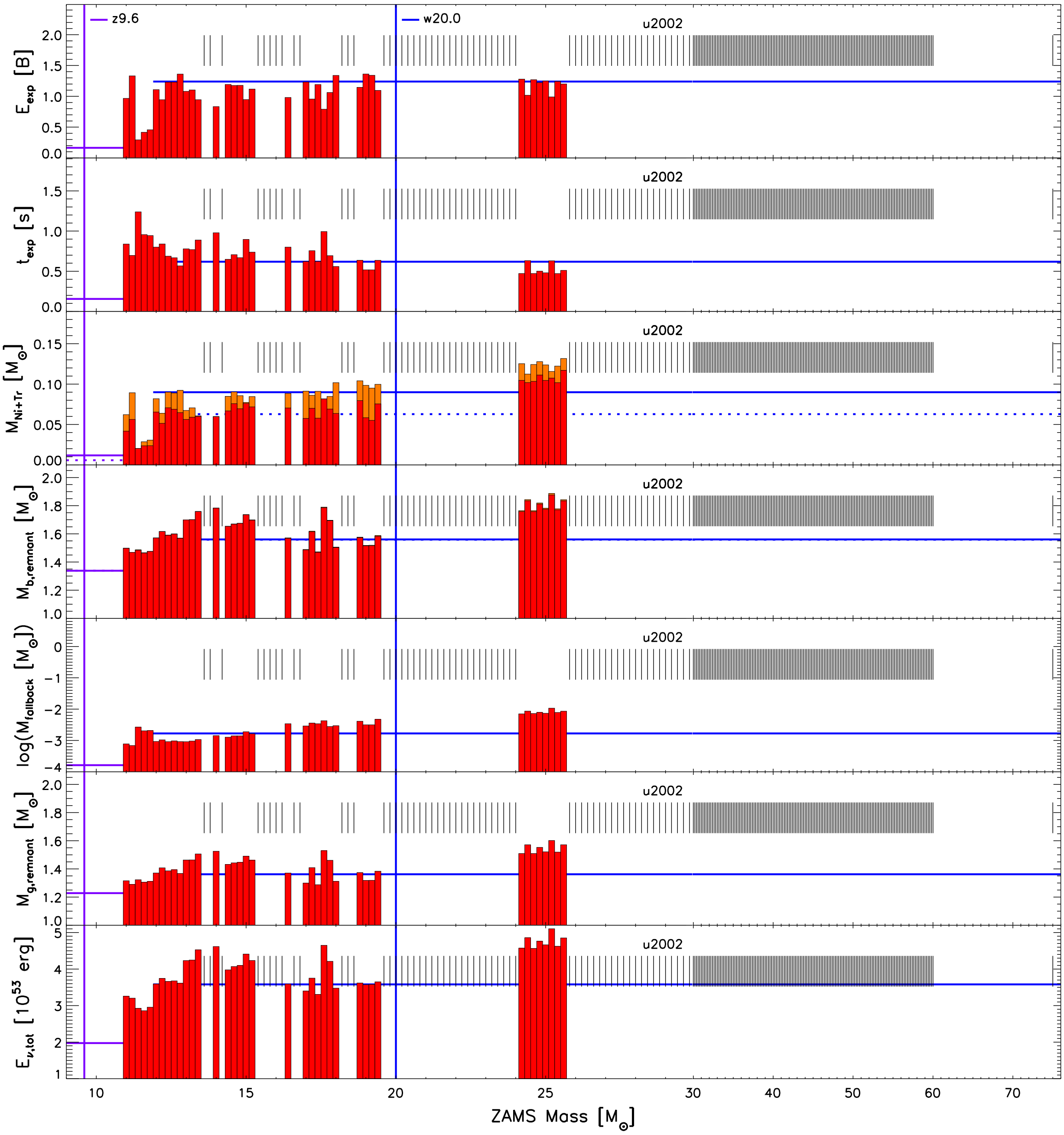

Figure B.24.: Same as Fig. B.1. The model series is u2002 with 10^{-4} solar metallicity, simulated with the z9.6 and w20.0 calibrations. The z9.6 calibration is applied up to and including the 11.8 $M_\odot$ star.

B.6. Metal-Free Set z2011

Note that the outcome systematics and the w18.0 calibration are already presented in the Figs. 6.8 and 6.10, respectively.

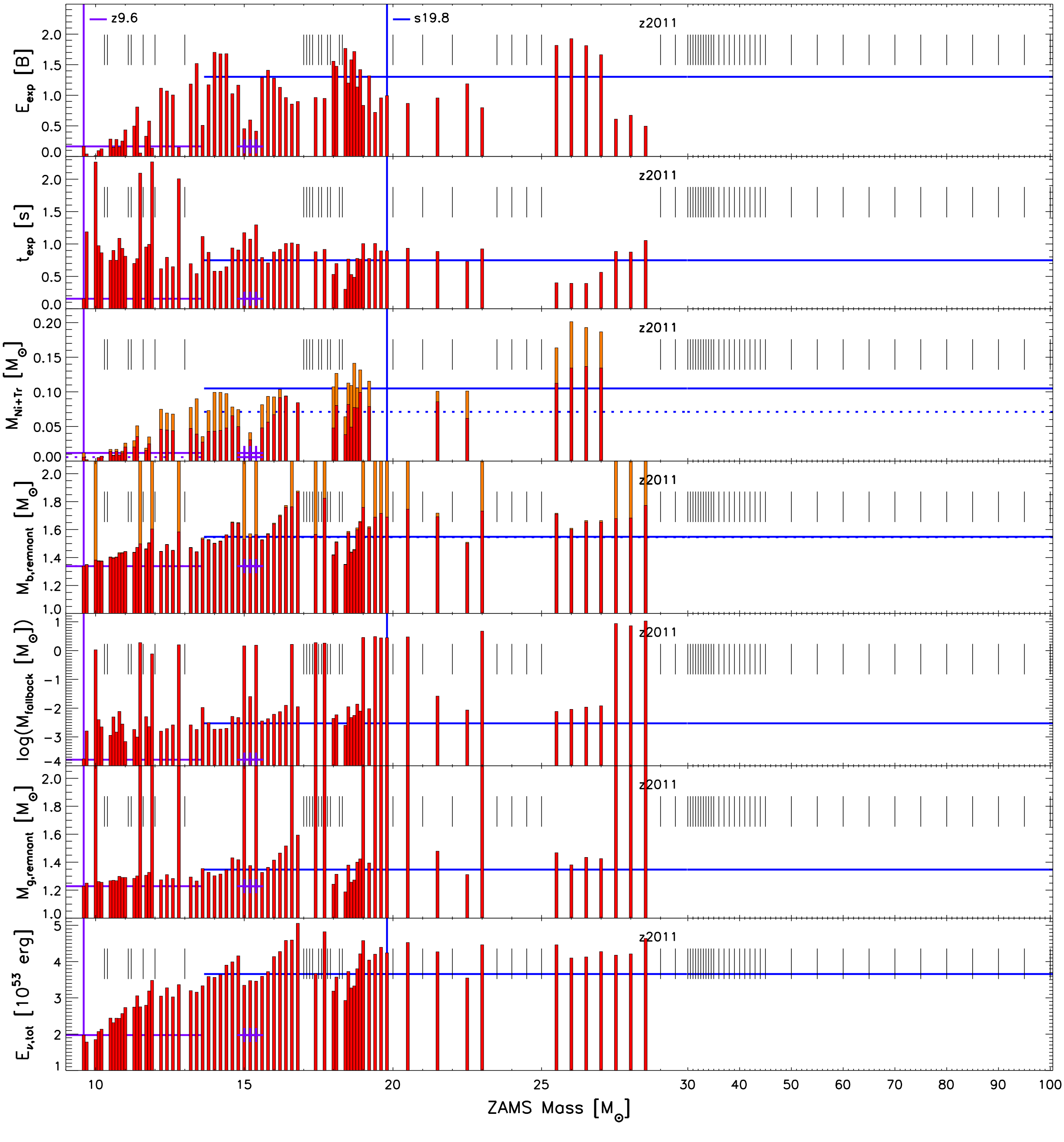

Figure B.25.: Same as Fig. B.1. The model series is z2011 with primordial metallicity, simulated with the z9.6 and s19.8 calibrations. A violet cross marks models that are also simulated with the z9.6 calibration.

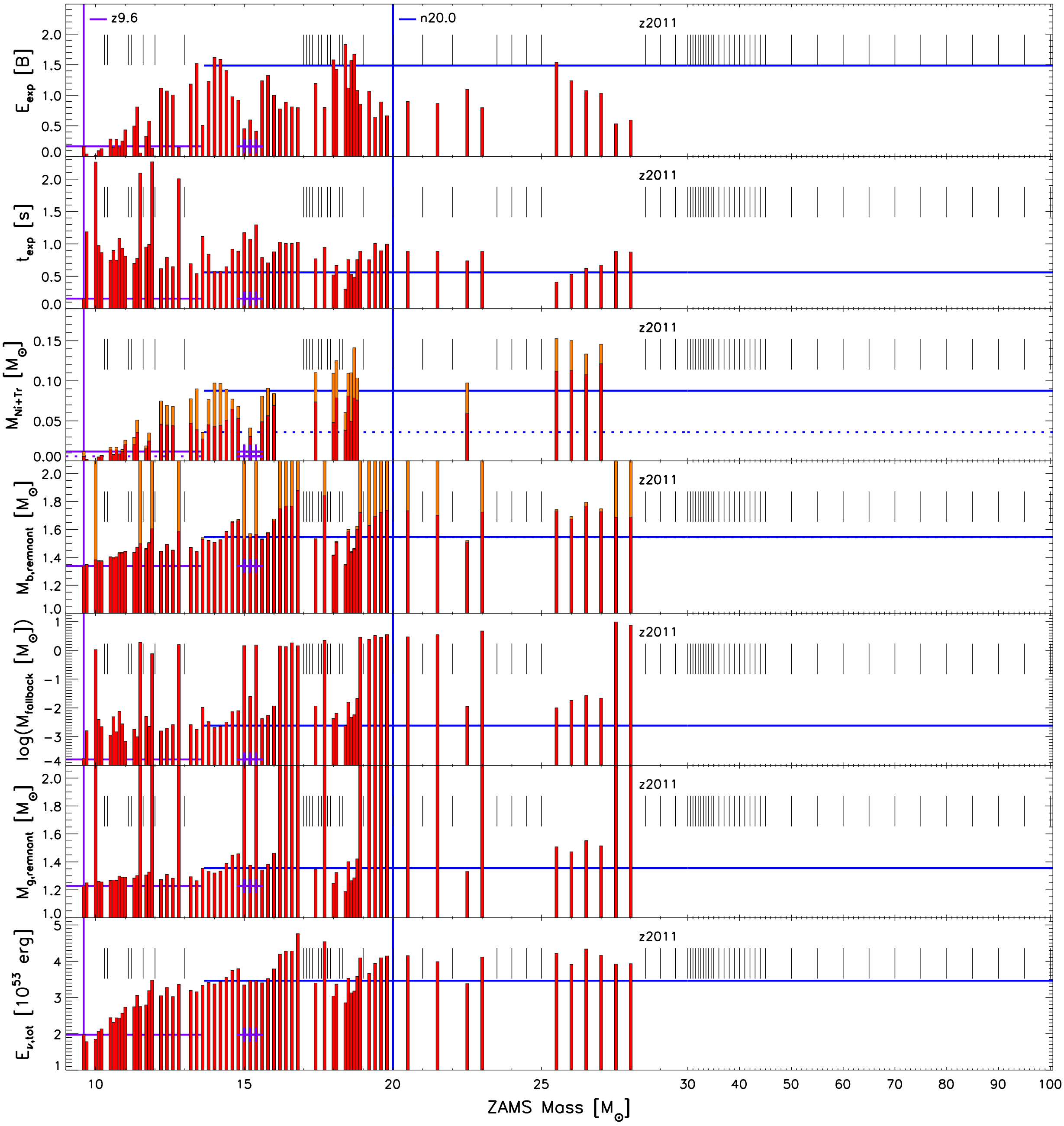

Figure B.26.: Same as Fig. 6.2. The model series is z2011 with primordial metallicity, simulated with the z9.6 and n20.0 calibrations. A violet cross marks models that are also simulated with the z9.6 calibration.

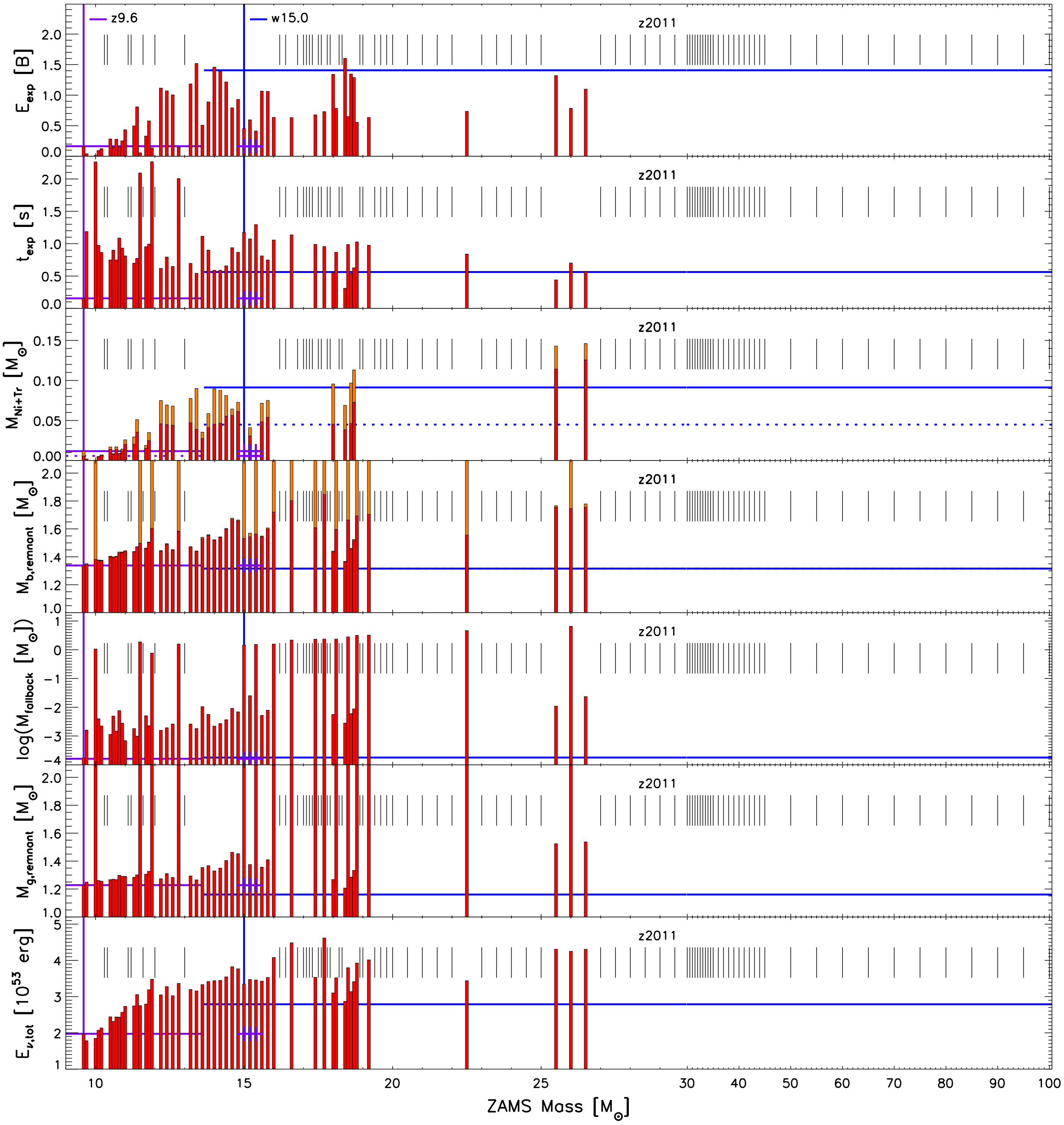

Figure B.27.: Same as Fig. B.1. The model series is z2011 with primordial metallicity, simulated with the z9.6 and w15.0 calibrations. A violet cross marks models that are also simulated with the z9.6 calibration.

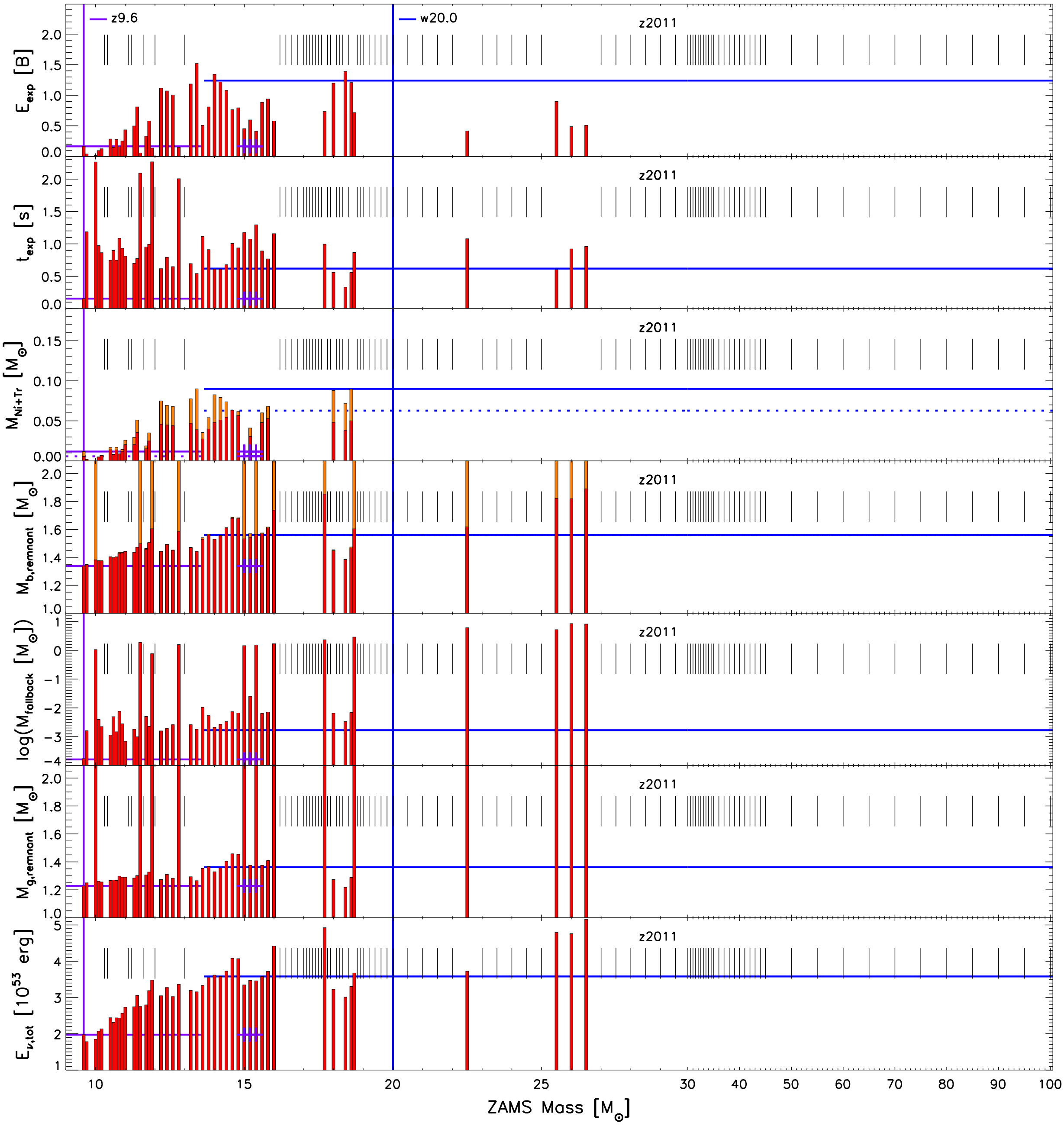

Figure B.28.: Same as Fig. B.1. The model series is z2011 with primordial metallicity, simulated with the z9.6 and w20.0 calibrations. A violet cross marks models that are also simulated with the z9.6 calibration.

B.7. Metal-Free Set z2002

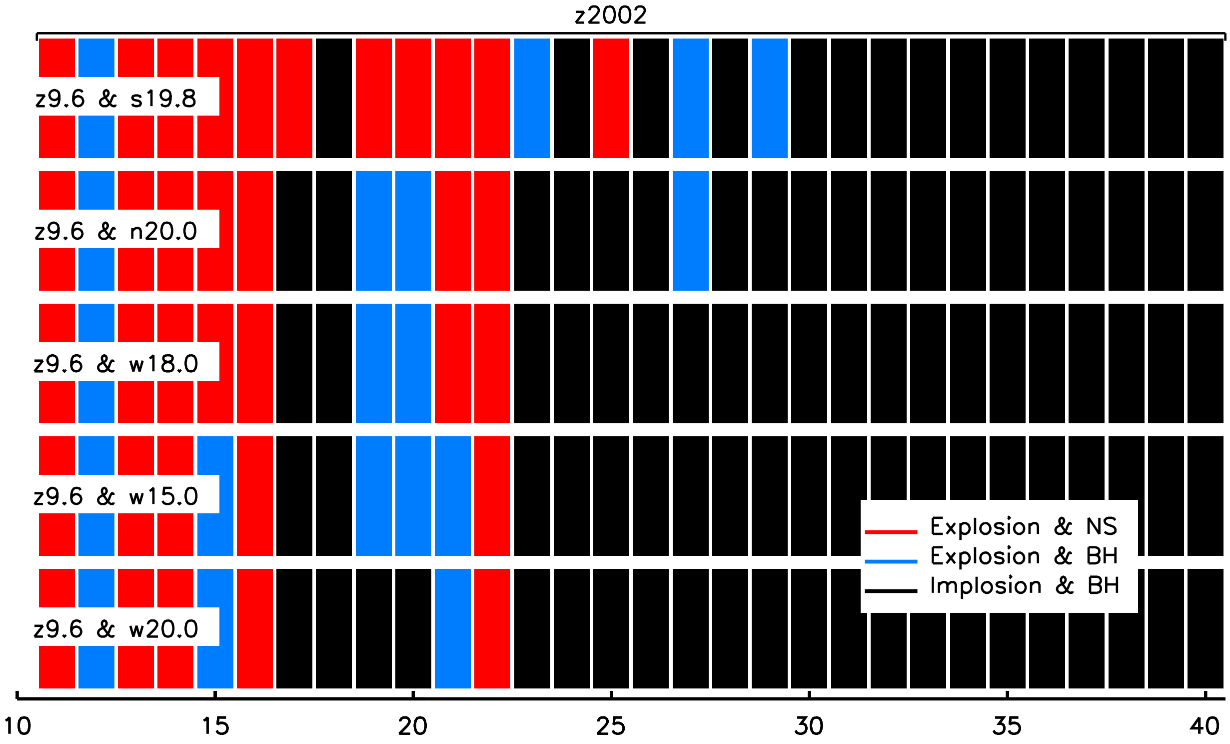

Figure B.29.: Outcome systematics for the metal-free progenitor models of the z2002 series. Each row depicts the results for a certain calibration and they are sorted by the number of explosions starting with the one that yielding the most at the top. Unsuccessful cases, without revival of the stalled shock, are marked by a black bar, while cases of successful shock-revival forming a NS or a BH are by a red and a blue line, respectively. The ZAMS-mass interval of the progenitor models is $1\,M_\odot$ starting at $11\,M_\odot$ up to a cut-off mass of $40\,M_\odot$.

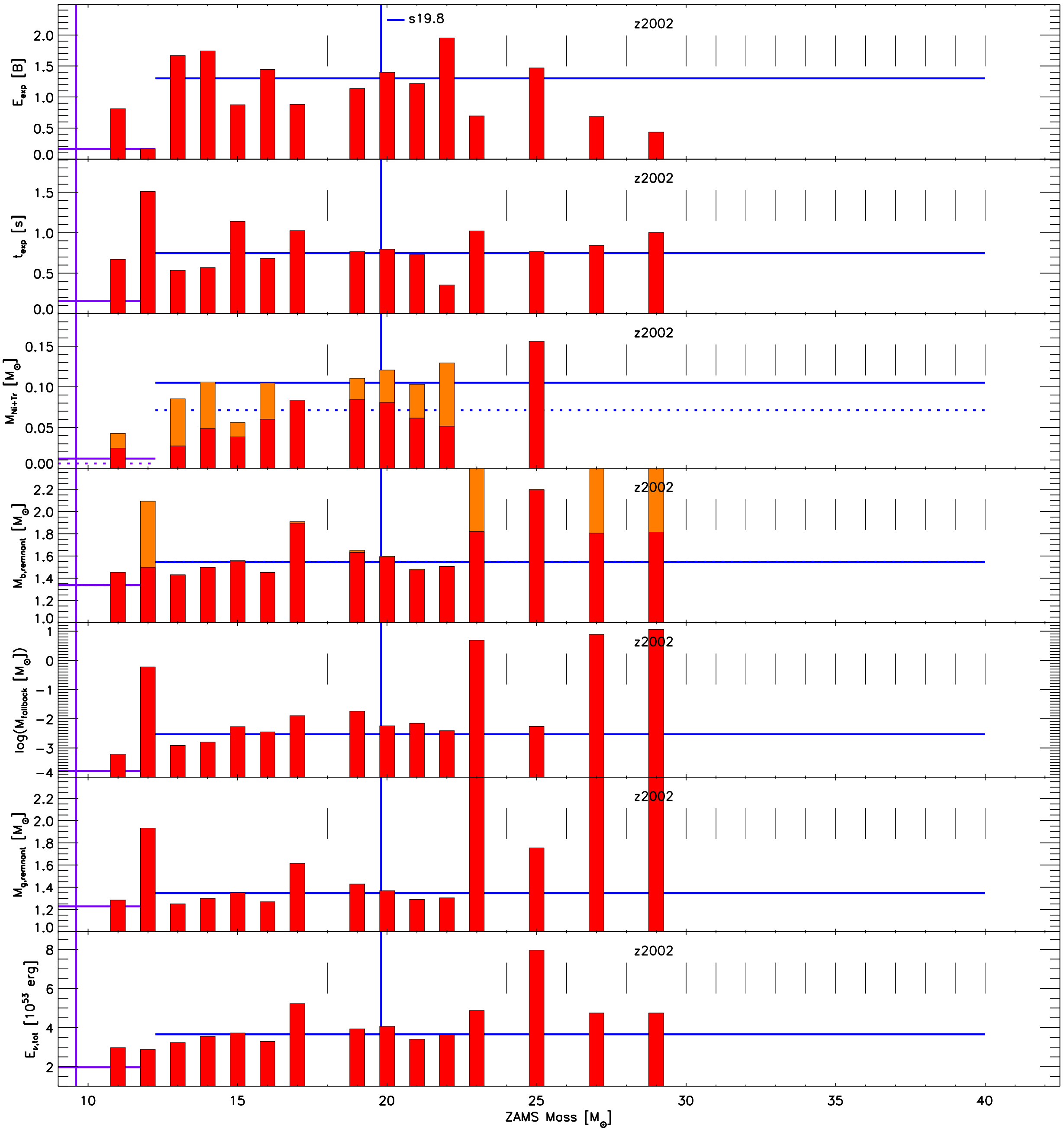

Figure B.30.: Same as Fig. B.1, but for the model set z2002 simulated with the s19.8 calibration combined with the z9.6 calibration for low-mass stars.

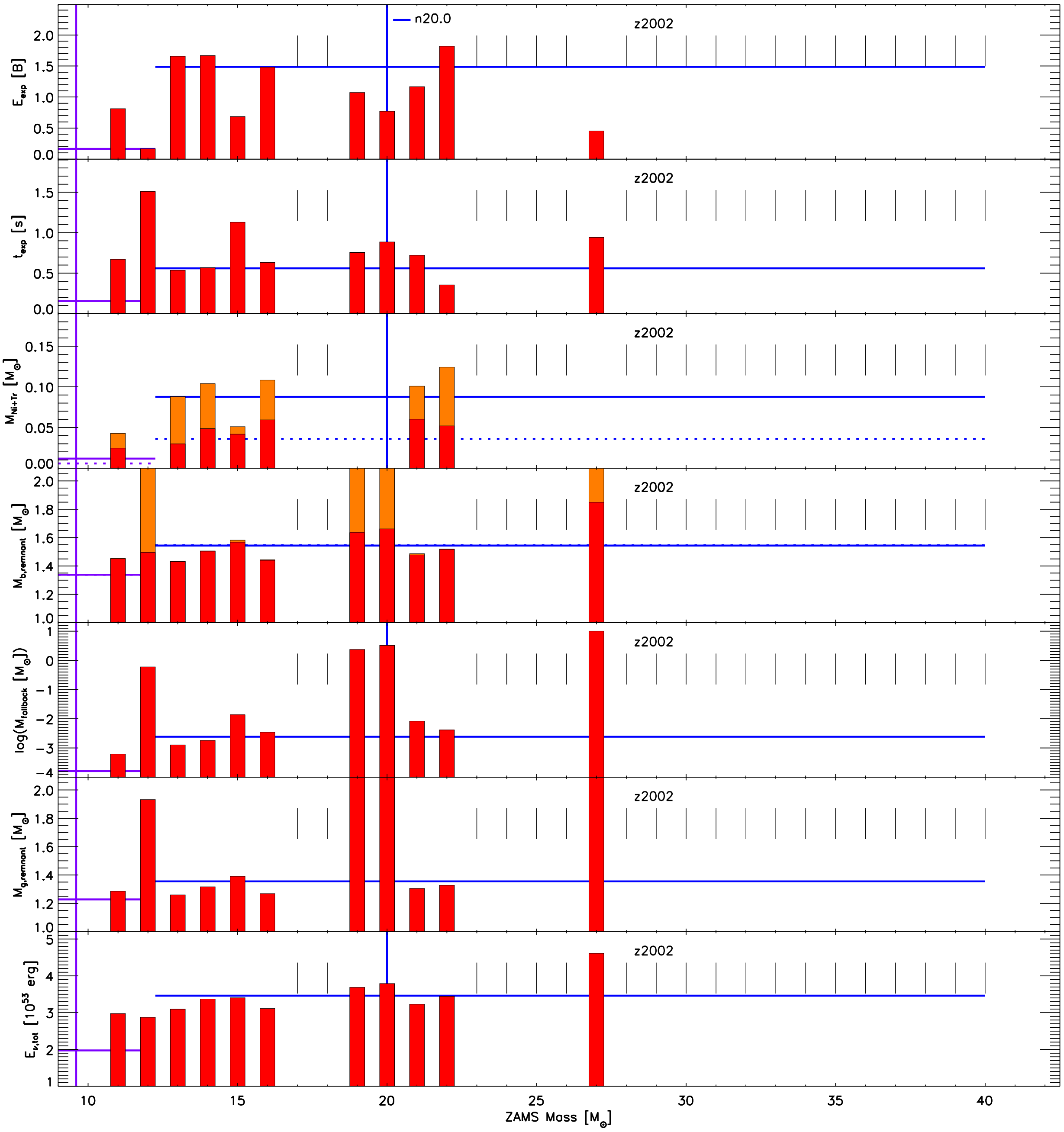

Figure B.31.: Same as Fig. B.1, but for the model set z2002 simulated with the n20.0 calibration combined with the z9.6 calibration for low-mass stars.

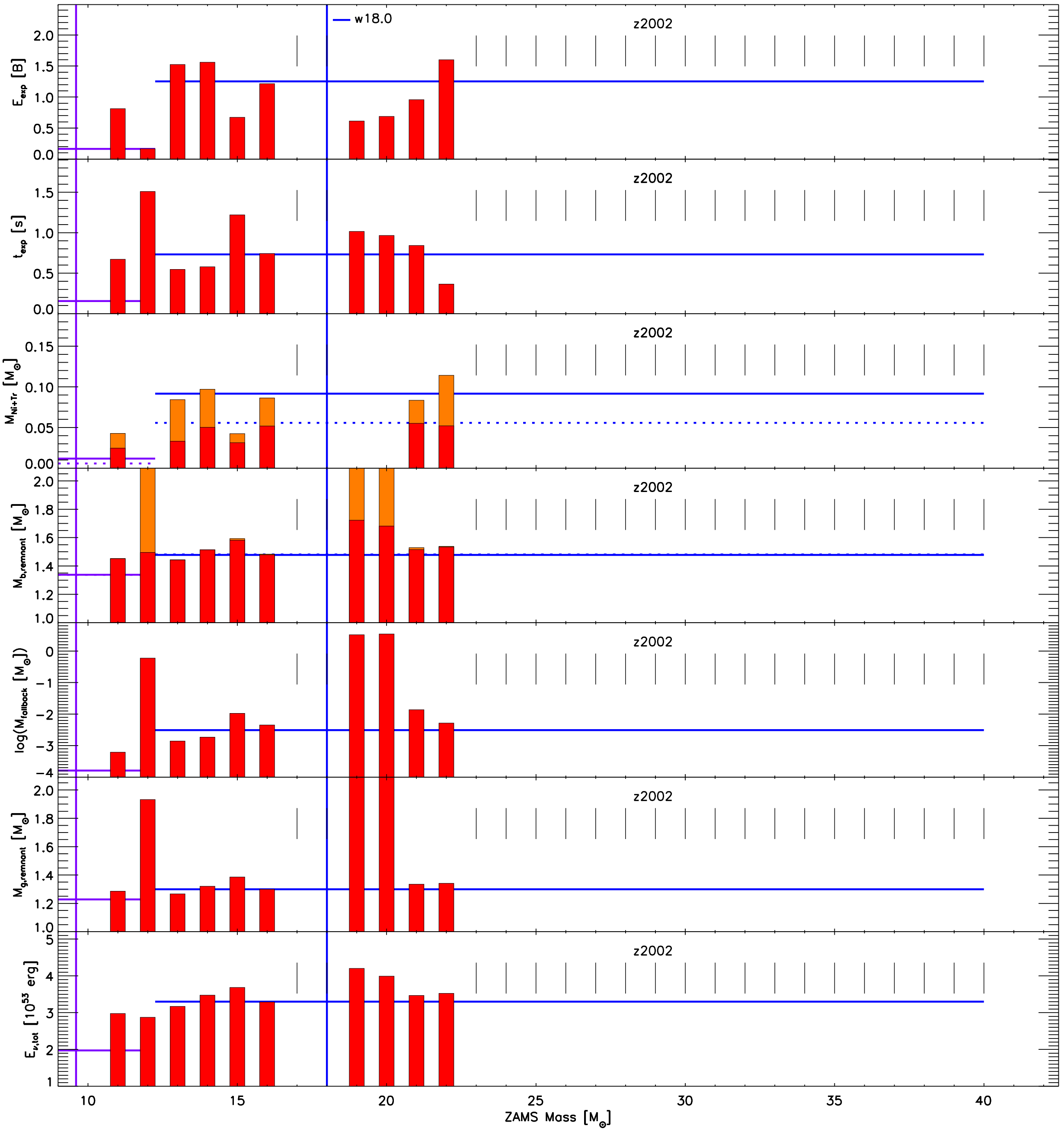

Figure B.32.: Same as Fig. B.1, but for the model set z2002 simulated with the w18.0 calibration combined with the z9.6 calibration for low-mass stars.

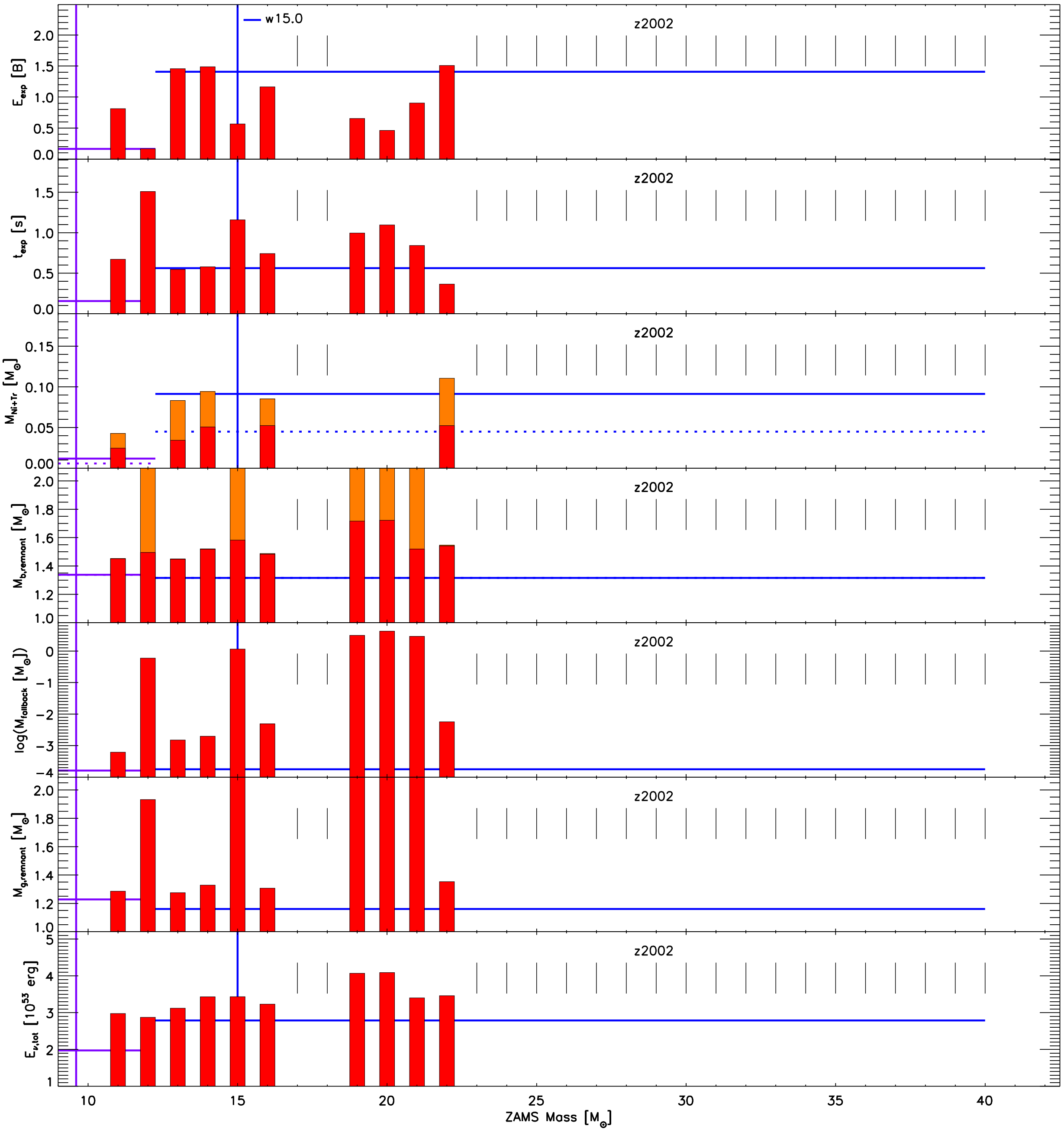

Figure B.33.: Same as Fig. B.1, but for the model set z2002 simulated with the w15.0 calibration combined with the z9.6 calibration for low-mass stars.

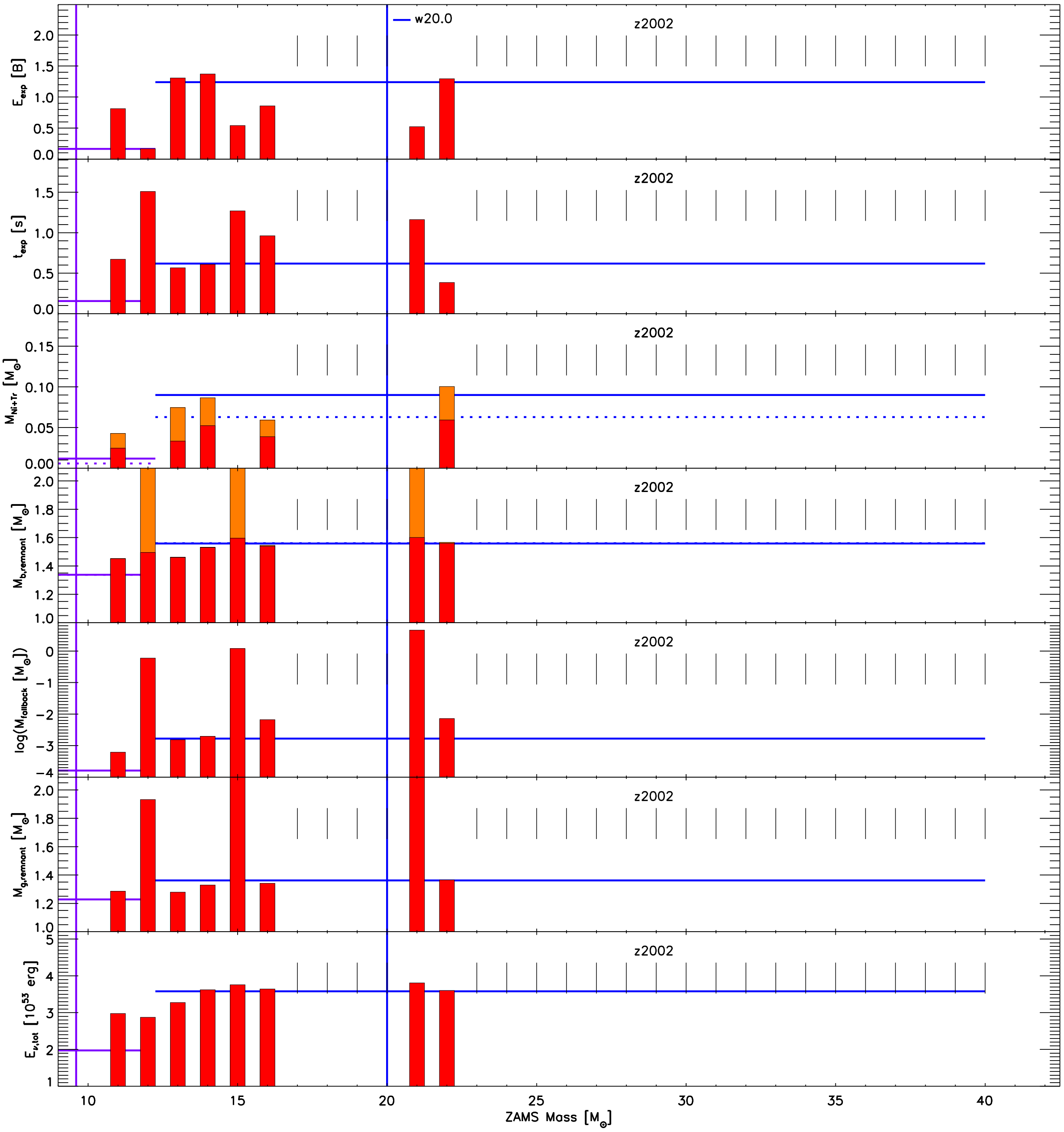

Figure B.34.: Same as Fig. B.1, but for the model set z2002 simulated with the w20.0 calibration combined with the z9.6 calibration for low-mass stars.

C. List of Abbreviations

1D	Spherically symmetric
2D	Axially symmetric
3D	Full geometry
BH(s)	Black hole(s)
CCSN(e)	Core-collapse supernova(e)
CMA	Consistent multi-fluid advection by Plewa & Müller (1999)
EOS	Equation of state
FBH	Black hole collapse by late-time fallback
GR	General relativity
GW	Gravitational Waves
HR	Hertzsprung-Russel
IMF	Initial mass function
ISM	Interstellar medium
L&S 220	High-density EOS by Lattimer & Swesty (1991) with a compressibility of $K = 220\,\mathrm{MeV}$
LMC	Large Magellanic Cloud
NSE	Nuclear statistical equilibrium
(P)NS(s)	(Proto-)neutron star(s)
PPM	Piecewise parabolic method
SN(e)	Supernova(e)
Tr	Iron-group tracer element
TOV	Tolman-Oppenheimer-Volkoff
ZAMS	Zero-age main-sequence mass

Bibliography

Abbott, B. P., Abbott, R., Abbott, T. D., et al. 2016, Physical Review Letters, 116, 061102

Antoniadis, J., Freire, P. C. C., Wex, N., et al. 2013, Science, 340, 448

Arcones, A. & Janka, H.-T. 2011, A&A, 526, A160

Arcones, A., Janka, H.-T., & Scheck, L. 2007, A&A, 467, 1227

Arnett, W. D., Bahcall, J. N., Kirshner, R. P., & Woosley, S. E. 1989, ARA&A, 27, 629

Arnett, W. D. & Meakin, C. 2011, ApJ, 733, 78

Arnett, W. D., Meakin, C., Viallet, M., et al. 2015, ApJ, 809, 30

Aufderheide, M. B., Baron, E., & Thielemann, F.-K. 1991, ApJ, 370, 630

Baade, W. & Zwicky, F. 1934, Proceedings of the National Academy of Science, 20, 254

Belczynski, K., Wiktorowicz, G., Fryer, C. L., Holz, D. E., & Kalogera, V. 2012, ApJ, 757, 91

Bethe, H. A. 1990, Reviews of Modern Physics, 62, 801

Bionta, R. M., Blewitt, G., Bratton, C. B., Casper, D., & Ciocio, A. 1987, Physical Review Letters, 58, 1494

Bouchet, P., Phillips, M. M., Suntzeff, N. B., et al. 1991, A&A, 245, 490

Brown, J. M. & Woosley, S. E. 2013, ApJ, 769, 99

Bruenn, S. W., Lentz, E. J., Hix, W. R., et al. 2016, ApJ, 818, 123

Bruenn, S. W., Mezzacappa, A., Hix, W. R., et al. 2013, ApJ, 767, L6

Buras, R., Janka, H.-T., Rampp, M., & Kifonidis, K. 2006a, A&A, 457, 281

Buras, R., Rampp, M., Janka, H.-T., & Kifonidis, K. 2003, Physical Review Letters, 90, 241101

Buras, R., Rampp, M., Janka, H.-T., & Kifonidis, K. 2006b, A&A, 447, 1049

Burrows, A. 2013, Reviews of Modern Physics, 85, 245

Burrows, A. & Goshy, J. 1993, ApJ, 416, L75

Chabrier, G. 2003, PASP, 115, 763

Chevalier, R. A. 1989, ApJ, 346, 847

Clausen, D., Piro, A. L., & Ott, C. D. 2015, ApJ, 799, 190

Colella, P. & Glaz, H. M. 1985, Journal of Computational Physics, 59, 264

Colella, P. & Woodward, P. R. 1984, Journal of Computational Physics, 54, 174

Colgate, S. A. & White, R. H. 1966, ApJ, 143, 626

Couch, S. M. 2013, ApJ, 775, 35

Couch, S. M., Chatzopoulos, E., Arnett, W. D., & Timmes, F. X. 2015, ApJ, 808, L21

Couch, S. M. & O'Connor, E. P. 2014, ApJ, 785, 123

Couch, S. M. & Ott, C. D. 2013, ApJ, 778, L7

Couch, S. M. & Ott, C. D. 2015, ApJ, 799, 5

Crowther, P. A., Lennon, D. J., & Walborn, N. R. 2006, A&A, 446, 279

Demorest, P. B., Pennucci, T., Ransom, S. M., Roberts, M. S. E., & Hessels, J. W. T. 2010, Nature, 467, 1081

Dessart, L., Hillier, D. J., Livne, E., et al. 2011, MNRAS, 414, 2985

Dolence, J. C., Burrows, A., Murphy, J. W., & Nordhaus, J. 2013, ApJ, 765, 110

Dolence, J. C., Burrows, A., & Zhang, W. 2015, ApJ, 800, 10

Einfeldt, B. 1988, Shock tubes and waves; Proceedings of the Sixteenth International Symposium, Aachen, Federal Republic of Germany, July 26-31, 1987, VCH Verlagsgesellschaft mbH, Weinheim, Germany, 671

Eldridge, J. J., Fraser, M., Smartt, S. J., Maund, J. R., & Crockett, R. M. 2013, MNRAS, 436, 774

Ertl, T. 2012, diploma thesis, Technische Universität München

Ertl, T., Janka, H.-T., Woosley, S. E., Sukhbold, T., & Ugliano, M. 2016a, ApJ, 818, 124

Ertl, T., Ugliano, M., Janka, H.-T., Marek, A., & Arcones, A. 2016b, ApJ, 821, 69

Farr, W. M., Sravan, N., Cantrell, A., et al. 2011, ApJ, 741, 103

Fernández, R. 2012, ApJ, 749, 142

Fischer, T., Whitehouse, S. C., Mezzacappa, A., Thielemann, F.-K., & Liebendörfer, M. 2010, A&A, 517, A80

Fransson, C. & Kozma, C. 2002, New A Rev., 46, 487

Fryer, C. L., Belczynski, K., Wiktorowicz, G., et al. 2012, ApJ, 749, 91

Fryxell, B., Müller, E., & Arnett, W. 1989, Hydrodynamics and Nuclear Burning, preprint MPA-Preprint 449, Max Planck Institut für Astrophysik, Garching

Hamuy, M. 2003, ApJ, 582, 905

Handy, T., Plewa, T., & Odrzywołek, A. 2014, ApJ, 783, 125

Hanke, F. 2014, PhD thesis, Technische Universität München

Hanke, F., Marek, A., Müller, B., & Janka, H.-T. 2012, ApJ, 755, 138

Hanke, F., Müller, B., Wongwathanarat, A., Marek, A., & Janka, H.-T. 2013, ApJ, 770, 66

Heger, A. 2003, private communication

Heger, A. 2015, private communication

Heger, A. & Woosley, S. E. 2010, ApJ, 724, 341

Hester, J. J. 2008, ARA&A, 46, 127

Hillebrandt, W. & Niemeyer, J. C. 2000, ARA&A, 38, 191

Hirata, K., Kajita, T., Koshiba, M., Nakahata, M., & Oyama, Y. 1987, Physical Review Letters, 58, 1490

Horiuchi, S., Beacom, J. F., Kochanek, C. S., et al. 2011, ApJ, 738, 154

Horiuchi, S., Nakamura, K., Takiwaki, T., Kotake, K., & Tanaka, M. 2014, MNRAS, 445, L99

Humphreys, R. M. & McElroy, D. B. 1984, ApJ, 284, 565

Janka, H.-T. 2001, A&A, 368, 527

Janka, H.-T. 2012, Annual Review of Nuclear and Particle Science, 62, 407

Janka, H.-T., Hanke, F., Hüdepohl, L., et al. 2012, Progress of Theoretical and Experimental Physics, 2012, 01A309

Janka, H.-T. & Keil, W. 1998, in Supernovae and cosmology, ed. L. Labhardt, B. Binggeli, & R. Buser, 7

Janka, H.-T., Kifonidis, K., & Rampp, M. 2001, in Lecture Notes in Physics, Berlin Springer Verlag, Vol. 578, Physics of Neutron Star Interiors, ed. D. Blaschke, N. K. Glendenning, & A. Sedrakian, 333

Janka, H.-T., Langanke, K., Marek, A., Martínez-Pinedo, G., & Müller, B. 2007, Phys. Rep., 442, 38

Janka, H.-T., Müller, B., Kitaura, F. S., & Buras, R. 2008, A&A, 485, 199

Janka, H.-T. & Müller, E. 1996, A&A, 306, 167

Kasen, D. & Bildsten, L. 2010, ApJ, 717, 245

Kifonidis, K. 2004, private communication

Kifonidis, K., Plewa, T., Janka, H.-T., & Müller, E. 2003, A&A, 408, 621

Kifonidis, K., Plewa, T., Scheck, L., Janka, H.-T., & Müller, E. 2006, A&A, 453, 661

Kitaura, F. S., Janka, H.-T., & Hillebrandt, W. 2006, A&A, 450, 345

Kreidberg, L., Bailyn, C. D., Farr, W. M., & Kalogera, V. 2012, ApJ, 757, 36

Langanke, K., Martínez–Pinedo, G., Sampaio, J. M., et al. 2003, Physical Review Letters, 90, 241102

Lattimer, J. M. & Prakash, M. 2001, ApJ, 550, 426

Lattimer, J. M. & Swesty, D. F. 1991, Nuclear Physics A, 535, 331

Lattimer, J. M. & Yahil, A. 1989, ApJ, 340, 426

Lentz, E. J., Bruenn, S. W., Hix, W. R., et al. 2015, ApJ, 807, L31

Liebendörfer, M. 2005, ApJ, 633, 1042

Lodders, K. 2003, ApJ, 591, 1220

Lovegrove, E. & Woosley, S. E. 2013, ApJ, 769, 109

Marek, A., Dimmelmeier, H., Janka, H.-T., Müller, E., & Buras, R. 2006, A&A, 445, 273

Marek, A. & Janka, H.-T. 2009, ApJ, 694, 664

Mazzali, P. A., McFadyen, A. I., Woosley, S. E., Pian, E., & Tanaka, M. 2014, MNRAS, 443, 67

Melson, T., Janka, H.-T., Bollig, R., et al. 2015a, ApJ, 808, L42

Melson, T., Janka, H.-T., & Marek, A. 2015b, ApJ, 801, L24

Mezzacappa, A., Bruenn, S. W., Lentz, E. J., et al. 2015, ArXiv e-prints

Mirizzi, A., Tamborra, I., Janka, H.-T., et al. 2016, Nuovo Cimento Rivista Serie, 39, 1

Mueller, E. 1986, A&A, 162, 103

Müller, B. 2013, private communication

Müller, B. 2015, MNRAS, 453, 287

Müller, B., Heger, A., Liptai, D., & Cameron, J. B. 2016a, MNRAS, 460, 742

Müller, B. & Janka, H.-T. 2014, ApJ, 788, 82

Müller, B. & Janka, H.-T. 2015, MNRAS, 448, 2141

Müller, B., Janka, H.-T., & Heger, A. 2012a, ApJ, 761, 72

Müller, B., Janka, H.-T., & Marek, A. 2012b, ApJ, 756, 84

Müller, B., Janka, H.-T., & Marek, A. 2013, ApJ, 766, 43

Müller, B., Viallet, M., Heger, A., & Janka, H.-T. 2016b, ArXiv e-prints

Murphy, J. W. & Burrows, A. 2008, ApJ, 688, 1159

Nadezhin, D. K. 1980, Ap&SS, 69, 115

Nakamura, K., Takiwaki, T., Kuroda, T., & Kotake, K. 2015, PASJ, 67, 107

Nomoto, K. 1987, ApJ, 322, 206

Nomoto, K. & Hashimoto, M. 1988, Phys. Rep., 163, 13

Nomoto, K., Sugimoto, D., Sparks, W. M., et al. 1982, Nature, 299, 803

Nomoto, K., Tominaga, N., Umeda, H., Kobayashi, C., & Maeda, K. 2006, Nuclear Physics A, 777, 424

Nordhaus, J., Burrows, A., Almgren, A., & Bell, J. 2010, ApJ, 720, 694

O'Connor, E. & Couch, S. 2015, ArXiv e-prints

O'Connor, E. & Ott, C. D. 2011, ApJ, 730, 70

Özel, F. & Freire, P. 2016, Annual Review of Astronomy and Astrophysics, 54 (Volume publication date September 2016)

Özel, F., Psaltis, D., Narayan, R., & McClintock, J. E. 2010, ApJ, 725, 1918

Pejcha, O. & Thompson, T. A. 2012, ApJ, 746, 106

Pejcha, O. & Thompson, T. A. 2015, ApJ, 801, 90

Perego, A., Hempel, M., Fröhlich, C., et al. 2015, ApJ, 806, 275

Plewa, T. & Müller, E. 1999, A&A, 342, 179

Poznanski, D. 2013, MNRAS, 436, 3224

Rampp, M. & Janka, H.-T. 2002, A&A, 396, 361

Reynolds, T. M., Fraser, M., & Gilmore, G. 2015, MNRAS, 453, 2885

Saio, H., Nomoto, K., & Kato, M. 1988, Nature, 334, 508

Salpeter, E. E. 1955, ApJ, 121, 161

Scheck, L., Janka, H.-T., Foglizzo, T., & Kifonidis, K. 2008, A&A, 477, 931

Scheck, L., Kifonidis, K., Janka, H.-T., & Müller, E. 2006, A&A, 457, 963

Scheck, L., Plewa, T., Janka, H.-T., Kifonidis, K., & Müller, E. 2004, Physical Review Letters, 92, 011103

Sedov, L. I. 1959, Similarity and Dimensional Methods in Mechanics

Shigeyama, T. & Nomoto, K. 1990, ApJ, 360, 242

Shigeyama, T., Nomoto, K., & Hashimoto, M. 1988, A&A, 196, 141

Smartt, S. J. 2015, PASA, 32, e016

Smartt, S. J., Eldridge, J. J., Crockett, R. M., & Maund, J. R. 2009, MNRAS, 395, 1409

Smith, N. 2007, AJ, 133, 1034

Smith, N. 2013, MNRAS, 434, 102

Spiro, S., Pastorello, A., Pumo, M. L., et al. 2014, MNRAS, 439, 2873

Steiner, A. W., Hempel, M., & Fischer, T. 2013, ApJ, 774, 17

Sukhbold, T., Ertl, T., Woosley, S. E., Brown, J. M., & Janka, H.-T. 2016, ApJ, 821, 38

Sukhbold, T. & Woosley, S. E. 2014, ApJ, 783, 10

Summa, A., Hanke, F., Janka, H.-T., et al. 2016, ApJ, 825, 6

Suntzeff, N. B., Phillips, M. M., Elias, J. H., Walker, A. R., & Depoy, D. L. 1992, ApJ, 384, L33

Suwa, Y. 2012, in IAU Symposium, Vol. 279, Death of Massive Stars: Supernovae and Gamma-Ray Bursts, ed. P. Roming, N. Kawai, & E. Pian, 397–398

Suwa, Y., Yamada, S., Takiwaki, T., & Kotake, K. 2016, ApJ, 816, 43

Takiwaki, T., Kotake, K., & Suwa, Y. 2014, ApJ, 786, 83

Tamborra, I., Hanke, F., Janka, H.-T., et al. 2014, ApJ, 792, 96

Thielemann, F.-K., Nomoto, K., & Hashimoto, M.-A. 1996, ApJ, 460, 408

Thompson, C. 2000, ApJ, 534, 915

Thompson, T. A., Quataert, E., & Burrows, A. 2005, ApJ, 620, 861

Timmes, F. X. & Swesty, F. D. 2000, ApJS, 126, 501

Tominaga, N., Blinnikov, S. I., & Nomoto, K. 2013, ApJ, 771, L12

Ugliano, M. 2012, PhD thesis, Technische Universität München

Ugliano, M., Janka, H.-T., Marek, A., & Arcones, A. 2012, ApJ, 757, 69

Utrobin, V. P. 2005, Astronomy Letters, 31, 806

Utrobin, V. P. & Chugai, N. N. 2011, A&A, 532, A100

Utrobin, V. P., Wongwathanarat, A., Janka, H.-T., & Müller, E. 2015, A&A, 581, A40

Valentim, R., Rangel, E., & Horvath, J. E. 2011, MNRAS, 414, 1427

Walborn, N. R., Lasker, B. M., Laidler, V. G., & Chu, Y.-H. 1987, ApJ, 321, L41

Wanajo, S., Janka, H.-T., & Müller, B. 2011, ApJ, 726, L15

Weaver, T. A., Zimmerman, G. B., & Woosley, S. E. 1978, ApJ, 225, 1021

Wiktorowicz, G., Belczynski, K., & Maccarone, T. 2014, in Binary Systems, their Evolution and Environments, 37

Wilson, J. R. 1985, in Numerical Astrophysics, ed. J. M. Centrella, J. M. Leblanc, & R. L. Bowers, 422

Wongwathanarat, A., Janka, H.-T., & Müller, E. 2013, A&A, 552, A126

Wongwathanarat, A., Müller, E., & Janka, H.-T. 2015, A&A, 577, A48

Woosley, S. E. 1988, ApJ, 330, 218

Woosley, S. E. 2007, private communication

Woosley, S. E. 2010, ApJ, 719, L204

Woosley, S. E. & Heger, A. 2007, Phys. Rep., 442, 269

Woosley, S. E. & Heger, A. 2015, ApJ, 810, 34

Woosley, S. E., Heger, A., & Weaver, T. A. 2002, Reviews of Modern Physics, 74, 1015

Woosley, S. E., Heger, A., Weaver, T. A., & Langer, N. 1997, ArXiv Astrophysics e-prints

Woosley, S. E., Heger, A., Weaver, T. A., & Langer, N. 2007, private communication

Woosley, S. E., Pinto, P. A., & Ensman, L. 1988, ApJ, 324, 466

Woosley, S. E. & Weaver, T. A. 1995, ApJS, 101, 181

Yang, H. & Chevalier, R. A. 2015, ApJ, 806, 153

Zhang, W., Woosley, S. E., & Heger, A. 2008, ApJ, 679, 639

Danksagung

Allem vorweg möchte ich mich bei meinen Eltern und meinen Geschwistern für die Unterstützung während der dreieinhalb Jahre Doktorarbeit bedanken.

Ein besonderer Dank gebührt meinem Betreuer PD Dr. Hans-Thomas Janka, der immer verfügbar war, immer konstruktiv und kritisch nachgefragt hat.

Ich bin dem MPA und dem Exzellenzcluster Universe für die Ermöglichung dieser Doktorarbeit sehr dankbar.

Meine Zeit am MPA, vor allem als Doktorandenvertreter, habe ich sehr genossen, wofür ich mich bei allen am Institut bedanken will. Einigen will ich jedoch im Folgenden besonderes danken:

Marcella Ugliano, die mich mit dem Code und ihrer Arbeit vertraut machte, und auch nach ihrer Zeit am MPA immer für Fragen und Diskussionen zur Verfügung stand.

Tobias Melson, der weite Teile dieser Arbeit korrekturgelesen hat und aber vielmehr dafür, dass er ein angenehmer Bürokollege und guter Freund ist.

Tyrone Woods for being a perfect office mate and a good friend.

Alexander Summa für das Korrekturlesen dieser Arbeit und als ausgezeichneter Begleiter für jede Reise, dem kein Weg zu weit ist.

Oliver Just für das hilfreiche Beantworten von Fragen während meiner ganzen Zeit am MPA und auch für das Korrekturlesen der Einleitung.

Den Admins am Institut und im Besonderen Andi Weiss.

Frank Schindler, der als Werkstudent sehr sogfältig gearbeitet hat und mir damit die Auswertung in Kapitel 7 sehr erleichtert hat.

Allen in unserer Arbeitsgruppe, die ich hier vielleicht nicht explizit erwähnt habe, die aber für ein angenehmes Arbeitsumfeld unersetzlich waren.

A special thanks goes to my collaborators, Stan E. Woosley, Tuguldur Sukhbold, and Justin Brown as well as Alexander Heger for providing his primordial stars.